

ABSTRACT

Title of dissertation: An Experimental Investigation
 of Ground Effect on a Quad Tilt Rotor
 in Hover and Low Speed Forward Flight

Anand Radhakrishnan, Doctor of Philosophy, 2006

Dissertation directed by: Professor Fredric H. Schmitz
 Department of Aerospace Engineering

The performance of a Quad Tilt Rotor (QTR) in helicopter mode was experimentally studied in ground effect (IGE) and out of ground effect (OGE). A 0.03 geometrically scaled fuselage/wing model of the QTR was tested in hover and very low speed forward flight. Fixed-pitch propellers were used to model the rotors. In order to avoid the boundary layer problems associated with wind tunnel testing of rotorcraft IGE, a unique moving setup was developed for testing in forward flight. The effect of ground proximity was tested by varying the height of the model above the ground. Download on the airframe; thrust, torque and rpm of the rotors, and pressures along the centerline of the bottom of the fuselage were measured. The downwash distributions of the rotors were measured and found to compare well with V-22 rotor measurements. Tuft flow visualization was used to identify the physical processes causing changes in the download and pressure measurements. An uncertainty analysis was performed on the measured quantities to determine the 95% confidence levels.

A strong download (9% of the rotor thrust) was observed in hover, OGE. The download reduced substantially IGE and become an upload (9% of the rotor thrust), when the wheels of the QTR were on the ground. The upload IGE was found to be caused by the entrapment of the rotor wakes under the fuselage. The upload was observed to persist in forward flight IGE, but reduced slightly at certain low skew angles. The measured downloads, coupled with power measurements, indicate that for a given power, the available vehicle thrust greatly increases IGE. Therefore, the QTR displays a potential for significant increase in payload carrying capacity by operating IGE.

AN EXPERIMENTAL INVESTIGATION OF GROUND EFFECT
ON A QUAD TILT ROTOR IN HOVER AND LOW SPEED
FORWARD FLIGHT

by

Anand Radhakrishnan

Dissertation submitted to the Faculty of the Graduate School of the
University of Maryland, College Park in partial fulfillment
of the requirements for the degree of
Doctor of Philosophy
2006

Advisory Committee:
Professor Fredric H. Schmitz, Chair/Advisor
Professor James D. Baeder
Professor Christopher Cadou
Professor Inderjit Chopra
Professor James Wallace

© Copyright by
Anand Radhakrishnan
2006

Dedication

To my parents.

ACKNOWLEDGMENTS

I would like to express my gratitude to my advisor, Dr. Fredric Schmitz, for his constant guidance and support over the last six years. I have gained a lot of knowledge from him, both about engineering and about life.

I would like to thank the members of my committee, Dr. James Baeder, Dr. Chris Cadou, Dr. Inderjit Chopra and Dr. James Wallace, both for their time and for their advice.

I would like to acknowledge Dr. Tom Wood of Bell Helicopter Textron for supporting my research and lending his valuable time and resources.

Fellow graduate students, Sudharshana Kaushik and Eric Greenwood, have been especially helpful by lending me a hand with my experiments and with their insights into my research. I am also indebted to Dr. Ben Sim, who has also sacrificed his time and his holidays in order to help me out. The students and faculty at the Rotorcraft Center have made it a wonderful place for me to spend the past six years of my life.

I would like to thank my parents, my brother and the rest of my family for their constant words of encouragement throughout my academic career and my life. I would also like to thank my girlfriend, Yyannu, and my friends, Sudharsan, Sean, Isabel and many others who have helped me along the way.

Table of Contents

List of Tables	viii
List of Figures	ix
1 Introduction	1
1.1 QTR Design and Configuration	3
1.2 Problem Statement	5
1.2.1 Download Problem in Helicopter Mode	6
1.2.2 Challenges in Low Speed Testing	9
1.3 Background	11
1.3.1 Helicopters	11
1.3.2 Tilt Rotors	12
1.3.2.1 Tilt Rotor Development	14
1.4 Survey of V/STOL Performance Research in Hover and Low Speed Forward Flight	17
1.4.1 Research on Rotor Performance, IGE	18
1.4.1.1 Hover	18
1.4.1.2 Low Speed Forward Flight	19
1.4.2 Previous Investigations on Tilt Rotors in Hover	22
1.4.2.1 Experimental Investigations	22
1.4.2.2 Computational/Analytical Studies	25
1.4.3 Tilt Rotor Investigations in Low Speed Flight	27
1.4.4 QTR Investigations in Hover	29
1.4.4.1 Experimental Studies	29
1.4.4.2 Computational Studies	31
1.4.5 QTR Investigations in Low Speed Forward Flight	33
1.4.6 Summary of Previous Research	34
1.5 Research Objectives	35
1.5.1 Experimentally Obtain QTR Performance	36
1.5.2 Understanding of Mechanisms Causing Changes in QTR Performance	37
1.5.3 Scalability, Verification and Validation of the Results	37
1.6 Dissertation Outline	38
2 Approach	40
2.1 Vertical Force Balance	40
2.2 Dimensional Analysis	42
2.2.1 Forces	42
2.2.1.1 Download to Thrust Ratio	43
2.2.1.2 Normalized Height	44
2.2.1.3 Rotor Wake Skew Angle	45
2.2.1.4 Wing Drag Coefficient	46
2.2.1.5 Wing Reynolds Number	47

2.2.1.6	Downwash Distribution	47
2.2.2	Rotor Power	48
2.2.2.1	Rotor Induced Power	48
2.2.2.2	Rotor Profile Power	50
2.2.3	Pressure Coefficient	51
2.3	Experimental Approach and Scaling	52
2.4	Experimental Setup	56
2.4.1	Model Configuration	56
2.4.1.1	Airframe Model	56
2.4.1.2	Rotor Assembly	59
2.4.2	Drive Mechanism	60
2.4.3	Mounting	60
2.4.3.1	Motor Mount	60
2.4.3.2	Airframe Mount	66
2.4.4	Pressure Measurement	67
2.4.5	Instrumentation and Data Acquisition	69
2.4.6	Equipment for Forward Flight Testing	70
2.4.7	Test Location	72
2.4.8	Test Assumptions	73
2.5	Test Objectives	74
2.6	Uncertainty Analysis	74
2.7	Flow Visualization	75
3	Isolated Rotor	77
3.1	Rotor Description	77
3.2	Rotor Geometry	77
3.3	Isolated Rotor Performance	80
3.4	Ground Effect on Rotor Performance	82
3.5	Rotor Wake Velocimetry	84
4	Quad Tilt Rotor in Hover	88
4.1	Test Procedure	89
4.2	Download to Thrust Ratios	89
4.2.1	Download at the front and rear airframe mounts	90
4.2.2	Effect of varying the disk loading	92
4.2.3	Effect of varying the flap angle	93
4.3	Comparison with previous studies	95
4.3.1	Experiments	95
4.3.2	CFD studies	95
4.4	Power Consumption	99
4.4.1	Power Required For a Given Vehicle Thrust	99
4.4.1.1	Corrections for Profile Effects	99
4.4.1.2	Corrections for Induced Effects	101
4.4.1.3	Power Ratio	103
4.4.2	Available Thrust For A Given Power	104

4.5	Pressure Measurements	106
5	QTR in Low Speed Forward Flight	112
5.1	Test Procedure	112
5.2	Download to Thrust Ratios	113
5.2.1	Download at the front and rear airframe mounts	119
5.3	Power Required For a Given Vehicle Thrust	128
5.3.1	Corrections for Profile Effects	128
5.3.2	Corrections for Induced Effects	129
5.3.3	Power Ratio	130
5.4	Available Thrust For A Given Power	134
5.5	Pressure Measurements	138
5.6	Comparison with CFD	144
6	Flow Visualization	147
6.1	Camera Angles	147
6.2	Hover	149
6.2.1	Top Surface	149
6.2.2	Bottom Surface	152
6.2.3	Ground Flow Images	155
6.3	Low Speed Forward Flight	158
6.3.1	Top Surface Flow Patterns	158
6.3.2	Ground Plane	161
6.4	Comparison with CFD	166
6.4.1	Hover	166
6.4.2	Low Speed Forward Flight	172
6.5	Comparison with Previous Experiment	172
7	Closure	174
7.1	Conclusions	175
7.1.1	Experimental Approach	176
7.1.2	Hover Performance	176
7.1.3	Low Speed Forward Flight	177
7.1.4	Comparison with other studies	179
7.2	Ramifications for a Full-Scale QTR	180
7.3	Direction of Future Research	183
7.3.1	Studies on the QTR	183
7.3.1.1	Effect of Crossflow and Yaw	183
7.3.1.2	Effect of Nacelles and Sponsons	183
7.3.1.3	Configuration Studies	184
7.3.2	Testing of Other Designs	184
7.3.2.1	Tilt Rotors	184
7.3.2.2	Other V/STOL Designs	185
A	Power Corrections	186

B	Comparison with CFD QTR Geometry	189
C	Uncertainty analysis	192
C.1	Example: Download to Thrust Ratio	192
C.1.1	Define the Measurement Process	192
C.1.2	List Elemental Uncertainty Sources	193
C.1.3	Calculate Random Standard Deviation	194
C.1.4	Calculate Systematic Uncertainties	194
C.1.4.1	Calibration	194
C.1.4.2	Resolution of the DAS	195
C.1.4.3	Calibration weights	195
C.1.5	Combining Elemental Systematic Uncertainties	195
C.1.6	Total Uncertainty of the measurement	195
C.2	Uncertainty Analysis of other measurements	198
	Bibliography	199

List of Tables

1.1	Tilt-rotor experiments in hover, OGE	23
2.1	Comparison of full-scale Bell QTR with the small-scale model	54
2.2	Comparison of small-scale models that were tested	59
2.3	Longitudinal Distance of the Pressure Taps From the Nose	68
3.1	Propeller Geometry for 14x7 Master Airscrew	79
B.1	Differences between Gupta & Baeder’s CFD Geometry and the Experimental QTR Configuration	190
C.1	Absolute Values of Systematic Uncertainties of Independent Parameters for $T/A=4.7$ lb/sq.ft, at $z=1.5$	196
C.2	Absolute Contributions of Systematic Uncertainties of Independent Parameters for $T/A=4.7$ lb/sq.ft, at $z=1.5$	197
C.3	Summary: Nominal Value; Systematic, Random and Total Uncertainties in Absolute Terms for DL/T for $T/A=4.7$ lb/sq.ft, at $z=1.5$.	197
C.4	Uncertainties in Absolute Terms for DL/T for $T/A=0.9$ lb/sq.ft., at $z=1.5$	197
C.5	Uncertainties in Absolute Terms for DL/T for $T/A=0.9$ lb/sq.ft.	198

List of Figures

1.1	Artist's impression of the QTR[2]	3
1.2	Preliminary QTR arrangement[2]	4
1.3	Tilt rotor flowfield OGE (from Reference [11, 12])	7
1.4	Tilt rotor flowfield OGE (from Reference [11, 12])	8
1.5	Difference between wind-tunnel testing and actual helicopter operation near ground	10
1.6	V-22 Tilt Rotor in conversion (Courtesy of US Navy)	13
1.7	Bell XV-3 Tilt Rotor (from Reference [23])	15
1.8	Bell XV-15 Tilt Rotor (from Reference [23])	16
1.9	Helicopter in low speed flight near the ground (adapted from Curtiss, et al.,[16] and Leishman[30])	21
1.10	QTR Hover Download Model (Wood, et al.) (from Reference [5])	30
2.1	Vertical Force Balance Diagram	41
2.2	Rotor wake skew angle, χ	43
2.3	Height above the ground, z	45
2.4	Different airframe models tested	58
2.5	Mounting	62
2.6	Test Stand	63
2.7	Motor Mount	64
2.8	Sketch of the Motor Mount Apparatus	65
2.9	Airframe Mount	66
2.10	Sketch of the Airframe Mounts	67
2.11	Location of the Pressure Taps	68
2.12	Test Setup	71

2.13	Test Location	72
3.1	Radial Chord Distribution	78
3.2	Radial Twist Distribution	78
3.3	Isolated Rotor Thrust vs. RPM	80
3.4	Isolated Rotor Thrust Coefficient vs. RPM	81
3.5	Isolated Rotor Torque vs. RPM	81
3.6	Isolated Rotor Power vs. Thrust	82
3.7	Isolated Rotor Power at a constant thrust, IGE	83
3.8	Calculated Uniform Hover Induced Velocity vs. Thrust	84
3.9	Radial Distribution of Wake Downwash for 1 lb. thrust	86
3.10	Radial Distribution of Wake Downwash for 5 lbs thrust	87
4.1	Download to thrust ratio vs Height above the ground	90
4.2	Normalized Downloads measured at the front and rear airframe mount vs Height above the ground	91
4.3	Effect of varying the thrust level on Download to Thrust ratio	93
4.4	Effect of varying the flap angle on Download to Thrust ratio	94
4.5	Comparison with the experiment conducted by Wood, et al.[1]	96
4.6	Comparison with CFD (Lestari, et al.[14])	97
4.7	Comparison with CFD (Gupta and Baeder[15, 12])	98
4.8	Power Ratio vs Height above the ground	103
4.9	Available Thrust at a given power vs Height above the ground	105
4.10	Location of the Pressure Taps	107
4.11	Pressure Coefficient vs. Longitudinal distance from the nose, for z=3.5 (OGE)	108
4.12	Pressure Coefficient vs. Longitudinal distance from the nose, for z=1.14108	

4.13	Pressure Coefficient vs. Longitudinal distance from the nose, for $z=1.0109$	
4.14	Pressure Coefficient vs. Longitudinal distance from the nose, for $z=0.86109$	
4.15	Pressure Coefficient vs. Longitudinal distance from the nose, for $z=0.75110$	
4.16	Pressure Coefficient vs. Longitudinal distance from the nose, for $z=0.61$ (wheels on ground)	110
4.17	Illustration of entrapment of rotor wakes under the fuselage	111
5.1	Download to thrust ratio vs Rotor Wake Skew Angle for $z=3.5$ (OGE)	114
5.2	Download to thrust ratio vs Rotor Wake Skew Angle for $z=1.5$	115
5.3	Download to thrust ratio vs Rotor Wake Skew Angle for $z=1.14$	115
5.4	Download to thrust ratio vs Rotor Wake Skew Angle for $z=1.0$	116
5.5	Download to thrust ratio vs Rotor Wake Skew Angle for $z=0.86$	116
5.6	Download to thrust ratio vs Rotor Wake Skew Angle for $z=0.75$	117
5.7	Download to thrust ratio vs Rotor Wake Skew Angle for $z=0.61$ (wheels on ground)	118
5.8	Downloads at the front and rear airframe mounts for $z=3.5$ (OGE)	120
5.9	Downloads at the front and rear airframe mounts for $z=1.5$	121
5.10	Downloads at the front and rear airframe mounts for $z=1.14$	122
5.11	Downloads at the front and rear airframe mounts for $z=1.0$	123
5.12	Downloads at the front and rear airframe mounts for $z=0.86$	124
5.13	Downloads at the front and rear airframe mounts for $z=0.75$	125
5.14	Downloads at the front and rear airframe mounts, $z=0.61$ (wheels on ground)	126
5.15	Corrected Power Ratio vs Rotor Wake Skew Angle for $z=3.5$ (OGE)	131
5.16	Corrected Power Ratio vs Rotor Wake Skew Angle for $z=1.5$	131
5.17	Corrected Power Ratio vs Rotor Wake Skew Angle for $z=1.14$	132
5.18	Corrected Power Ratio vs Rotor Wake Skew Angle for $z=1.0$	132

5.19	Corrected Power Ratio vs Rotor Wake Skew Angle for $z=0.75$	133
5.20	Corrected Power Ratio vs Rotor Wake Skew Angle for $z=0.61$, wheels on ground	133
5.21	Vehicle Thrust Ratio vs Rotor Wake Skew Angle for $z=3.5$ (OGE) . .	135
5.22	Vehicle Thrust Ratio vs Rotor Wake Skew Angle for $z=1.5$	135
5.23	Vehicle Thrust Ratio vs Rotor Wake Skew Angle for $z=1.14$	136
5.24	Vehicle Thrust Ratio vs Rotor Wake Skew Angle for $z=1.0$	136
5.25	Vehicle Thrust Ratio vs Rotor Wake Skew Angle for $z=0.75$	137
5.26	Vehicle Thrust Ratio vs Rotor Wake Skew Angle for $z=0.61$, wheels on ground	137
5.27	Location of the Pressure Taps	139
5.28	Pressure Distribution on the Centerline of the Fuselage Bottom Sur- face for $z=3.5$ (OGE)	140
5.29	Pressure Distribution on the Centerline of the Fuselage Bottom Sur- face for $z=1.14$	140
5.30	Pressure Distribution on the Centerline of the Fuselage Bottom Sur- face for $z=1.0$	141
5.31	Pressure Distribution on the Centerline of the Fuselage Bottom Sur- face for $z=0.86$	141
5.32	Pressure Distribution on the Centerline of the Fuselage Bottom Sur- face for $z=0.75$	142
5.33	Pressure Distribution on the Centerline of the Fuselage Bottom Sur- face for $z=0.61$ (wheels on ground)	142
5.34	Comparison with CFD, OGE	145
5.35	Comparison with CFD.for $z=0.61$ (IGE, wheels on ground)	146
6.1	Camera Locations	148
6.2	Tuft Flow Visualization of Top Surface for $T/A=0.9$ lb/sq.ft.	150
6.3	Tuft Flow Visualization of Top Surface for $T/A=4.7$ lb/sq.ft.	151

6.4	Tuft Flow Visualization of Bottom Surface for $T/A=0.9$ lb/sq.ft . . .	153
6.5	Tuft Flow Visualization of Bottom Surface for $T/A=4.7$ lb/sq.ft. . . .	154
6.6	Tuft Flow Image of the Ground Plane at $z=0.61$, $T/A=0.9$ lb/sq.ft .	156
6.7	Tuft Flow Images of the Ground Plane at $z=0.61$, $T/A=4.7$ lb/sq.ft .	157
6.8	Tuft Flow Image of the Ground Plane at $z=1.14$, $T/A=0.9$ lb/sq.ft .	158
6.9	Tuft Flow Visualization of Top Surface in Forward Flight ($z=0.61$) . .	159
6.10	Tuft Flow Visualization of Top Surface in Forward Flight ($z=0.75$) . .	160
6.11	Tuft Flow Visualization of the Ground Plane in Forward Flight ($z=0.61$)	162
6.12	Tuft Flow Visualization of the Ground Plane in Forward Flight ($z=0.75$)	163
6.13	Tuft Flow Visualization of the Ground Plane in Forward Flight ($z=1.0$)	164
6.14	CFD Surface velocity vectors in hover (OGE), from Gupta[12]	168
6.15	CFD Surface Velocity vectors in hover (wheels on ground, $z=0.61$), from Gupta[12]	169
6.16	CFD Velocity vectors at a vertical plane through the front rotor hub (wheels on ground, $z=0.61$), from Gupta[12]	170
6.17	CFD Velocity vectors on a plane 2 feet above the ground in forward flight (wheels on ground, $z=0.61$), from Gupta[12]	171
6.18	Smoke Flow Visualization, from Wood, et al.[1]	173
7.1	Trends of Vehicle Thrust for a Given Power in Forward Flight	181
7.2	Trends of Power Required for a Given Vehicle Thrust in Forward Flight	182
A.1	Rotor Induced Power Correction Factor vs. Thrust Coefficient (from Bartie, et al.[79]	188
B.1	Overlay of the QTR Geometries used for the experimental and CFD studies	191

Nomenclature

A	rotor disk area
C_P	rotor power coefficient
C_{P0}	rotor profile power coefficient
C_{Pi}	rotor induced power coefficient
C_T	rotor thrust coefficient
D	rotor diameter, ft
DL	total download, lbs
DL_f	download at the front airframe mount, lbs
DL_r	download at the rear airframe mount, lbs
DL/T	download-to-thrust ratio %
K_i	non-uniform inflow correction factor
P	rotor power, lb.ft/sec
P_{av}	rotor power available, lb.ft/sec
P_{0j}	rotor profile power, lb.ft/sec
P_{ij}	rotor induced power, lb. ft/sec
$P_{j_{corr}}$	rotor corrected induced power, lb.ft/sec
P_{corr}	total corrected induced power, lb.ft/sec
P^*	induced power ratio, $\frac{P_{corr}}{(P_{corr})_{hover, OGE}}$
R	rotor radius, ft
T	rotor thrust, lbs
T_{av}	total vehicle thrust available for a given power, $\sum_{j=1}^4 T_i + DL_f + DL_r$, lbs

T_{av}^*	vehicle thrust ratio
T_{veh}	total vehicle thrust, $\sum_{j=1}^4 T_i + DL_f + DL_r$, lbs
T_{set}	given total vehicle thrust, lbs
T/A	rotor disk loading, lbs/sq.foot
U_p	Absolute total uncertainty in parameter 'p'
V_∞	forward speed, feet/sec
v_h	hover induced velocity, $\sqrt{\frac{T}{2\rho A}}$, feet/sec
v_i	rotor induced velocity, feet/sec
z	front rotor height above ground, feet
χ	rotor wake skew angle, $\tan^{-1}\left(\frac{V_\infty}{v_i}\right)^\circ$
Ω	rotor rotational speed
κ	induced power coefficient
ρ	Air density

List of Abbreviations

CFD	Computational Fluid Dynamics
DOD	Department of Defense
IGE	In Ground Effect
LHD	Landing Helicopter Deck
OGE	Out of Ground Effect
PDMT	Princeton Dynamic Model Track
QTR	Quad Tilt Rotor
RIA	Runway Independent Aircraft
RPM	Rotations Per Minute
TPP	Tip Path Plane
TRAM	Tilt Rotor Acoustic Model
UAV	Unmanned Air Vehicle
UM	University of Maryland
VTOL	Vertical TakeOff and Landing
V/STOL	Vertical/Short TakeOff and Landing

Chapter 1

Introduction

One of the important requirements of the military today is the ability to quickly move large numbers of troops and their supporting military equipment directly to the battlefield. Because conventional fixed-wing aircraft require friendly airstrips, these missions are accomplished by moving the supplies to nearby airports and using slower helicopters and road vehicles to provide the supply lines. The net effect is to slow the ability of troops to move quickly into battle and to limit the payloads of the re-supply efforts to those that could be lifted by the conventional helicopters. Therefore, two needs of a future military have been identified: a larger lifting capability from unprepared terrain; and an increase of the block speed of these aircraft.

The current requirements call for an aircraft that can provide the cargo-carrying capacity, range and speed of a C-130 Hercules transport aircraft, while being capable of landing and taking off directly from the battlefield[1]. This aircraft would have to be capable of satisfying the requirements of the Future Transport Rotorcraft (FTR) program of the US Army, the “Operational Maneuver from the Sea” requirement of the US Marines, the shipboard requirement of the US Navy

and the Global Rescue Mission of the DOD. The FTR program calls for carrying between 12 to 20 tons of cargo for 310 miles distance and return[1]. The US Marines mission requires the supply of 9 to 13 tons over 250 nmi, with a sea level hover OGE during take-off and a midmission hover OGE at 3000 ft[2]. The DOD Global Rescue Mission would involve rescuing a large number of people from a remote location[1]. The US Navy requires shipboard compatibility with the Landing Helicopter Deck (LHD) on existing ships[2].

In the civilian realm, the congestion of air traffic at airports has necessitated the development of Runway Independent Aircraft (RIA). These aircraft could operate from shorter runways, helipads and smaller airports[3], thereby alleviating the gridlock at major airports. However, shortening or eliminating the runway would inherently reduce the take-off efficiency of such aircraft, thereby increasing the cost of operation. Therefore, in order to be commercially viable, such transport aircraft would need to be able to carry a large payload of passengers or cargo to justify their higher operating costs.

Next generation tilt rotor aircraft are a natural choice for meeting the specifications of these military and civilian missions because of their ability to deliver payloads directly to remote areas without prepared runways at high cruise speeds. However, the maximum payload capacity of the V-22 Osprey, the largest existing tilt rotor aircraft, is limited to 6000 lbs in the VTOL configuration and 8300 lbs in the STOL configuration. Therefore, in order to satisfy the military long-range, heavy lift mission, an aircraft called the Quad Tilt Rotor (QTR), has been proposed by Bell Helicopter Textron[2].

1.1 QTR Design and Configuration

A QTR is a larger variant of a conventional V-22 tilt rotor, designed to carry higher payloads and fly at similar high cruise speeds. Conceptually, the QTR design can be visualized as two V-22 tilt rotors placed in tandem, as shown in Figure 1.1. A 3-view of the QTR is shown in Figure 1.1. It consists of four tilting prop-rotors mounted at the tips of two sets of fixed wings. The rear wing is slightly longer and higher than the front wing, and the rear rotors are outboard of the front rotors for higher performance and fuel economy in cruise.



Figure 1.1: Artist's impression of the QTR[2]

In order to select the appropriate aircraft for the FTR program of the U.S. Army, trade-off studies were conducted between a helicopter, a “growth” version of a conventional tilt rotor and a QTR [1]. While the “growth” tilt rotor was a good starting point for this design, this would require a very large prop-rotor with

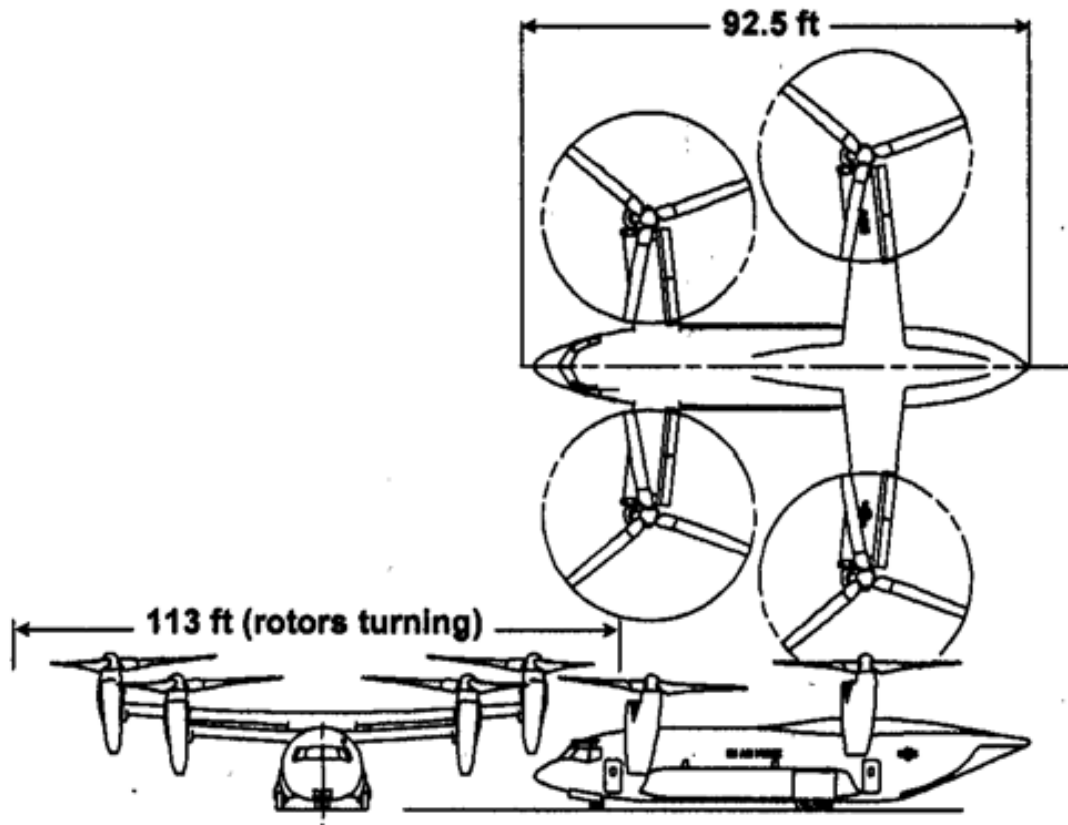


Figure 1.2: Preliminary QTR arrangement[2]

large torque requirements. According to preliminary design studies for the heavy lift mission, the QTR configuration was found to be comparable in performance to that of the growth tilt rotor aircraft[2, 1]. However, because the QTR configuration planned to use many common systems to the V-22 Osprey tilt rotor, the development risk was lesser than the growth tilt rotor.

The common systems that the QTR has been designed to share with the V-22 are the nacelles (including the rotors, the powerplants and the drive systems),

the outboard sections of the wings, the tilt rotor conversion mechanism, the cross-shafting between the rotors and the flight control systems[2]. Using blade fold, the QTR would be compatible with the landing helicopter deck (LHD) of existing ships. The fuselage has been designed to have the same utility as that of a C-130 Hercules aircraft and can carry standard shipping containers.

If the development of the QTR is realized, it could mean a rapid transformation of both military and civilian transportation. Militaries could be more agile and the need for large bases and hostile airfields could be eliminated. In the case of civilian transportation, the capacity of existing airports could be expanded without extra runways and smaller or more remote locations could be more easily connected.

1.2 Problem Statement

The main goal of this dissertation is to improve the payload carrying capacity of a QTR by studying the aerodynamics and performance of this aircraft while operating in hover and low speed forward flight near the ground.

The QTR is being developed as a heavy lift aircraft, capable of carrying large payloads over long distances. For such an aircraft, the key design consideration would be to maximize the lifting capacity. For this purpose, more information is needed on the performance of this vehicle in the crucial take-off flight regime, which consists of hover and low speed forward flight near the ground. Under these flight conditions, a QTR will operate in helicopter mode. Previous studies on conventional tilt rotors have indicated a large download penalty on the wings while operating in

hover, OGE[4, 5, 6]. This download was found to reduce while operating IGE[7, 8, 9, 10].

If this were true for a QTR also, this would substantially reduce the lifting capacity of the vehicle, OGE. However, by operating IGE, it might be possible to offset or even overcome the loss in payload OGE. Ultimately, the behavior of these loads on the airframe as the vehicle transitions into forward flight will determine the feasibility of any increase. In addition to the download on the vehicle, information on rotor power consumption is necessary for determining the increase or decrease in lifting capacity at various operating conditions. Prior to the commencement of this study, very little information was available about the aerodynamics and performance of a QTR in the take-off flight regime. Therefore, the objective of this research is to gain a deeper understanding of the quantitative and qualitative behavior of QTR performance in helicopter mode, in hover and low speed forward flight, IGE and OGE.

1.2.1 Download Problem in Helicopter Mode

In hover, a QTR will operate in helicopter mode, where the wings are located directly in the wakes of the rotors. Conventional tilt rotors, which have a similar configuration, have been found to experience a large download on the wings, while operating OGE. This download is caused by a combination of two effects, which is conceptually illustrated in Figure 1.3 for a conventional tilt rotor. The main reason is that in hover, the wings of these aircraft are located directly in the wake of the

rotors, at an incidence angle of 90° . This results in a high vertical drag on the wings causing a download on the aircraft. In addition, expansion of the rotor wake along the upper surface of the wing causes spanwise flows towards the center of the fuselage. The spanwise flows from the two wingtips meet at the centerline of the fuselage and form an unsteady fountain flow, which gets recirculated into the rotors. The momentum change produced from turning the flow from a spanwise to an upward direction causes a downward force on the aircraft, thereby adding to the download. The total download for a tilt rotor is typically around 10% of the total rotor thrust in hover OGE. For a QTR, this can lead to a loss of payload carrying capacity of about 30% in VTOL operation.

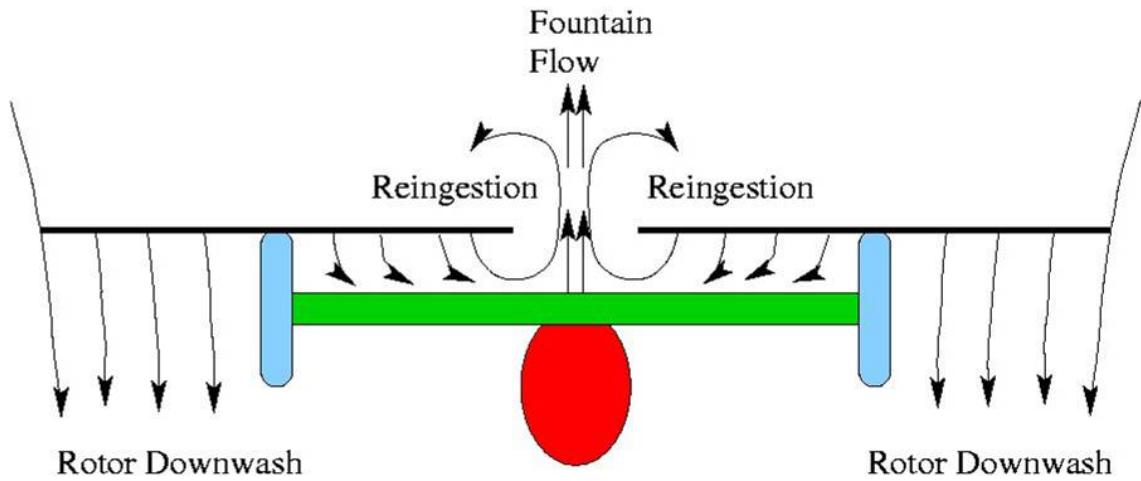


Figure 1.3: Tilt rotor flowfield OGE (from Reference [11, 12])

The flow around a tilt rotor while hovering IGE is more complex. The presence of the ground modifies the wake of the rotors underneath the fuselage, as conceptually shown in Figure 1.4. The rotor wakes form spanwise flows along the ground, which meet underneath the centerline of the fuselage and form a fountain flow in an

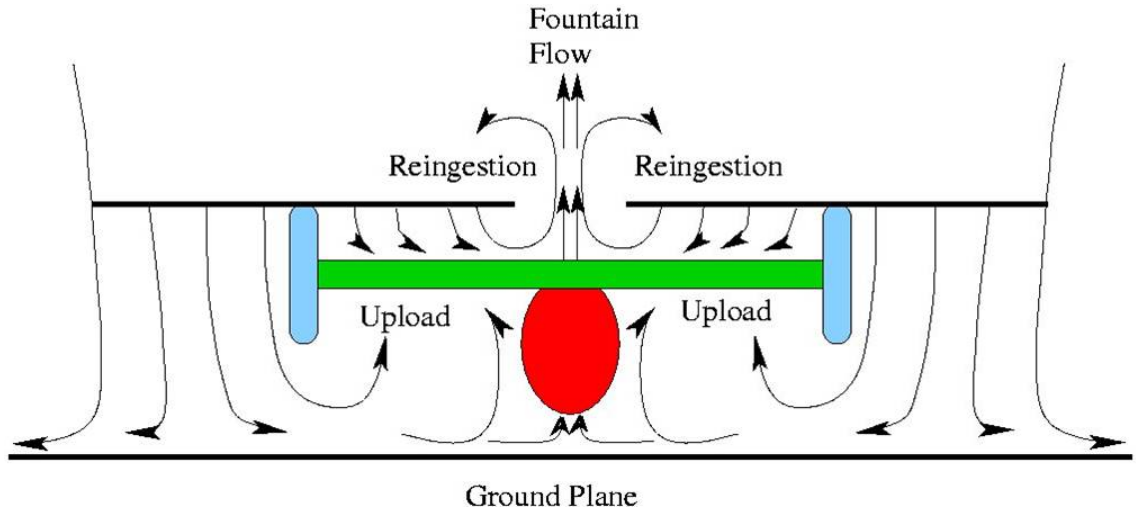


Figure 1.4: Tilt rotor flowfield OGE (from Reference [11, 12])

similar fashion to what happens on the wing upper surface[13]. This fountain flow will impinge on the bottom surface of the fuselage and produce an upward force on the aircraft. This has the net effect of reducing the download produced on the vehicle IGE.

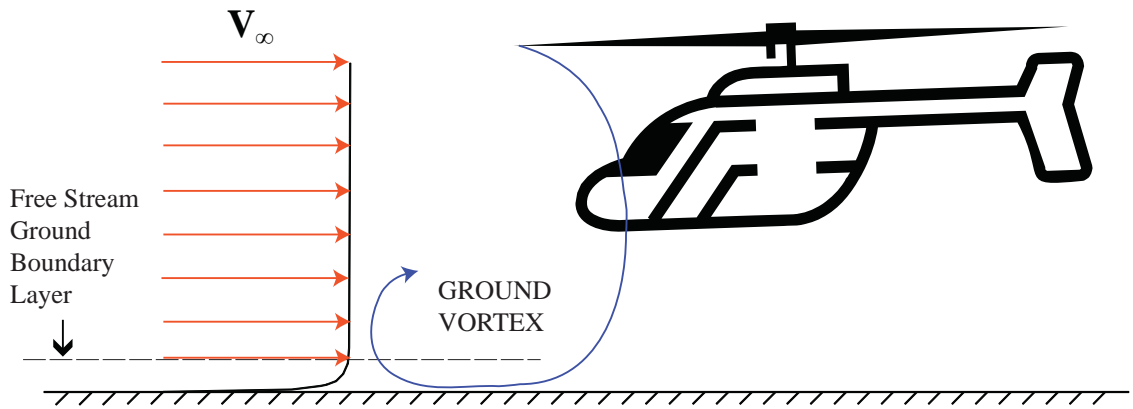
For a QTR, which has 4 rotors and an extra set of wings, recent studies[1, 14, 12, 15] have found that the wakes of the four rotors will meet underneath the fuselage between the front and rear wings and will actually produce a net upward force on the vehicle when operating very close to the ground. This upload, which could be as high as 9% of the total rotor thrust[15, 12], would not only offset the payload loss caused by the download, OGE, but could actually increase the lifting capacity beyond the maximum thrust of the rotors. Therefore, by operating in close proximity to the ground, the QTR design shows the potential for substantial payload gains.

1.2.2 Challenges in Low Speed Testing

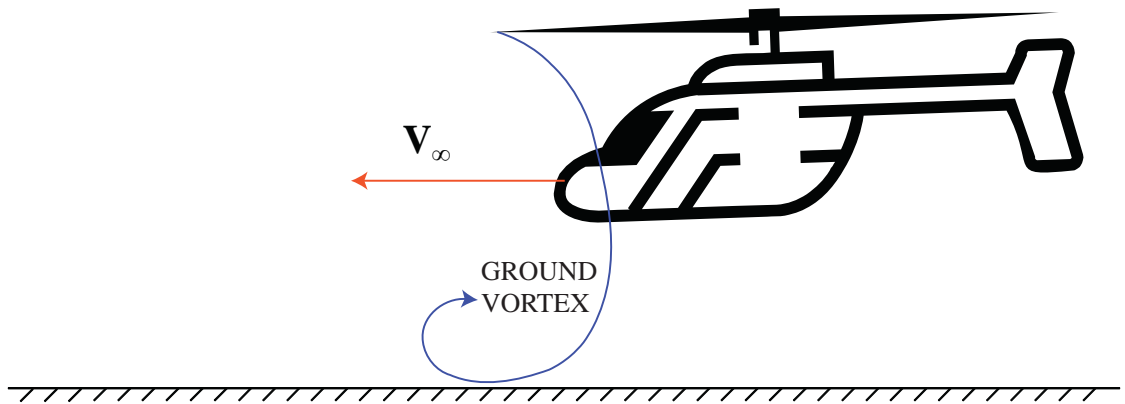
It is not clear whether this upload IGE will prevail as the vehicle begins to move forward at low speeds and at different small heights above the ground. A deeper understanding of the behavior of this upload is needed to determine the usability of the performance gains that could be obtained. In order to make this determination, experimental tests on the QTR in this low speed regime are necessary.

However, wind tunnel testing is not representative of the physical boundary conditions of this problem. In a wind-tunnel, the model is stationary with respect to the ground plane. Because there is a relative velocity between the ground plane and the free-stream of the wind-tunnel, a boundary layer is formed near the ground plane. When a real rotorcraft operates near the ground, the ground is stationary with respect to the free stream, and the vehicle moves with respect to both of them. Therefore, there is no boundary layer formed on the ground plane with respect to the free stream.

At low forward speeds, the interaction of a rotor wake with the free stream has been found to cause a horseshoe shaped vortex near the ground ahead of the rotor[16]. In a wind tunnel, the behavior of this ground vortex was found to have been modified because of interaction with the boundary layer, as conceptually illustrated for a helicopter in Figure 1.5. In a wind tunnel, the ground vortex was formed at higher wind speeds, was projected further upstream, was wider in size and extended for a larger range of relative forward speeds as compared to forward flight operation near the ground[17].



(a) Wind Tunnel Test



(b) Actual Helicopter in Forward Flight

Figure 1.5: Difference between wind-tunnel testing and actual helicopter operation near ground

While there are techniques for removing the boundary layer from the ground plane in a wind tunnel, using moving belts or boundary layer suck-off devices[18, 19], it has been shown that there is still a discrepancy in the performance data obtained from these experiments and free air testing[20]. Additionally, the spanwise extent of

the ground vortex would cause interference with the side walls of the wind tunnel. In order to reduce this interference, the size of the wind tunnel test section would have to be increased, which would increase the cost of testing. Also, because of turbulence effects, wind-tunnels have a lower limit of free stream velocity below which meaningful testing is not possible. A larger test section would increase the lowest speed at which testing is possible.

One solution to this problem is by testing a moving model of the vehicle over the ground, through free air, which will be the approach used in this study. This will not only solve the boundary layer issues, but also allow the accurate control of forward speed, right down to hover[21].

1.3 Background

The QTR is a rotary wing vehicle, which owes a lot of its technology to helicopters and conventional tilt rotors. Therefore, it would be useful to describe the history and development of the technology behind these vehicles.

1.3.1 Helicopters

The fixed-wing airplane is the universal vehicle of choice for efficient, economic flight over long distances. Following the development of the first successful helicopter by Igor Sikorsky in 1940, helicopters became the ideal vehicles for short range flight serving rough terrain. Helicopters are vehicles that use rotating wings to provide vertical lift. As compared to fixed wing aircraft, the performance of helicopters is

optimized for hover and low speed forward flight. Because of the low disk loading of helicopter rotors, they have high hover efficiency and low downloads on the airframe. Therefore, helicopters are ideally suited for Vertical Takeoff and Landing (VTOL) operations.

At higher forward speeds, compressibility effects on the advancing blades and stall on the retreating blades limit the lifting capacity of the rotor. High parasitic drag on the main rotor hub and support structures will further reduce the aerodynamic efficiency in forward flight. These effects will reduce the overall lift-to-drag ratio of helicopters in forward flight and will increase the propulsive requirements of the aircraft. Therefore, in forward flight, helicopters are limited to lower values of cruise speeds and efficiency than fixed wing propeller aircraft, which leads to lower values of range and endurance.

1.3.2 Tilt Rotors

Tilt rotor aircraft are vehicles that combine the VTOL ability of helicopters and the higher cruise speeds, range and efficiency of fixed-wing propeller aircraft. These aircraft have a pair of tilting rotors mounted at the tips of fixed wings. In hover and low speed forward flight, the rotors are in helicopter mode, where they thrust vertically in a helicopter configuration. This gives tilt rotors the ability to operate from unprepared surfaces and shorter runways than fixed wing aircraft. At higher speeds, the rotors are progressively tilted forward until they ultimately operate in propeller mode while in cruise (Figure 1.6). This allows a tilt rotor to

operate at substantially higher cruise speeds (upto 300 knots) than helicopters.

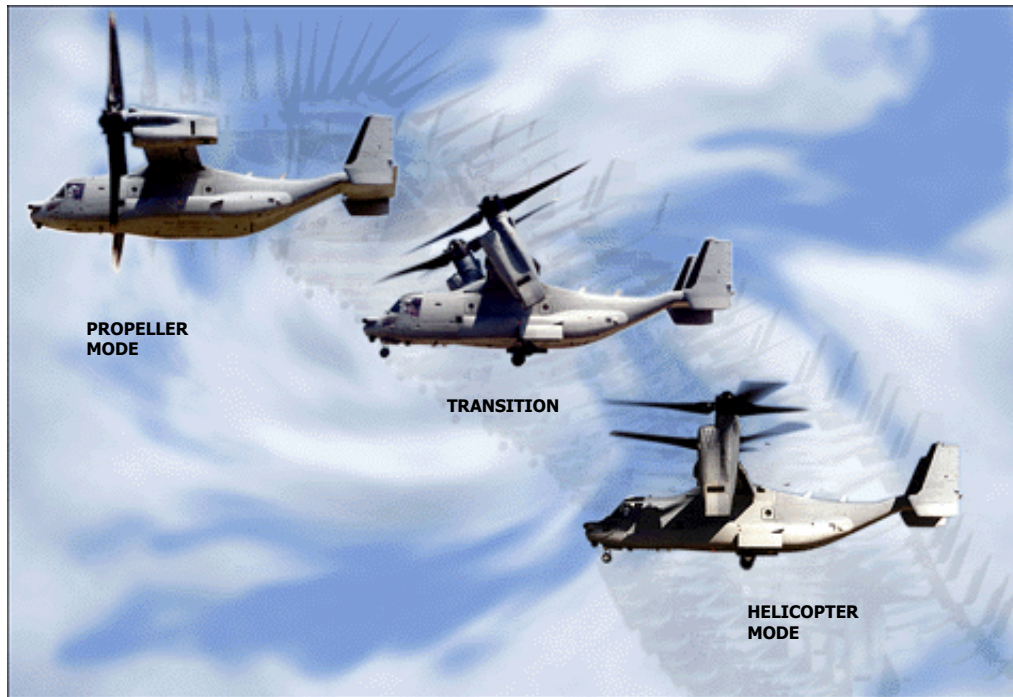


Figure 1.6: V-22 Tilt Rotor in conversion (Courtesy of US Navy)

The operational benefits of tilt rotors come at a price both in the helicopter mode and the propeller mode. As compared to a helicopter of equivalent gross weight, a tilt rotor will have smaller diameter rotors and higher twist. As a result, a tilt rotor will have a higher disk loading and downwash velocities. In addition, as mentioned in Section 1.2.1, the presence of the wings in the rotor downwash will cause a large download on the vehicle in helicopter mode. Therefore, tilt rotor performance in helicopter mode is inferior to that of a helicopter.

In cruise, a tilt rotor operates in propeller mode, where the prop-rotors will

be operating in axial flight. The prop-rotors of the tilt rotor are larger in diameter and have lower twist than an equivalent propeller. Because of the lower rpm and larger rotor diameter, the torque requirements for prop-rotors will be higher than for a propeller. As compared to a propeller, the prop-rotor hub is more complex and has more profile area. Also, the wings of a tilt rotor have to be thicker in order to house the prop-rotor shaft[22]. As a result, tilt rotors have a higher drag coefficient in forward flight than an equivalent fixed-wing propeller aircraft. Therefore, the maximum speed and efficiency of a tilt rotor will be lower than a comparable fixed-wing propeller aircraft.

1.3.2.1 Tilt Rotor Development

By the late 1940s, because of the limitations of helicopters, a need was identified for a convertible aircraft that could combine the abilities of helicopters and fixed-wing aircraft. To fulfill these requirements, several candidates emerged, including the tilt rotor, tilt wing, compound helicopters and stopped rotors. One of the candidates for the joint U.S. Army and U.S. Air Force Convertiplane Program was the XV-3 program (1953-66.) The XV-3, shown in Figure 1.7, was an experimental, single-engine tilt rotor built for the purpose of successfully demonstrating tilt rotor feasibility. The XV-3 configuration consisted of a metal fuselage with a slender wing, which had two helicopter-style rotors mounted at each wing tip. These rotors were powered by a single piston engine, using a system of gear boxes and drive shafts[23]. During its lifespan, the XV-3 completed over 250 flight tests, totaling over 125 flying hours, and successfully demonstrated the feasibility of tilt rotor op-

eration by achieving 110 full conversions from helicopter mode to propeller mode and back again. However, this underpowered aircraft used a helicopter rotor and had poor hover and cruise performance, in addition to several stability and handling issues.



Figure 1.7: Bell XV-3 Tilt Rotor (from Reference [23])

This was followed by another experimental effort, the XV-15 program, which was jointly funded by NASA and the Army. The XV-15, shown in Figure 1.8, was a twin-engine tilt rotor, and was built to be representative of “large diameter, low disc loading, wingtip mounted prop-rotors that provide the thrust for vertical lift and forward flight.” [23] The two engines were mounted in the nacelles at the wingtips and tilted along with the rotor shaft. Because of the lessons learnt from the XV-3, which used helicopter rotors, the XV-15 had specially designed rotors optimized for tilt rotor operation. Two of these aircraft were built in 1977 and the last one was retired recently, after accumulating over 800 hours of flight testing.



Figure 1.8: Bell XV-15 Tilt Rotor (from Reference [23])

Using the expertise gained from the XV-15 and XV-3 programs, full scale development of the first operational tilt rotor, the V-22 Osprey, was commenced in 1986, as part of the the Joint Services Advanced Vertical Lift Aircraft (JVX) program. The multi-mission V-22, shown in Figure 1.6, was jointly developed b Bell Helicopter Textron and Boeing Vertol to satisfy multi-service combat operational requirements. The first operational V-22 was flight tested in 1989. After two fatal crashes in the early 1990s and another one in 2000, the V-22 was grounded several times and was finally approved for production by the Pentagon in September, 2005.[24]

On the civilian side, the Bell/Agusta BA609 has been developed as a civilian

tilt rotor with a similar configuration to that of the V-22. The BA609 has been designed to carry 2 crew and upto 9 passengers and is planned to be certified by 2008[25]. This aircraft will have a pressurized cabin, an advanced glass cockpit and will feature an all composite construction[23].

The HV-911D Eagle Eye Tilt Rotor UAV, which is also being developed by Bell for the Coast Guard, is expected to be delivered by 2007. This aircraft was developed to provide an unmanned platform for the purpose of reconnaissance, surveillance, border patrols, supply delivery, fire detection and other critical military and civilian missions[26].

1.4 Survey of V/STOL Performance Research in Hover and Low Speed Forward Flight

The QTR operates in helicopter mode in hover and low speed forward flight. Therefore, a survey of literature on helicopter rotor performance and wake behavior in these regimes will be useful in understanding similar challenges that could be experienced by a QTR. Also, because the QTR shares many components with a V-22 tilt rotor, it is crucial to obtain an understanding of tilt rotor performance in the helicopter mode. This section will survey the previous research on helicopters, tilt rotors and QTRs in helicopter mode, in hover and low speed forward flight.

1.4.1 Research on Rotor Performance, IGE

1.4.1.1 Hover

The operation of a helicopter rotor in proximity to a ground plane or other boundary causes changes in the aerodynamics and performance. In hover, the rotor wake expands rapidly as it approaches the ground, as the ground has to be a streamline to the flow. This causes changes in the slipstream velocity and for a constant rotor thrust, the induced velocity and rotor power have been found to decrease.

The performance of helicopter rotors in hover, IGE, has been studied thoroughly by a number of researchers. The earliest experimental study documenting the effects of ground proximity on the lifting performance of propellers was by Kussner [27] in 1937. An approximate analytical model for predicting the ground effect on a hovering rotor was introduced by Betz[28] in the same year. These studies showed that for a constant thrust, the power required to hover at rotor heights of less than 1 radius above the ground rapidly decreased. Knight & Hefner (1941)[29] developed and experimentally verified an analytical method for rotor performance predictions IGE, by treating the ground effect as a modification to the rotor induced power. Leishman[30] (2000) provides a summary plot on rotor thrust variation IGE from experiments conducted by Zbrozek[31] (1947), Betz[28] (1937), Knight & Hefner[29] (1941), Cheeseman & Bennett[32] (1955), Fradenburgh[9] (1960) and Stepniewski & Keys[33] (1984). Heyson[34] (1960) and Cheeseman & Bennett[32] (1955) used a ground image plane to theoretically calculate the power required to hover at constant disk loadings. Light[35] (1989) obtained shadowgraph images of the tip vortex

structure of a hovering helicopter rotor, IGE, and obtained good agreement with the results with the predictions of a free wake analysis.

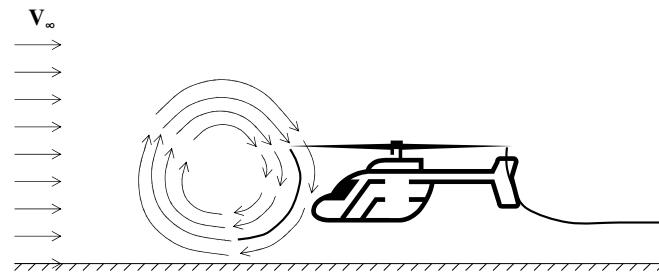
1.4.1.2 Low Speed Forward Flight

Rotor performance in forward flight, IGE, has also been studied thoroughly. Jenkins[36] (1965) observed a wake rollup ahead of the rotor at low forward speeds, IGE. While studying the effect of rearward crosswinds on tail-rotor interference with the main rotor, IGE, Huston & Morris[37] (1971) observed a ground vortex that was formed ahead of the main rotor, by using a tuft-grid. They found that interaction of the ground vortex with the tail rotor, IGE caused directional control issues at certain speeds. Empey & Ormiston[38] (1974) and Weisner & Kohler[39] (1974) followed up on this research by obtaining smoke and helium bubble flow visualization and further studied the effects of this ground vortex on tail-rotor performance. Heyson[40] (1970) theoretically predicted the development of this ground vortex with forward speed. Sheridan & Weisner[41] (1977) also studied the formation of this ground vortex ahead of the helicopter. This vortex was found to cause a sudden increase in power required at low forward speeds, for constant disk loading. Once the ground vortex passed under the rotor, the power required reduced back to the normal trend. Similar tests were conducted by Ganesh, et al,[42, 43, 44] and similar results were obtained. Boer, et al,[17] (2002) conducted studies on the ground vortex phenomena in ground effect in a wind-tunnel with boundary layer control techniques.

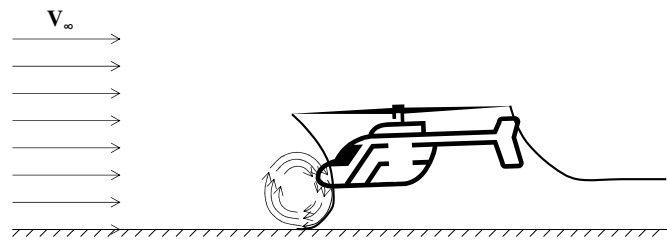
The previously mentioned experimental studies on rotor ground effect at low forward speeds were conducted in wind tunnels. The results from Putman[45] (1968)

and Putman & Curtiss[20] (1979) suggest that wind-tunnels do not properly represent the boundary conditions experienced by a helicopter in forward flight near the ground, as discussed in Section 1.2.2.

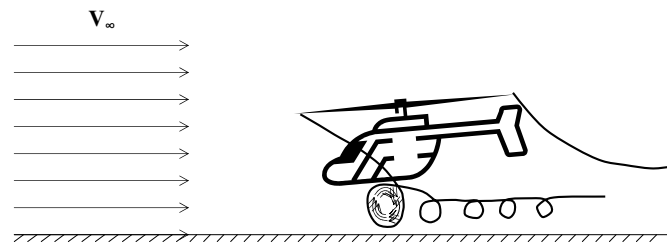
In order to correctly predict the rotor performance, it is necessary to match the boundary conditions on the ground. For this purpose, Curtiss, et al. [21, 16, 20] tested helicopter rotors at different heights above the ground and at different forward speeds using the Princeton Dynamic Model Track (PDMT). At the PDMT, the rotor model was moved through still air in a long enclosed building using a servo-controlled carriage. This facility not only allowed the ground boundary conditions to be simulated properly, but enabled the precise control of the forward speed right down to hover. From the results of this study, four different regimes were identified, as shown in Figure 1.9. A non-dimensional parameter, the rotor wake skew angle (defined as the inverse tangent of the free stream velocity divided by the rotor induced velocity), was found to govern the existence of these different flow regimes. At very low forward speeds, flow recirculation of the wake into the rotor was observed upstream of the rotor [Fig. 1.9 (a)]. With an increase in forward speed, the diameter of the recirculating flow decreases and a well-defined vortical structure is formed between the ground and the leading edge of the rotor [Fig. 1.9 (b)]. Above a certain critical rotor wake skew angle, an elliptically-shaped horseshoe vortex is formed under the leading edge of the rotor [Fig. 1.9 (c)]. At the forward speed increases, this vortex becomes smaller and smaller and eventually vanishes [Fig. 1.9 (d)].



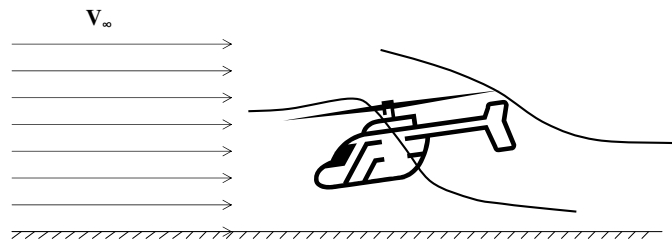
(a) Large Scale Recirculation



(b) Ground Vortex



(c) Low Speed Forward Flight



(d) Higher Speeds

Figure 1.9: Helicopter in low speed flight near the ground (adapted from Curtiss, et al.,[16] and Leishman[30])

1.4.2 Previous Investigations on Tilt Rotors in Hover

1.4.2.1 Experimental Investigations

Tilt rotors are longitudinally symmetrical aircraft. Therefore, experimental investigations of the complicated flowfield of a hovering tilt rotor can be conducted either by using a full-span model or by using a semi-span model and an image plane. Most of the previous experiments on tilt rotors till date have used semi-span models in order to minimize cost and complexity.

In order to isolate the effects of the individual interactions in hover, tests have been conducted on an isolated rotor, rotor and wing, rotor and image plane and rotor/wing/image plane combinations. Wing download, rotor performance data, flowfield and acoustic information have been obtained from small, medium and large scale models. Table 1.1 provides a summary of several different experimental tests done on tilt rotor aircraft. These results found that there was a substantial download on this aircraft in hover, which can be as large as 15%. Rotor hover performance and blade surface pressures were obtained for a tilt rotor rotor.[46, 47, 48, 49] Although there are favorable effects on rotor performance because of the presence of the wing alone, the addition of an image plane caused a net reduction in thrust as a result of the recirculation caused by the fountain flow[6, 4]. Change in the rotor thrust coefficient was found to cause a change in rotor downwash velocity distribution, which caused the download to thrust ratio to decrease slightly with increase in rotor thrust coefficient[50, 4, 5, 6]. Wing incidence angle, rotor-wing separation distance, wing flap angle and direction of rotor rotation were all found to have a

significant effect on the wing download[50, 13, 4]. Increasing the wing flap angle was found to cause a reduction in download to thrust ratio until a flap angle of 67° [7, 6, 4]. Shadowgraph visualizations were used to obtain tip vortex geometry and wake structure. The presence of the wing and image plane was found to cause unsteadiness in the rotor wake and radial expansion of the wake along the wing[51]. Devices to reduce wing download were evaluated and were found to increase hover lift capability by about 3% [5, 52]. Acoustic measurements from a 0.184 model indicated an increase in far field noise aft of the rotor, compared to an isolated rotor[53] and an increase in overall rotor noise[54]. Aerodynamic evaluations of a V-22 Wing section were obtained by Narramore, et al., [55] (1994) and characterized the performance of the wing sections in different flow conditions.

Table 1.1: Tilt-rotor experiments in hover, OGE

	<i>TestDescription</i>	<i>Span</i>	<i>TestData</i>
McVeigh[6]	0.658-scale V22 rotor+wing	Semi	Rotor performance & downwash, Wing download
Felker & Light[4]	0.658-scale V22 rotor + wing	Semi	Rotor performance & downwash, Wing download
	0.16-scale S-76 rotor + wing	Semi	Wing download
Felker[50]	0.658-scale V22 rotor + wing	Semi	Wing download
Swanson & Light[51]	0.184-scale V22 rotor + wing	Semi	Tip vortex trajectories
Wood & Peryea[5]	0.15-scale V22 rotor + wing + fuselage	Semi	Wing download, rotor downwash
Mosher & Light[53]	0.184-scale V22 rotor + wing	Semi	Far field acoustics
Polak <i>et al.</i> [56]	0.08-scale XV-15 rotor + wing + fuselage + tail	Semi & Full	Flow visualization, inflow velocity
Liu, et al.[57]	0.15-scale V22 rotor + wing + fuselage	Semi	Flowfield, Turbulence ingestion noise

Polak et al.[56] (2000) investigated the difference between full- and semi-span

testing for a tilt-rotor in hover. Mean inflow velocities were the same for both the cases over most of the rotor span. However, there was a difference in the flowfield measured in the region of the fountain flow as the image plane forces the mean velocity and the turbulence kinetic energy to be zero at the boundary. The fountain flow was found to be higher on the semi-span model and the fountain turbulence was found to be circulated farther inboard. Also, an aperiodic lateral shifting of the fountain flow was observed in the full-span model which caused intermittent turbulence ingestion by the rotors. Thus, full-span models need to be used to accurately represent the aerodynamics of tilt rotors.

In ground effect, the hover flowfield around a tilt rotor is more complex and studies have shown that the download decreases as the height above the ground decreases[7, 8, 9, 10]. The results obtained from investigations conducted in References [7, 8, 9, 10] show that the download reduces to zero at rotor height-to-diameter ratios between 0.25 and 0.75, and can even become an upload with further reduction with height. At height-to-diameter ratios above 1.5, the download remains constant. More recent investigations[11, 58], reveal similar trends for tilt rotor download for decreasing height-to- radius ratios. It has been postulated that when the wakes from the rotors impact the ground, they form spanwise flows, which meet below the centerline of the fuselage to form a fountain flow in a manner analogous to what occurs on the upper surface of the wing[13]. This fountain impacts the bottom of the fuselage and the lower surfaces of the wings, resulting in a reduction in download IGE.

1.4.2.2 Computational/Analytical Studies

Computational investigations of the tilt-rotor flowfield in hover have been attempted using a number of methods. Panel methods for the wing combined with blade element theory for the rotor were used by Clark [59] (1987). The calculations were in reasonable agreement with wind tunnel data, although separated flows cannot be accurately predicted without knowing the location of separation, a priori. Fejtek and Roberts [60] (1992) solved thin-layer compressible Navier-Stokes equations using an implicit, finite differencing scheme. An actuator disk rotor model and a Chimera grid method were used. The details of the edge of the rotor wake were lost because of coarse grid geometry in that region. Also, nacelle and rotor hub were not modeled as it is very time consuming to setup the tilt-rotor nacelle, wing and rotor combination using body-fitted finite difference methods. Meakin [61] (1995) used an unsteady, thin-layer, Navier-Stokes simulation of Felker's experiment [13, 4] that accounts directly for the motion of the V-22's 3-bladed rotor using moving body Chimera overset grids. Although wing download is predicted accurately, this method requires high storage, lengthy computation and grid generation that is time consuming. Also, blade vortices are under-resolved and an appropriate turbulence model does not exist for this flowfield. Tadghighi et al. [62] (1995) used a 3D-steady incompressible Navier-Stokes formulation linked to an acoustic code to study the acoustics and aerodynamics of a tilt-rotor in hover. Overall flow properties were captured and noise signatures were similar to experimental measurements. Poling et al. [63] used a 3-D steady incompressible Navier-Stokes solver in a Cartesian

grid to study different configurations of the tilt-rotor aircraft in hover. Flowfields and rotor performance that showed good agreement with experiment were obtained. Full-span and semi-span models were also compared.

Although the computational efforts detailed above were able to capture the overall flowfield and were able to obtain rotor performance and wing download data comparable with experiments, the challenge lies in the numerical prediction of all the flow features associated with this problem at a reasonable computational cost. More accurate turbulence models and more appropriate grid generation methods are required to capture the details of the fountain flow and the rotor wake structure.

A semi-empirical model to predict the download on a tilt-rotor aircraft was developed by Felker and Light [64, 13]. This model was developed using flow visualization studies on the upper surface of the wing and rotor downwash velocities measured on different tilt rotor configurations. The flow visualization studies performed on the wing provided information on whether the flow at a given location was primarily chordwise or spanwise. Also, the downwash distribution in the rotor wake was measured for an isolated rotor at a plane, which was at the same distance away from the rotor as the wing. For the chordwise flow regions, the download was estimated by multiplying the drag coefficient of the wing airfoil section at an angle of attack of -90° with the dynamic pressure of the rotor downwash. In the regions with spanwise flow, the download was assumed to be equal to the momentum flux of the fountain flow multiplied by the area of the fountain. The blocking effect of the wing and the fountain flow effect were also modeled using momentum theory to predict the change in the rotor performance. This model was used by Heuze, et al.

at Onera to develop a download model for the European tilt rotor program [58].

1.4.3 Tilt Rotor Investigations in Low Speed Flight

There have been several studies on the performance of tilt rotors and their components in low speed flight in helicopter mode.

The performance of isolated prop-rotors in low speed helicopter mode has been studied by Young, et al., [65, 66] (1999) and Betzina [67] (2002). Weiberg & Maisel [68] (1980) conducted a full-scale wind-tunnel test on a complete XV-15 in helicopter mode, conversion and propeller mode. In helicopter mode, rotor performance and airframe lift and drag data were obtained for different values of speed, flap deflection and thrust coefficient. Flap deflection was found to increase the lift on the aircraft.

McVeigh, et. al [69], (1988) studied the performance of a complete V-22 aircraft at low forward speeds, in helicopter mode. This was an experimental study that was performed in an open-jet wind tunnel, OGE. The maximum rotor wake skew angle for which these measurements were conducted was 72° . The test was repeated for fuselage angles of attack of 0° and -10° . For fuselage at 0° angle of attack, the download to thrust ratio was found to increase slightly at low forward speeds before reducing with a further increase in forward speed. The behavior of the download in forward speed was found to be affected by the thrust coefficient.

Desopper, et al. [11], (2002) experimentally investigated the effect of forward speed on the download of a tilt rotor by using a semi-span model at the higher end of the low-speed spectrum, in and out of ground effect. The results show

that the download reduces with an increase in forward speed for both OGE and IGE operation, when flaps are not deflected. When flaps are deflected by 60, the download IGE was found to increase with an increase in forward speed. However, this investigation was carried out only for hover and speeds greater than 30 knots.

Young, et al.[70], (2002) studied the rotor/airframe interactions on the Tilt Rotor Acoustic Model (TRAM). The results were preliminary and did not address the download-to-thrust ratios at different forward speeds. While studying the interactions between two tilt rotors operating in formation near the ground, Yamauchi, et al. [71], (2003) also studied the performance of a single tilt rotor operating at different heights above the ground at different forward speeds. In helicopter mode, the aircraft experienced an increase in overall thrust when the height of the aircraft above the ground was reduced. When the forward speed was increased, this increased thrust was found to diminish.

Potsdam, et al. [72], (2004) conducted a CFD study on a tilt rotor in helicopter mode, while hovering in crosswinds from several different directions. For crosswinds at zero azimuth angle, download-to-thrust ratio was found to reduce with an increase in wind velocity.

All the prior studies on tilt rotor in low speed flight in helicopter mode have been wind tunnel studies or hover studies in cross-winds. As mentioned earlier in Section 1.2.2, these studies do not accurately represent the ground boundary conditions for an aircraft operating in low speed flight near the ground.

1.4.4 QTR Investigations in Hover

The QTR shares many common design features with the V-22 Osprey and therefore will share many aerodynamic issues. However, by virtue of having an additional set of rotors and an extra set of wings, the QTR is bound to have additional aerodynamic interactions between the various components. This should cause the flow around the QTR to be more complex than tilt rotors.

In hover, the location of the wings directly in the rotor wake will ensure that the QTR will also experience a large download in hover, OGE. Also, there will be fountain flows produced on both the front and rear wings in a manner similar to that of the V-22. However, the fountain flow on the rear wing should be weaker than the front wing as the rotor separation distance is larger.

1.4.4.1 Experimental Studies

Because the QTR is a relatively new concept, there are few related publications in the open literature. There have been no full-scale experimental studies of the QTR performance so far because of the size and the complexity of the aircraft. There is only one published experimental study of the QTR in hover, conducted by Wood, et al. [1], (2002) of Bell Helicopter Textron. The experimental model that was tested, was a small 0.07-scale hover download model (Figure 1.10) that included the fuselage, wings, nacelles and sponsons. The fuselage, wings and sponsons formed one unit, which was mounted on a 5-component balance capable of measuring the lift, drag, side force, pitching and rolling moments. The nacelles and the rotors were

mounted separately on independent mounts capable of measuring the rotor thrust and torque. The rotors had the same airfoil shape, twist and solidity as the V-22 rotors and operated at the same tip-speed as the full-scale rotors.

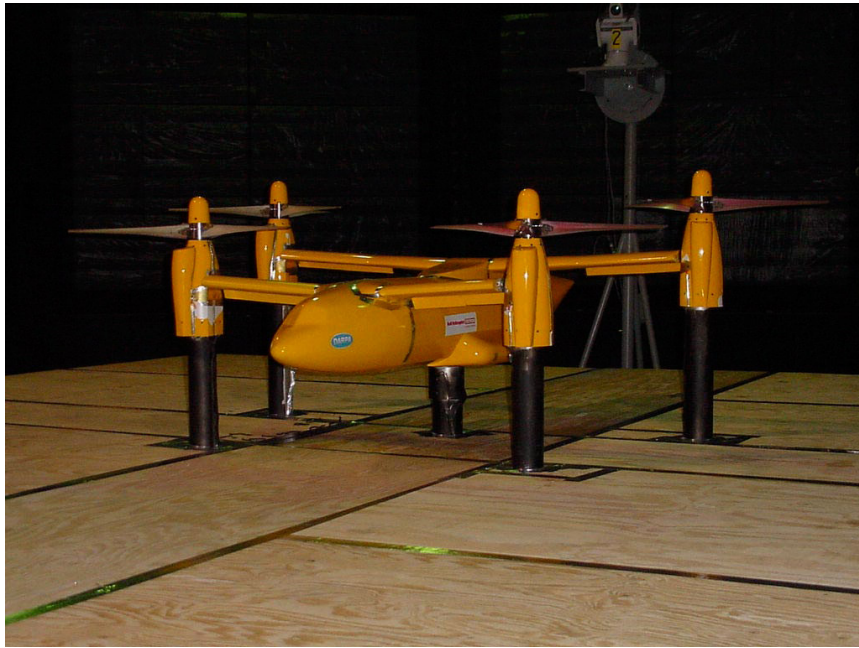


Figure 1.10: QTR Hover Download Model (Wood, et al.) (from Reference [5])

In hover, OGE, a download of 8% of the total rotor thrust was measured. This download-to-thrust ratio was found to remain relatively constant with a change in rotor thrust coefficient. This is in contrast to studies conducted on the V-22, where the download-to-thrust ratio was found to decrease with an increase in rotor thrust coefficient[4, 5, 6]. It was postulated by Wood, et al., that this could be a result of the difference in the lateral separation of rotors between the QTR and the V-22. Smoke and tuft flow visualization was used to observe the features of the flowfield

around the QTR model. A recirculating fountain flow was observed on the front wing the QTR, whereas the fountain flow on the rear wing was much weaker and displayed no noticeable recirculation.

This model was also tested IGE at a front rotor height of 0.87 rotor diameters. An upload of 5% of the total rotor thrust was observed at this condition. A fountain flow underneath the fuselage, as described by the CFD studies[14, 73, 15] was observed using smoke flow visualization.

1.4.4.2 Computational Studies

One preliminary CFD study of the QTR in hover, IGE and OGE, was conducted by Lestari, et al[14] (2001). The airframe body was modeled using a Cartesian grid of a QTR with a wing trailing edge flap deflection angle of 67° . The airframe included the fuselage, wings, nacelles and the sponsons. The rotors were modeled as a thin actuator disk using source terms that actively exchanged information with the flow grid. Two different cases were studied. The first case was hover, OGE and the second case was hover, IGE at a front rotor height of 1.13 rotor diameters from the ground. Overall flowfields, pressure distributions, and total forces were studied. A download of 9.1% of the total rotor thrust was observed on the airframe, OGE. The flowfield was found to be highly unsteady and a swirling fountain flow was observed on the upper surface of the front wing. Most of the download produced on the airframe was experienced by the front and rear wings. For hover, IGE, the airframe loads were transformed into an upload of 0.5% of the total rotor thrust, at a front rotor height of 1.13D. The download on both the front

and rear wings were found to be reduced and the fuselage experienced a substantial upload of 3.6%. A high pressure flow region caused by stagnation of upward flow underneath the fuselage was observed. The pressure under the forward portion was found to be higher than the rear of the fuselage. This is possibly because the front rotors are closer together than the rear rotors.

As part of the QTR research program at the University of Maryland, along with the experimental studies that form the basis for this dissertation, parallel CFD investigations of the QTR in hover and low speed forward flight have been conducted. An initial CFD study of the performance of a simplified QTR in hover and low speed forward flight, IGE and OGE, was conducted by Gupta and Baeder[73]. This study modeled a simplified QTR, which included the fuselage, front and rear wings with 0° wing trailing edge flap deflection angle using overset meshes. The nacelles and the sponsons were not included. The rotor was modeled as a thin actuator disk. Four different heights were studied: OGE, wheel heights of 6 feet, 2 feet and on the ground. In hover, OGE, a download on the airframe, of about 15% of the total rotor thrust, was observed. Hovering, IGE, was found to cause a reduction in the download produced on the airframe. This was attributed to an upward flow produced between the ground and the underside of the airframe. At low heights above the ground, the download was found to change to an upload, which was as high as 5% of the total rotor thrust, when the rotor wheels were on the ground. However, the inability of the CFD code to operate at zero free stream Mach numbers forced simulation of slight climb or descent (free stream Mach number = 0.015) as an approximation to hover.

The compressibility issues of the solver limited the free stream Mach number to be a fairly high number. Lower free stream velocities were desired for this approximation to be more meaningful. Therefore, low Mach number preconditioning scheme was incorporated in the solver to solve the aforementioned issue[74].

This preconditioning scheme was utilized to conduct further studies of an updated QTR configuration, which had a wing trailing edge flap deflection of 67° [15, 12]. These subsequent CFD results obtained have managed to obtain a closer approximation to hover values. In this study, the download in hover was found to reduce to a value of 9.1% of the total rotor thrust because of the increase in the wing flap deflection. It should be noted that the wing flap deflection of 67° is the likely configuration that will be used in helicopter mode, in order to reduce the download on the aircraft[5]. In hover, IGE, with wheels on the ground, an upload of 8.8% of the total rotor thrust was noted. This is a substantial upload and shows potential for use in increasing the payload of the aircraft.

1.4.5 QTR Investigations in Low Speed Forward Flight

The initial CFD study of Gupta & Baeder[73] also studied the QTR performance in helicopter mode for rotor wake skew angles ranging from 1° to 52° . An increase in forward speed, OGE, was found to cause a reduction in the downloads on the airframe. At the higher speeds, the download on the wings were found to disappear and the wings actually produced lift. Also, the upload produced IGE was found to reduce at low forward speeds, because the stagnated flow under the

fuselage moves backward.

These trends were confirmed in the subsequent CFD study of the QTR model with the wing trailing edge flap angle of 67° , although the downloads were reduced [15, 12]. IGE, the upload was found to reduce for low values of rotor wake skew angle and increased again with a further increase in forward speed.

There have been no prior experimental studies on QTR performance in low speed forward flight.

1.4.6 Summary of Previous Research

From the literature review in the previous sections, it is clear that the study of QTR downloads and performance is still quite nascent. While there were some CFD studies exploring QTR performance in hover and low speed forward flight, the prior experimental research on this subject was limited to one hover study and only for two different heights above the ground. The CFD studies of the QTR were also limited to one case OGE and one case IGE, for hover and low speed forward flight. There have been no previous experimental studies of QTR operating in the helicopter mode, in low speed forward flight, IGE or OGE.

From the previous studies, a ground cushion under the airframe was found to produce significant payload gains for the QTR by hovering IGE. However, if these performance benefits are dissipated at low forward speeds, it will not be possible to utilize ground effect to increase the payload of the vehicle. On the other hand, if the payload gains are shown to persist for a range of low speeds near the ground,

the takeoff trajectory could potentially be modified to operate close to the ground to take advantage of this ground cushion. Also, the prior studies did not provide any information about the changes in rotor power consumption for the different operating conditions. In order to determine the usability of these payload benefits, power measurements are needed.

The previous research on helicopters and tilt rotors illustrated the challenges faced by experimental studies of low speed flight IGE. In order to properly model the aerodynamics of the problem, careful consideration of the boundary conditions is needed. For this purpose, the most accurate representation of the boundary conditions will be obtained by employing a moving test apparatus similar to the setup employed by Curtiss, et al,[16, 21] at the PDMT.

The objectives of this dissertation are described in detail in the following section.

1.5 Research Objectives

The goal of this research is to study the possibility of increasing the payload of a QTR by improving the understanding of QTR aerodynamics and performance in the take-off regime. The specific research objectives are as follows:

- To experimentally obtain the download and aerodynamic performance of a QTR in hover & very low speed forward flight, IGE and OGE.
- To increase the level of understanding of the mechanisms that contribute to the changes in QTR performance at different operating conditions in this regime.

- To determine the scalability of the results, to verify the accuracy of the obtained quantitative measurements using uncertainty analysis and to validate the results by comparison with other experiments and computational predictions.

These objectives are explained in further detail below:

1.5.1 Experimentally Obtain QTR Performance

As explained in the previous sections, there are very specific challenges to the testing of V/STOL aircraft at low speeds, IGE. Therefore, one of the goals of this study was to develop an experimental setup, which can test the performance of a QTR model while accurately modeling the boundary conditions of a QTR moving at low speeds close to the ground. This was done by employing a somewhat unique experimental testing method, i.e., using an instrumented moving test apparatus. This concept was similar to the PDMT apparatus used by Curtiss et al.,[16, 21], which does not exist anymore. However, as the PDMT was about 1 mile long, a facility of the same scale would be very expensive to build and maintain. In order to meet logistical and financial constraints, the experimental setup had to be small-scale, very compact, inexpensive and did not require the use of a custom built building such as the PDMT.

In order to determine the feasibility of increasing the payload carrying capacity of a QTR by operating the aircraft close to the ground, information on the download to thrust ratio and power consumption is required . There, the quantities that

were measured were the airframe download and rotor thrust, in order to obtain the download-to-thrust ratio; and also rotor torque and rpm, to obtain the rotor power. These quantities were studied as a function of height above the ground and forward speed. Therefore, the parameters that were varied were the forward speed and height above the ground.

1.5.2 Understanding of Mechanisms Causing Changes in QTR Performance

While quantitative measurements of QTR performance are extremely useful, a physical understanding of the mechanisms causing the changes in download and power consumption is necessary. This will provide a designer with the tools to design around existing hurdles to maximizing QTR performance and also the ability to deal with future challenges. This physics of the problem was explored by performing tuft flow visualization and measuring the pressure at strategic points on the fuselage.

1.5.3 Scalability, Verification and Validation of the Results

Unless the assumptions and simplifications made during the modeling of the problem are accurate, the results of a small-scale experiment may not be directly scalable. Therefore, the validity of the results were ascertained by comparing with results obtained from hover experiment of Wood, et al.[1] and the CFD predictions of Gupta & Baeder[73, 74, 12] and Lestari, et al.[14]. Important scaling parameters were identified and used to compare the characteristics of the small-scale model with

the other results. The wake velocity distribution of the rotors were measured and compared to a full-scale V-22 rotor. In addition, an uncertainty analysis of all the measured quantities was performed to determine the measurement uncertainty.

1.6 Dissertation Outline

The importance of take-off performance of a QTR to its success as a heavy lift vehicle was explained in this chapter. Through a comprehensive survey of prior literature, the underlying problems and potential benefits of the QTR design and its operation in proximity to the ground were emphasized. The challenges in testing V/STOL aircraft at low forward speeds were also highlighted.

Chapter 2 explains the approach used to address the research objectives. The important scaling parameters relevant to the problem are identified and the experimental methodology is presented. This is followed by detailed description of the setup used for the experiment.

Chapter 3 presents the details and performance one of the rotors, without the airframe present. First, the rotor is described and the geometric details are presented. Then, the OGE performance of the rotor is presented in terms of measured thrust, torque, rpm and power data. This is followed by the measured performance data for the rotor, IGE. Finally, the measured rotor wake velocity profiles are compared with results from a full-scale V-22 rotor.

Chapter 4 presents the hover performance of the QTR, IGE and OGE. First, the test procedure is described. This is followed by the measurements of the variation

of download with height above the ground. The effect of varying the flap angle and the rotor disk loading are also explored. These download results are then compared with previous experimental and CFD studies in hover. The analytical methodology used to convert the measured power into a meaningful quantity is then described. The behavior of this corrected power at a constant vehicle thrust for different heights above the ground is presented. The total vehicle thrust available at a given power is also presented. Finally, the distribution of pressure on the bottom surface of the fuselage are measured at different heights and discussed.

Chapter 5 presents the performance of a QTR in low speed forward flight, at different heights above the ground. The results presented in Chapter 4 are extended to low speed forward flight and discussed.

In order to understand the physical processes influencing the QTR performance results presented in Chapters 4 and 5, tuft flow visualization images are presented in Chapter 6. Flow visualization images from the top and the bottom surfaces of the airframe for both hover and low speed forward flight are presented. Also, images from tufts located on a ground plane are obtained and discussed, for hover and low speeds. These images are then compared with the flowfields predicted by other CFD and experimental studies.

Chapter 7 summarizes the contribution of this research and explains the major conclusions of this study. Suggestions for future work are also provided.

Chapter 2

Approach

As mentioned in Chapter 1, an experimental approach has been used to perform this research. In hover and low speed forward flight, a QTR will be in the helicopter mode. Therefore, the focus of this research was to study the performance of a QTR with the rotors tilted up at a 90° nacelle tilt angle, at different flight conditions.

2.1 Vertical Force Balance

The vertical force balance diagram for a QTR in helicopter mode is shown in Figure 2.1. The main vertical forces experienced by the vehicle are the thrust of the four rotors and the download on the airframe (which comprises the wings, fuselage, nacelles and sponsons) and the weight of the vehicle.

A positive value of download will indicate a downward force acting on the aircraft, whereas a negative value will indicate an upload. The total vehicle thrust available to the aircraft, T_{veh} , can be expressed as the sum of the thrust on the four rotors reduced by the download on the vehicle,

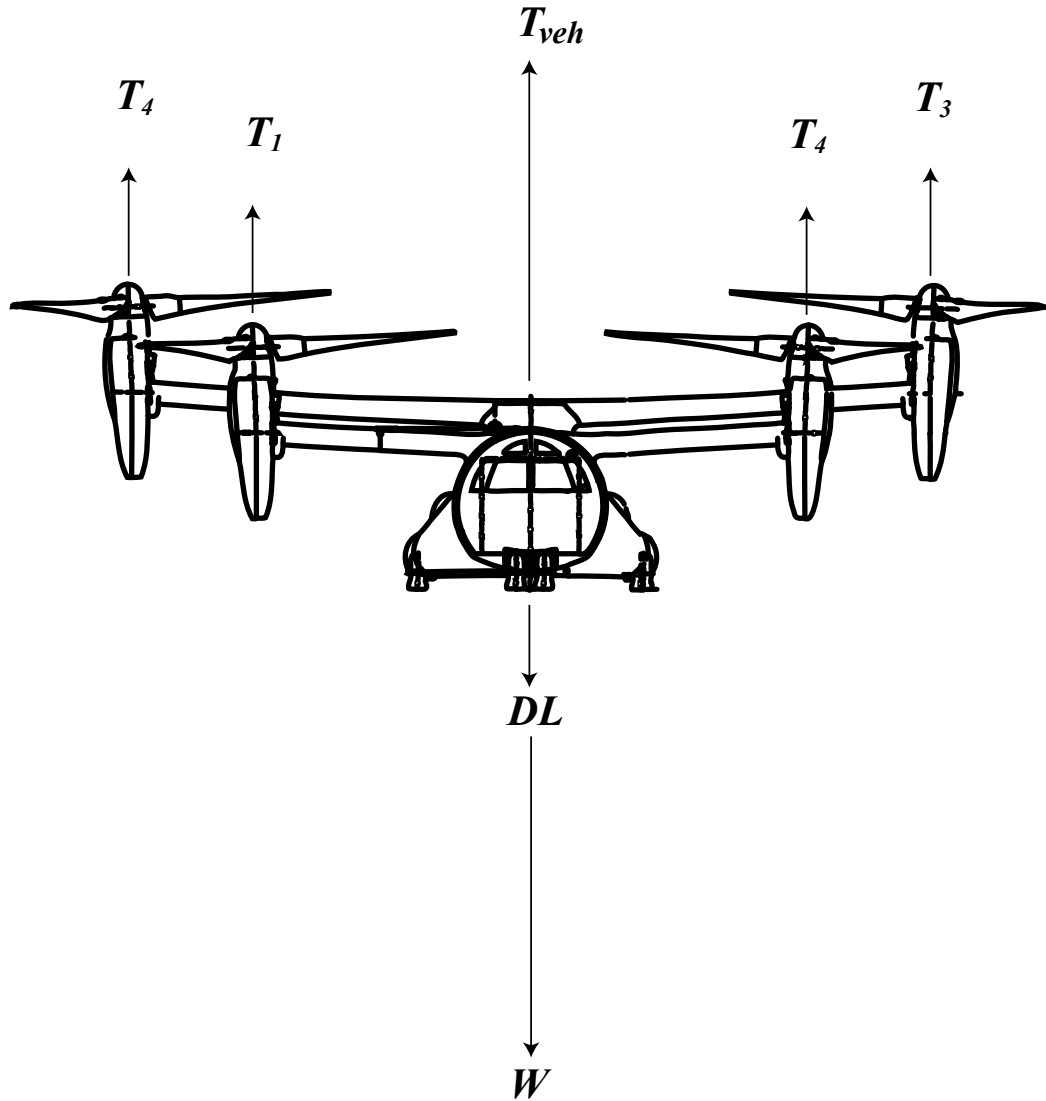


Figure 2.1: Vertical Force Balance Diagram

$$T_{veh} = \sum_{j=1}^4 T_j - DL \quad (2.1)$$

For the purpose of this study, steady, level flight is assumed. For this assumption, the total vehicle thrust will be equal to the weight of the vehicle, W .

$$W = T_{veh} \quad (2.2)$$

2.2 Dimensional Analysis

For steady level flight, the lifting capacity of the vehicle is determined by the total vehicle thrust, T_{veh} , which depends upon the download, DL , and the rotor thrust, T as shown in Equation 2.1. In addition to the vehicle thrust, another important factor affecting the lifting capacity is the rotor power consumption. In order to accurately scale the experiment, the key non-dimensional variables affecting the lifting capacity were identified by performing dimensional analysis on the download, rotor thrust and rotor power.

2.2.1 Forces

The download, DL , is a vertical drag force, which is dependent on the rotor thrust, T , air density, ρ , rotor diameter, D , rotor induced velocity, v_i , forward velocity, V_∞ , air viscosity, μ , front rotor height above the ground, h and wing area in the rotor wake, A_w . Dimensional analysis is performed by applying Buckingham's Pi Theorem[75, 76] to this problem. This theorem states that if an equation involves n physical variables, which are expressible in terms of k independent fundamental quantities, the original expression can be expressed in terms of $n - k$ dimensionless variables.

$$f(DL, T, \rho, D, v_i, V_\infty, \mu, h, A_w) = 0 \quad (2.3)$$

The rotor induced velocity is a derived quantity dependent on rotor thrust and forward velocity. Therefore, the number of independent physical variables in

the above expression is 8. This equation can be expressed in terms of 3 fundamental quantities: mass, m , length, l , and time, t . Therefore, the number of dimensionless quantities required for this expression is $8 - 3 = 5$. Equation 2.3 can be re-written in terms of five dimensionless quantities as follows:

$$f\left(\frac{DL}{T}, \frac{h}{D}, \left(\frac{V_\infty}{v_i}\right), \frac{DL}{\rho A_w v_r^2}, \frac{\rho v_r \sqrt{A_w}}{\mu}\right) = 0 \quad (2.4)$$

where, $v_r = \sqrt{V_\infty^2 + v_i^2}$ is the resultant velocity at the rotor disk (as shown in Figure 2.2) and A is the rotor disk area.

These non-dimensional quantities are explained in greater detail below:

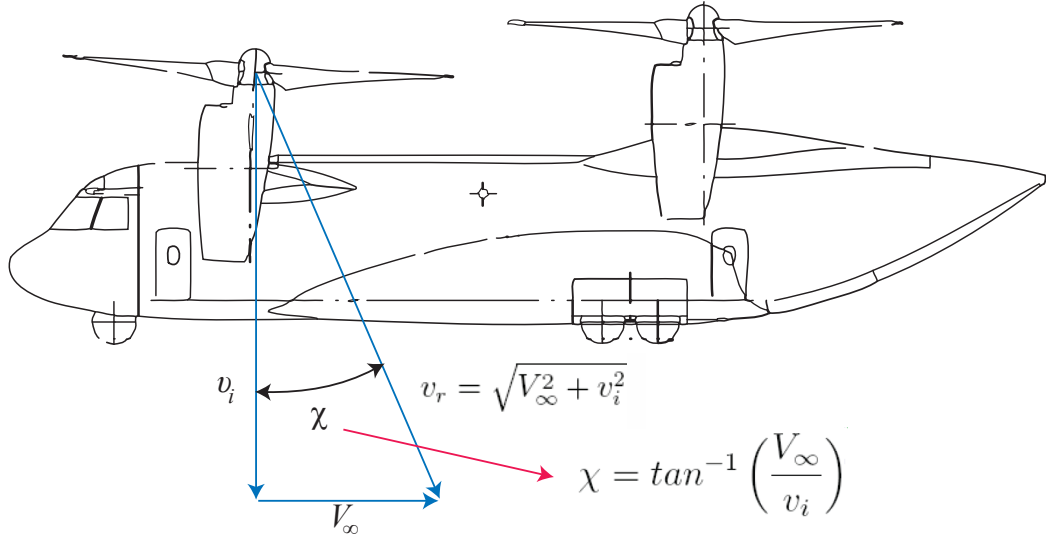


Figure 2.2: Rotor wake skew angle, χ

2.2.1.1 Download to Thrust Ratio

As discussed in Section 1.4.4, a QTR has been observed to experience a downward force on the airframe while operating OGE. However, IGE, this download was

found to reduce and actually become an upward force while operating close to the ground.

A key factor that will determine the lifting capacity of a QTR is the “Download to Thrust Ratio” or DL/T , expressed as a percentage. This is defined as the ratio of the downward force experienced by the airframe to the total thrust produced by the four rotors.

$$\frac{DL}{T}\% = \frac{DL}{\sum_{j=1}^4 T_j} * 100\% \quad (2.5)$$

where,

DL = Download on the airframe

$\sum_{j=1}^4 T_j$ =Sum of the thrust produced by the four rotors

To obtain the download to thrust ratio, independent measurements of the download on the airframe and the thrust on each rotor were obtained.

2.2.1.2 Normalized Height

The height of the vehicle above the ground will affect the intensity of the up-wash that is produced underneath the vehicle. Therefore, another key dimensionless quantity is the normalized height, z , which can be expressed as the height of the front rotors above the ground, h , divided by the rotor diameter, D . Figure 2.3 illustrates the front rotor height above the ground for a QTR. This is a geometric parameter, which depends only on the scale of the model.

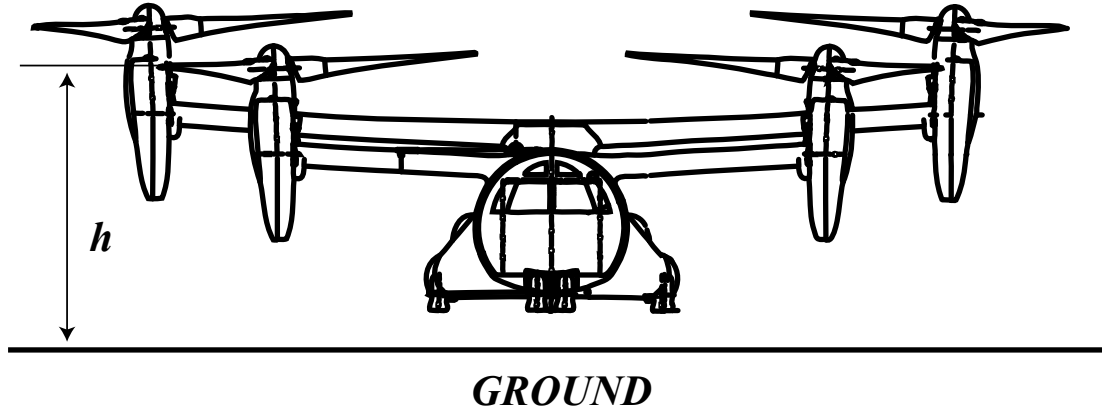


Figure 2.3: Height above the ground, z

$$z = \frac{h}{D} \quad (2.6)$$

2.2.1.3 Rotor Wake Skew Angle

As mentioned in Section 1.4.1.2, Curtiss, et al. [21, 16, 20] found that the wake geometry and performance of a rotor in low speed flight near the ground will be governed by a non-dimensional parameter called the rotor wake skew angle, χ . This quantity is defined as the inverse tangent of the free stream velocity, V_∞ divided by the rotor induced velocity, v_i , as illustrated in Figure 2.2. This is again a

geometric parameter, which describes the flow geometry of the rotor wake in forward flight.

$$\chi = \tan^{-1} \left(\frac{V_\infty}{v_i} \right) \quad (2.7)$$

The rotors used in this experiment were rigid and mounted in the horizontal plane, with no flapping allowed. The rotor induced velocity in low speed forward flight can be obtained from momentum theory, for zero tip path plane angle, which is given by,

$$v_i = V_\infty \sqrt{\sqrt{\frac{1}{4} + \left(\frac{v_h}{V_\infty} \right)^4} - \frac{1}{2}} \quad (2.8)$$

where v_h is the average hover induced velocity of the rotor and can be expressed as:

$$v_h = \frac{T}{2\rho A} \quad (2.9)$$

2.2.1.4 Wing Drag Coefficient

The download can be expressed as a dimensionless drag co-efficient, which is related to the density of air, the wetted area of the airframe in the rotor wake, A_w , and the effective velocity experienced by the wings. The effective velocity can be calculated from the downwash velocity and the forward speed, as shown in Figure 2.2.

$$C_{D_w} = \frac{DL}{\rho A_w (V_\infty^2 + v_i^2)} \quad (2.10)$$

2.2.1.5 Wing Reynolds Number

The wing Reynolds number is the ratio of inertial and viscous forces and can be calculated based on the viscosity and density of air, a characteristic length and the effective velocity experienced by the wing. The characteristic length chosen in this case is the square root of the wetted area of the wing in the rotor downwash, A_w .

$$Re_W = \frac{\rho \sqrt{V_\infty^2 + v_i^2} \sqrt{A_w}}{\mu} \quad (2.11)$$

The main effect of the wing Reynolds number on the download to thrust ratio would be through the wing drag coefficient, if the flow around the wing is attached. However, in helicopter mode, the wing will operate at a high angle of attack with respect to the flow. For separated flows, the Reynolds number will not have a significant effect on the wing drag coefficient.

2.2.1.6 Downwash Distribution

In addition to the previous quantities, another important parameter that will affect the download will be the radial distribution of the rotor downwash. Although this factor is not captured by the preceding dimensional analysis, it will affect the intensity of the fountain flow and also the velocity that will be experienced by different wing sections.

2.2.2 Rotor Power

In order to evaluate the usability of any performance benefits of operating in close proximity to the ground, power measurements were obtained at different flight conditions. These power measurements for each test condition were normalized by the power measurements in hover, OGE, for a given total vehicle thrust (T_{veh}). This was done to indicate the relative change in power required to operate the aircraft as compared to hovering flight, OGE. This normalized power, P^* , is defined as follows:

$$P^* = \frac{\sum_{j=1}^4 P_j}{(\sum_{j=1}^4 P_j)_{hover, OGE}} \quad (2.12)$$

where P_j is the corrected power of each rotor.

The total power can be thought of as the sum of induced power and profile power. These two components of the total power can be analyzed separately to determine the scaling factors affecting them:

2.2.2.1 Rotor Induced Power

The rotor induced power, P_i , is dependent on rotor thrust, T , the air density, ρ , air viscosity, μ , rotor height above the ground, h , blade chord, c , rotor diameter, D , forward speed, V_∞ , rotor tip speed, V_{tip} and the speed of sound in air, c_a . This relation can be expressed as:

$$f(P_i, T, \rho, h, c, D, V_\infty, V_{tip}, c_a) = 0 \quad (2.13)$$

There are a total of eight physical quantities in the above relationship. These can be expressed in terms of three fundamental quantities: mass, length and time. By applying Buckingham's Pi theorem, the above relationship can be expressed in terms of five dimensionless quantities as follows:

$$f\left(\frac{N_b c}{\pi D/2}, \frac{T}{\rho(\pi D^2/4)V_{tip}^2}, \frac{P_i}{T^{3/2}/\sqrt{(2\rho(\pi D^2/4))}}, \frac{V_{tip} + V_\infty}{c_a}, \frac{h}{D}, \frac{V_\infty}{v_i}\right) = 0 \quad (2.14)$$

These quantities are the the blade solidity, σ , rotor thrust coefficient, C_T , induced power correction factor, κ , rotor tip Mach number, M_R , normalized rotor height, z , and rotor wake skew angle, χ . The last two quantities were already discussed in the preceding section. The rest of the parameters are discussed as follows:

Rotor Solidity: The rotor solidity is the ratio of the blade area to the disk area and is expressed as:

$$\sigma = \frac{N_b c}{\pi D/2} \quad (2.15)$$

Rotor Thrust Coefficient: The rotor thrust coefficient, C_T , is a dimensionless parameter, which when divided by the rotor solidity, gives the average loading on the rotor blades.

$$C_T = \frac{T}{\rho(\pi D^2/4)V_{tip}^2} \quad (2.16)$$

The quantity C_T/σ is referred to as blade loading and affects the distribution of the rotor downwash.

Induced Power Correction Factor: The induced power correction factor, κ , is the factor used to account for all non-ideal effects on rotor induced power and is defined as the ratio of actual induced power to ideal induced power (calculated from momentum theory).

$$\kappa = \frac{P_i}{T^{3/2}/\sqrt{(2\rho(\pi D^2/4))}} \quad (2.17)$$

This correction factor is affected by the shape of the downwash distribution curve and is therefore a function of the blade loading (C_T/σ).

Rotor Tip Mach Number: The rotor tip Mach number expresses the compressibility of the flow experienced by the rotor blades. This is the maximum Mach number that will be experienced by the advancing rotor blade in forward flight and can be expressed as:

$$M_R = \frac{V_{tip} + V_\infty}{c_a} \quad (2.18)$$

2.2.2.2 Rotor Profile Power

The rotor profile power, P_0 , is dependent on the air density, ρ , air viscosity, μ , blade chord, c , rotor diameter, D , forward speed, V_∞ , and rotor tip speed, V_{tip} . This relation can be expressed as:

$$f(P_0, \rho, \mu, c, D, V_\infty, V_{tip}) = 0 \quad (2.19)$$

There are a total of seven physical quantities in the expression above. These can be expressed in terms of three fundamental quantities: mass, length and time. By

applying Buckingham's Pi theorem, the above relationship can be expressed in terms of four dimensionless quantities as follows:

$$f\left(\frac{P_0}{\rho(\pi D^2/4)V_{tip}^3}, \frac{\rho V_{tip}c}{\mu}, \frac{V_\infty}{V_{tip}}, \frac{N_b c}{\pi D/2}\right) = 0 \quad (2.20)$$

These dimensional quantities are the rotor profile power coefficient, C_{P_0} , rotor Reynolds number, Re_r , and the rotor solidity, σ .

Rotor Reynolds Number: The rotor Reynolds number will affect the viscous drag on the rotor blades and therefore, the profile power.

$$Re_r = \frac{\rho V_{tip}c}{\mu} \quad (2.21)$$

In this study, fixed-pitch, variable RPM propellers were used to model the fixed-RPM, variable pitch prop-rotors of a QTR. Also, the study was conducted at a much smaller geometric scale.

2.2.3 Pressure Coefficient

In order to investigate the causes for the changes in download IGE, pressure measurements were obtained along the centerline of the bottom surface of the fuselage. These pressures were obtained using differential pressure transducers. These transducers measured the difference between the absolute pressure at pressure taps on the bottom of the fuselage and the atmospheric pressure. This differential pressure is divided by the rotor disk loading to obtain a non-dimensional quantity, the coefficient of pressure (C_{pDL}),

$$C_{pDL} = \frac{p - p_\infty}{T/A} \quad (2.22)$$

This quantity enables the comparison of the measured pressures even when operating at different values of rotor induced velocity, *i.e.*, thrust level. The nomenclature, C_{pDL} , is chosen to differentiate it from the coefficient of power, C_P .

2.3 Experimental Approach and Scaling

While full-scale testing will provide the best representation of the aerodynamics of a vehicle, cost and complexity make such experimentation a prohibitive affair. Therefore, it was necessary to develop a small-scale model of a QTR configuration for the purpose of testing in hover and low speed forward flight, in and out of ground effect. In order to perform the test with the facilities and materials available, a scale of 0.031 was chosen. The aerodynamic features of the model are compared with that of a full-scale QTR, in Table 2.1. The main concern with such small-scale testing is that the aerodynamics of the problem may not be adequately represented because of the lower values of induced velocity, disk loading, tip speed and Reynolds numbers for the model.

Simple momentum theory indicates that ideal rotor thrust in hover, OGE, is related to downwash velocity by

$$T = 2\rho A v_h^2, \quad (2.23)$$

where, v_h is the induced velocity in hover.

At constant density, large disk loading (T/A) causes large downwash velocities. For TR and QTR aircraft, these downwash velocities also cause a net download, DL , on the vehicle that is generally proportional to the induced velocity,

$$DL \sim \rho A_w v_h^2 \cdot C_{Dw}, \quad (2.24)$$

where A_w is the wetter area of the airframe submerged in the wake.

In helicopter mode, the wings of a QTR operate at very high angles of attack, which would result in flow separation. For such separated flows, it can be assumed that the wing drag coefficient, C_{Dw} would not vary much even at these low Reynolds numbers. By keeping geometric similarity and assuming that the rotor downwash distributions are similar to the full-scale QTR,

$$\left(\frac{DL}{T}\right)_{OGE} \approx \frac{\rho A_w v_h^2 \cdot C_{Dw}}{2\rho A v_h^2} = k \quad (2.25)$$

where, k is a constant.

Under these simplifying assumptions, download to thrust ratios, in hover, should be dependent only upon the geometry of the configuration being investigated. Because of small-scale motor power limitations, the UM scale model was not able to duplicate the downwash velocities (disk loadings) of the full-scale QTR. However, as discussed above, the download normalized by total rotor thrust, should remain constant, if the flow fields surrounding the small-scale model are similar to the full-scale QTR aircraft.

Table 2.1: Comparison of full-scale Bell QTR with the small-scale model

Feature		Full-Scale QTR	UM Scale Model
Rotor Diameter	in	456	14
Blades per hub		3	3
Rotor Blade Loading (C_T/σ)		0.091 to 0.14	0.1 to 0.11
Rotor Downwash Distribution		V-22 Prop-Rotor Distribution	Model Propeller Distribution
Rotor Wake Skew Angle	degrees	0 to 70	0 to 70
Front Rotor Height, $z = h/D$		0.61 to OGE	0.61 to 3.5
Hover Induced Velocity	ft/ sec	55^a to 70^b	14 to 31.5^c
Wing Reynolds Number		2.8×10^{6a} to 3.5×10^{6b}	2.1×10^4 to 4.8×10^4
Rotor Reynolds Number ^d		6.8×10^6	6.0×10^4 to 1.33×10^5
Rotor Mach Number		0.71	0.15 to 0.33
Nacelles & Sponsons		Yes	Removed

^aCalculated from momentum theory, based on empty weight[2]

^bCalculated from momentum theory, based on max. VTOL weight[2]

^cbased on measured thrust in hover

^dCalculated based on 3/4 radius section

In order to validate these assumptions, the experiment was conducted at different values of disk loadings, which correspond to different induced velocities and

wing Reynolds numbers. These results are presented in Chapter 4.

As the twist and downwash distributions of a QTR prop-rotor are closer to that of a propeller than that of a helicopter rotor, it was decided that model airplane propellers would be used for the experiment. While the full-scale rotors are controlled by varying the collective pitch at a constant rpm, because of motor power limitations at the model scale, it would be very difficult to maintain an equal thrust on all four rotors using such a method. In order to reduce the complexity of controls, fixed-pitch propellers were chosen.

The downwash velocity distribution of the rotors will determine the relative velocities experienced by the wing at different sections, thus influencing wing download. Therefore, the downwash profiles of the propellers were measured and compared to the full-scale QTR rotor, as described in Chapter 3.

The thrust of these propellers is controlled by varying the rpm. This change in the rpm will cause a change in the profile power of the propellers for different test conditions. In addition, the profile power is highly dependent on the Reynolds number at these low Reynolds numbers. Therefore, the measured power was corrected to have the profile power contributions removed. In addition, the measured power was also adjusted to account for induced effects caused by the use of fixed-pitch, variable-rpm propellers instead of fixed-rpm, variable-pitch prop-rotors. These power corrections are described in detail in Appendix A

The Mach numbers at which the experiment was conducted was lower than the full scale. However, as we are studying very low speed forward flight, the Mach number will not approach sonic conditions and therefore, compressibility effects can

be neglected.

The fixed pitch propellers are frozen at a zero tip path plane (TPP) angle even when operating at different forward speeds. However, the range of rotor wake skew angles, i.e., advance ratios are in the very low speed range. For lower values of rotor wake skew angles, because of low drag, the TPP angles will be quite small and can be neglected. The work of McVeigh, et al.[69], showed that the effect of TPP angle on download is approximately the as the effect of rotor wake skew angle. Therefore, the skew angle at the higher speeds can be corrected for the TPP angle.

2.4 Experimental Setup

2.4.1 Model Configuration

The experiment was conducted using a 1:33 scale model of the QTR configuration specified by Bell Helicopter. The rotors were 14" in diameter and the distance between the front and rear rotors was 1 rotor diameter (D). The front rotors were separated by a distance of $1.35D$ while the rear rotors were separated by $1.97D$. The front and rear rotors had a vertical separation of $0.1D$. The rotorwing separation distance was $0.21D$.

2.4.1.1 Airframe Model

There were two different models of the QTR that were tested, Model A and Model B. Model A, shown in Figure 2.4.1.1(a), was constructed at the University of Maryland using design drawings of the QTR configuration obtained from Bell

Helicopter. The front wings were made of NACA 0012 balsa sections at zero angle of attack, zero sweep angle and zero dihedral. The rear wings had outer sections made of NACA 0012 balsa at zero angle of attack, zero sweep angle and zero dihedral. The tapered inner sections were made of balsa ribs with NACA 0012 airfoil sections held together with balsa spars and covered with MonoKote® plastic sheeting. The fuselage was made of plastic PVC piping. The nose was made of wood that was turned down in a lathe to approximately the shape given by the design drawings. The flap angle was zero for both the front and the rear wings. There were no nacelles and sponsons included for this model.

Model B, shown in Figure 2.4.1.1(b), was a scale replica of the QTR configuration and was constructed by Bell Helicopter using rapid prototyping techniques. The airframe was constructed in several different segments, which were assembled at the University of Maryland. The nacelles and sponsons were constructed as removable attachments. For the purpose of this study, all results obtained from Model B were conducted with the nacelles and sponsons removed. Both the front and rear wings had trailing edge flaps that were frozen at a flap deflection angle of 67 degrees. The front wings were at an angle of attack of 3 degrees, while the rear wings had a zero degree angle of attack. Both the front and rear wings had a dihedral angle of 3.5 degrees and a forward sweep angle of 6 degrees. The fuselage had a ridge on the upper surface, running lengthwise from the front wing to the rear wing, as shown in Figure 2.4.1.1(b). This ridge contained the cross-shafting between the two rotors and was offset from the centerline of the fuselage towards the starboard side.

The features of these two models are compared in Table 2.2.



(a) Model A



(b) Model B

Figure 2.4: Different airframe models tested

Table 2.2: Comparison of small-scale models that were tested

Feature	Model A	Model B
Scale	1:33	1:33
Wing Flap Angle	0°	67°
Front Wing Angle of Attack	0°	3°
Wing Airfoil Shape	NACA 0012	Cambered QTR airfoil
Cross-shafting	No	Yes
Nacelles & Sponsons	No	Removable

2.4.1.2 Rotor Assembly

The rotors that were used for this experiment were three-bladed, rigid, 14x7 Master Airscrew fixed-pitch model airplane propellers, manufactured by Windsor Propeller Company. These propellers were chosen because of the availability of identical geometries in pusher and tractor versions. Also, the QTR has highly twisted rotor blades, which are closer in geometry to propellers than rotors. The physical geometry of the propellers, in terms of radial distribution of chord and pitch angles, are presented in Chapter 3.

The QTR has the rotors on the port side rotating in a clockwise direction, while the rotors on the starboard side rotate in an anti-clockwise direction. Therefore, the tractor propellers were used for the port side and the pusher propellers were used for the starboard side.

2.4.2 Drive Mechanism

The rotors were powered by Astroflight Cobalt 90 motors, which were high-speed direct drive, model airplane electric motors. These motors were chosen for their ability to provide the high torque that was required to turn the propellers at high RPMs and for their relatively small size.

2.4.3 Mounting

The motors were mounted on a load-cell balance that measured thrust, torque and RPM. Four of these motor mounts were attached to a rectangular mounting frame constructed from T-slotted Aluminum extrusions, as shown in Figure 2.5. The mounting frame was attached on each side to the vertical members of a support frame, which was also constructed from the T-slotted extrusions, as shown in Figure 2.6. The setup was designed to allow the height of the model above the ground to be adjusted easily using linear motion slides. The airframe, consisting of the fuselage and wings, was also suspended from the rectangular frame on a load cell balance that measured the download or upload of the front and rear airframe.

2.4.3.1 Motor Mount

The motor mount, as shown in Figure 2.8, included instrumentation that consisted of a miniature tension/compression load-cell, with a ± 25 lbs range to measure thrust, a miniature tension/compression load-cell with a ± 10 lbs range to measure

torque and an optical sensor to measure RPM. These sensors were chosen based on the size and the thrusting power of the motors.

The thrust load-cell was constrained to measure the load in the vertical direction by means of parallel track rods passing through linear bearings. The track rods and linear bearings were 0.375" in diameter and were manufactured by Thomson Industries. Figure 2.8 shows the details of the torque measurement apparatus of the motor mount. The motor, fits inside the inner housing and is attached using screws on the bottom plate. The inner housing is attached to the inner race of the radial bearing using the bearing lock-screw, which screws on to the threaded bottom part of the inner housing. The outer race of the radial bearing is attached to a groove inside the outer housing, by means of a locking plate.

By means of this arrangement, the rotor thrust is isolated from the torque by the radial bearing, which provides radial freedom of movement between the inner and the outer housing. By attaching a load cell between the inner and the outer moment arms, which are attached to the inner and the outer housing respectively, the reaction torque produced by the motor can be measured. Because of the radial nature of this loading, double constraining of the torque load cell could result in extra moments. Therefore, the load cell is constrained by the use of a spring, which pre-loads the load cell and prevents the displacement of the load cell when the motor is idle.

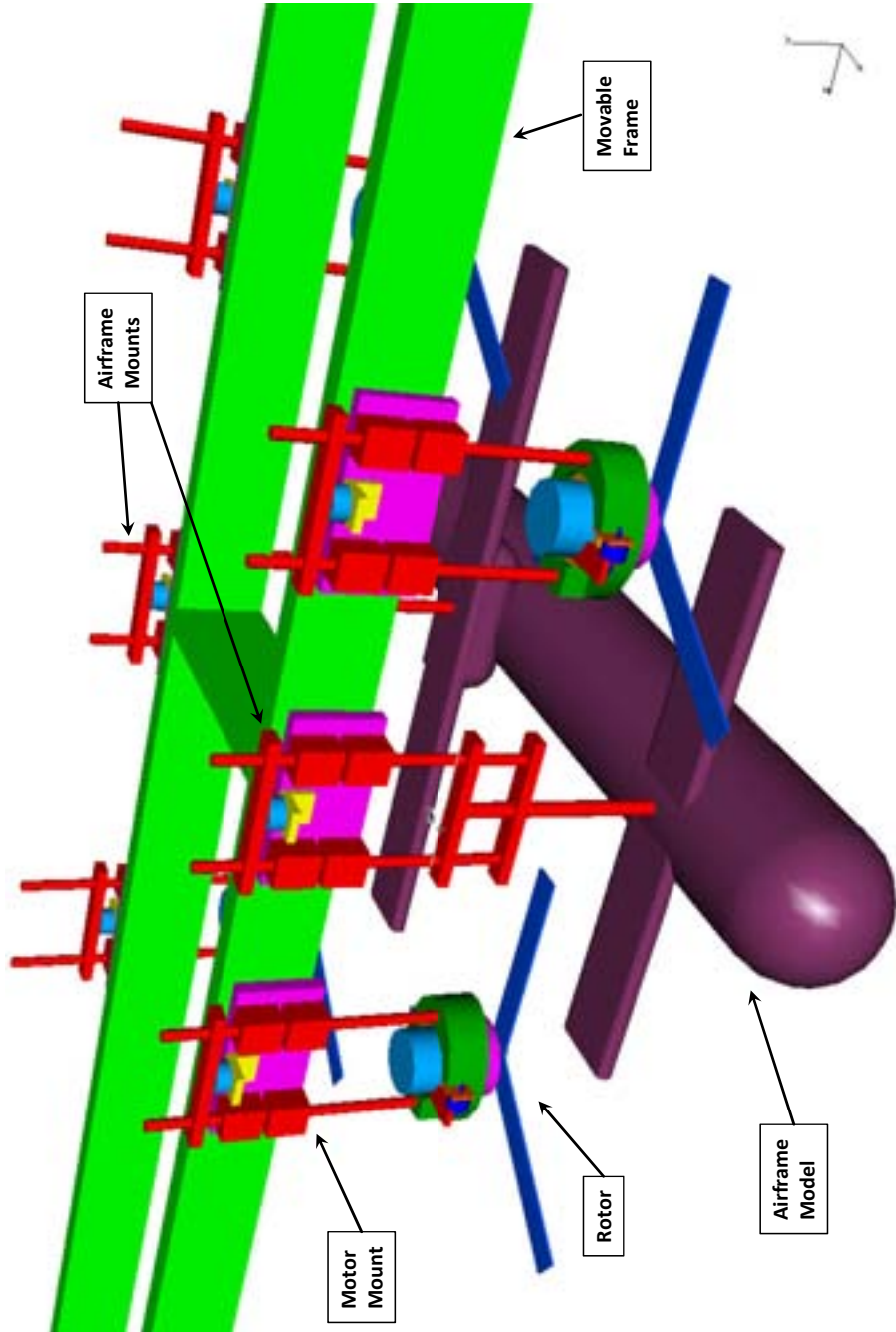


Figure 2.5: Mounting

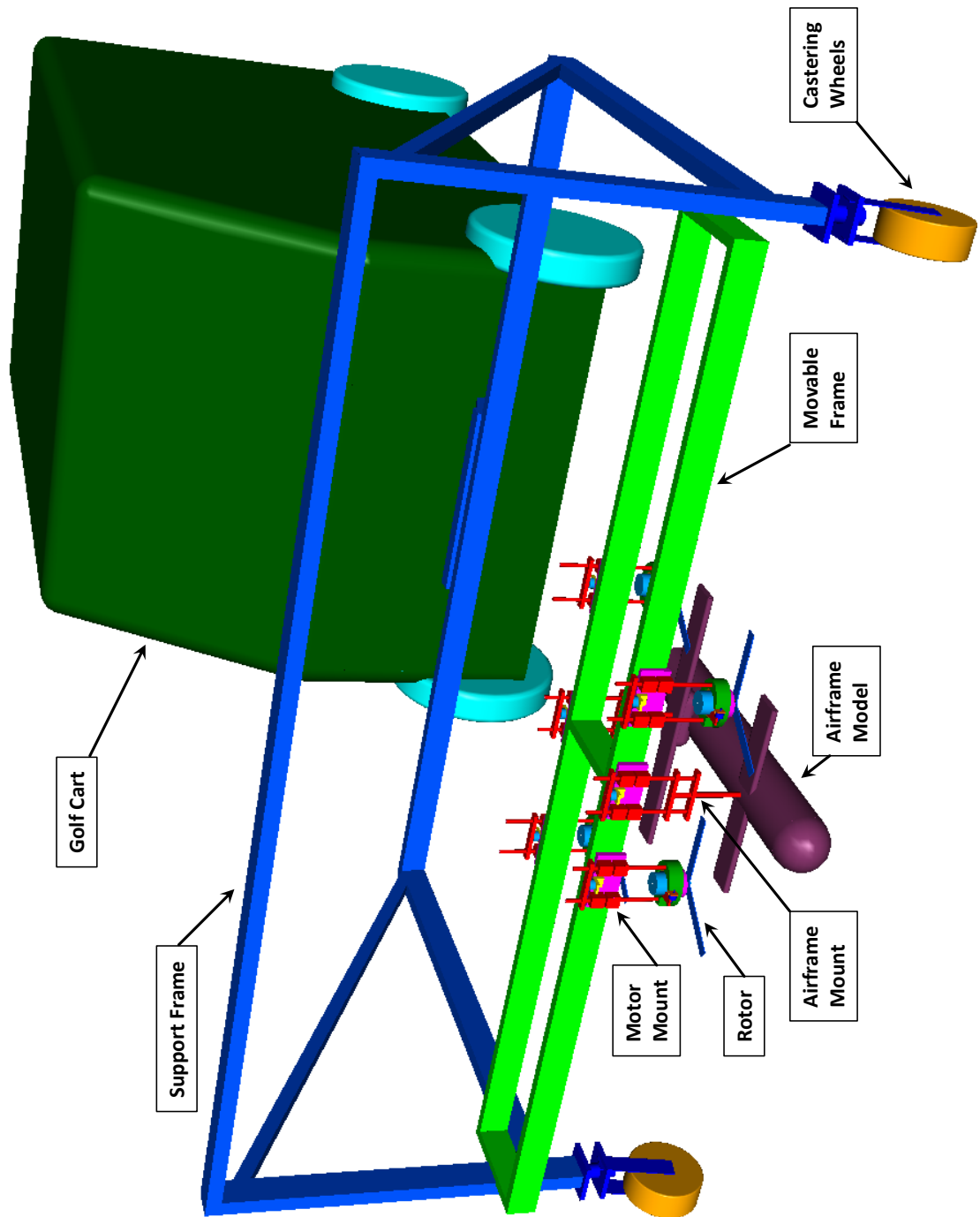


Figure 2.6: Test Stand

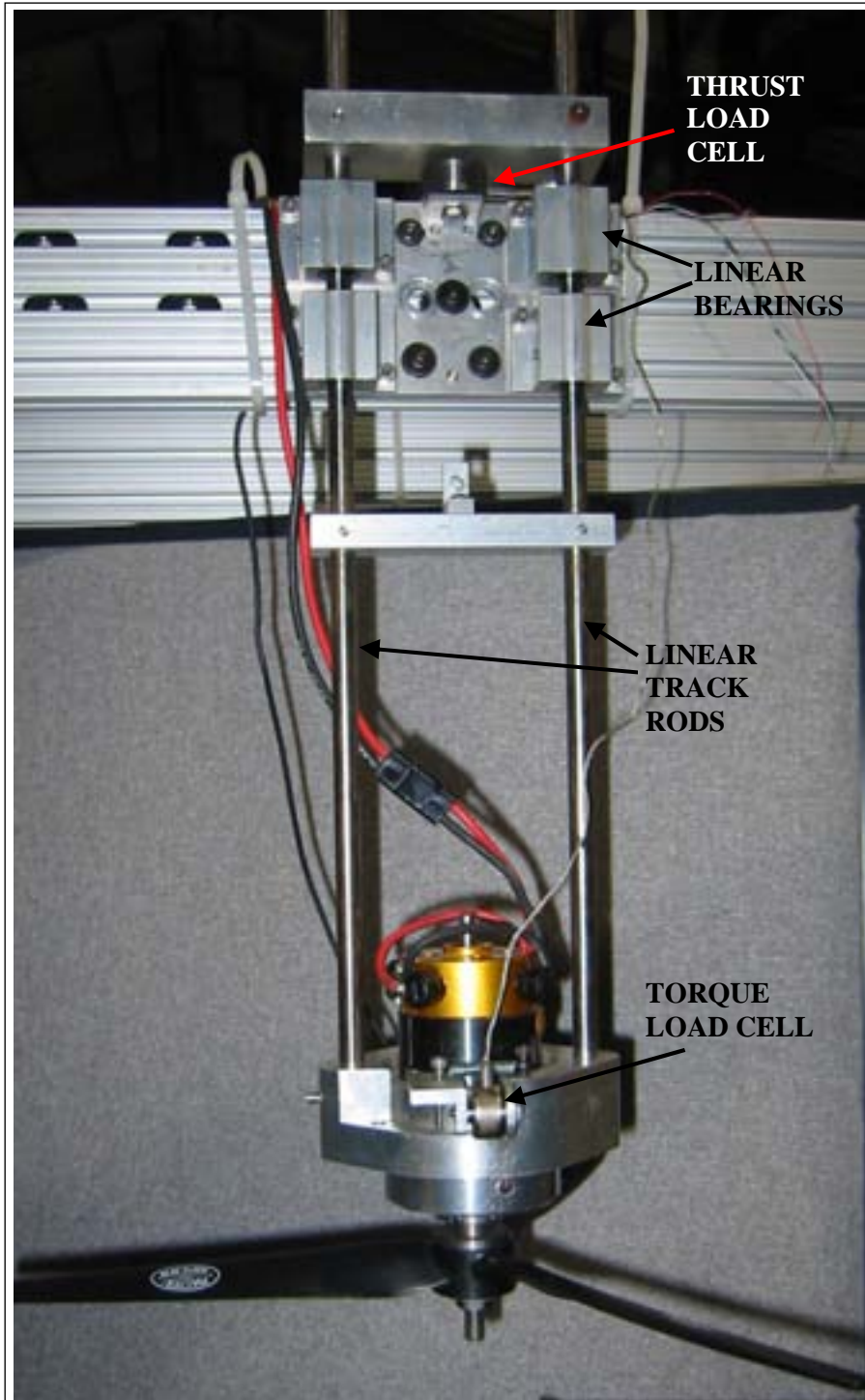
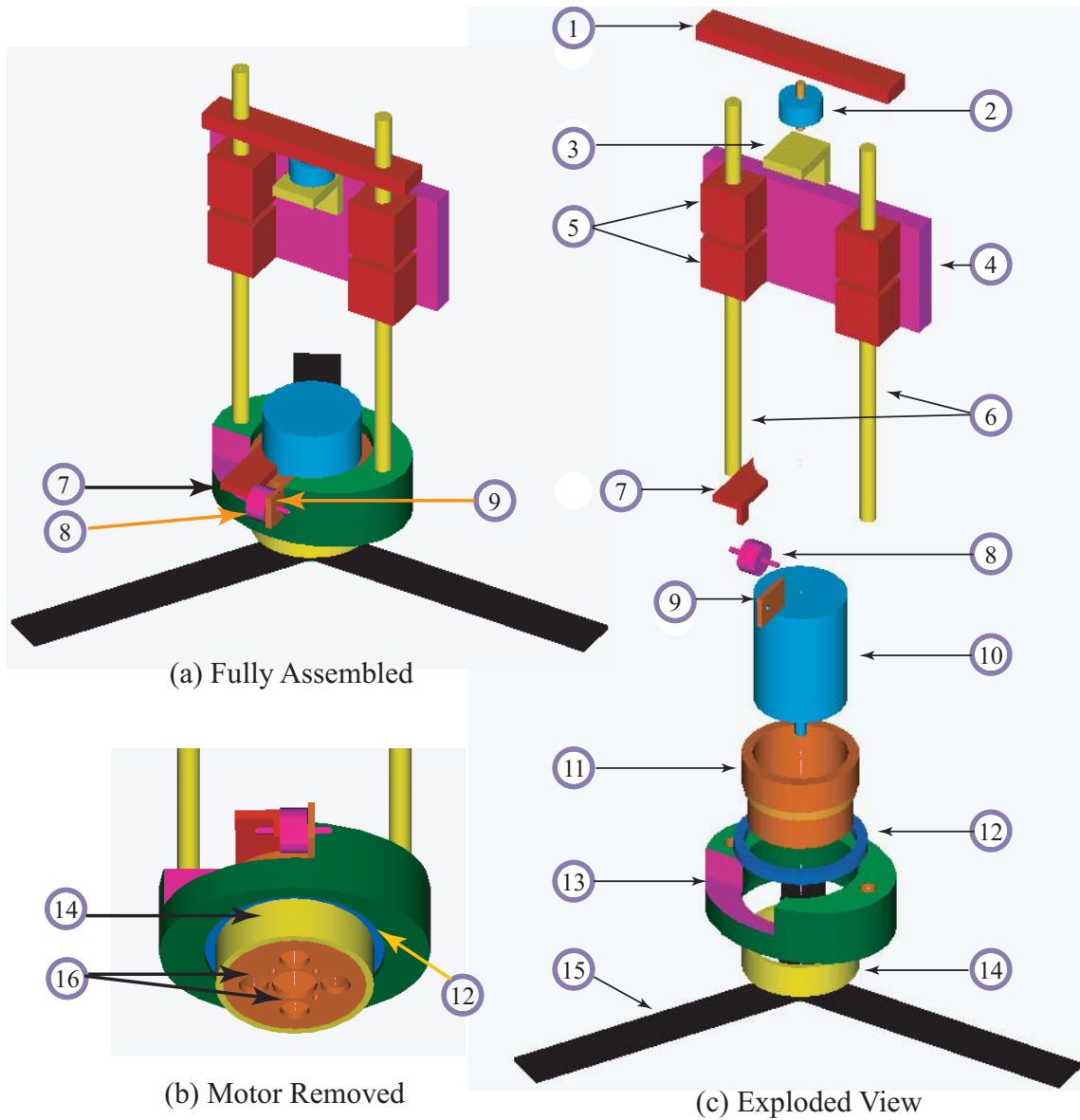


Figure 2.7: Motor Mount



Parts List	
1. Thrust Load Plate	9. Inner Moment Arm
2. Thrust Load Cell	10. Electric Motor
3. Thrust Bracket	11. Inner Housing
4. Frame Mounting Plate	12. Radial Bearing
5. Linear Bearings	13. Outer Housing
6. Bearing Guide Rods	14. Bearing Lock-screw
7. Outer Moment Arm	15. Propeller/Rotor
8. Torque Load Cell	16. Motor vent-holes

Figure 2.8: Sketch of the Motor Mount Apparatus

2.4.3.2 Airframe Mount

The airframe, which included the fuselage and wings, formed an independent entity that was isolated from the rotors and separately mounted on the frame. It was mounted at 2 locations, which enabled the separate measurement of the downloads produced near the front and rear on the airframe, shown in Figure 2.9.

The loads were measured by miniature tension/compression load-cells, with a ± 10 lbs range. The airframe mount, sketched in Figure 2.10, was similar to the thrust measurement apparatus in the motor mount, and also used linear bearings to constrain the load cells to measure loads only in the vertical direction.

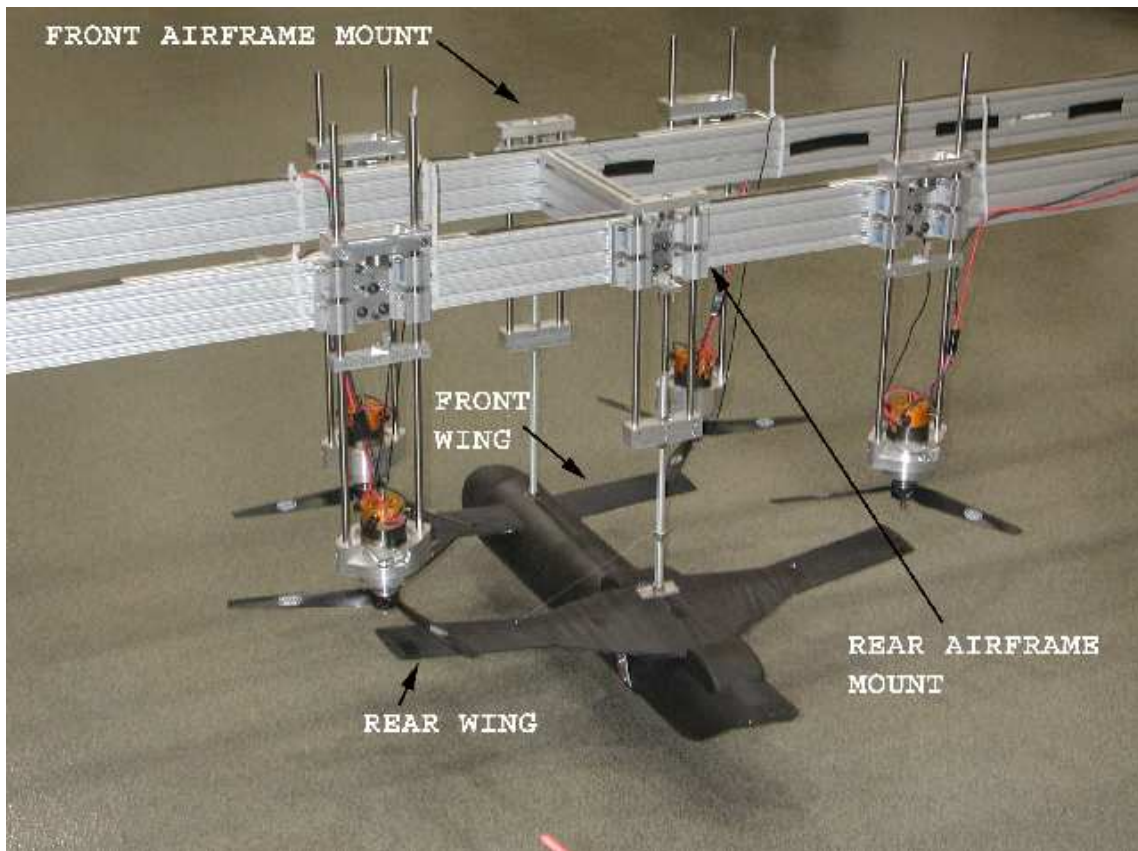


Figure 2.9: Airframe Mount

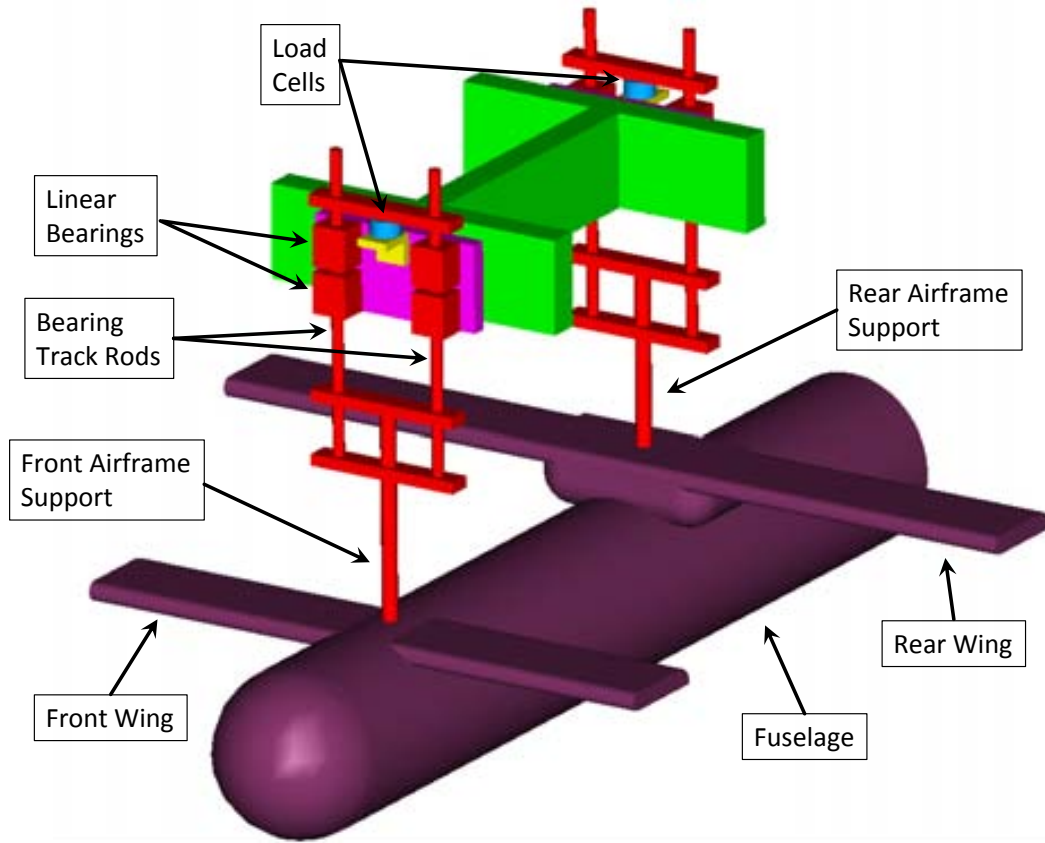


Figure 2.10: Sketch of the Airframe Mounts

By performing careful calibration, the loads measured at these two airframe mounts were found to have negligible amounts of cross-coupling. Therefore, the downloads measured at the two mounts can be thought of as independent measurements.

2.4.4 Pressure Measurement

Vertical holes were drilled along the center-line of the of the fuselage in order to obtain pressure measurements on the bottom surface. Rigid 1/16" ID metal tubes were passed through the fuselage and connected to pneumatic tubes on the top

surface of the fuselage. These pneumatic tubes are routed to differential pressure transducers located on the mounting frame. There were a total of 8 pressure taps, as shown in Figure 2.11.

Table 2.3: Longitudinal Distance of the Pressure Taps From the Nose

Port Number	1	2	3	4	5	6	7	8
x/D	0.33	0.62	0.73	1.13	1.40	1.66	1.75	2.04

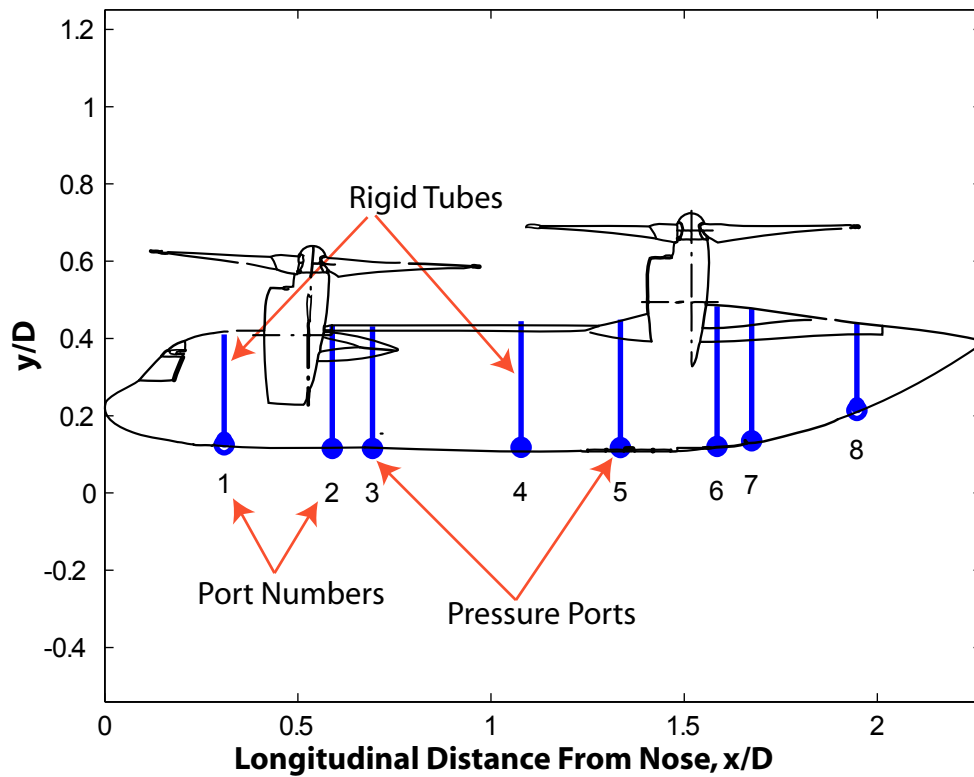


Figure 2.11: Location of the Pressure Taps

The longitudinal distances of the pressure taps from the nose of the fuselage, normalized by the rotor diameter, x/D , are listed in Table 2.4.4.

The pressure transducers measured the difference in pressure between the pressure taps and the atmosphere. These transducers were manufactured by All Sensors Corporation and had a range of $\pm 1 \text{ in. } H_2O$.

2.4.5 Instrumentation and Data Acquisition

The motors were powered by a bank of heavy duty car batteries and their speeds were regulated by digital speed controllers. The load cells and RPM gages were connected to signal conditioners, which were fed the data into a data acquisition system on a portable computer. The motor speed controllers were also controlled by output signals from the data acquisition system. Since the rotors were really fixed-pitch propellers, the rotor thrust was controlled by varying the RPM. The thrust on each rotor was maintained within 1% of the desired thrust, by means of a closed loop software controller. The quantities that were recorded were thrust, torque and RPM of the four rotors and download or upload of the front and rear airframe.

The data acquisition system consisted of a signal conditioning board and a data recording component. The signal conditioning board had 10 load cell signal conditioners for the thrust and torque of the four motors and the two airframe mounts, and 4 frequency signal conditioners for the motor RPM. These signal conditioners were mounted on a powered backplane, as shown in Figure 2.12. The conditioned signal was routed to a 12-bit, 16 single-ended input channel data acquisition card on a notebook computer. Because of vibration of the frame and the highly turbulent flow environment, the measured quantities were found to be

unsteady. This unsteadiness in the readings was further aggravated by operation IGE. Therefore, a real-time averaging of the data had to be performed, in order to control the rotor thrust at the desired level.

2.4.6 Equipment for Forward Flight Testing

For testing in low speed forward flight, the structure was supported by castering aircraft nosewheel landing gear struts, which were equipped with oleo-pneumatic shock absorbers, fully pneumatic wheels and shimmy dampening, as shown in Figure 2.12. The experimental rig was attached to the front of an electric golf cart to push it forward at selected airspeeds, as shown in Figure 2.12. The golf cart is capable of providing forward speeds up to 25 miles per hour.

Originally, the entire frame and the supporting structural members were constructed out of wood. However, there were issues with strength and rigidity of the frame in forward motion, which caused one of the legs of the supporting frame to break off in mid-test. Therefore, for subsequent tests, the support structures were redesigned and constructed from stiffer T-slotted aluminum extrusions.



Figure 2.12: Test Setup

2.4.7 Test Location

The test was performed in the lobby floor of the Health and Human Performance Building on the University of Maryland campus in College Park, Maryland. The forward speed cases were conducted in a long hallway, shown in Figure 2.13, which was 20 feet (17 rotor diameters, D) wide, approximately 400 feet long and three floors high.



Figure 2.13: Test Location

The hover tests were conducted in a waiting area in which the nearest solid boundaries were about $17D$ away from the center of the model, and repeated in a large closed laboratory in the Manufacturing Building on the same campus, where the nearest boundaries were about $8.5D$ away from the center of the model and the roof was about $34D$ high.

2.4.8 Test Assumptions

The experiment was performed based on the following assumptions:

- The average of the measured quantities over the test run is representative of steady state operation.
- Nacelle tilt angle of 90° is representative of the operational state of the QTR in hover and low speed forward flight.
- Rotor TPP angle in helicopter mode is small.
- Motor and airframe supports will not affect the flowfield and measured quantities significantly.
- Model orientation is level.
- Height above ground is constant during the test run.

2.5 Test Objectives

In order to measure the quantitative performance of the QTR, the following quantities were measured:

- The download on front and rear of the airframe
- The thrust on each of the four rotors
- The torque of each of the rotors
- The RPM of each of the rotors
- The height of the front rotors above the ground
- The forward speed of the model
- The pressures along the centerline of the bottom surface of the fuselage

2.6 Uncertainty Analysis

To determine accuracy of the test measurements, a uncertainty analysis of all the key parameters was performed. The details of this analysis are presented in Appendix C. The values of uncertainty that are presented in this dissertation are all calculated for 95% confidence levels.

2.7 Flow Visualization

The previously mentioned tests measured the performance of the QTR in terms of fuselage loads and rotor thrust, torque and RPM. However, in order to physically understand the mechanisms causing the performance changes at different operating conditions, tuft flow visualization was conducted.

White tufts made of knitting yarn were attached to the top and bottom surface of the airframe using black tape, which preserved the contrast in color between the tufts and the background. The tufts were 3/4 inches in length and were arranged in a 3/4 inch square grid. The tufts were extremely light and flexible, so that they would move freely with the flow field.

A digital camcorder was used to record the video and a digital still camera was used to record certain still images in hover. Different camera angles were used to study flow on different parts of the aircraft. A fisheye lens was used to obtain top surface flow images. Because of this, the images may appear distorted. Mirrors on the ground were used to view the flow patterns on the bottom surface of the aircraft.

A ground plane was used to study the surface flow patterns on the ground around the aircraft. This plane was made of a black rubber sheet in which, 1 inch long tufts were arranged in a 1 inch square grid. In hover, this ground plane was used to determine the mechanism causing the upload on the aircraft and to corroborate the flow visualization images obtained by previous CFD and experimental studies. In forward flight, the ground plane was used to determine the direction of flow along

the ground just ahead of the front rotors to predict the location of a ground vortex that could be formed.

Chapter 3

Isolated Rotor

The results from several tests conducted on an isolated rotor are presented in this chapter. The geometry of the rotors is presented, followed by the rotor performance data. Then, the performance of an isolated rotor IGE is discussed. Finally, measured wake velocity profiles are compared with full-scale rotor data.

3.1 Rotor Description

The rotors used for the experiment were rigid fixed-pitch propellers used for model airplanes. These were three-bladed 14x7 Master Airscrew propellers, manufactured by Windsor Propeller Company. The notation signifies that the propellers were 14 inches in diameter and 7 inches in pitch. Here pitch refers to the theoretical axial distance that a propeller would move in one revolution.

3.2 Rotor Geometry

The measured radial variation of blade chord and twist angle is presented in Table 3.1 and in Figures 3.1 and 3.2. It can be seen that the blade chord does not

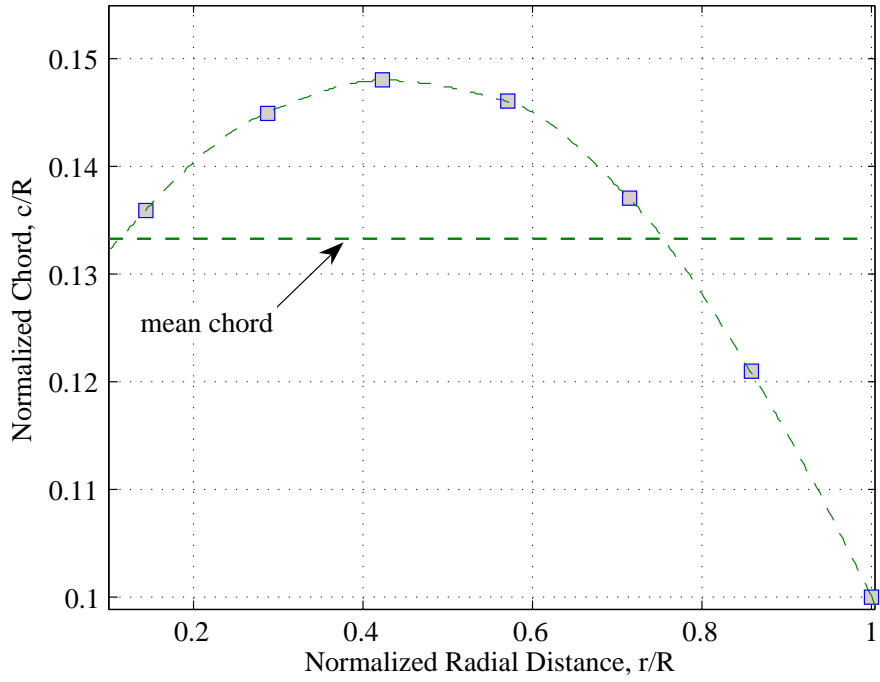


Figure 3.1: Radial Chord Distribution

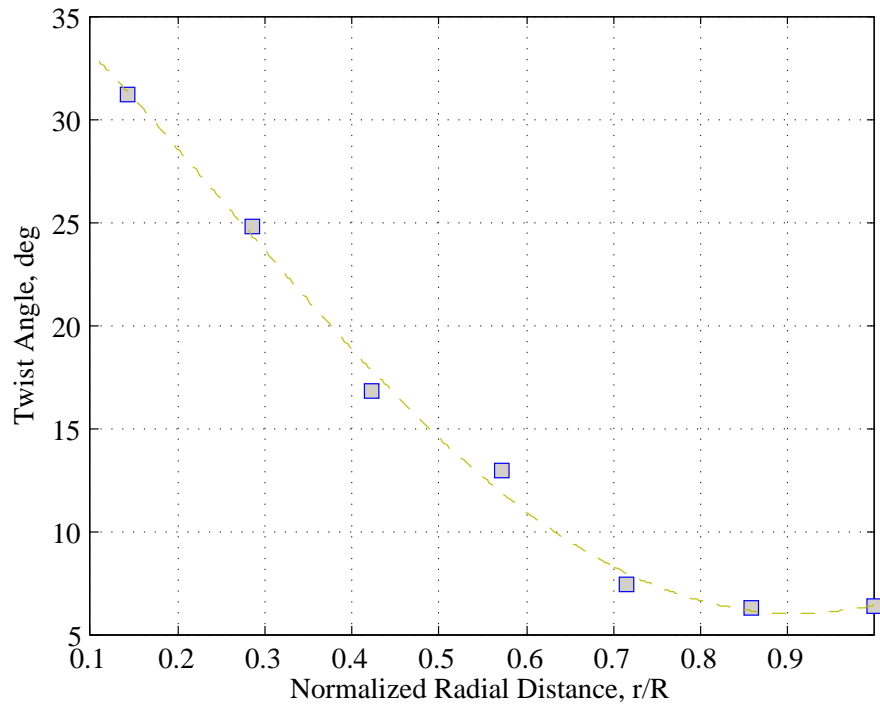


Figure 3.2: Radial Twist Distribution

Table 3.1: Propeller Geometry for 14x7 Master Airscrew

Radial Location	Chord	Twist Angle
r/R	c/R	Twist
0.143	0.136	31.2°
0.286	0.145	24.8°
0.423	0.148	16.8°
0.571	0.146	12.9°
0.714	0.137	7.4°
0.857	0.121	6.3°
1.0	0.100	6.4°

vary substantially along the radius. The chord shows a slight increase from the root to the center of the blade span and the decreases slightly till the 3/4 radius section. From the 3/4 radius location to the tip, there is a more rapid taper. The twist angles were obtained by calculating the inverse tangent of the ratio of the difference in measured elevations of the leading and trailing edges of the blade and the chord at different radial locations. The twist angle distribution is almost elliptic, as would be expected for a propeller.

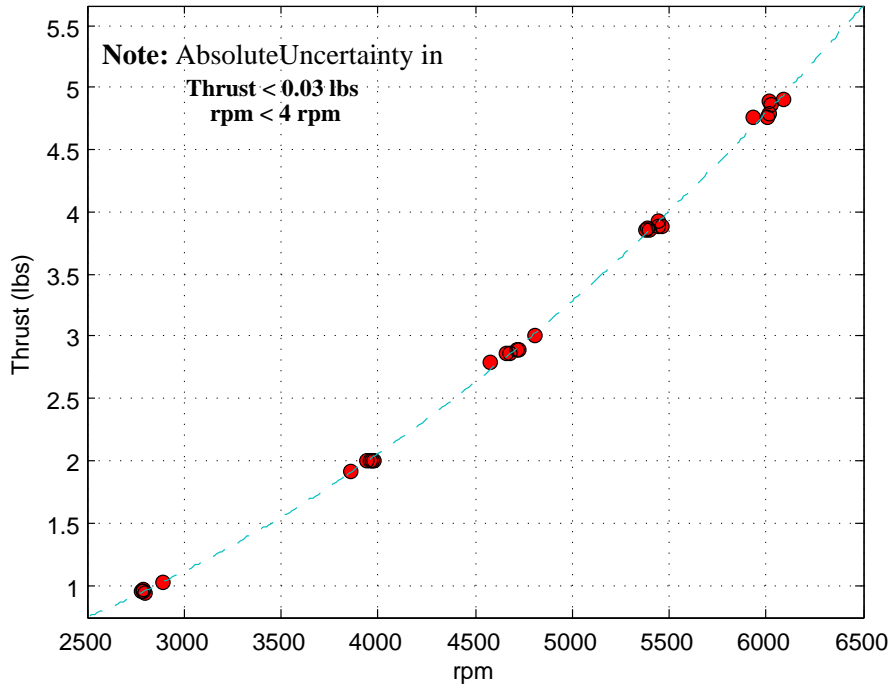


Figure 3.3: Isolated Rotor Thrust vs. RPM

3.3 Isolated Rotor Performance

The hover performance of each of the four rotors was measured independently with the airframe removed. Figure 3.3 presents the measured thrust for different rpms for one of the rotors. The measured thrust values approximately vary from 1 lb at about 2800 rpm to 5 lbs at about 6000 rpm. The thrust coefficient, C_T , is also plotted vs rpm in Figure 3.4. It might seem unusual that the thrust coefficient varies only between 0.013 to 0.014, while the thrust values increase by a factor of 5. This is because the pitch of the propeller blades is fixed at a constant value and the thrust is controlled by varying the rpm. This is in contrast to a rotor, where the rpm is fixed and the thrust is controlled by varying the collective pitch.

The torque of the rotor is calculated by multiplying the force measured by the

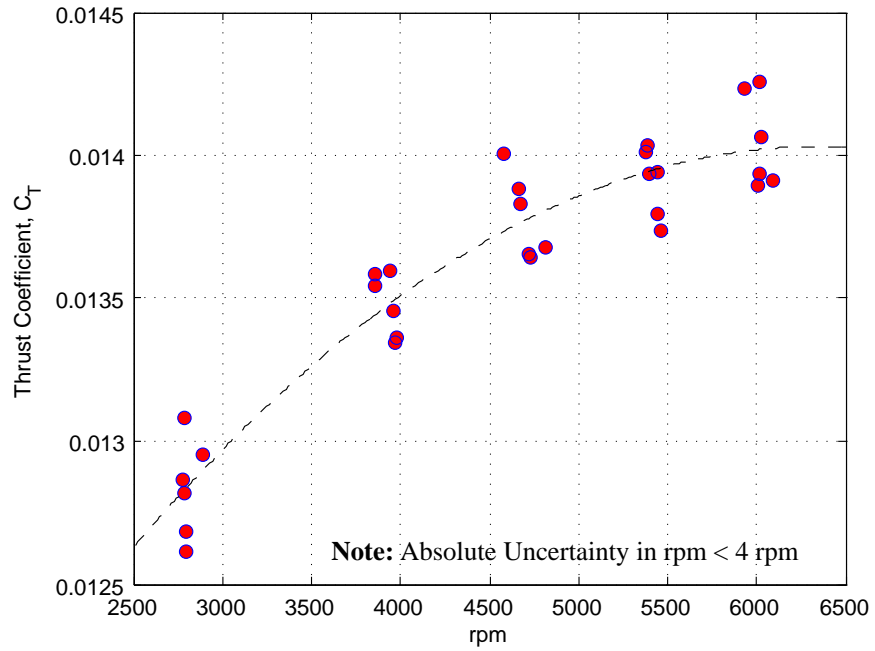


Figure 3.4: Isolated Rotor Thrust Coefficient vs. RPM

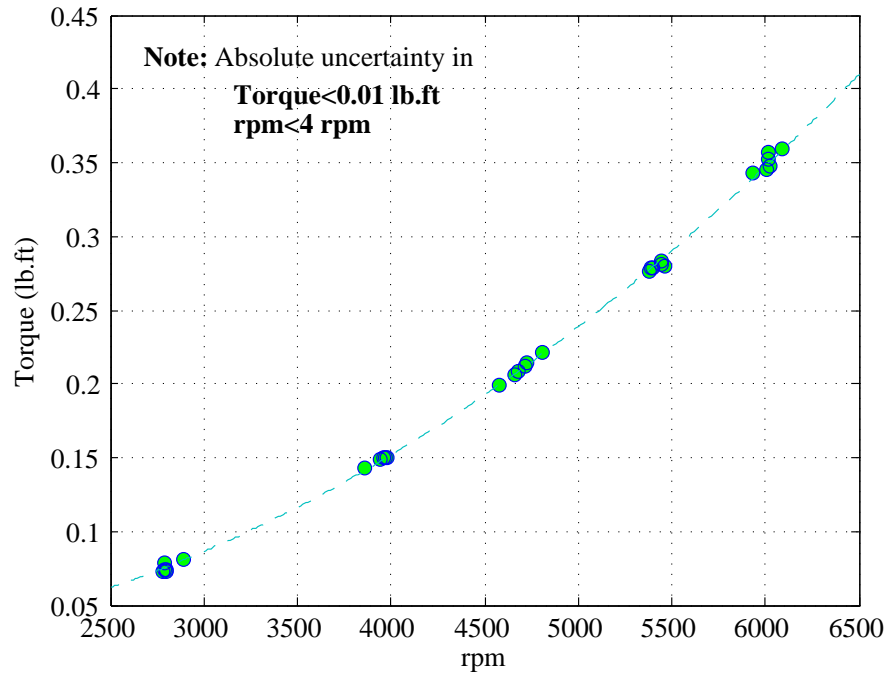


Figure 3.5: Isolated Rotor Torque vs. RPM

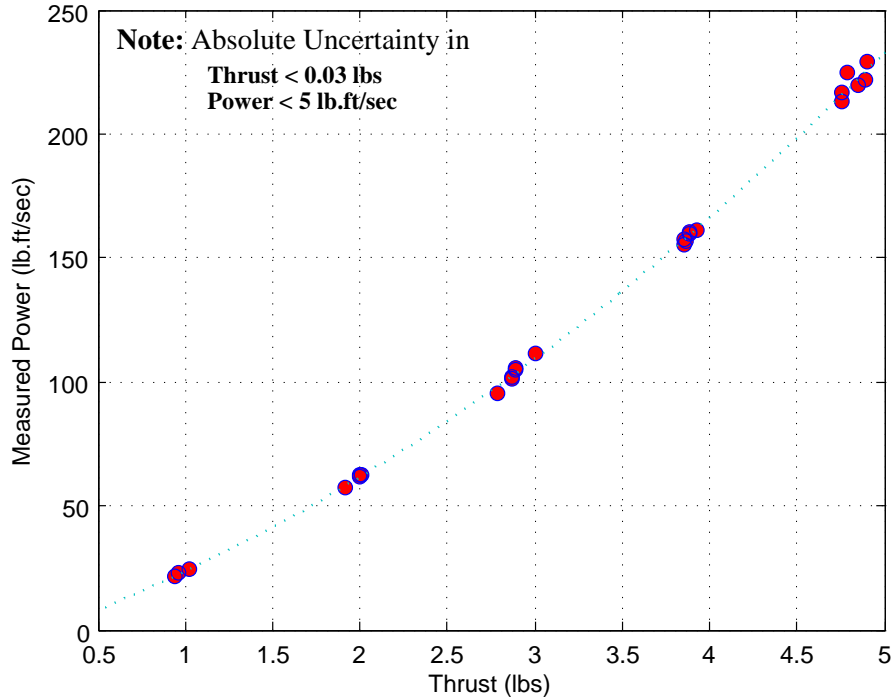


Figure 3.6: Isolated Rotor Power vs. Thrust

radially mounted torque load cell by the moment arm. The variation of torque with rpm is shown in Figure 3.5. The torque value is multiplied by the rpm to calculate the rotor power. The power vs. thrust curve is presented in Figure 3.6

These rotor performance characteristics are used to calculate the rotor profile power coefficient, C_{P0} , and the induced power factor, in Appendix A

3.4 Ground Effect on Rotor Performance

The effect of ground proximity on rotor performance is explored by studying the power measured while hovering at a constant thrust for a range of heights above the ground. The measured power is normalized by the power measured OGE and plotted against the normalized rotor height, z , in Figure 3.7. The height where the

QTR wheels would be on the ground, if the rotors were installed on the vehicle is indicated. The ground effect starts becoming apparent for $z < 1$ and the power required reduces to about 95% of the OGE power for the height where the wheels would be on the ground. As the z reduces further, the power reduces substantially to a value of close to 60% of the OGE power, for $z < 0.2$.

Therefore, for the QTR, for very close operation to the ground, the rotors are only marginally IGE.

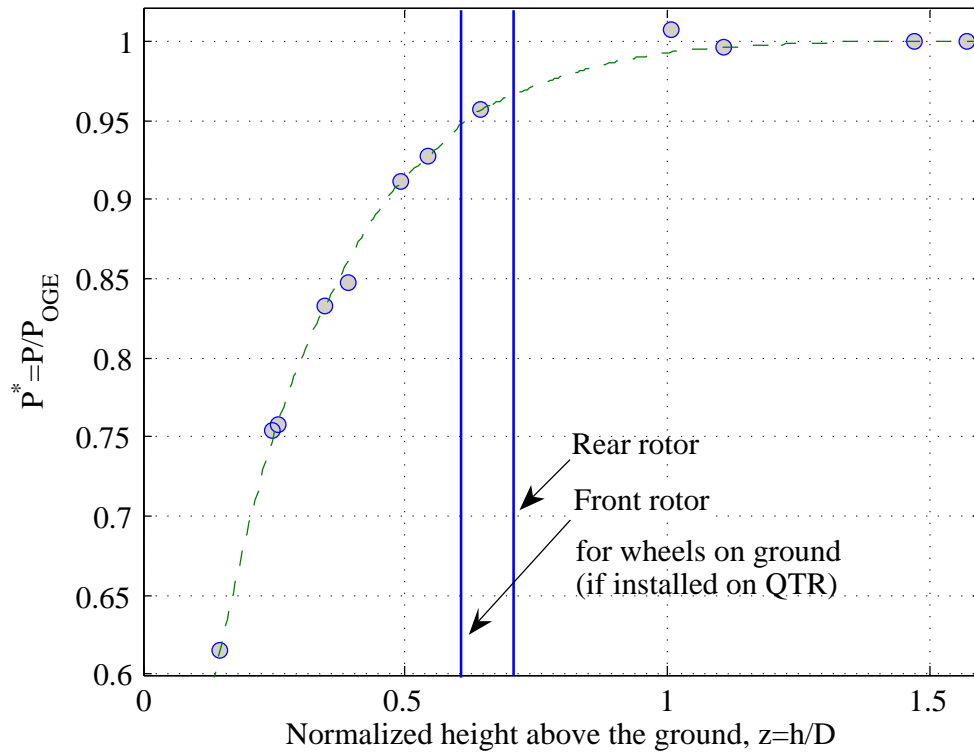


Figure 3.7: Isolated Rotor Power at a constant thrust, IGE

3.5 Rotor Wake Velocimetry

The theoretical value of hover induced velocity is calculated from momentum theory by rearranging Equation 2.23, as follows:

$$v_h = \sqrt{\frac{T}{2\rho A}} \tag{3.1}$$

This calculated hover induced velocity is plotted vs thrust in Figure 3.8. The hover induced velocity varies from approximately 14 ft/sec at a thrust of 1 lb to 31 ft/sec at a thrust of 5 lbs. This is in contrast to that of a full-scale QTR, which has a hover induced velocity that varies between 55 ft/sec for empty weight and 71 ft/sec, when fully loaded.

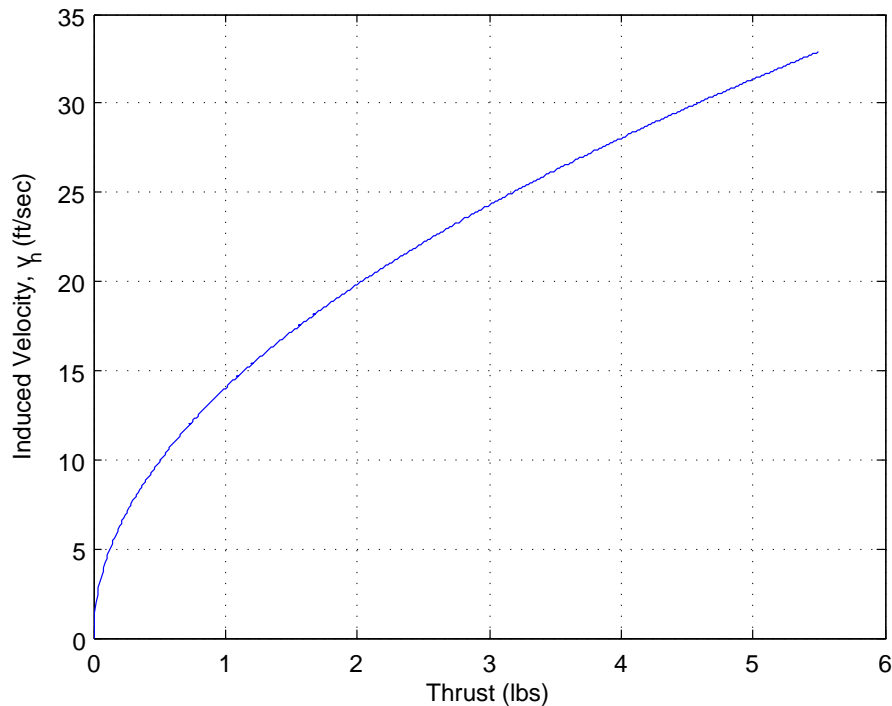


Figure 3.8: Calculated Uniform Hover Induced Velocity vs. Thrust

Previous studies on tilt rotors have shown that the rotor downwash velocity profile has significant effects on the measured download on the aircraft[4, 13]. Therefore, measurements of the rotor downwash velocities at different radial locations were obtained using a hot wire probe at an axial distance of 0.21 rotor diameters from the rotor plane. This axial distance corresponds to the relative wing location on the installed rotor. The measured velocities were normalized by momentum theory calculations of hover induced velocity, v_h , and compared with the wake distribution of a V-22 rotor from Felker & Light[4].

Figures 3.9 and 3.10 shows the downwash profiles measured at two different thrust values of 1 lb and 5 lbs. These thrust values correspond to rotor thrust coefficient, C_T , values of 0.0131 and 0.0140, respectively. Because the rotor is a fixed-pitch rotor, it must be noted that these two different thrust values were obtained at different values of rpm. These C_T values lie between two C_T values of 0.0120 and 0.0164, for which the V-22 rotor downwash was obtained, which are plotted for comparison. The downwash profiles obtained for both thrust levels for the current experiment are found to be quite similar in shape. These downwash profiles are closer in shape to the V-22 downwash profile obtained at a C_T of 0.0164.

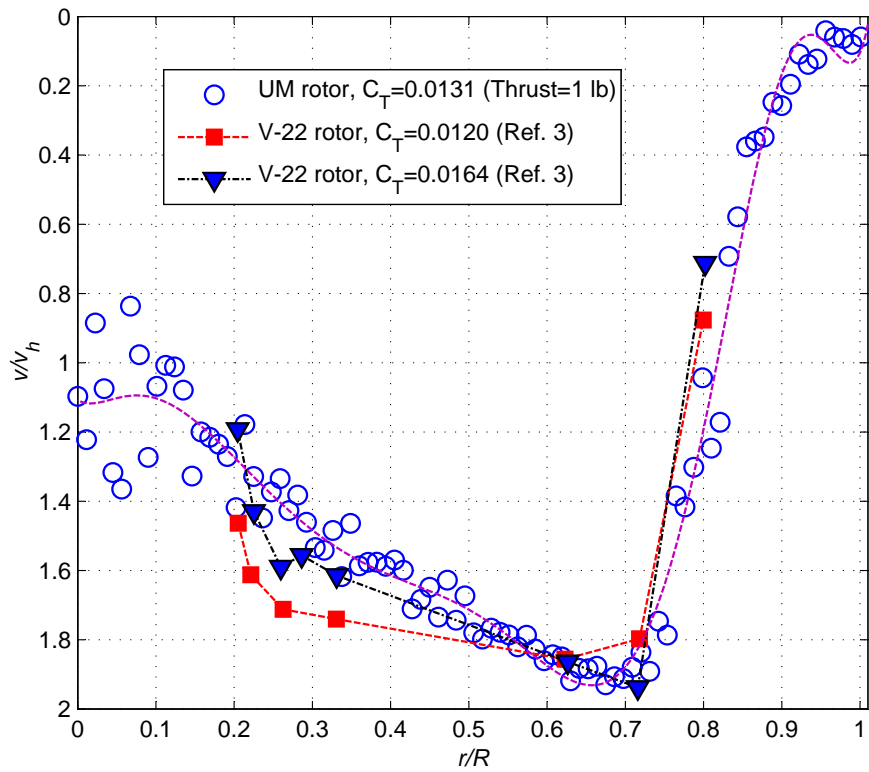


Figure 3.9: Radial Distribution of Wake Downwash for 1 lb. thrust

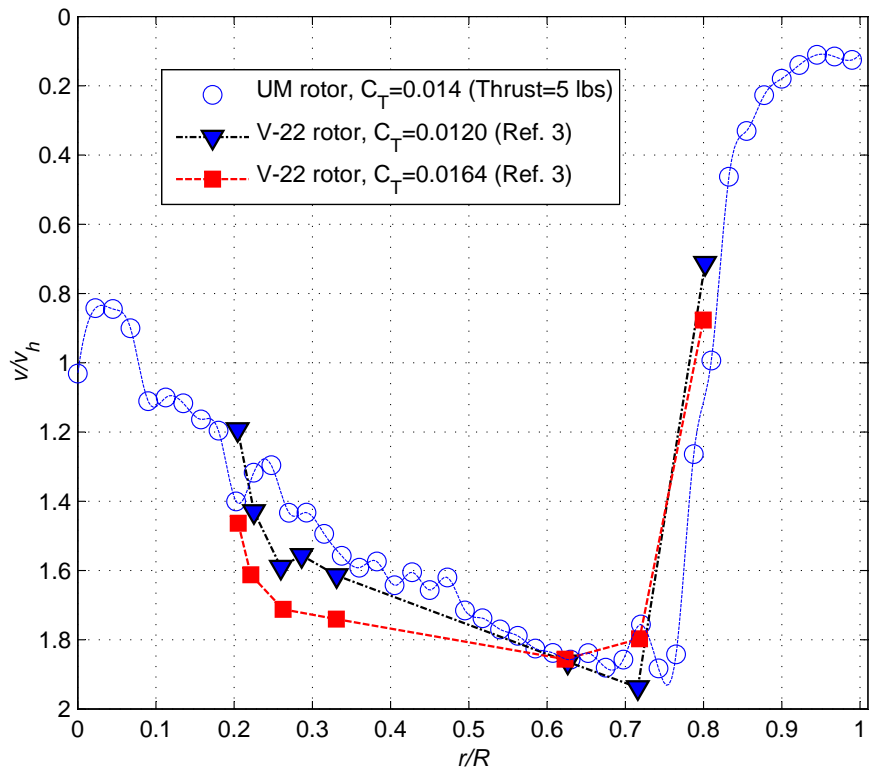


Figure 3.10: Radial Distribution of Wake Downwash for 5 lbs thrust

Chapter 4

Quad Tilt Rotor in Hover

Previous experimental and CFD studies [1, 14, 73, 74, 15, 12] have shown that the QTR experiences a high download in hover, OGE. The same studies also showed that there was a large reduction in download-to-thrust ratio in hover, IGE, even resulting in an upload during close operation to the ground.

To a great extent, the performance of a QTR in hover will determine the maximum take-off weight and configuration. This chapter will present the results and analysis from the tests conducted on the QTR in hover.

Firstly, the measured download to thrust ratios for the QTR (both Models A and B) are presented and discussed. Results from investigations on the effect of varying rotor height above the ground, wing flap angle and disk loading are presented. This is followed by measurements and analysis of power consumption of the QTR at different heights above the ground. In addition, pressure measurements along the centerline of the bottom of the fuselage are also presented.

4.1 Test Procedure

In hover, the test procedure is as follows. First, zero readings for all the instruments are measured and recorded. Then, using a signal from the computer, all the rotors are turned on and increased in speed until the required thrust is obtained. When all the rotors reach the desired thrust level, data acquisition is initiated. After 4 seconds of data are acquired and recorded, the data acquisition is stopped and the rotors are gradually powered down to a stop.

4.2 Download to Thrust Ratios

Download to thrust ratio for Model B, which has a wing flap deflection of 67° , is plotted as a function of normalized front rotor height above the ground, in hover, in Figure 4.1. These results are for a disk loading of 4.7 lb/sq.ft. on each rotor, with the nacelles and sponsons removed. The hover induced velocity for this thrust condition, calculated from momentum theory, is 31 ft/sec. The download is about $9\pm 0.5\%$ of the rotor thrust, OGE. At front rotor heights less than 1.5 rotor diameters ($z < 1.5$), the download to thrust ratio starts rapidly reducing. This is in similar to the behavior of tiltrotor download, IGE, as discussed in Chapter 1. The reduction is quite steep and the download becomes an upload of about $3\pm 0.5\%$ of the total rotor thrust, at a front rotor height of 1 rotor diameter. For the case where the rotor wheels are on the ground ($z=0.61$), an upload of $9\pm 0.5\%$ of the rotor thrust is measured. Therefore, the total change in download to thrust ratio from OGE operation to IGE operation with wheels on the ground is about 18%.

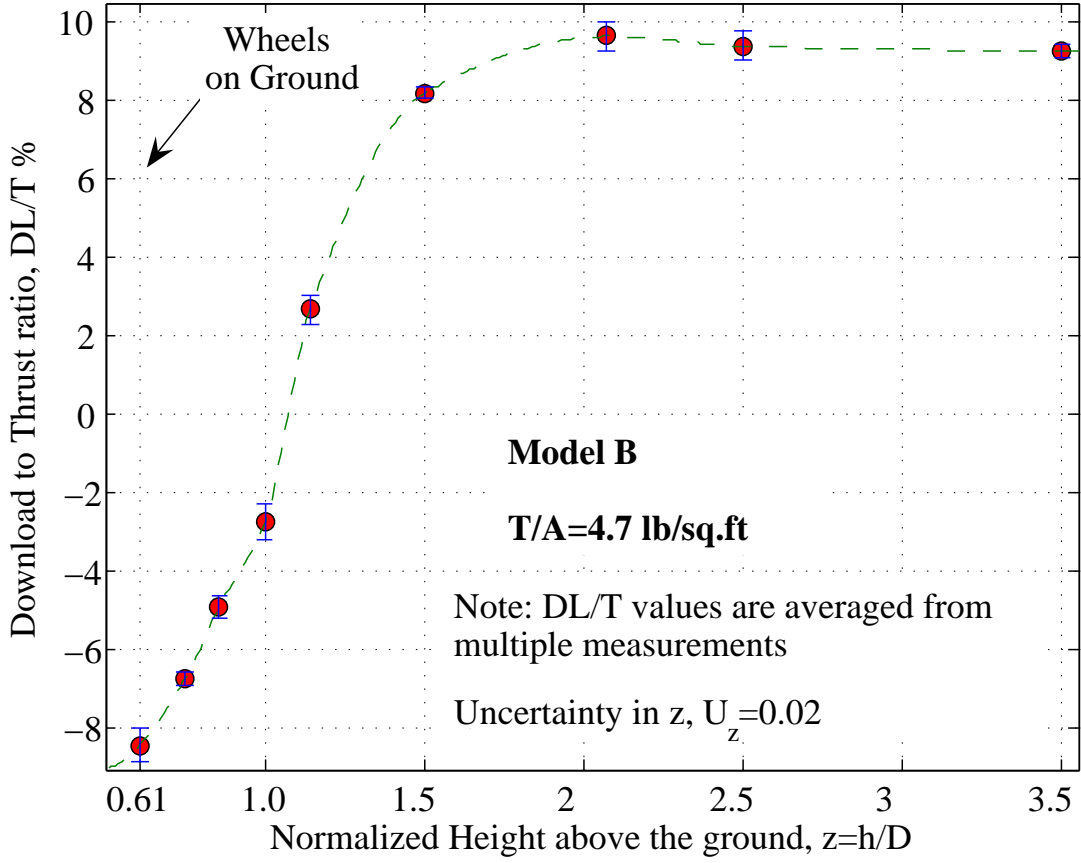


Figure 4.1: Download to thrust ratio vs Height above the ground

4.2.1 Download at the front and rear airframe mounts

The airframe model is mounted at two different points, one on the front wing and the other on the rear wing. The download measured at the front airframe mount and the rear airframe mount are measured separately using different airframe mount.

These quantities are normalized as follows:

$$\frac{DL_f}{T} = \frac{DL_f}{\sum_{j=1}^4 T_j} 100\% \quad (4.1)$$

$$\frac{DL_r}{T} = \frac{DL_r}{\sum_{j=1}^4 T_j} 100\% \quad (4.2)$$

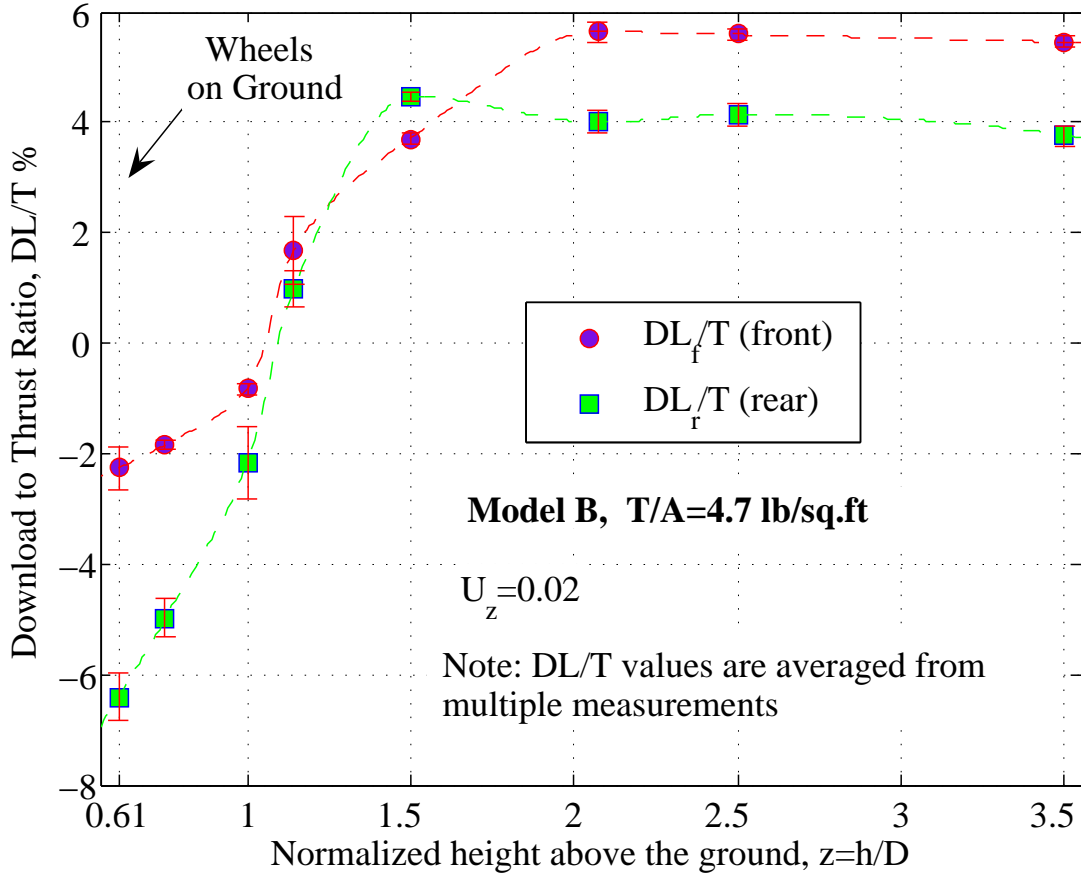


Figure 4.2: Normalized Downloads measured at the front and rear airframe mount vs Height above the ground

. The behavior of the normalized downloads measured at the front and the rear airframe mounts, for Model A, is presented in Figure 4.2. These measurements were also obtained at a disk loading of 4.7 lb/sq.ft. on each rotor ($v_h = 31$ ft/sec.)

Except for some intermediate heights, the download is higher at the front of the airframe than at the rear. The normalized download on the front airframe mount starts reducing below a front rotor height of $2D$, whereas the download on the rear mount starts reducing below a front rotor height of $1.5D$. In fact, there is a slight increase in download at the rear mount at $z = 1.5$. This disparity is possibly

because the front rotors are closer to the ground and also closer to each other than the rear rotors. Therefore, there should be a higher pressure under the front rotors. However, the decrease in download at the rear airframe mount is much more rapid than for the front airframe mount for $z < 1.5D$. This is an unexpected result and is possibly because of the larger planform area of the rear wing exposed to the upwash from the ground.

4.2.2 Effect of varying the disk loading

The full-scale QTR operates at hover induced velocities that vary between 53 ft/sec at empty weight and 68 ft/sec when fully loaded. Because of small scale rotor limitations, the model QTR operates at a maximum hover induced velocity of 31 ft/sec. While this value is much smaller than the full-scale, it is possible to investigate the effect of changing the induced velocity by varying the disk loading of the rotor. By changing the rotor disk loading from 0.9 lb/sq.ft. to 4.7 lb/sq.ft., the induced velocity will vary from 14 ft/sec to 31 ft/sec. The results of this investigation are presented in Figure 4.3. The download-to-thrust ratios at different levels of disk loading are remarkably similar at different heights above the ground. The difference in the measured downloads are within the uncertainty limits. This would imply that variation in induced velocity because of increased disk loadings has a negligible effect on the measured download to thrust ratios.

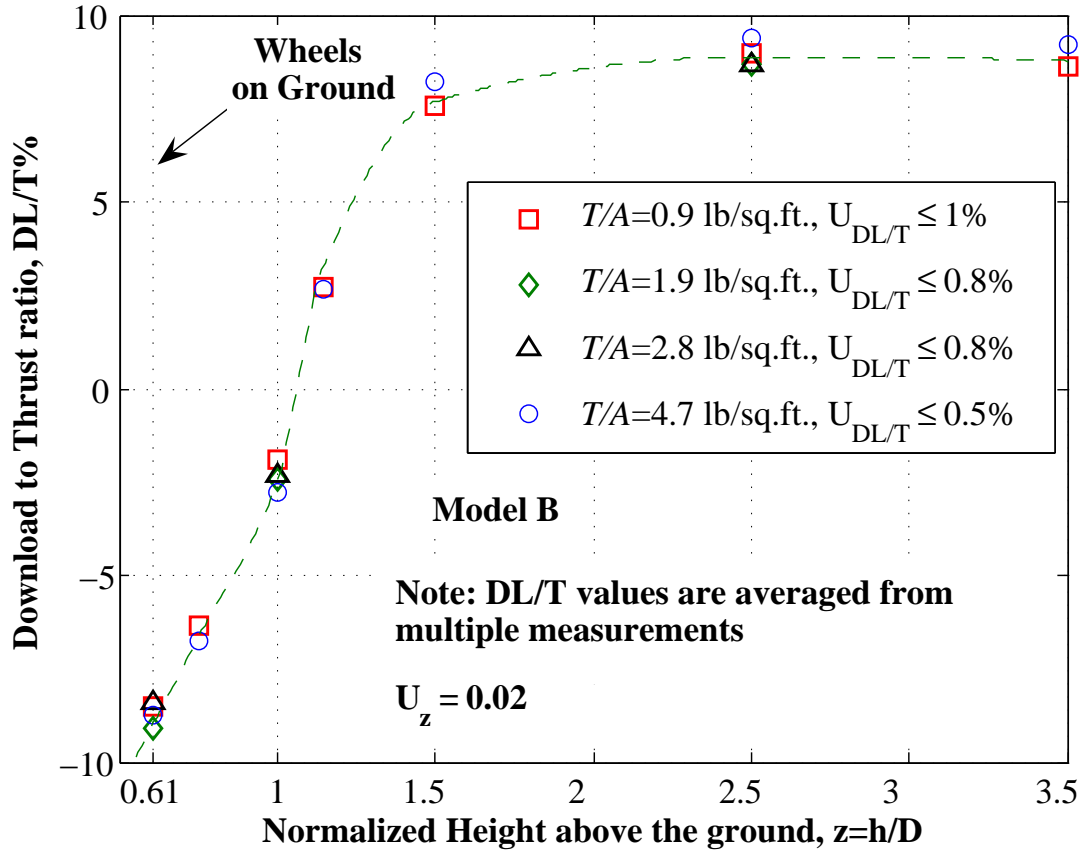


Figure 4.3: Effect of varying the thrust level on Download to Thrust ratio

4.2.3 Effect of varying the flap angle

Model A was the original model that was used for testing and had a wing flap deflection angle, $\delta_{flap} = 0^\circ$. In helicopter mode, the QTR is unlikely to operate with this value of δ_{flap} . As mentioned in Chapter 1, tilt rotor studies have shown that δ_{flap} of 67° is the optimal angle for minimizing the download. This is the angle that has been used in Model B, and in the previous experimental and CFD studies on the QTR. However, the results from Model A are useful in studying the effect of varying the wing flap deflection angle on the download to thrust ratio. These results are presented in Figure 4.4 for disk loading of 4.7 lb/sq.ft.

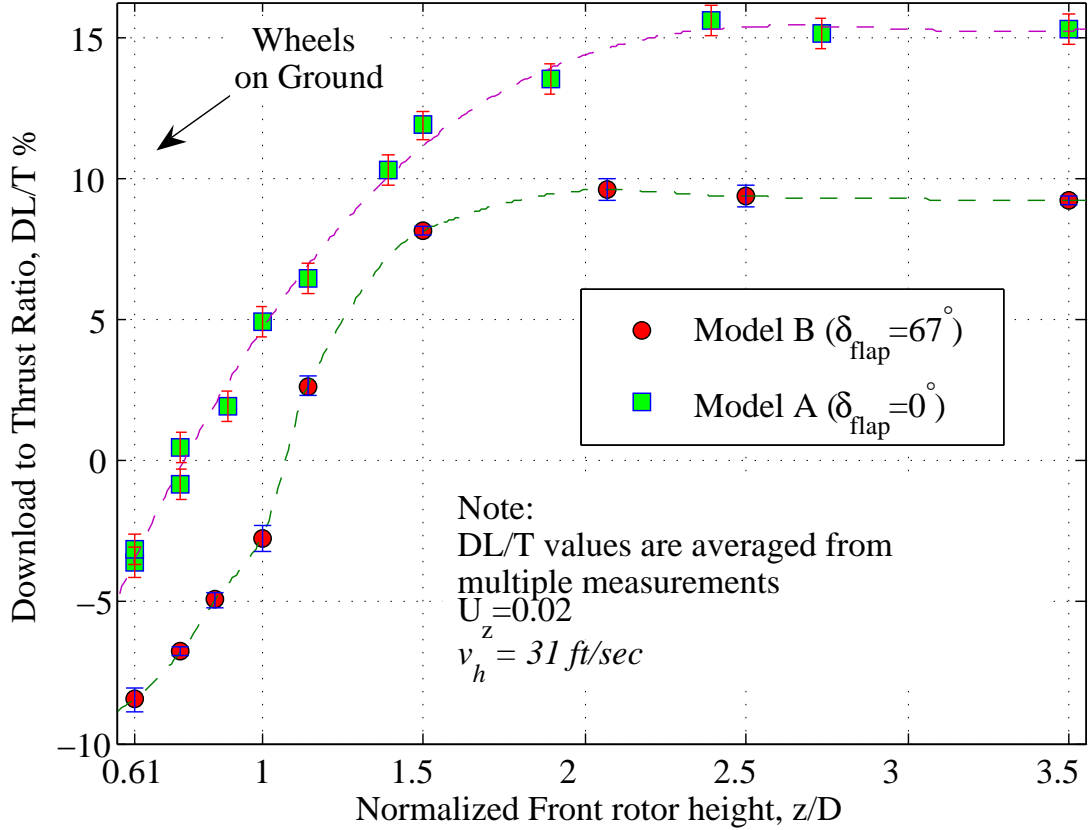


Figure 4.4: Effect of varying the flap angle on Download to Thrust ratio

Model A has a much higher OGE value of download to thrust ratio ($15 \pm .25\%$) than Model B ($9 \pm 0.5\%$.) This is because the exposed area of the wings in the rotor downwash is much higher for Model B, as $\delta_{flap} = 0^\circ$. For Model A, the download to thrust ratio starts decreasing for $z < 2$ as opposed to $z < 1.5$ for Model B. Also, the rate of decrease in download is more smooth for Model B. For the case where the wheels are on the ground, the download to thrust ratio is about $4 \pm 0.5\%$ for Model B, as opposed to $9 \pm 0.5\%$ for Model A. Therefore, the difference in download between the two models remains the same at the two ends of the curve. However, for z values between 1.2 and 2.0, the difference in download for the two models is

about $4\pm 0.5\%$, which is slightly less. These results confirm that using a wing flap deflection of 67° results in a significant reduction in download, both IGE and OGE.

4.3 Comparison with previous studies

4.3.1 Experiments

Wood, et al., at Bell Helicopters, conducted the only previous experimental study of QTR performance in hover[1]. The 0.07-scale model that was used had a similar configuration to Model B. However, the model used by Wood, et al., included the nacelles and sponsons, which were removed in Model B. The download to thrust ratio was measured OGE and for a wheel height of 10 ft from the ground, which corresponds to $z = 0.87$. These results are presented and compared with the results of this study in Figure 4.5. The download to thrust ratio for experiment conducted by Wood, et al., was 8%, which was about $1\pm 0.5\%$ less than the results of the current study. However, IGE, for $z = 0.87$, the download to thrust ratio was about 5%, which is within the uncertainty bounds of the current study.

4.3.2 CFD studies

The download to thrust ratios from the current study are compared with the CFD study by Lestari, et al.[14], in Figure 4.6. Using CFD, the download was calculated OGE and IGE ($z = 1.13$). The download predicted by the CFD study matches quite well with the experiment, OGE. An upload of 0.5% was predicted

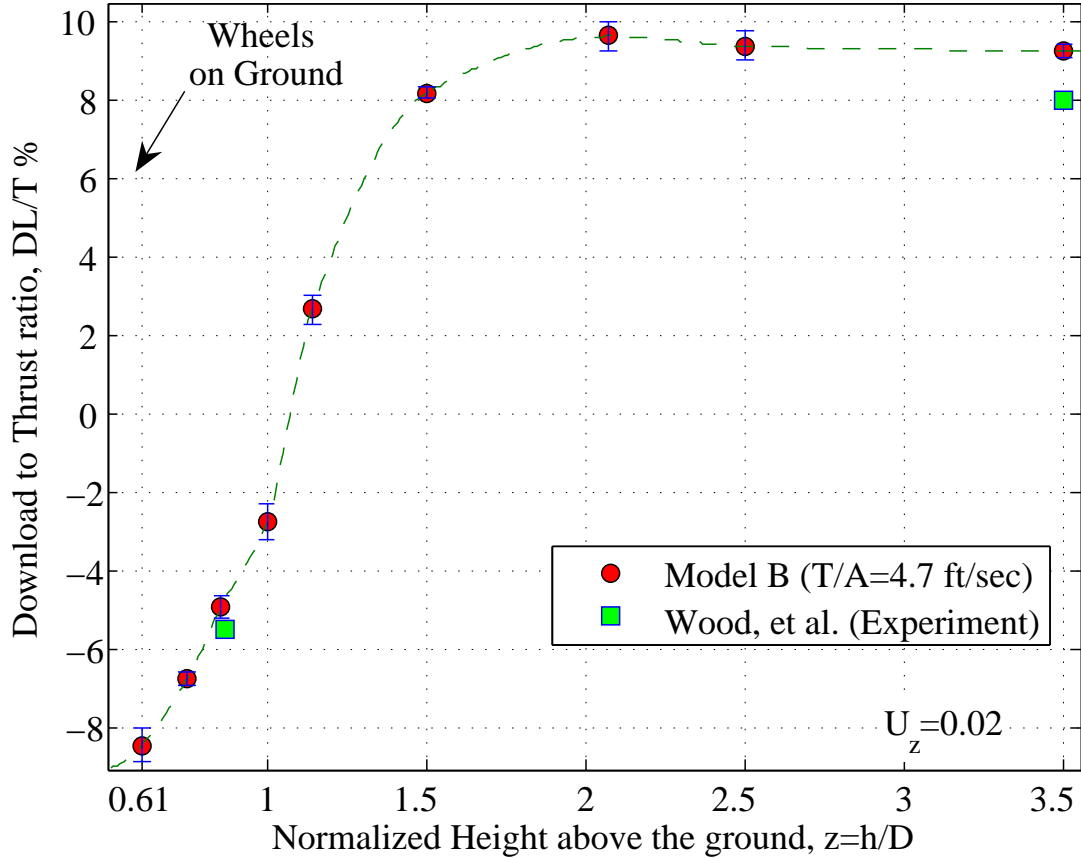


Figure 4.5: Comparison with the experiment conducted by Wood, et al.[1]

by the CFD study for $z = 1.13$, whereas a download of $2.5 \pm 0.5\%$ was measured by the experiment for $z = 1.14$. This CFD study used a cartesian mesh and had some inaccuracies in modeling the viscous terms. These could be reasons for the difference from the experimental measurements.

The experimental download to thrust ratios are compared with the CFD results from Gupta and Baeder[15, 12] in Figure 4.7. In this CFD study, hover was approximated either by simulating slight climb or slight forward speed. Both cases are presented in the figure. The download, OGE, agrees well with the experimental measurements both for the climb approximation and forward flight. For the case

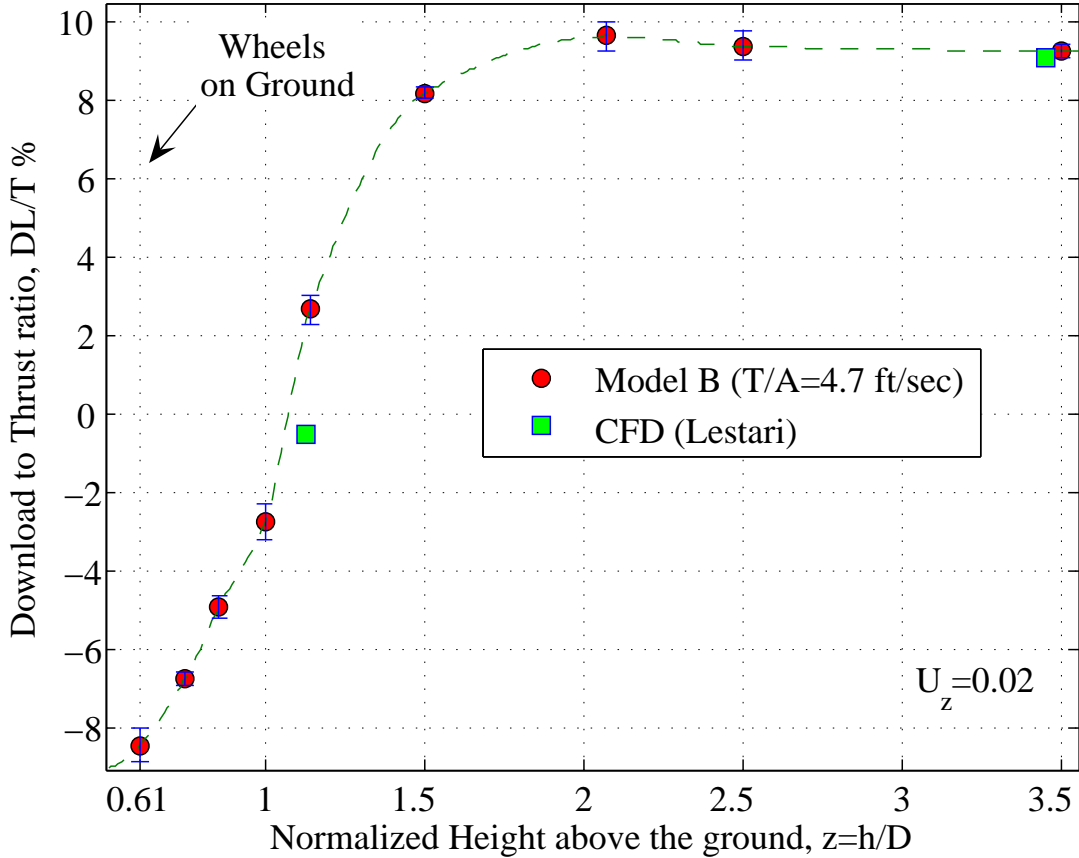


Figure 4.6: Comparison with CFD (Lestari, et al.[14])

where the wheels are on the ground, the climb approximation shows good agreement with the experimental measurements. However, using the approximation of 1° skew angle, the predicted upload is about 1% less. For $z = 0.87$, the predicted upload is about 3% less than the measurement. The QTR configuration used for this CFD study had some differences with the configuration used for both the experiments and Lestari's study. The differences between these configurations are explained in further detail in Appendix B. The longitudinal separation between the wings were larger for this CFD model and also the rotor wing separation was smaller. The fact that the rotor/wing separation distance is smaller for the CFD study would mean

that the fuselage and wings are at a greater elevation from the ground. This would cause the effective height of the vehicle above the ground to be higher for the CFD study. Also, the larger distance between the front and rear rotors for the CFD study would reduce the intensity of the high pressure region formed under the fuselage. The combination of these two effects suggest that the upload should be lower for the CFD study, if the geometry of the actual QTR had been modeled more closely.

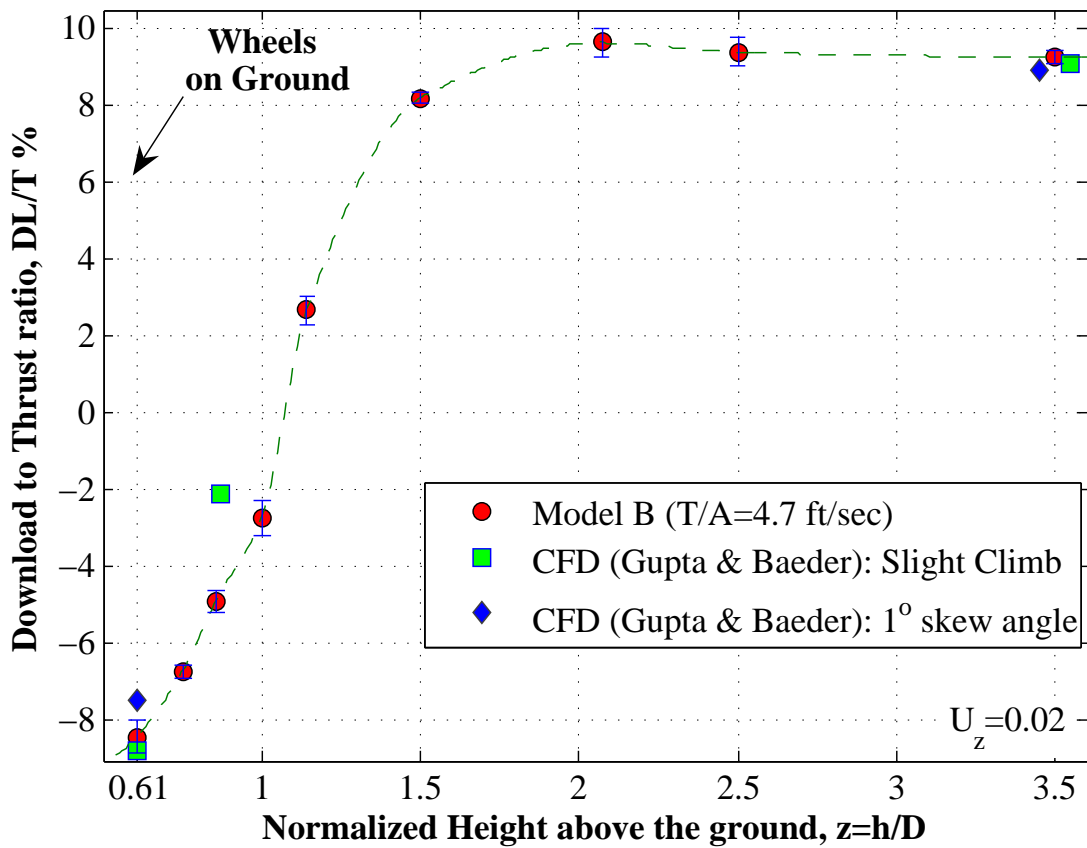


Figure 4.7: Comparison with CFD (Gupta and Baeder[15, 12])

4.4 Power Consumption

Download and thrust measurements obtained in hover, IGE and OGE, were presented in the previous sections. The performance benefits of the extra payload that will be obtained because of the upload in hover can be assessed in a more quantitative manner using rotor power measurements. This will enable the evaluation of the takeoff performance of a QTR either as an increase in power at a given vehicle thrust or as an increase in takeoff payload at a given power.

4.4.1 Power Required For a Given Vehicle Thrust

The power measurements were used to obtain the power required for a QTR operating at a constant vehicle thrust, T_{veh} , at different values of height above the ground. This is for the vehicle in hover, with the airframe installed and all four rotors operating at equal thrust in level flight.

The measured power of each rotor (P_j) can be calculated by multiplying the measured torque (Q_j) with the measured rpm (Ω_j).

$$P_j = Q_j \Omega_j \quad (4.3)$$

However, the measured power that was obtained had to be corrected for profile and induced effects, as follows:

4.4.1.1 Corrections for Profile Effects

Because fixed pitch propellers are used, the desired thrust is obtained by varying the rpm. Because of changes in the download, the rotor thrust required to

maintain a constant vehicle thrust will reduce, causing a corresponding reduction in rpm. In addition, because of interference with the ground, there will be differences in the inflow and flow environment even at a constant rotor thrust, causing the rotor rpm to change. As the rotor profile power varies as a function of rpm, the profile power will not remain constant. On a real QTR, the rpm will be held constant and the desired thrust will be obtained by changing the collective pitch of the rotor. Therefore, it can be reasonably assumed that the profile power will remain constant at a given rpm.

Also, because of differences in Reynolds number between the full-scale and the model-scale, the profile power at the model-scale will be a much greater proportion of the total power as compared to the full-scale. Therefore, it would be wise to remove the profile power contributions and use only the calculated induced power.

The profile power, P_0 can be calculated from the following relationship:

$$P_{0_j} = C_{P0_j} \rho A (\Omega_j R)^3 \quad (4.4)$$

where, the profile power coefficient for each rotor (C_{P0_j}) can be obtained using the relationship between C_{P0} and rpm, which is presented in Appendix A. The assumption is that the profile power coefficient remains constant at a given rpm, even for different heights above the ground. This assumption ignores the effects of rotor blade stall and compressibility on the profile power.

4.4.1.2 Corrections for Induced Effects

The induced power (P_{i_j}) of each rotor can be calculated by subtracting the profile power, P_{0_j} from the measured power, P_j .

$$P_{i_j} = P_j - P_0 \quad (4.5)$$

This is the induced power calculated for the measured thrust, T_j . The measured power was obtained while maintaining a constant rotor thrust even for different heights above the ground. Therefore, the total vehicle thrust available, T_{veh} , for each case changes depending on the download or upload experienced by the airframe.

$$T_{veh} = \sum_{j=1}^4 T_j - (DL_f + DL_r) \quad (4.6)$$

However, for a real vehicle operating in steady, level flight, there will not be any variation in vehicle thrust during flight, even for different operating conditions. Therefore, the rotor thrust will have to be varied in order to account for the changes in download. The required thrust on each rotor, T_{jreqd} , for a given total vehicle thrust (T_{set}) can be calculated for each height by adding the measured download on the aircraft to the total vehicle thrust.

$$T_{jreqd} = \frac{T_{set} + (DL_f + DL_r)}{4} \quad (4.7)$$

From momentum theory, the induced power (P_{i_j}), for each rotor, can be expressed as a function of induced power correction factor and measured rotor thrust

(T_j):

$$P_{ij} = \kappa_{meas} \frac{T_j^{3/2}}{\sqrt{2\rho A}} \quad (4.8)$$

where κ_{meas} is the induced power correction factor for the measured thrust, which can be calculated from the measured thrust coefficient as described in Appendix A.

In order to maintain a constant vehicle thrust, the required induced power would be different from the induced power calculated from the measured thrust because of the change in the required thrust. Also, as the rpm on a full-scale rotor will be held constant, the rotor thrust coefficient, C_T would also vary with changes in thrust. The change in C_T would cause a change in κ , which would also affect the induced power. For the purpose of this analysis, the rpm of the rotors will be assumed to be a constant for all the different heights above the ground.

Therefore, the induced power for a given vehicle weight was obtained by correcting for changes in the required thrust and the induced efficiency factor using the following relationship:

$$P_{j_{corr}} = P_{ij} \left(\frac{T_{j_{reqd}}}{T_j} \right)^{3/2} \frac{\kappa_{reqd}}{\kappa_{meas}} \quad (4.9)$$

where the value of induced efficiency factor for the required thrust coefficient (κ_{reqd}) can be obtained using the relationship presented in Appendix A.

This corrected induced power, $P_{j_{corr}}$, will be the induced power for each rotor at a constant vehicle thrust, if the rotor thrust were to be controlled by varying the collective pitch of the rotors, while holding the rpm constant.

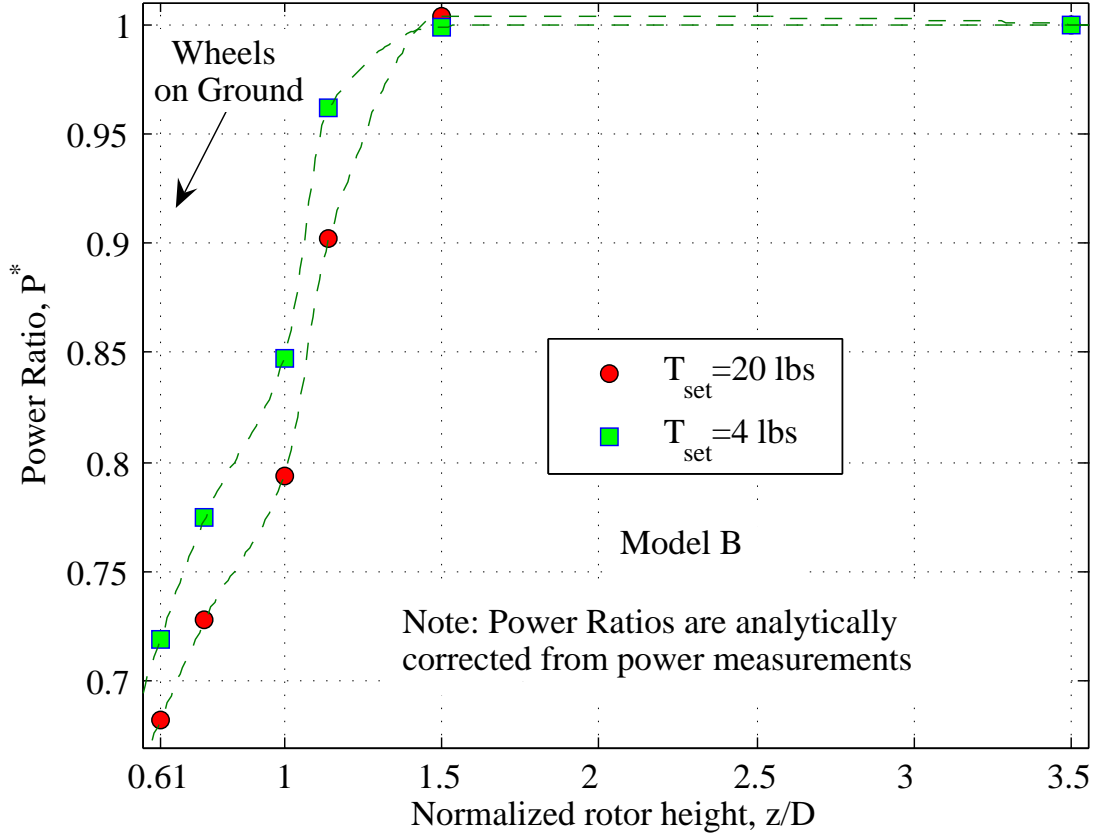


Figure 4.8: Power Ratio vs Height above the ground

4.4.1.3 Power Ratio

The total corrected induced power, P_{corr} , which is the sum of the corrected induced power on all the rotors, is normalized by the total corrected induced power in hover, OGE. This normalized corrected induced power, P^* can be expressed as follows:

$$P^* = \frac{P_{corr}}{(P_{corr})_{hover,OGE}} = \frac{\sum_{j=1}^4 P_{j_{corr}}}{(P_{corr})_{hover,OGE}} \quad (4.10)$$

The P^* in hover is plotted as a function of height above the ground for two

different levels of disk loading in Figure 4.8. The behavior of P^* for the two different levels of disk loading are quite similar. It can be seen that there is a substantial drop in power required to hover, IGE, at a given gross weight. A majority of this reduction is because of the reduction in required thrust as a result of the decrease in download on the aircraft. When the wheels are on the ground, the power required reduces to about 70% of the OGE value.

4.4.2 Available Thrust For A Given Power

From the induced power consumption values that were calculated in the previous section, it is possible to calculate the vehicle thrust that would be available at a given induced power. By setting the available power (P_{av}) as the OGE induced power in hover, the available vehicle thrust can be calculated for different heights above the ground and compared with the thrust available OGE. The available vehicle thrust, T_{av} , is calculated as:

$$T_{av} = \left(1 + \frac{DL}{T}\right) \left(P_{av} \frac{\sqrt{2\rho A}}{\kappa_{reqd}}\right)^{2/3} \quad (4.11)$$

The available vehicle thrust values are then normalized by the vehicle thrust available, OGE, to calculate the thrust ratio, T_{av}^* .

$$T_{av}^* = \frac{T_{av}}{(T_{av})_{OGE}} \quad (4.12)$$

The vehicle thrust ratio is plotted as a function of height above the ground in Figure 4.9 for two levels of disk loading, which correspond to $(T_{av})_{OGE} = 20$ lbs and

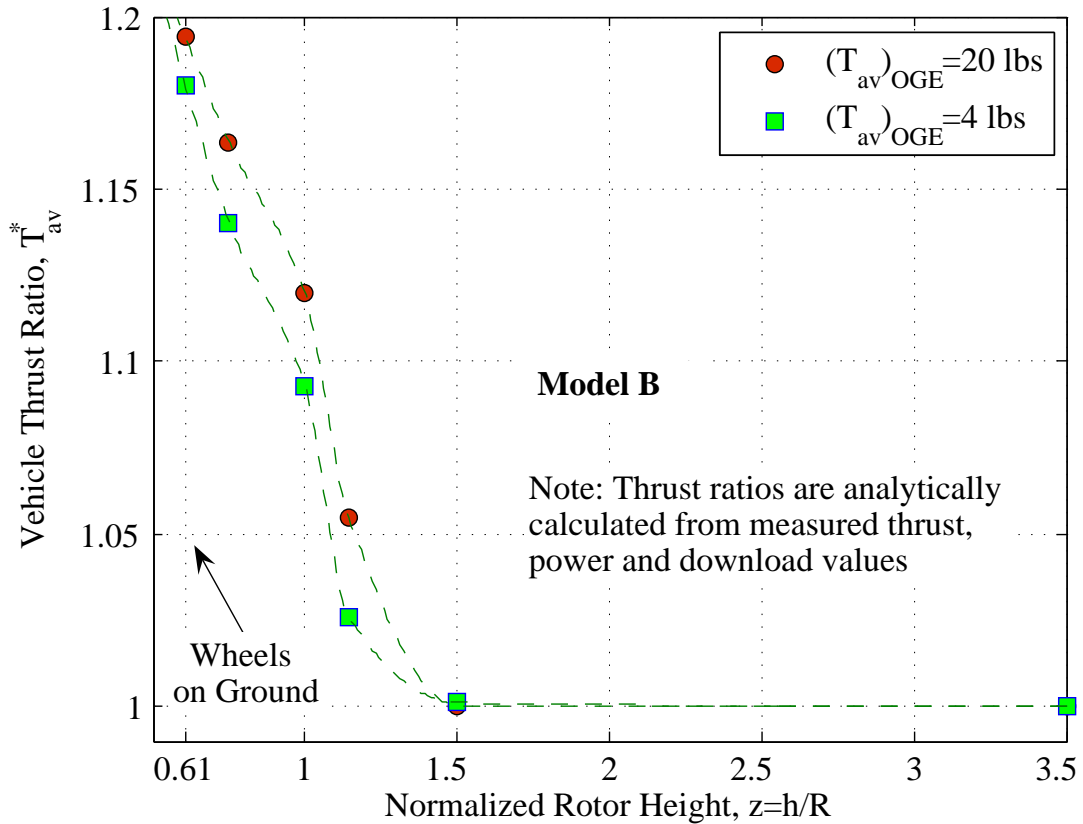


Figure 4.9: Available Thrust at a given power vs Height above the ground

4 lbs. The behavior of the vehicle thrust ratio vs. height above the ground is quite similar for both levels of disk loading. However, the available vehicle thrust IGE is higher for the higher disk loading. The plot shows that there is an increase of up to 20% in the thrust available for a given power, by operating IGE. For the QTR, the payload is about 40% of the maximum VTOL gross weight[2]. Therefore, such an increase would mean that payload carrying capacity could potentially be increased by 50%.

4.5 Pressure Measurements

The reduction in download and increase in upload on the QTR, IGE, are caused by higher pressures on the bottom surfaces of the fuselage and the wings[14, 15, 74, 12]. When the QTR operates close to the ground, the wakes from the four rotors meet under the bottom of the fuselage and get trapped, causing high pressures regions.

By applying pressure taps along the centerline of the bottom surface of the fuselage, it is possible to obtain the magnitude and distribution of these pressure forces under the fuselage. The location of these pressure taps is shown again in Figure 4.10 for reference.

The measured pressures are normalized by the rotor disk loading to obtain the coefficient of pressure, C_{pDL} . The variation of of the C_{pDL} along the centerline of the fuselage is presented for different heights above the ground in Figures 4.11 to 4.16. Each measurement is labeled to indicate the port number. Pressures from two different values of disk loading (4.7 lb/sq.ft and 0.9 lb/sq.ft) are presented for comparison.

For the OGE case, shown in Figure 4.11, the pressure coefficient measured on the bottom surface of the fuselage is zero. This is true of both the different levels of disk loading. This should be expected because the flow under the fuselage, OGE, should be quiescent.

Figure 4.12 shows that for $z = 1.14$, the pressure increases under the front and the rear wings. This should be because of the presence of the ground. The wakes

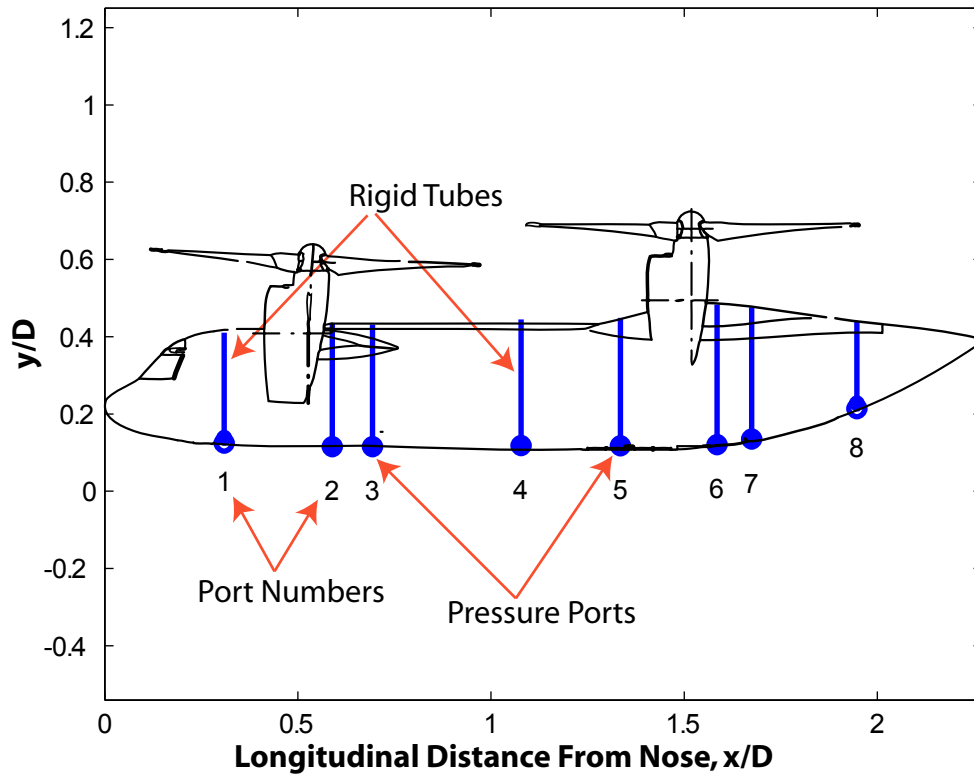


Figure 4.10: Location of the Pressure Taps

of the rotors should meet under the fuselage and form fountain flows, which cause high pressures under the wings. The pressure under the front wing is greater than that for the rear wing because the front rotors are closer together and to the ground than the rear rotors.

Figures 4.13, 4.14 and 4.15 show that the pressure under the entire length of the fuselage increases as the height above the ground decreases. This is true except for ports 7 and 8, which are behind the rear wing. The high pressure region that was only under the wings now also extends to the region between the wings for $z = 1.0, 0.86$ and 0.75 . This is possibly because the wake from the front and the

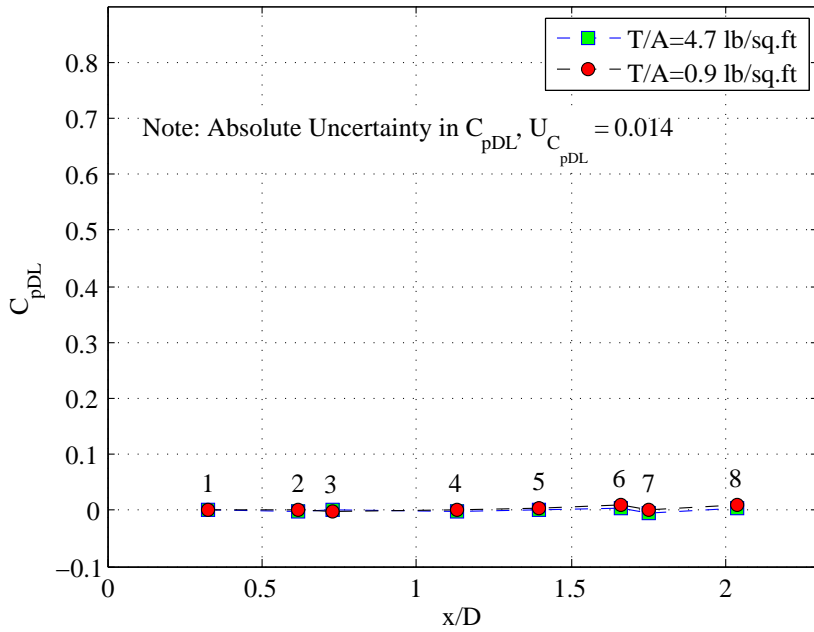


Figure 4.11: Pressure Coefficient vs. Longitudinal distance from the nose, for $z=3.5$ (OGE)

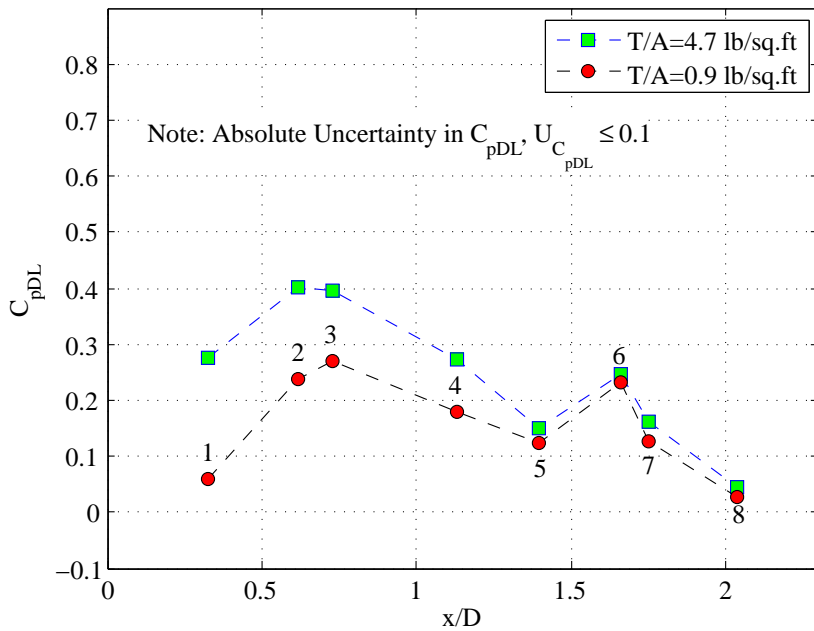


Figure 4.12: Pressure Coefficient vs. Longitudinal distance from the nose, for $z=1.14$

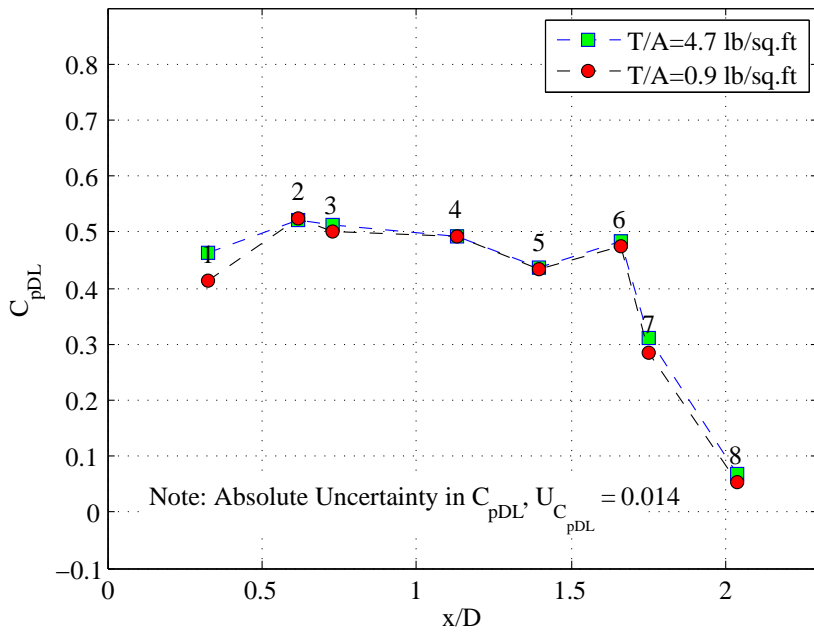


Figure 4.13: Pressure Coefficient vs. Longitudinal distance from the nose, for $z=1.0$

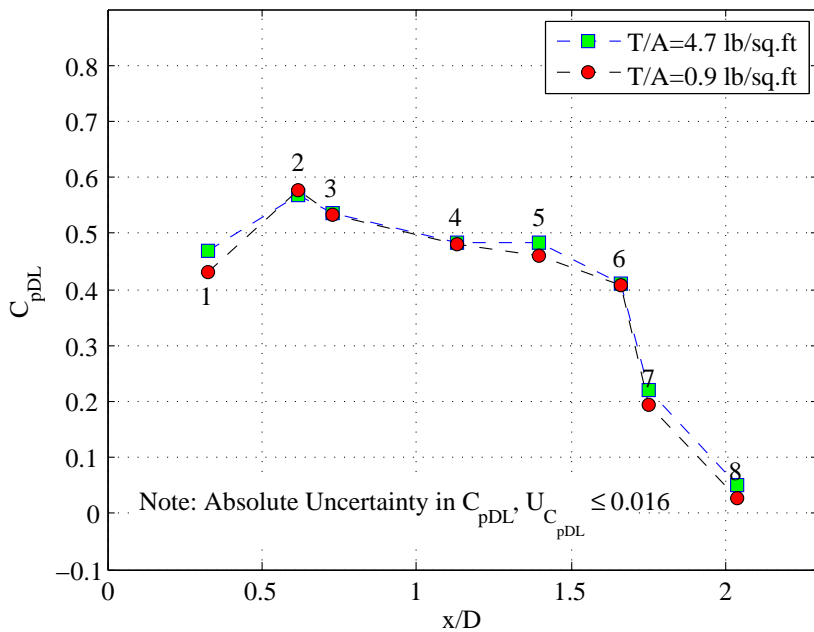


Figure 4.14: Pressure Coefficient vs. Longitudinal distance from the nose, for $z=0.86$

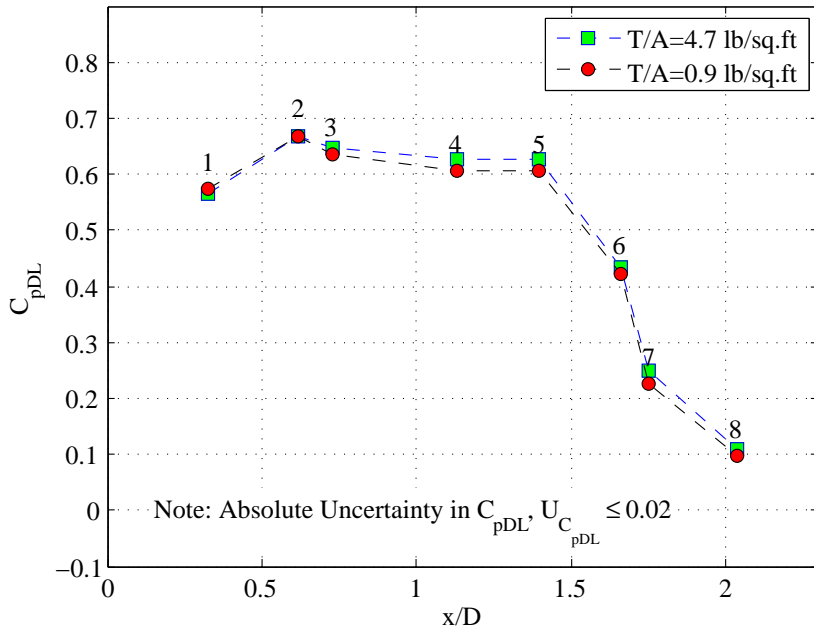


Figure 4.15: Pressure Coefficient vs. Longitudinal distance from the nose, for $z=0.75$

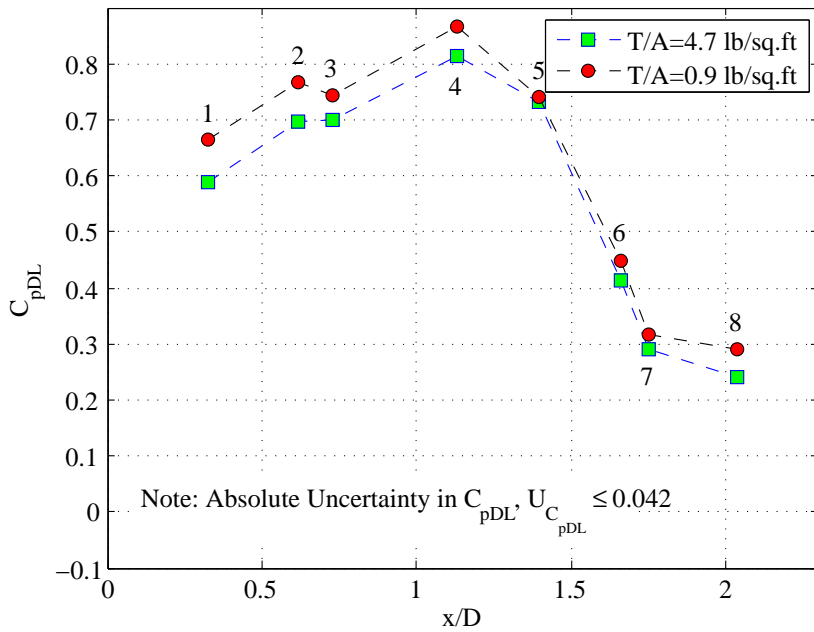


Figure 4.16: Pressure Coefficient vs. Longitudinal distance from the nose, for $z=0.61$ (wheels on ground)

rear rotor start interacting.

For the case where the wheels are on the ground ($z = 0.61$), an interesting effect is seen in Figure 4.16. The high pressure peak now lies in the region between the front and the rear wings. This is likely to be caused by entrainment of the wakes of the four rotors in the region between the wings, under the fuselage, as illustrated in Figure 4.17.

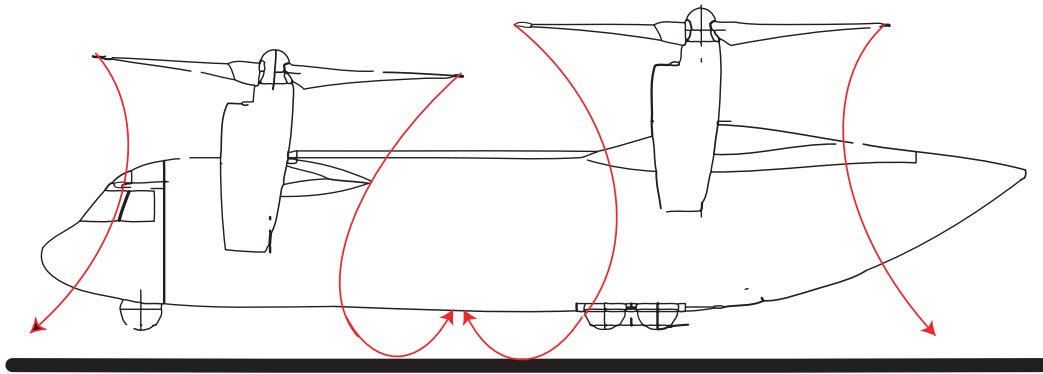


Figure 4.17: Illustration of entrainment of rotor wakes under the fuselage

Chapter 5

QTR in Low Speed Forward Flight

Results for the QTR in hovering flight, IGE and OGE, were presented in the previous chapter. The download and power required were found to reduce substantially while operating close to the ground. In order to determine the usability of this extra lifting capacity, the behavior of the download and power in slow forward flight needs to be studied.

In this chapter, performance characteristics of the QTR in low speed forward flight will be presented. As discussed in Chapter 2, the forward speeds will be non-dimensionalized as the rotor wake skew angle, χ . Download to thrust ratios will be presented for the whole airframe as well as the individual measurements at the front and rear airframe mounts. Power measurements will be converted to that of an equivalent full-scale QTR and presented. As was presented for hover, the pressure measurements along the bottom of the fuselage will also be presented.

5.1 Test Procedure

The test procedure in forward flight is as follows. Zero readings for the instruments are measured and recorded. Then, the rotors are turned on and increased in

rpm to obtain the desired thrust using a control signal from the computer. Once the thrust on all the rotors stabilizes at the desired thrust, the setup is set in forward motion using the golf cart. Once the desired speed is reached and stabilized, data acquisition is initiated and 4 seconds of data are acquired and recorded. Then, the golf cart is brought to a halt and the rotors are gradually turned off. The maximum speed of the cart is set for each run using shims placed under the accelerator pedal.

5.2 Download to Thrust Ratios

Measured overall download to thrust ratios are presented as a function of rotor wake skew angle for different heights above the ground, in Figure 5.1 to 5.7. There were seven different heights above the ground for which these results are presented, ranging from OGE ($z = 3.5$) to the case where the wheels are on the ground ($z = 0.607$). The uncertainty values that are shown were calculated in hover for each height. This was done because it was not possible to perform repetitive tests at exactly the same skew angle.

Initially, measurements were obtained for a disk loading of 4.7 lb/sq.ft. on each rotor ($v_h = 31$ ft/sec), for skew angles up to 37° . For this disk loading, the download to thrust ratio, OGE, starts reducing for skew angles greater than 10° . For the next height ($z = 1.5$), the download remains quite constant up to a skew angle of 20° and then reduces slightly. For the intermediate heights, the download gradually increases for $z = 1.14$, whereas the upload gradually decreases and becomes an upload for $z = 1.0$. While operating close to the ground, ($z = 0.85, 0.75$ and 0.607), the upload

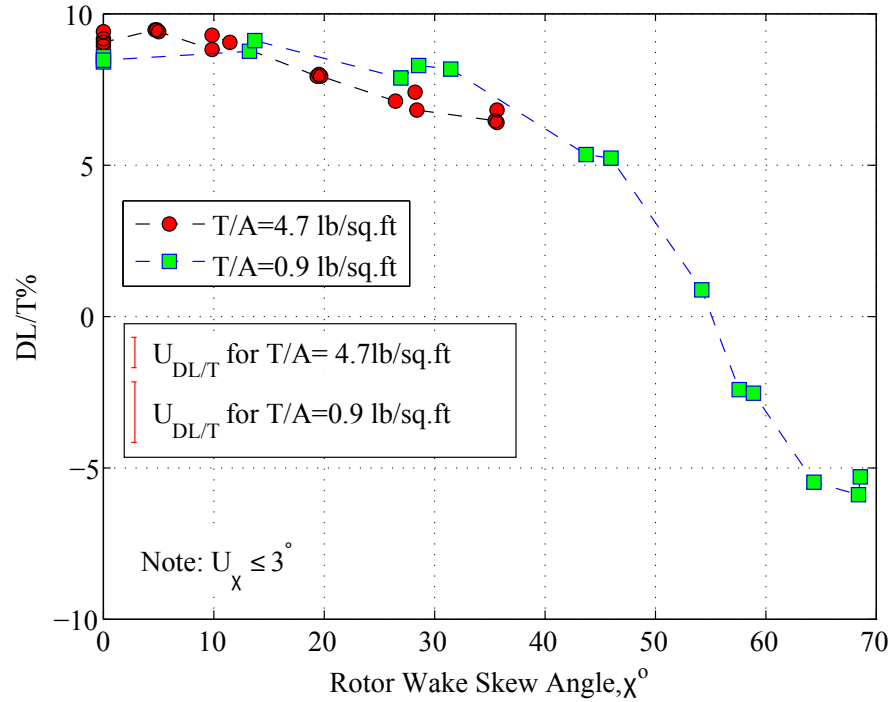


Figure 5.1: Download to thrust ratio vs Rotor Wake Skew Angle for $z=3.5$ (OGE)

remains quite constant up to a skew angle of 20° and then starts decreasing.

However, these trends do not seem to be fully developed. In order to provide the complete picture, further information on the behavior of the download beyond a skew angle of 35° were needed.

The rotor wake skew angle is a function of the rotor induced velocity and the forward velocity. The two possible ways of increasing the skew angle are by increasing the forward velocity or by reducing the rotor induced velocity, *i.e.*, rotor thrust. Because of the length of the test area, the maximum speed of the test setup is limited to about 20 ft/sec. At a disk loading of 4.7 lb/sq.ft. on each rotor, this speed corresponds to a skew angle of 37° . However, reducing the disk loading by a factor of 5, to 0.9 lb/sq.ft., nearly doubles the maximum skew angle to 67° .

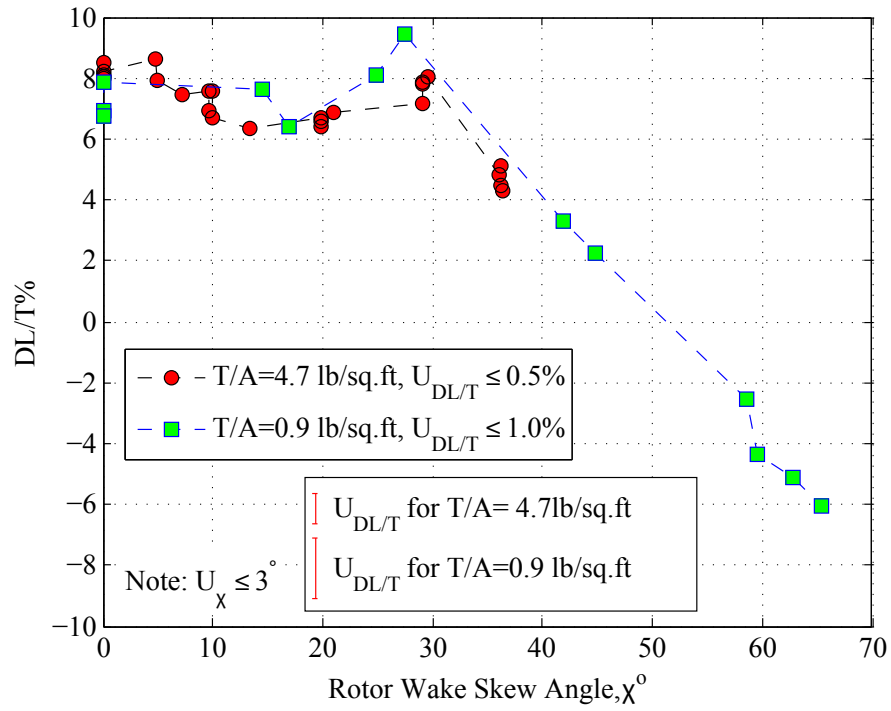


Figure 5.2: Download to thrust ratio vs Rotor Wake Skew Angle for $z=1.5$

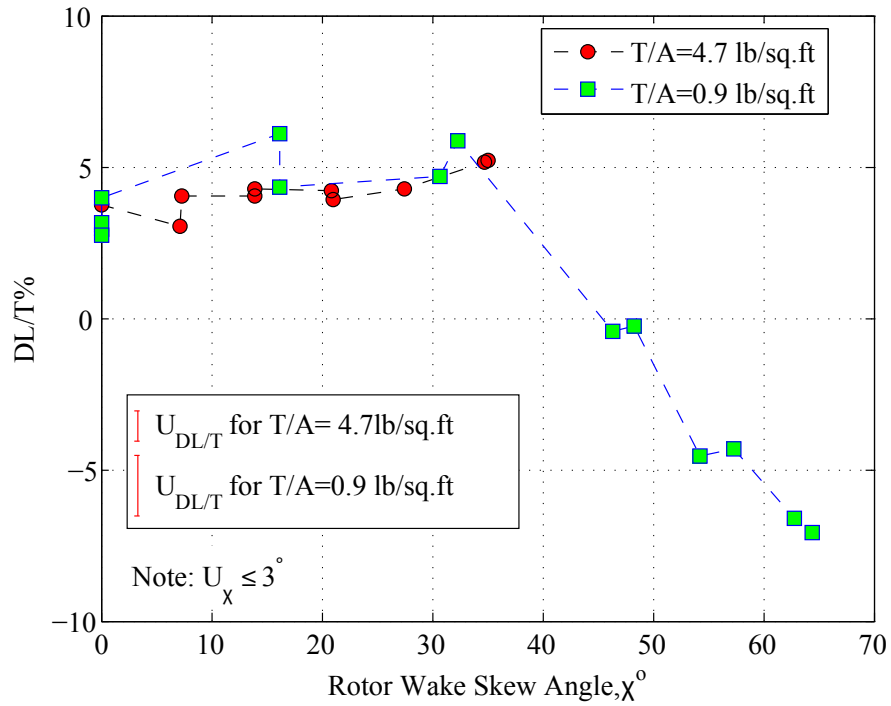


Figure 5.3: Download to thrust ratio vs Rotor Wake Skew Angle for $z=1.14$

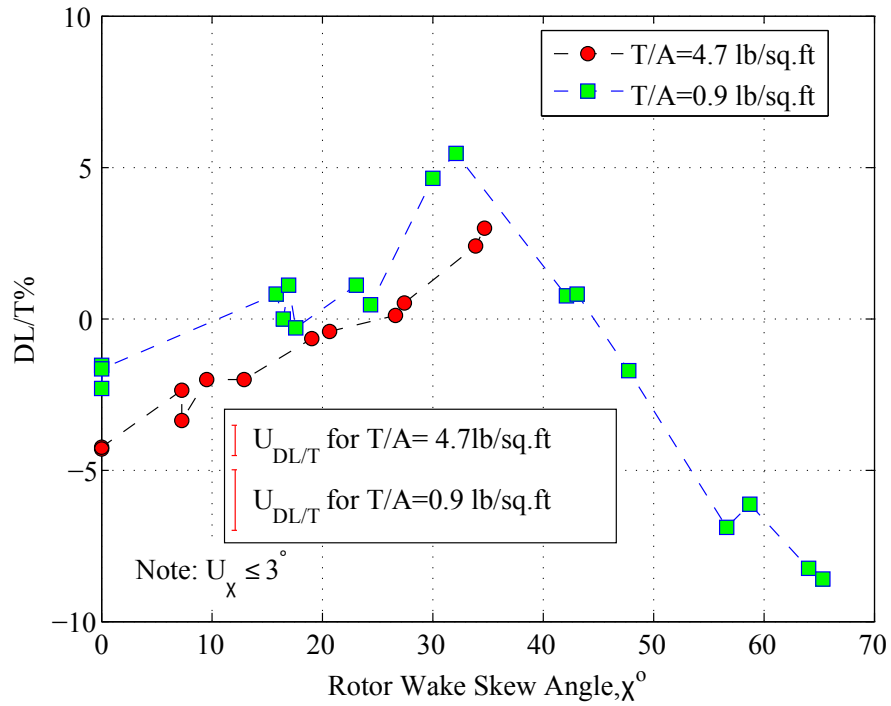


Figure 5.4: Download to thrust ratio vs Rotor Wake Skew Angle for $z=1.0$

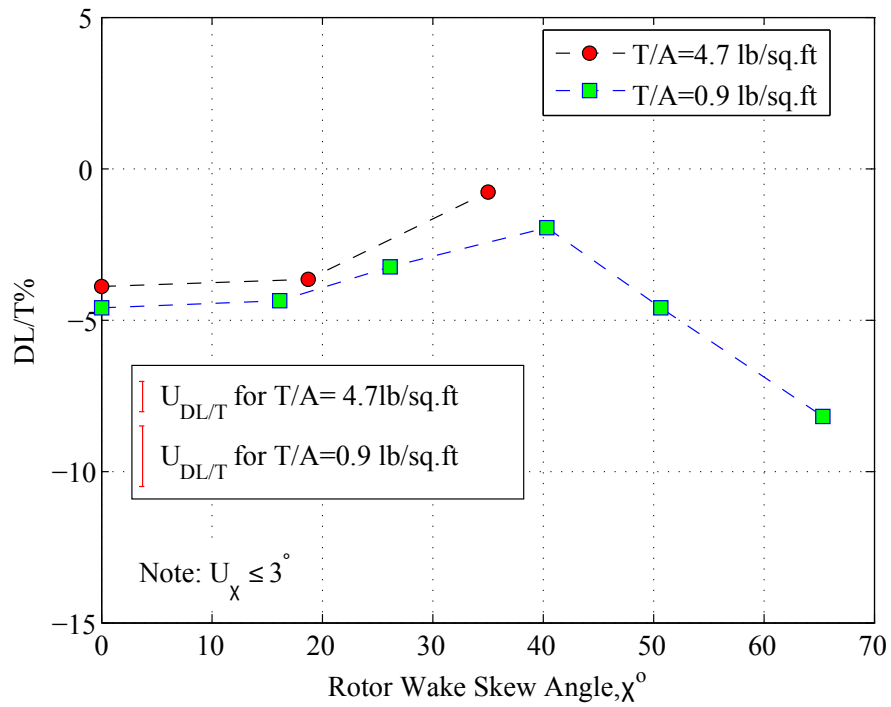


Figure 5.5: Download to thrust ratio vs Rotor Wake Skew Angle for $z=0.86$

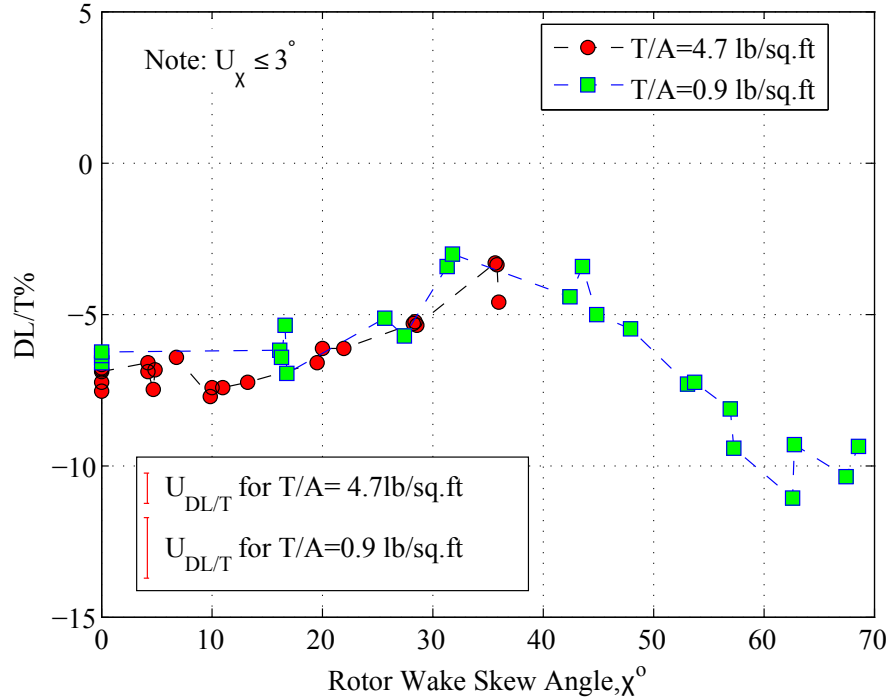


Figure 5.6: Download to thrust ratio vs Rotor Wake Skew Angle for $z=0.75$

In hover, it was found that the download to thrust ratios are quite similar, even while operating at different thrust levels, both IGE and OGE. This implies that lowering the rotor disk loading to 0.9 lb/sq.ft. should not affect the measured download to thrust ratios. The experiment was repeated at a disk loading of 0.9 lb/sq.ft, in order to take advantage of this increase in skew angle. The download to thrust ratios for this reduced disk loading are also presented vs. skew angle in Figures 5.1 to 5.7, for different heights above the ground. It can be seen that the download measured for the 4.7 lb/sq.ft. disk loading are very similar to the 0.9 lb/sq.ft. case for all heights.

The download, OGE, is found to decrease slowly for skew angles between 10° and 30° . For higher skew angles, the download decreases rapidly to become an

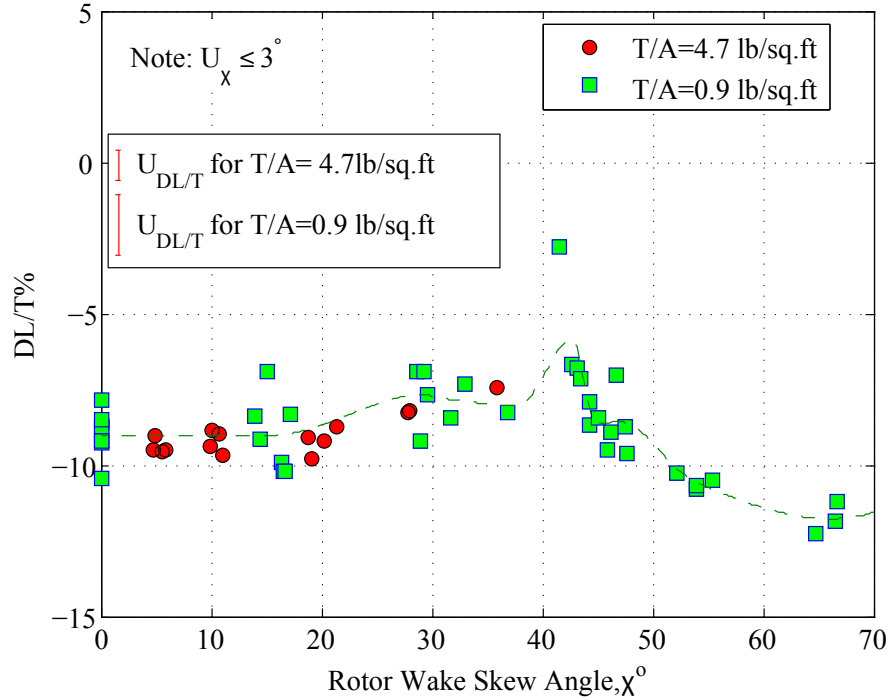


Figure 5.7: Download to thrust ratio vs Rotor Wake Skew Angle for $z=0.61$ (wheels on ground)

upload of about $5.5 \pm 1\%$ of the total rotor thrust at a skew angle of 68° .

While operating IGE, an increase in download (or an increase in upload) is observed at certain skew angles, which goes away with further increase in skew angle. The skew angle where the maximum download occurs at each height is found to reduce with an increase in height above the ground. This effect is particularly pronounced for $z=1.0$, where the upload, of $2 \pm 1\%$ of the thrust in hover, changes to a download of $4.5 \pm 1\%$, at a skew angle of 30° . With a further increase in skew angle the download drops substantially and becomes an upload of about $8.5 \pm 1\%$ at a skew angle of 65° .

For operation very close to the ground, ($z=0.75$ and $z=1.0$), the important

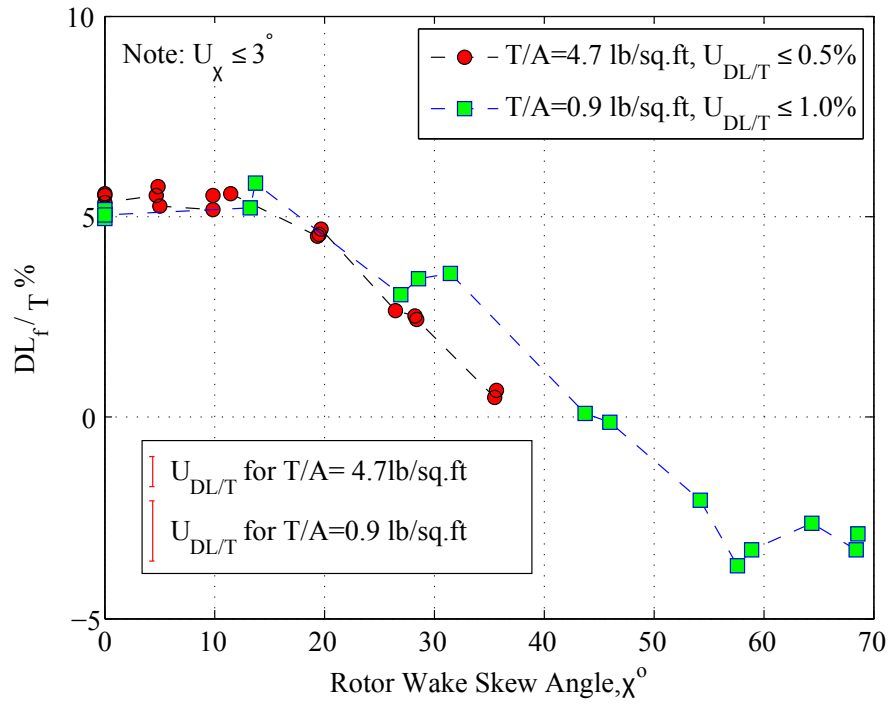
observation from these results is that the upload that is obtained IGE does not reduce by more than 2-3% from the hover value, at low skew angles (between 30° and 45°. Beyond a skew angle of 45°, the upload in fact increases with further increase in skew angle.

5.2.1 Download at the front and rear airframe mounts

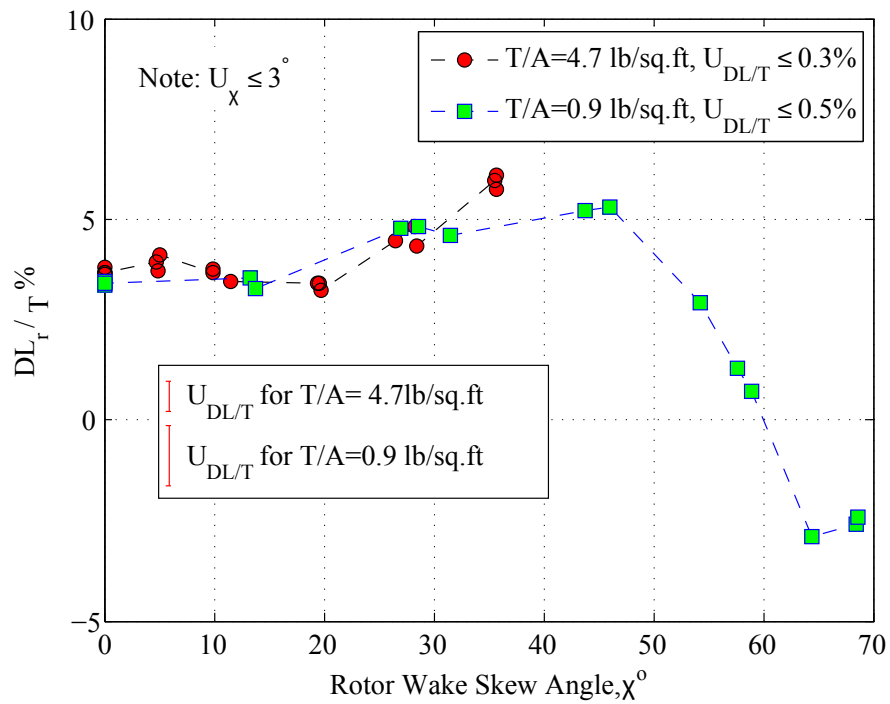
Download measurements at the front and rear airframe mounts are also available individually for different skew angles. The normalized downloads at the front and the rear airframe are plotted vs skew angle for different heights above the ground in Figures 5.8 to 5.14. Figure 5.8 shows that the download at the front airframe mount starts reducing with an increase in skew angle, OGE. However, the download at the rear mount increases slightly for skew angles between 20° and 45° skew angle and then starts reducing.

For the intermediate heights, ($z=1.5$, $z=1.14$ and $z=1.0$), the behavior of the download at the front and the rear of airframe mounts are similar up to a skew angle of 30°, where there is a small increase in the download. For the front airframe mount, the download starts reducing rapidly after this skew angle. However, at the rear airframe mount, the download does not reduce as rapidly with skew angle for $\chi > 30^\circ$.

For the three lowest heights, ($z=0.86$, $z=0.75$ and $z=0.61$), a similar effect is observed. However, the skew angle at which the reduction in the upload is observed occurs at a higher skew angle.

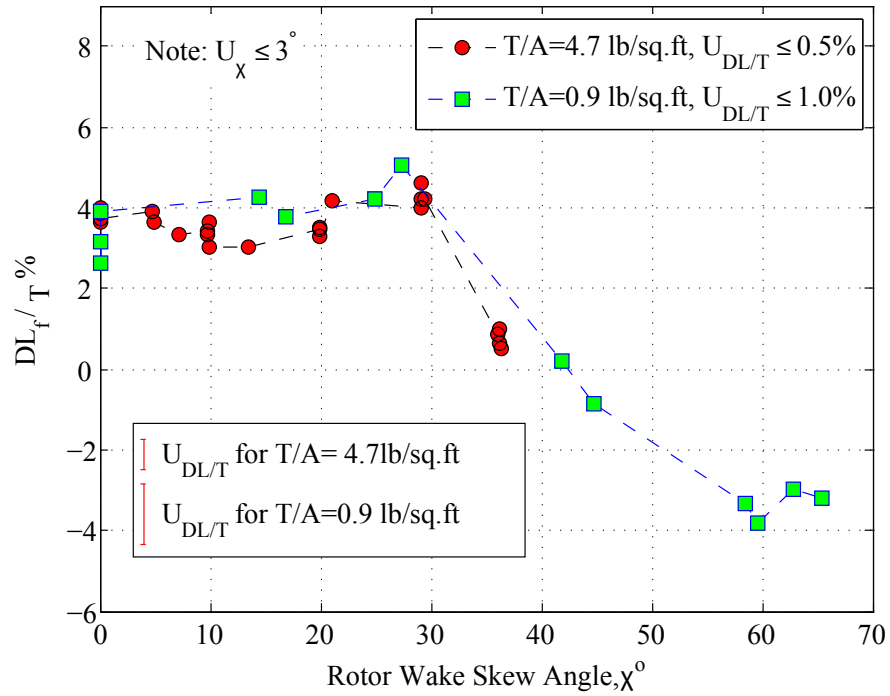


(a) Front Airframe Mount

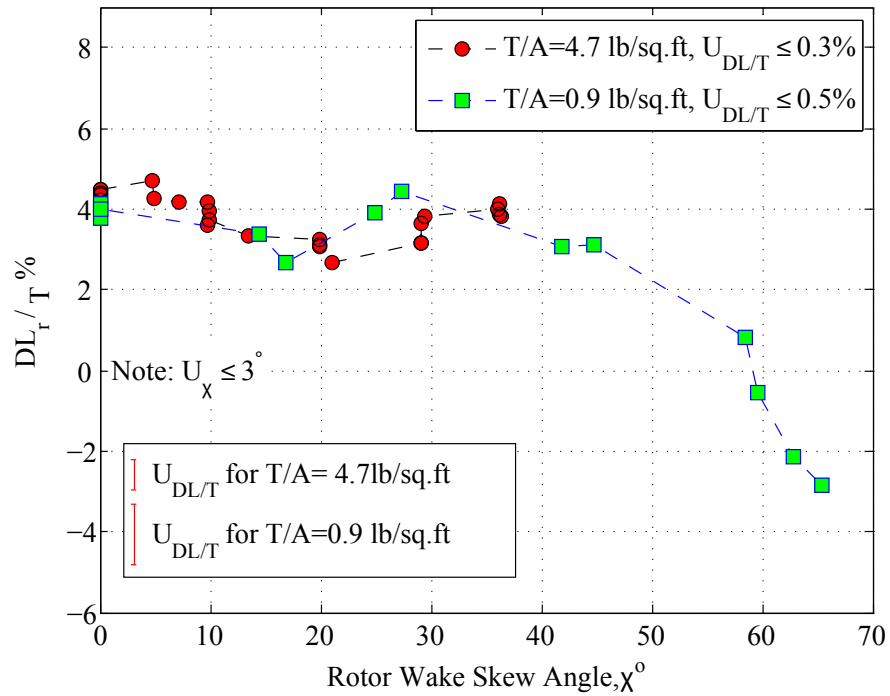


(b) Rear Airframe Mount

Figure 5.8: Downloads at the front and rear airframe mounts for $z=3.5$ (OGE)

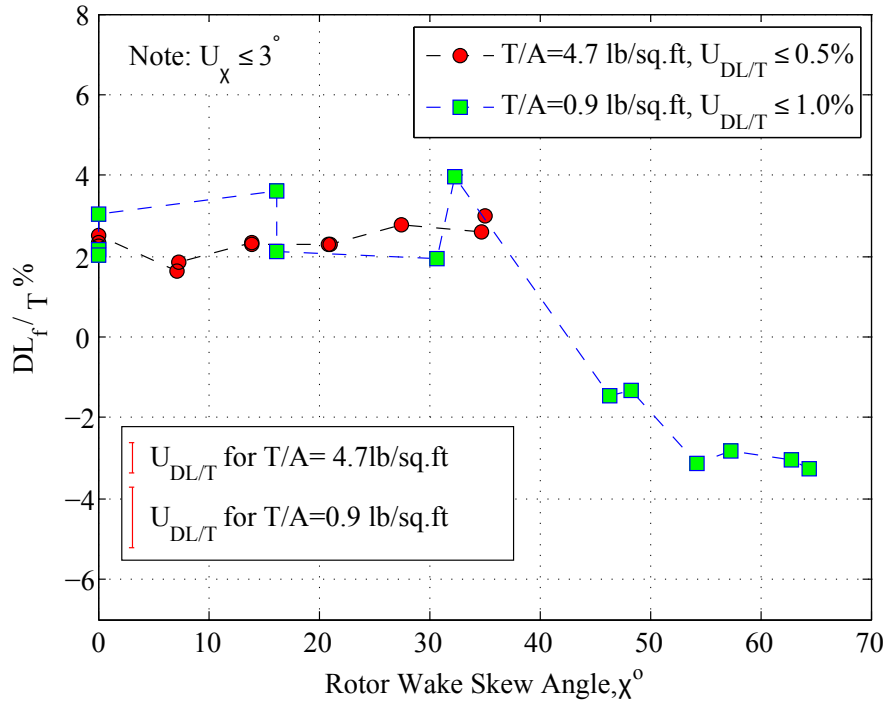


(a) Front Airframe Mount

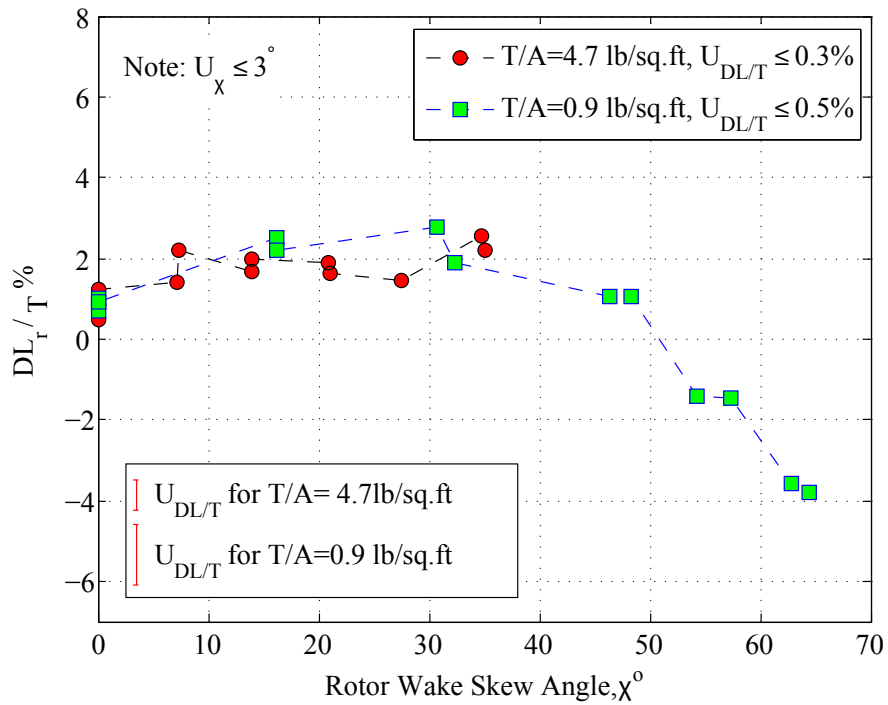


(b) Rear Airframe Mount

Figure 5.9: Downloads at the front and rear airframe mounts for $z=1.5$

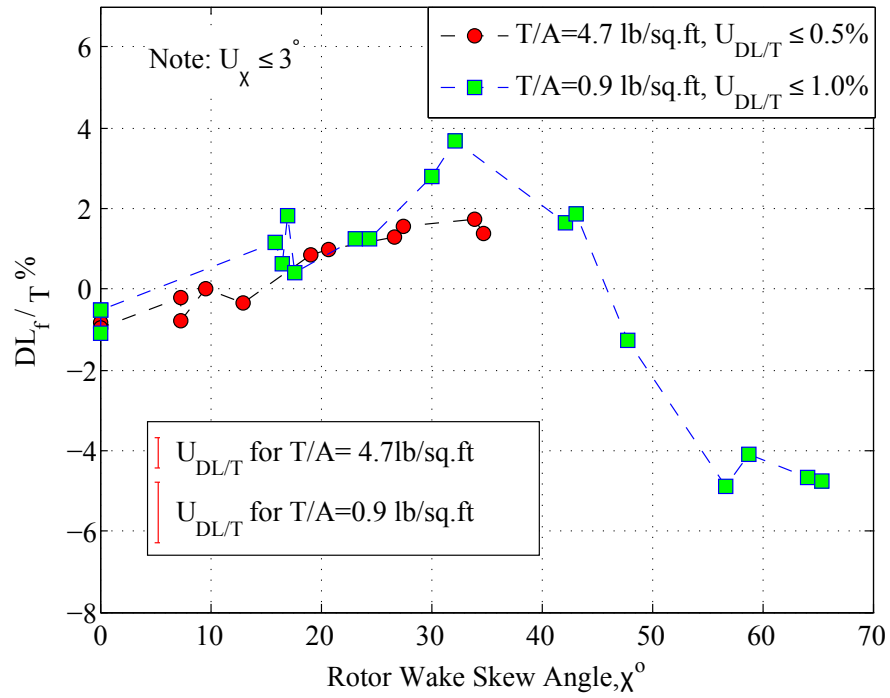


(a) Front Airframe Mount

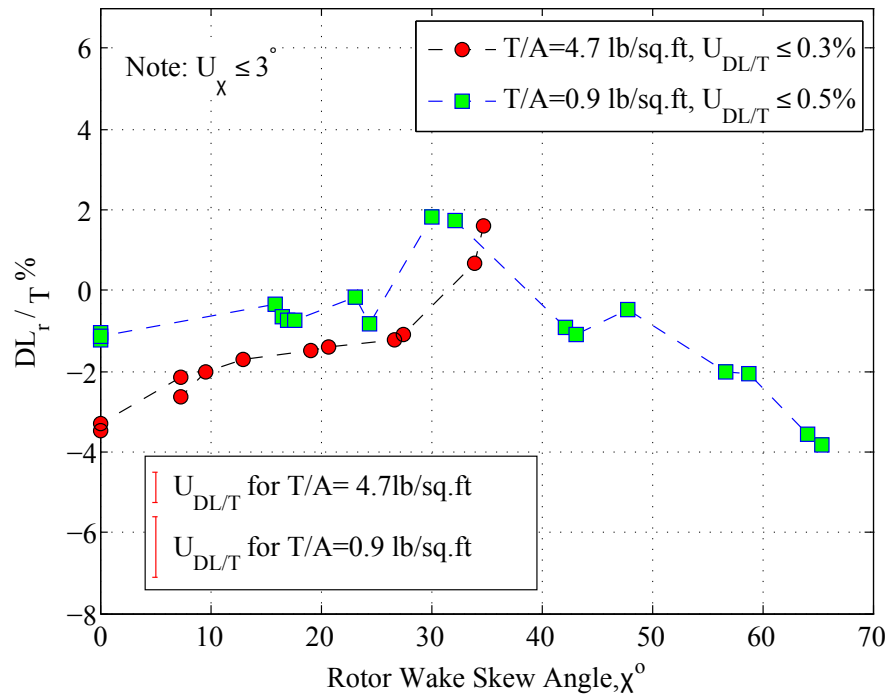


(b) Rear Airframe Mount

Figure 5.10: Downloads at the front and rear airframe mounts for $z=1.14$

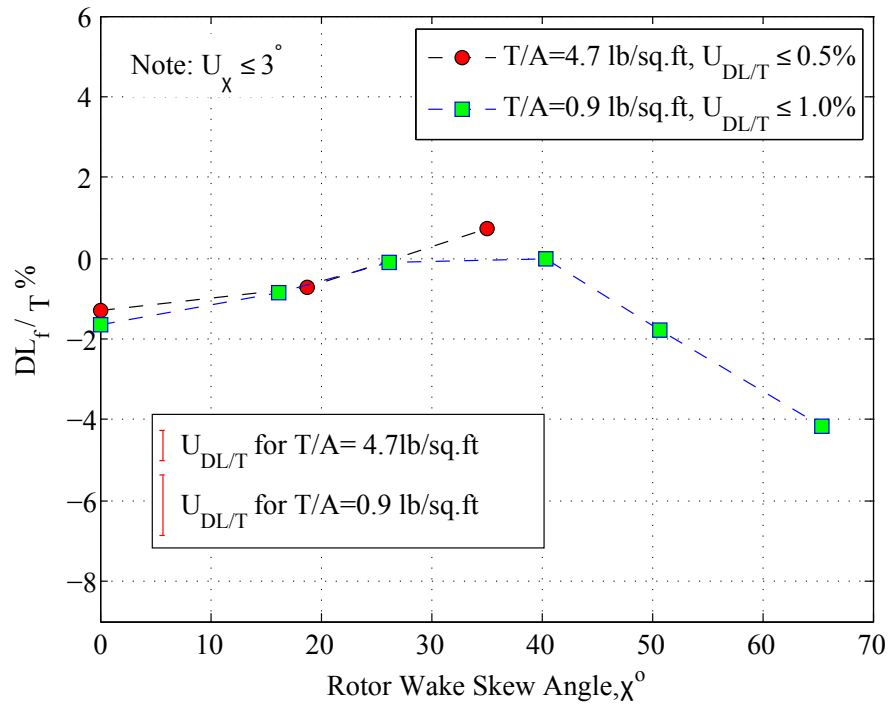


(a) Front Airframe Mount

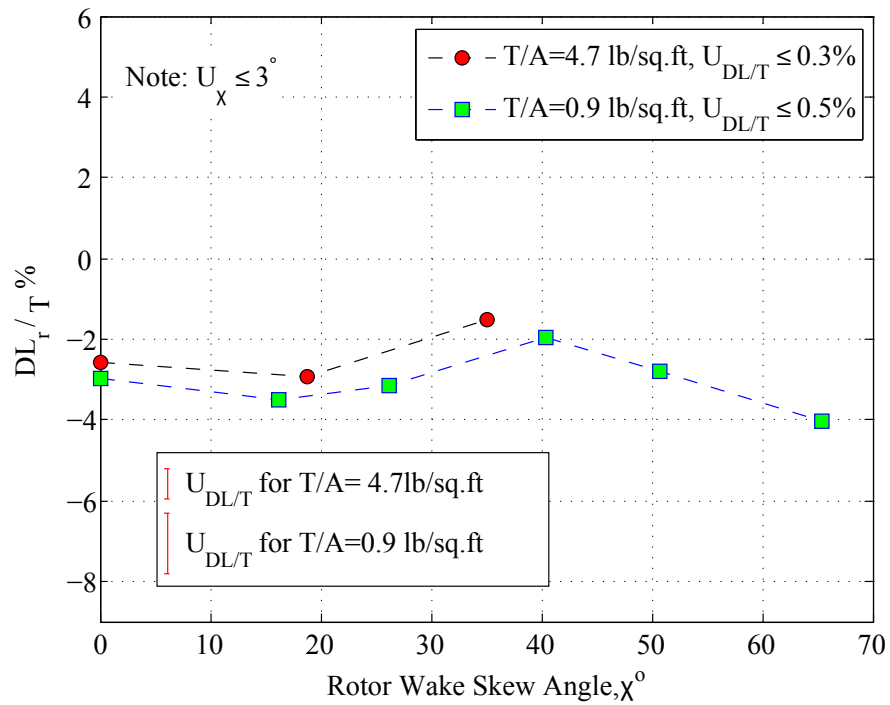


(b) Rear Airframe Mount

Figure 5.11: Downloads at the front and rear airframe mounts for $z=1.0$

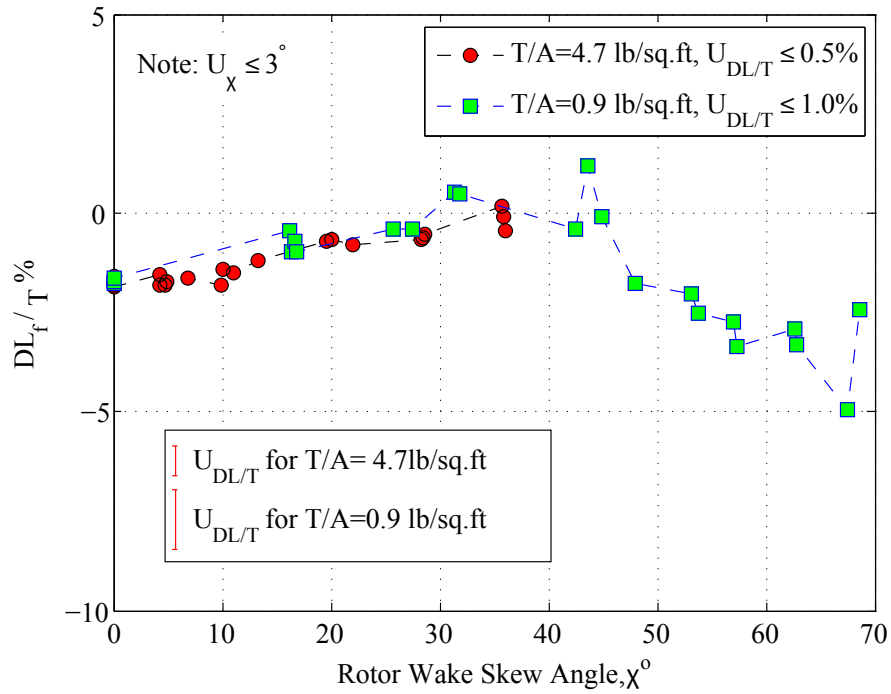


(a) Front Airframe Mount

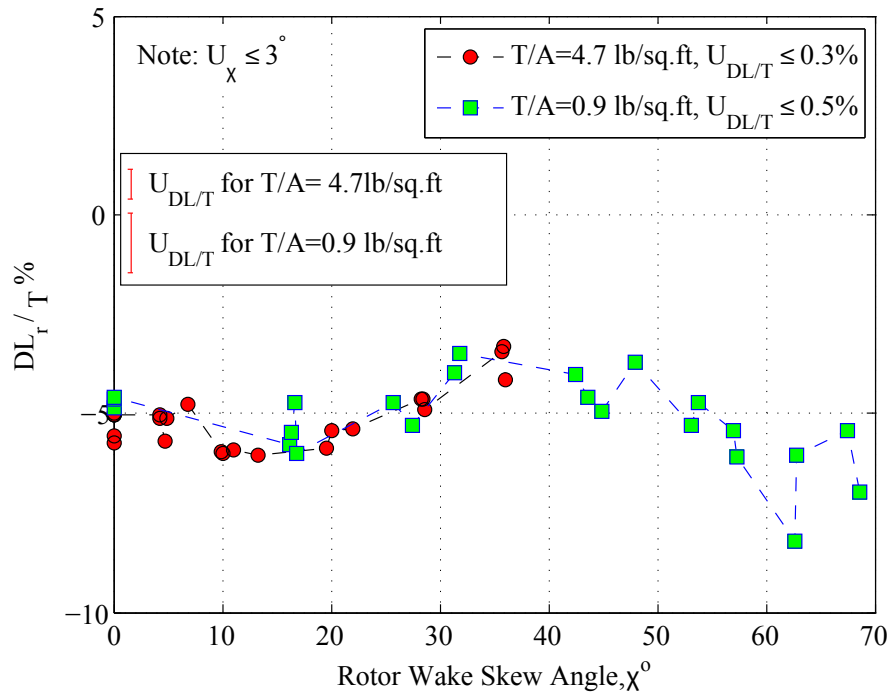


(b) Rear Airframe Mount

Figure 5.12: Downloads at the front and rear airframe mounts for $z=0.86$

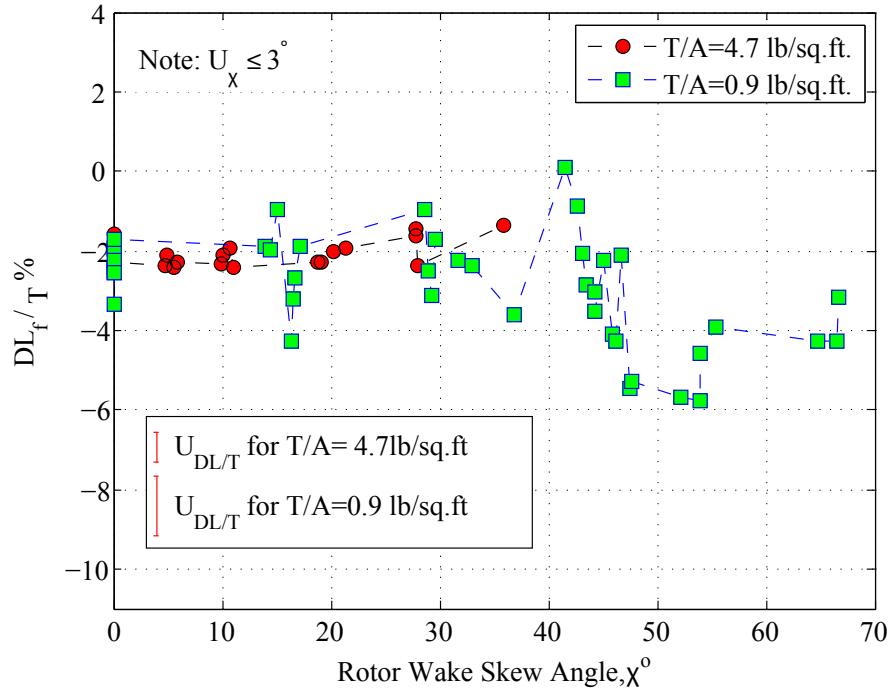


(a) Front Airframe Mount

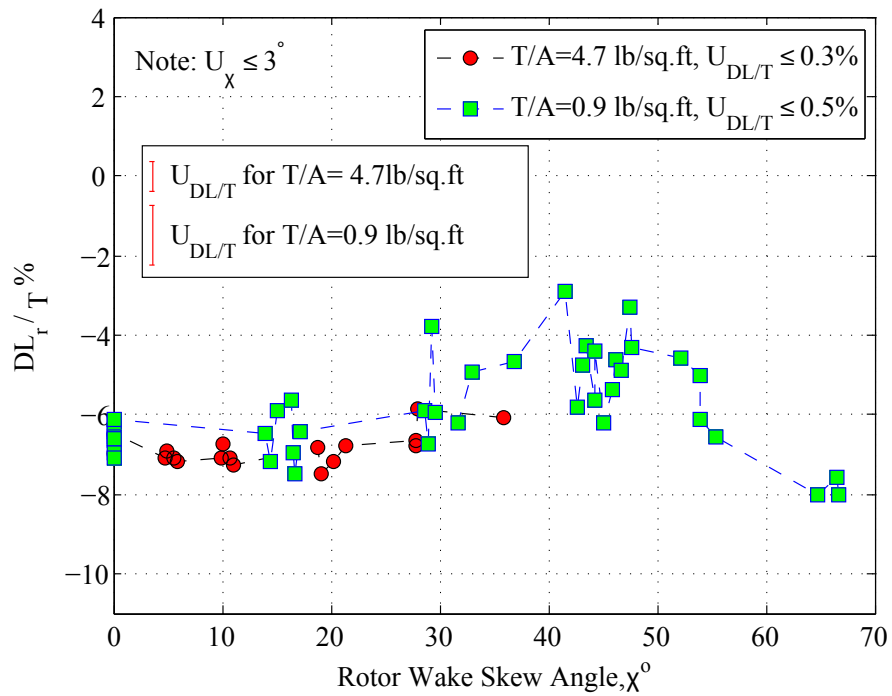


(b) Rear Airframe Mount

Figure 5.13: Downloads at the front and rear airframe mounts for $z=0.75$



(a) Front Airframe Mount



(b) Rear Airframe Mount

Figure 5.14: Downloads at the front and rear airframe mounts, $z=0.61$ (wheels on ground)

This reduction in upload and its subsequent increase at certain skew angles could be caused by a combination of reasons. The upward flow under the fuselage, caused by the interaction of the rotor wakes near the ground, is most likely convected back with an increase in skew angle. This causes a reduction in the upload over the front portion of the airframe. However, the download on the wings would still be present, because the wings would still be immersed in the rotor wake. Therefore, the net effect would be a reduction in upload.

CFD flow images obtained by Gupta[12], show a ground vortex being formed ahead of the aircraft, IGE, which gets convected under the front wing at a skew angle of 43° . From Figure 5.7, when the wheels are on the ground ($z=0.61D$), the peak in the reduction of the measured upload from the experiment occurs at a skew angle between 40° and 45° . For skew angles slightly lower than this, this vortex would be located just ahead of the vehicle. This would cause the front of the fuselage and the front wings. to be exposed to a downward flow, resulting in an increase in download. As the vortex passes underneath the vehicle, the vortex will become stronger and smaller in size and would result in increase in pressure under the vehicle. This might be one of the reason for the rapid recovery of upload at the higher skew angles.

Also, the wings have a trailing edge flap deflection angle of 67° . Therefore, at higher skew angles, the wings would start producing enough lift to offset the download.

It was suggested by Gupta[12] that the presence of the front rotors shields the rear rotors from the full forward velocity of the vehicle. As a result, the rear rotors would experience a lower value of effective skew angle than the front rotors. This

would reduce the lift produced by the rear wing and could be the reason for the slower rate of reduction in the download at the rear airframe mount.

For obtaining a better understanding of this behavior, further investigation using pressure measurement on the bottom of the fuselage and flow visualization were performed. The results in Section 5.5 and Chapter 6 confirm this hypothesis.

5.3 Power Required For a Given Vehicle Thrust

Section 4.4.1 describes the procedure used to convert the measured power in hover, to the induced power of a QTR operating at a constant vehicle weight, with variable pitch rotors, at a constant rpm. A similar calculation can be done in forward flight in order to correct the measured power.

5.3.1 Corrections for Profile Effects

The main difference in procedure from the hover analysis will be in the calculation of the profile power that will be subtracted. Leishman[30] (2000,) summarized the results from the analysis of Glauert[77] (1926) and Bennett[78] (1940) for the calculation of profile power coefficient in forward flight,

$$(C_{P0})_{fwd} = (C_{P0})_{hover}(1 + K\mu^2), \quad (5.1)$$

where μ is the rotor advance ratio and K is a numerical constant that varies between 4 in hover and 5 at $\mu = 0.5$. This analysis is for very low speed forward flight, where the advance ratio, μ varies between 0 and 0.1. Therefore, a value of 4 for K will be a valid assumption for this flow regime. The other assumptions used

in this analysis are steady, level flight at zero rotor tip-path-plane angle and equal thrust on all rotors.

Using this value of profile power coefficient, the profile power will be calculated:

$$P_{0j} = C_{P0}\rho A(\Omega_j R)^3 \quad (5.2)$$

5.3.2 Corrections for Induced Effects

As was done in hover, the induced power is calculated by subtracting the profile power from the measured power.

$$P_{i_j} = P_j - P_0 \quad (5.3)$$

Starting from momentum theory assumptions and adding corrections for the non-uniformity of the inflow, the induced power in forward flight can be expressed as:

$$P_{i_j} = (P_{i_j})_{hover} \frac{v_i}{v_h} \cdot K_i \quad (5.4)$$

where $(P_{i_j})_{hover}$ is the induced power in hover for the same thrust. K_i is a correction factor accounting for the non-uniformity of the inflow. The quantity v_i/v_h is just a different way of expressing the rotor wake skew angle.

This induced power is then corrected for changes in required thrust and induced power coefficient for maintaining a constant total vehicle thrust. The corrected induced power ($P_{j_{corr}}$) in forward flight can be expressed as follows:

$$P_{j_{corr}} = (P_{j_{corr}})_{hover} \frac{v_i}{v_h} \cdot K_i \quad (5.5)$$

The corrected induced velocity will be at the same skew angle and therefore, it should be a valid assumption to assume that there will be the same level of non-uniformity of the inflow.

Dividing Equation 5.5 by 5.4 and rearranging, it can be seen that the ratio of corrected induced power to the induced power for the measured thrust is the same as in hover.

$$\frac{P_{jcorr}}{P_{ij}} = \frac{(P_{jcorr})_{hover}}{(P_{ij})_{hover}} \quad (5.6)$$

Therefore, the corrected induced power in forward flight can be calculated using the same scaling relationship as in hover (from Equation 4.9):

$$P_{jcorr} = P_{ij} \left(\frac{T_{jreqd}}{T_j} \right)^{3/2} \frac{\kappa_{reqd}}{\kappa_{meas}} \quad (5.7)$$

5.3.3 Power Ratio

The corrected induced power values from the four rotors are then summed and normalized by the corrected induced power in hover, OGE to obtain the corrected induced power ratio, P*. The evolution of the corrected induced power ratio with increase in rotor wake skew angle, is shown in Figures 5.15 to 5.20. The power ratio is shown separately for different heights, at two different disk loadings of 0.9 lb/sq.ft. and 4.7 lb/sq.ft. As the behavior of this corrected induced power is related to the rotor thrust, the behavior of the power curves are very similar to the download curves. At very low forward speeds, OGE, the power reduces gradually until a skew

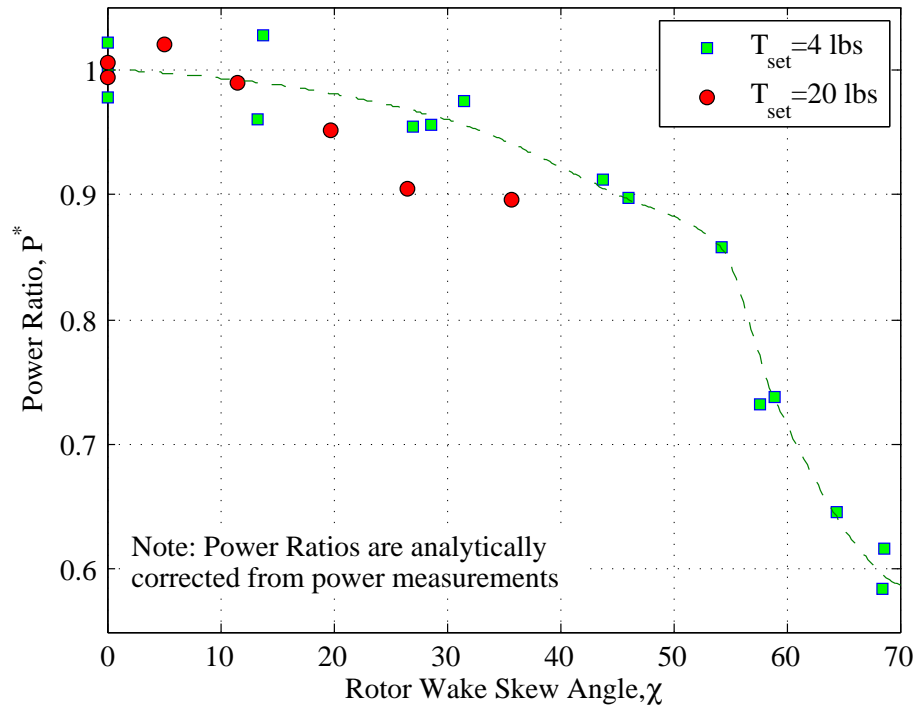


Figure 5.15: Corrected Power Ratio vs Rotor Wake Skew Angle for $z=3.5$ (OGE)

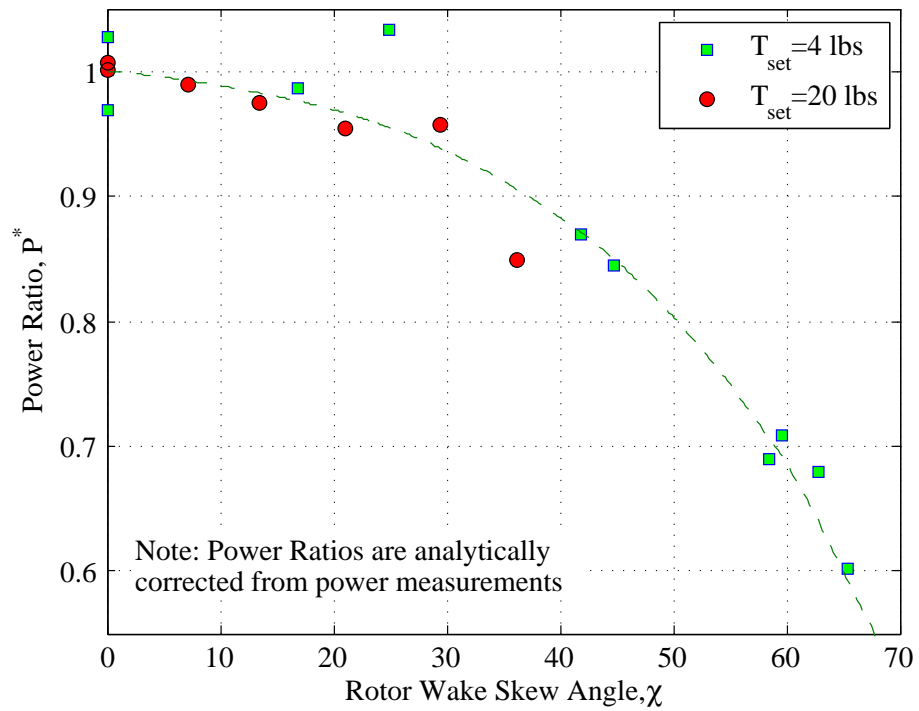


Figure 5.16: Corrected Power Ratio vs Rotor Wake Skew Angle for $z=1.5$

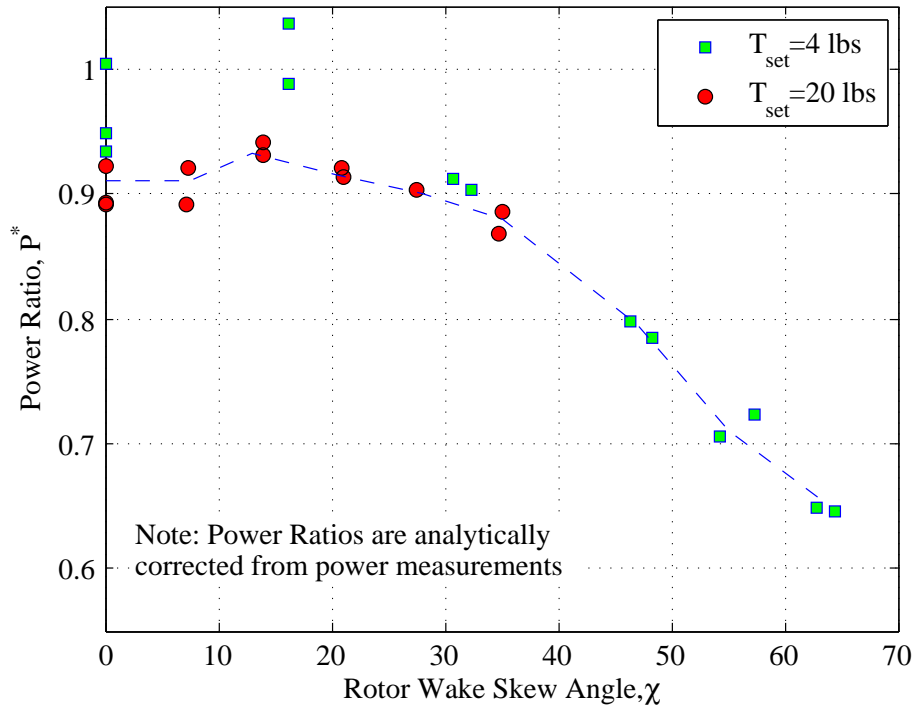


Figure 5.17: Corrected Power Ratio vs Rotor Wake Skew Angle for $z=1.14$

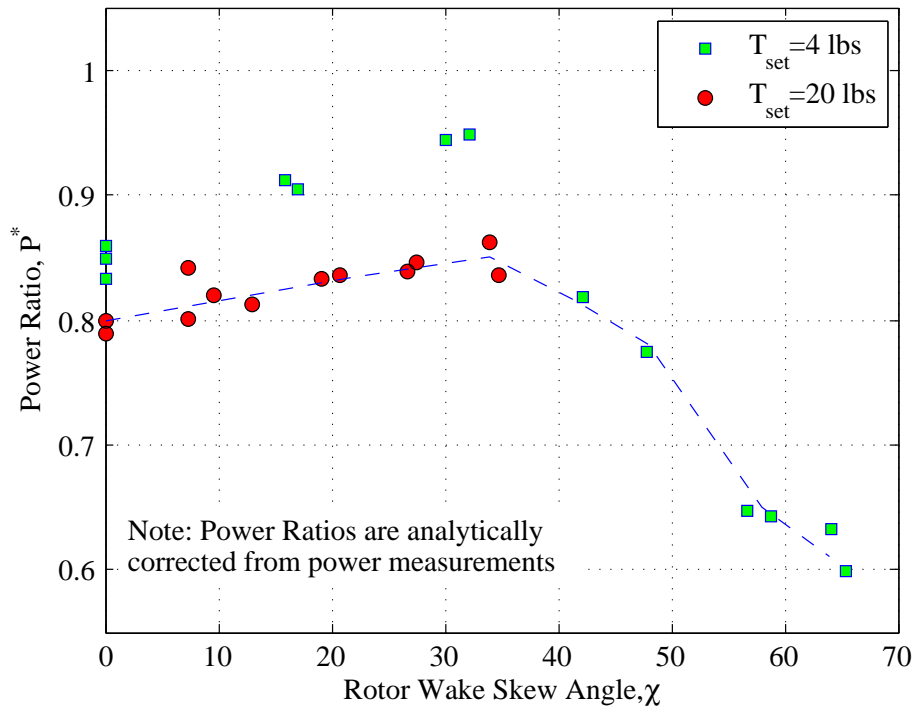


Figure 5.18: Corrected Power Ratio vs Rotor Wake Skew Angle for $z=1.0$

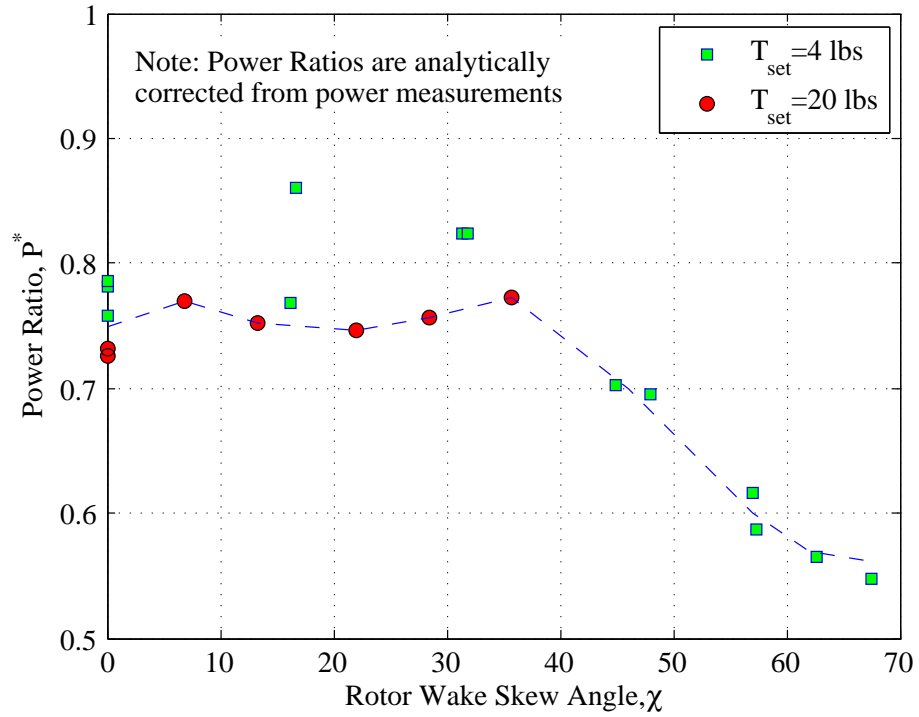


Figure 5.19: Corrected Power Ratio vs Rotor Wake Skew Angle for $z=0.75$

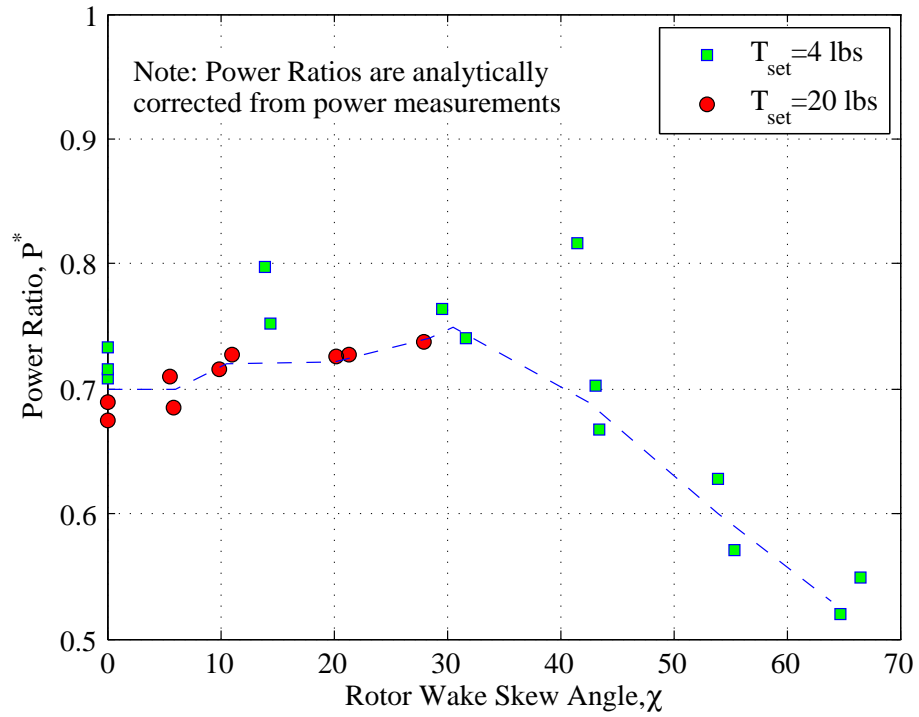


Figure 5.20: Corrected Power Ratio vs Rotor Wake Skew Angle for $z=0.61$, wheels on ground

angle of about 45 degrees and then rapidly reduces to about 60% of the OGE hover value at a skew angle of 67 degrees. For operation IGE, at certain low skew angles, the power increases with an increase in skew angle and then reduces with further increase in skew angle. As observed for the download, the skew angle where the required power is maximum decreases with an increase in height above the ground. For the case where the wheels are on the ground ($z = 0.61$), the power shows an increase of about 5% up to a skew angle of 43° , compared to power in hover. With a further increase in skew angle, the power reduces to nearly 50% of the OGE power in hover, at a skew angle of about 65° .

5.4 Available Thrust For A Given Power

The vehicle thrust available in forward flight for a given power can be calculated in a manner similar to the procedure followed for hover, in Section 4.4.2:

$$T_{av} = \left(1 + \frac{DL}{T}\right) \left(P_{av} \frac{\sqrt{2\rho A}}{\kappa_{reqd}} (1 + (\tan \chi)^2)^{1/4}\right)^{2/3} \quad (5.8)$$

The vehicle thrust available is calculated using the OGE induced corrected power value as the available power. The vehicle thrust values were normalized by the vehicle thrust available in hover, OGE, to calculate the vehicle thrust ratio, T_{av}^* . Figures 5.21 to 5.26 show the vehicle thrust ratio plotted against skew angle, for different heights.

For all heights, there is a slight reduction in the available vehicle thrust from the hover values, at low values of skew angle. At higher skew angles of about 68°

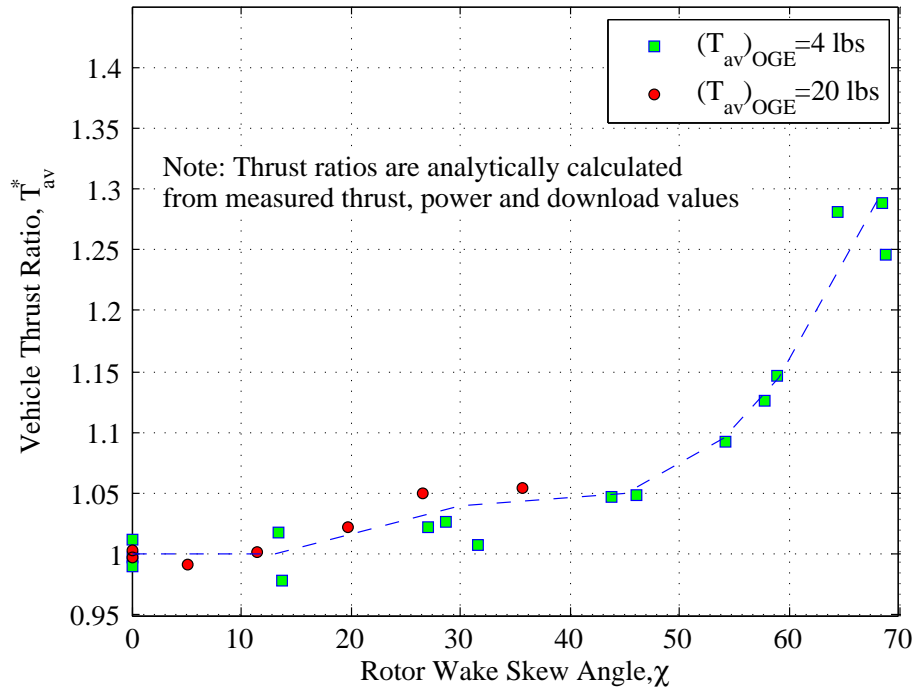


Figure 5.21: Vehicle Thrust Ratio vs Rotor Wake Skew Angle for $z=3.5$ (OGE)

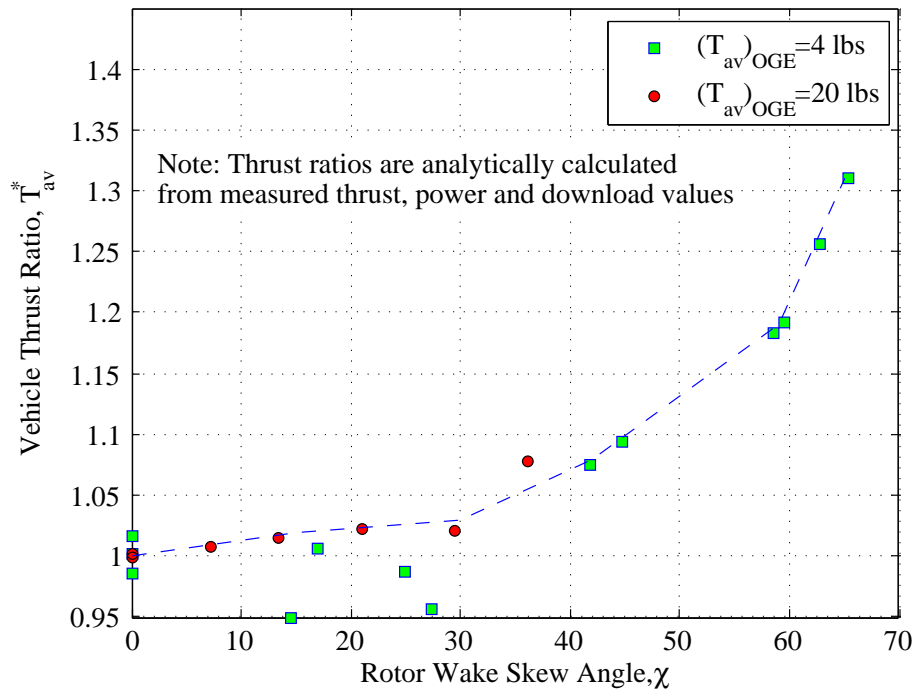


Figure 5.22: Vehicle Thrust Ratio vs Rotor Wake Skew Angle for $z=1.5$

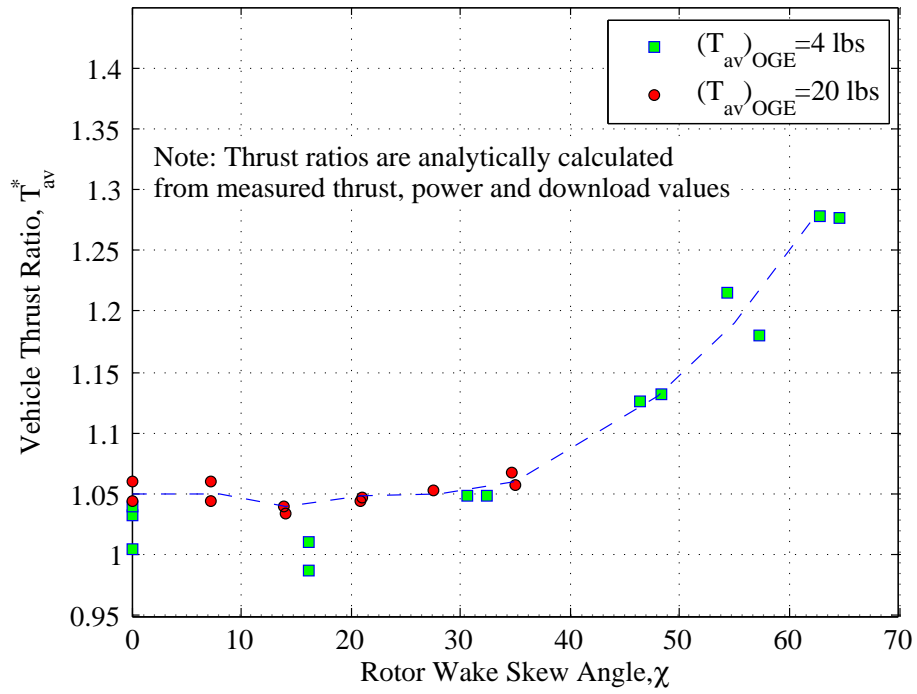


Figure 5.23: Vehicle Thrust Ratio vs Rotor Wake Skew Angle for $z=1.14$

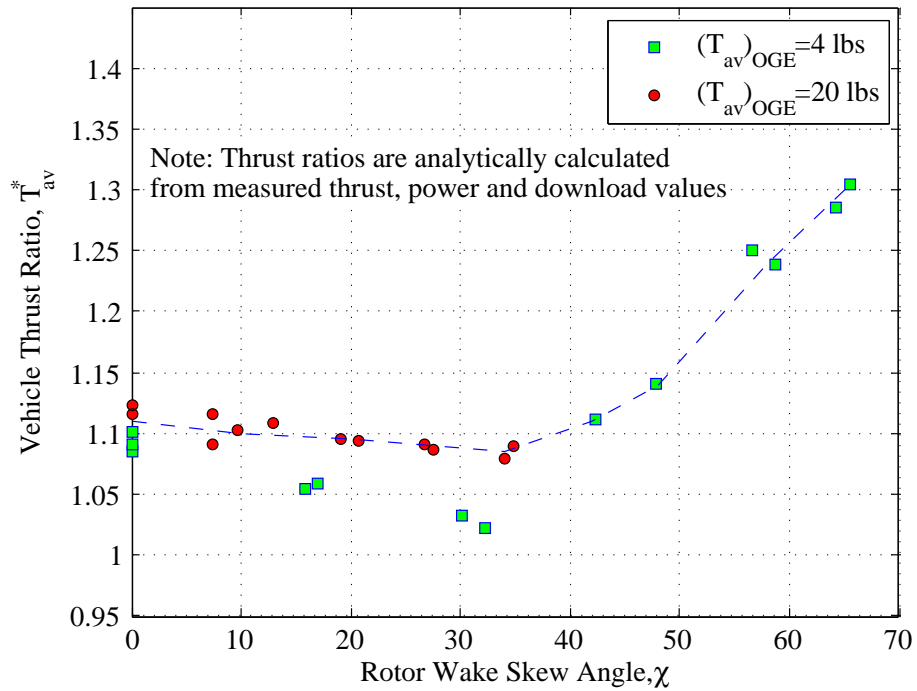


Figure 5.24: Vehicle Thrust Ratio vs Rotor Wake Skew Angle for $z=1.0$

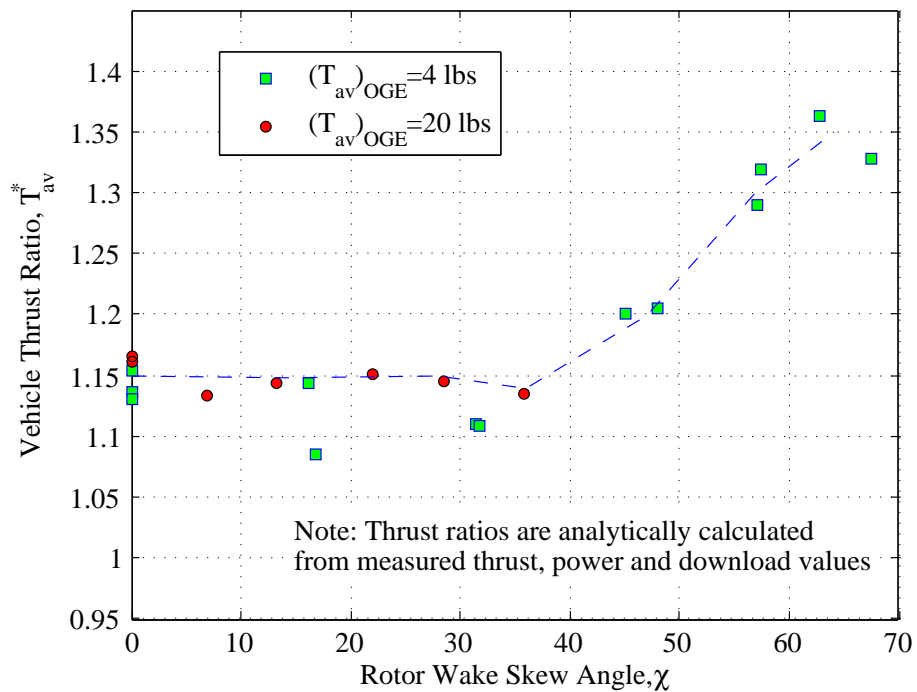


Figure 5.25: Vehicle Thrust Ratio vs Rotor Wake Skew Angle for $z=0.75$

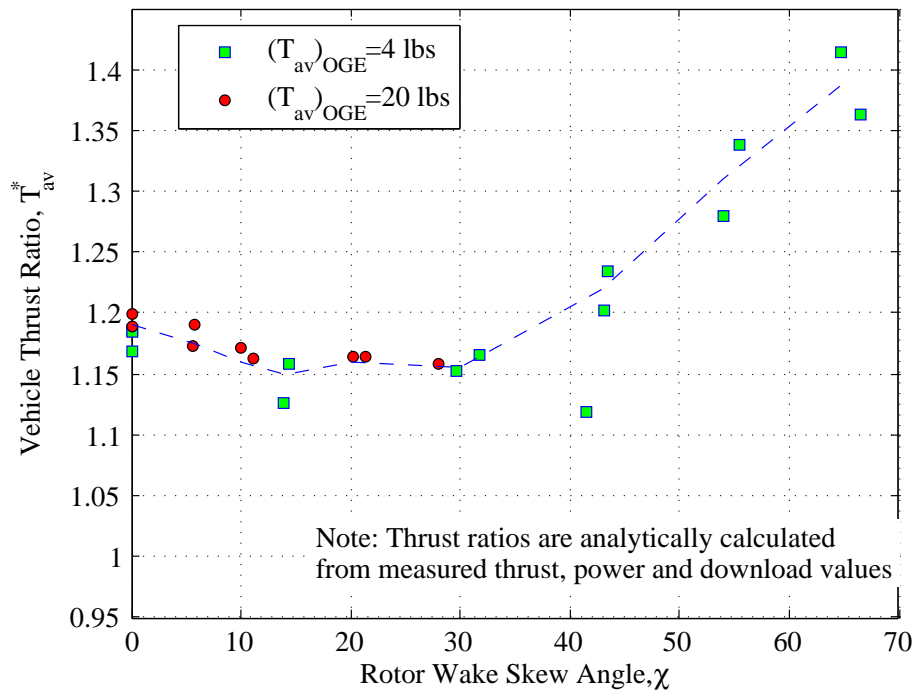


Figure 5.26: Vehicle Thrust Ratio vs Rotor Wake Skew Angle for $z=0.61$, wheels on ground

degrees, OGE, the available thrust increases to about 128% of the OGE thrust in hover.

For the case where the wheels are on the ground, the available vehicle thrust decreases from a value of 120% of the OGE thrust to a value of about 115% of the OGE thrust in hover, at a skew angle of around 30 degrees. With a further increase in skew angle, the available thrust starts increasing and reaches a value of about 140% of the OGE thrust in hover at a skew angle of about 65 degrees.

Overall, these plots show that there is a substantial increase in the payload carrying capacity of this aircraft IGE, at constant power. This would mean that there can be a significant advantage to be gained by operating this aircraft IGE. However, because of the increase in upload at certain intermediate skew angles, the overall gain in payload is reduced somewhat from the hover values.

5.5 Pressure Measurements

Pressure measurements along the centerline of the fuselage bottom surface were also obtained in low speed forward flight for the same range of heights as in hover. The location of the pressure taps is shown again in Figure 5.27 for reference. The lengthwise variation of the pressure coefficient, C_{pDL} , along the fuselage centerline are presented for different skew angles at each height, in Figures 5.28 to 5.33. For the OGE case in Figure 5.28, the pressure at all the ports are near zero in hover and for a skew angle of 16° . At skew angles of 28° and 45° , the pressure under the front portion of the fuselage starts increasing, with the peak pressure located under

the front wing. With further increase in skew angle, the pressure over the entire length increases substantially, and the peak pressure under the front wing intensifies slightly.

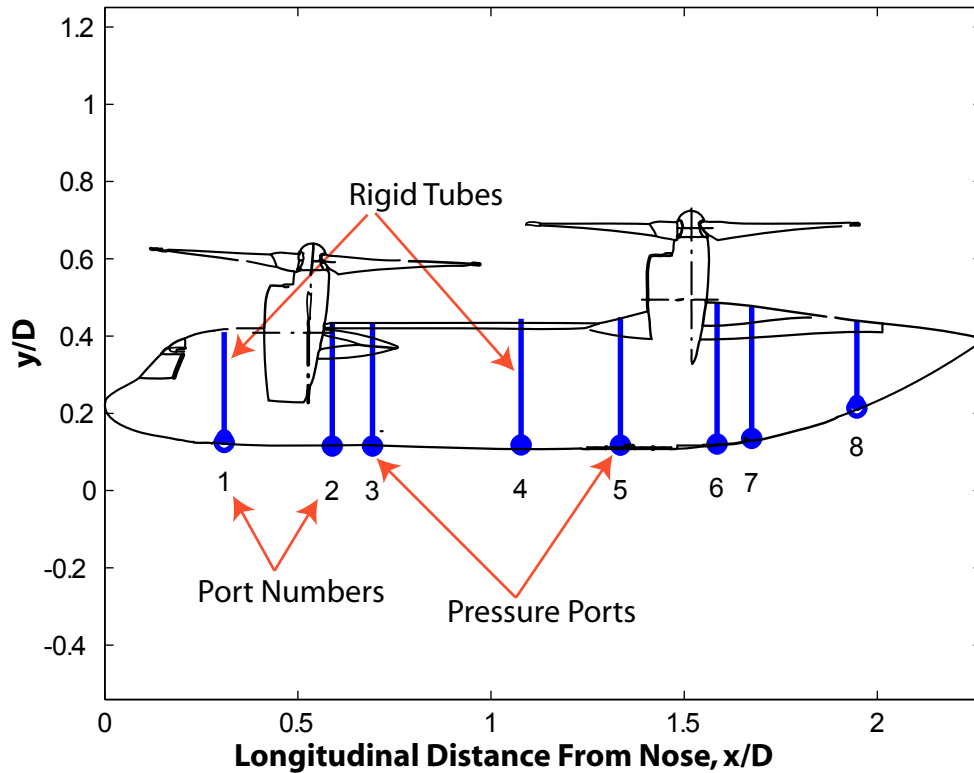


Figure 5.27: Location of the Pressure Taps

Figure 5.29 shows that for $z = 1.14$, in hover, there is a large peak in high pressure under the front wing. There is a smaller peak in high pressure under the rear wing also. From the pressure distribution, it can be seen that there is a substantial drop in pressure under the fuselage ahead of the rear wing, as the skew angle increases to 35° . In fact, the pressure at Port 1 becomes slightly negative. With further increase in skew angle, the pressure measured in the ports ahead of

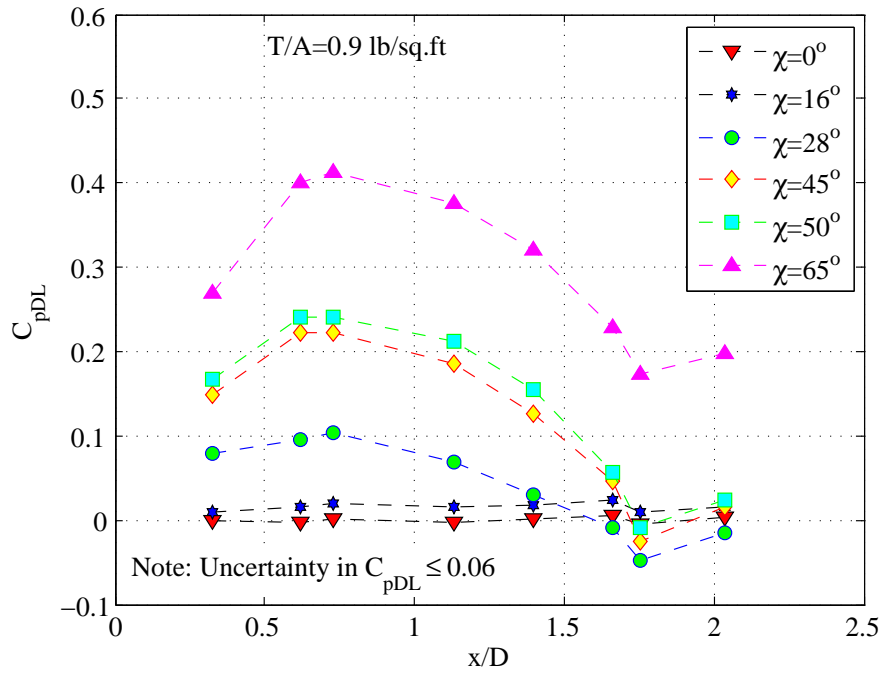


Figure 5.28: Pressure Distribution on the Centerline of the Fuselage Bottom Surface for $z=3.5$ (OGE)

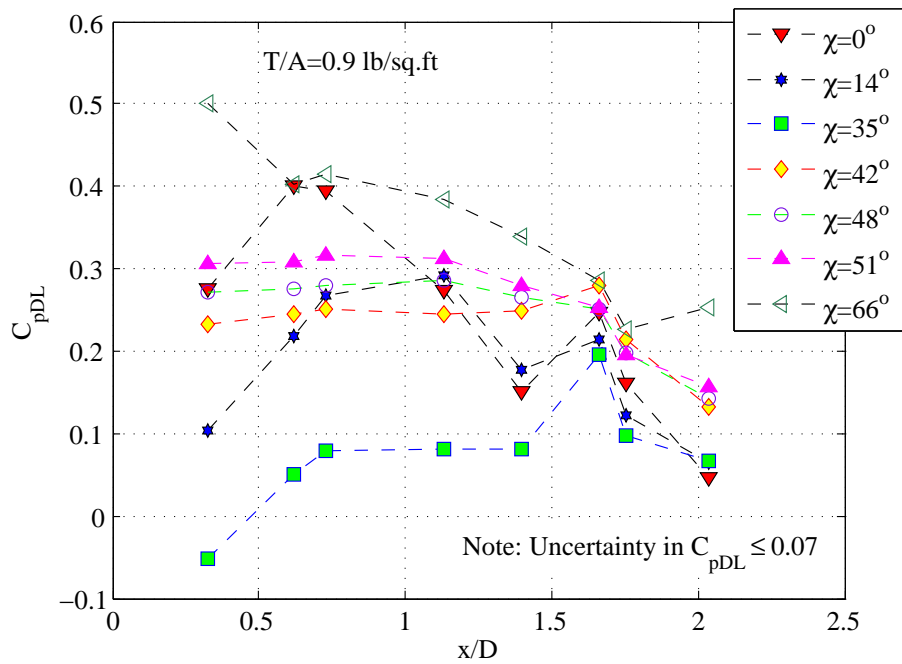


Figure 5.29: Pressure Distribution on the Centerline of the Fuselage Bottom Surface for $z=1.14$

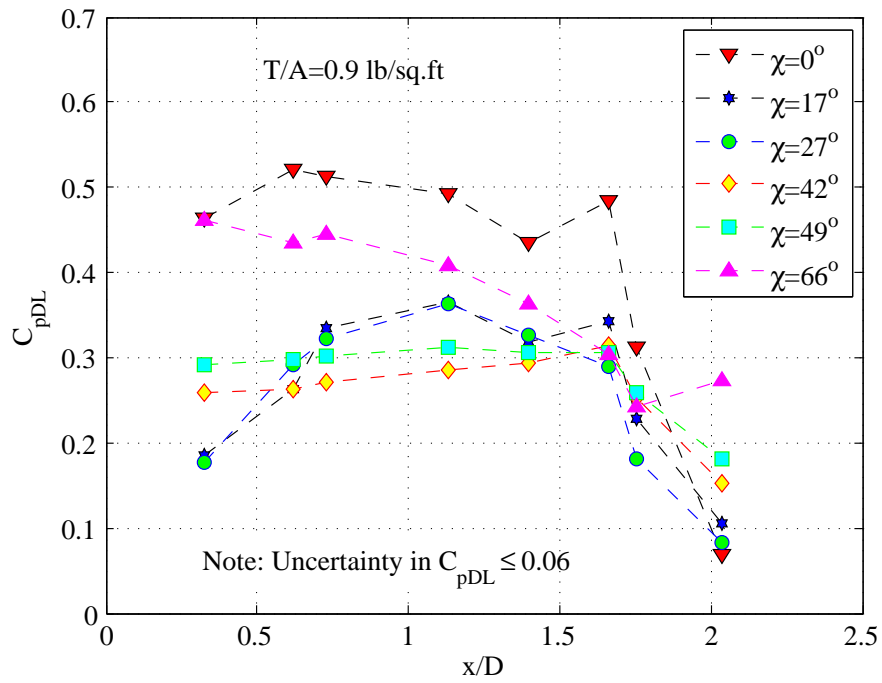


Figure 5.30: Pressure Distribution on the Centerline of the Fuselage Bottom Surface for $z=1.0$

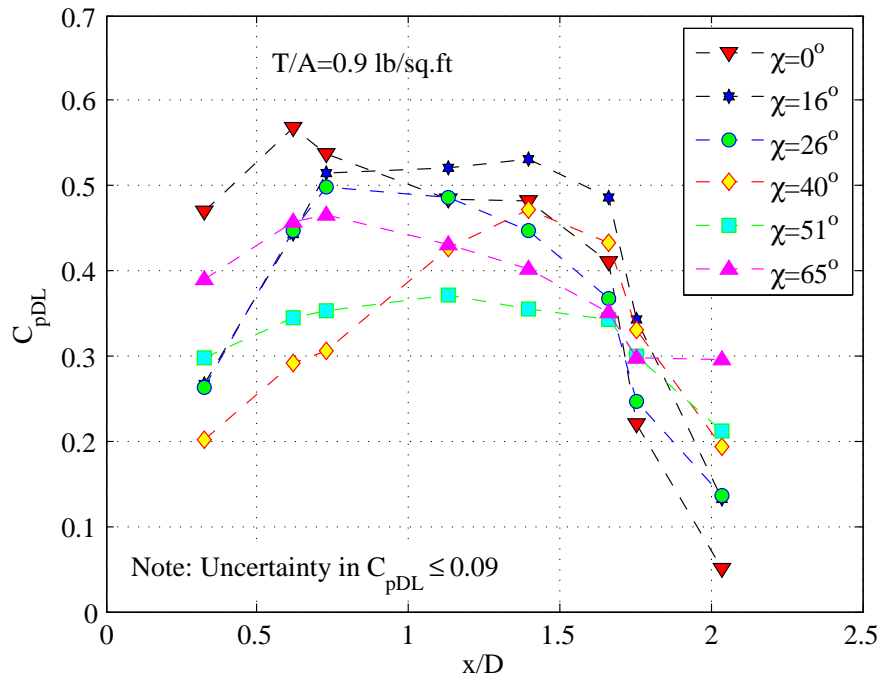


Figure 5.31: Pressure Distribution on the Centerline of the Fuselage Bottom Surface for $z=0.86$

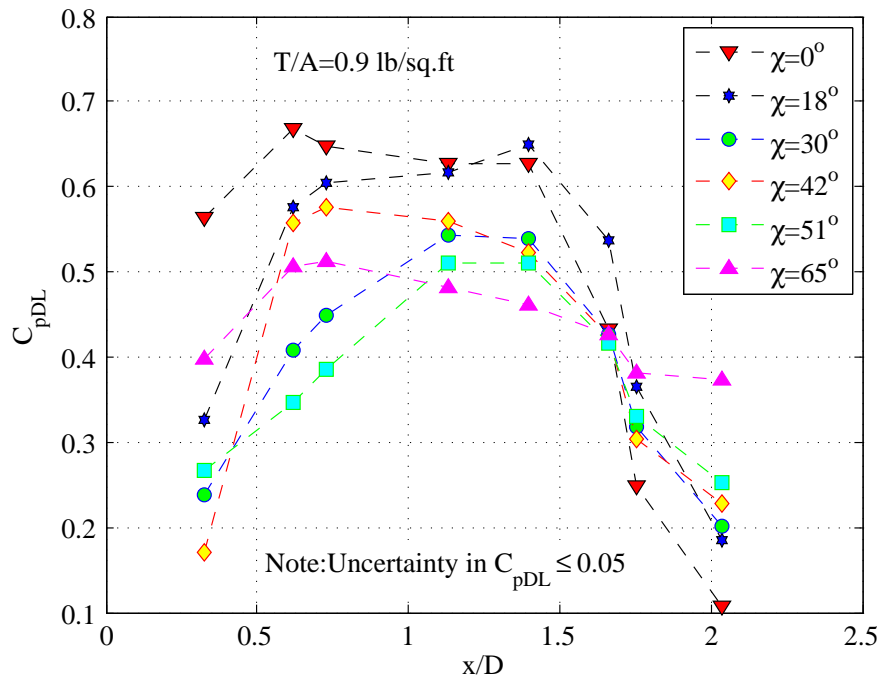


Figure 5.32: Pressure Distribution on the Centerline of the Fuselage Bottom Surface for $z=0.75$

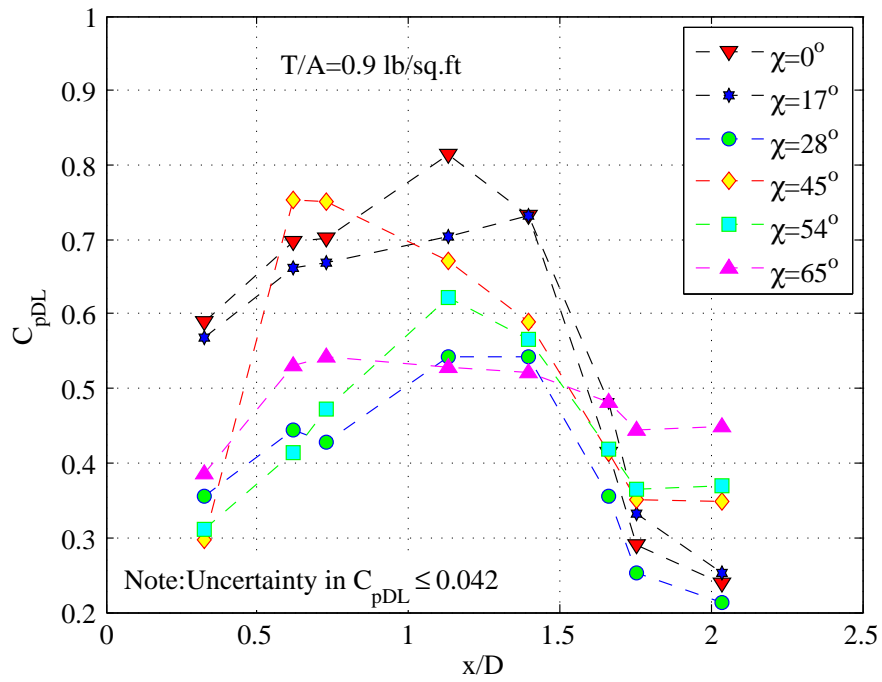


Figure 5.33: Pressure Distribution on the Centerline of the Fuselage Bottom Surface for $z=0.61$ (wheels on ground)

the rear wings increases and the distribution of pressures becomes nearly level, for skew angles of 42° to 51° . At the highest skew angle of 65° , the pressure increases under the front portion of the fuselage, with the peak pressure located at Port 1, which is ahead of the front wing.

A similar behavior is observed in Figure 5.30, for $z = 1.0$. This was the height at which the vehicle displayed a significant increase in download up to a skew angle of 30° and showed a substantial reduction at higher skew angles. The reason for this behavior could be that at low skew angles, the rotor wakes get washed backwards, thereby dissolving the high pressure regions under the front of the fuselage. In addition, a ground vortex might subject the nose of the fuselage to a downward flow, which might cause a further increase in download. The reason for the increase in pressure ahead of the front wing at higher skew angles is unclear.

From Figures 5.31 and 5.32, for $z=0.86$ and $z=0.75$, it can be seen that an increase in skew angle from hover does not dissolve the high pressure region under the front wing, but merely causes it to be washed back between the front rotors, until a skew angle of about 42° . For higher skew angles, the high pressure peak is washed away and is replaced by a more uniform distribution of pressure over the length. As the skew angle increases from 51° to 65° , there is an increase in magnitude of the pressures over the whole length.

The pressure distribution for the case where the wheels are on the ground is shown in 5.33. The peak in pressure in hover occurs between the front and the rear wings, in hover as discussed in Chapter 4. Increase in skew angle causes the pressure ahead of the rear wing to reduce. However, at a skew angle of 45° , a peculiar rise in

pressure under the front wing is observed. At higher speeds, the pressure reduces and the distribution becomes more flat over the length. This anomaly at $\chi = 45^\circ$ coincides with the reduction in upload observed at this height. This phenomenon is also noticed to a lesser degree for $z = 0.75$. This is probably caused by a ground vortex that gets convected backwards behind the rotor, under the vehicle. Further investigation using flow visualization is necessary to confirm this conjecture.

5.6 Comparison with CFD

The download to thrust ratios obtained from this experiment are compared with the CFD results from Gupta [12] in Figures 5.34 and 5.35. As was the case in hover, there is a good comparison between the experimental results and CFD results, OGE, up to a skew angle of about 45° . The CFD result at a skew angle of 64° shows a value of download that is about 4% higher than experimental results at similar skew angles.

The uploads predicted by the CFD study IGE are uniformly lower than the experimental measurements for the entire range of skew angles. However, the qualitative behavior of the upload vs. skew angle curve is quite similar for both studies. The differences in configuration between the airframe models used in the two studies, was mentioned in Chapter 4, and explained in Appendix B. The reasons for the lower value of upload predicted by the CFD were also discussed in Chapter 4 in Section 4.3.2. These reasons are also valid in forward flight. However, it was postulated in Sections 5.2 and 5.5 that one of the reasons for the decrease in upload,

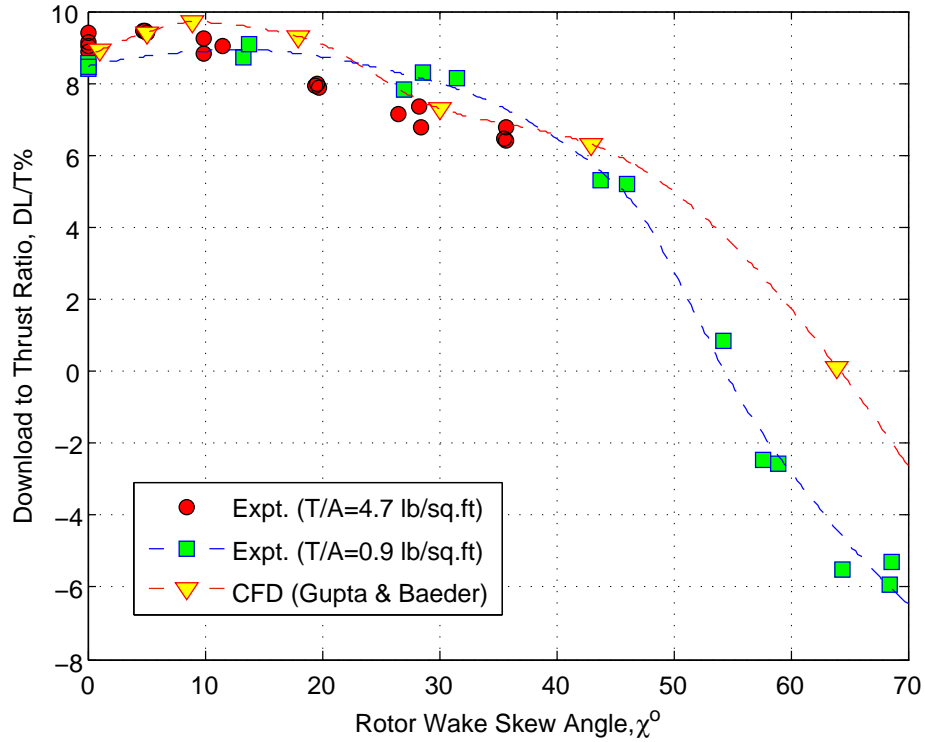


Figure 5.34: Comparison with CFD, OGE

IGE, could be a ground vortex formed under the vehicle. The behavior of this ground vortex is governed by the rotor wake skew angle and the height of the rotor above the ground[21]. As these geometric parameters would remain the same for both the CFD study and the experiment, so would the strength and behavior of the ground vortex at different skew angles. This would explain why the qualitative behavior of the uploads is similar for the two studies.

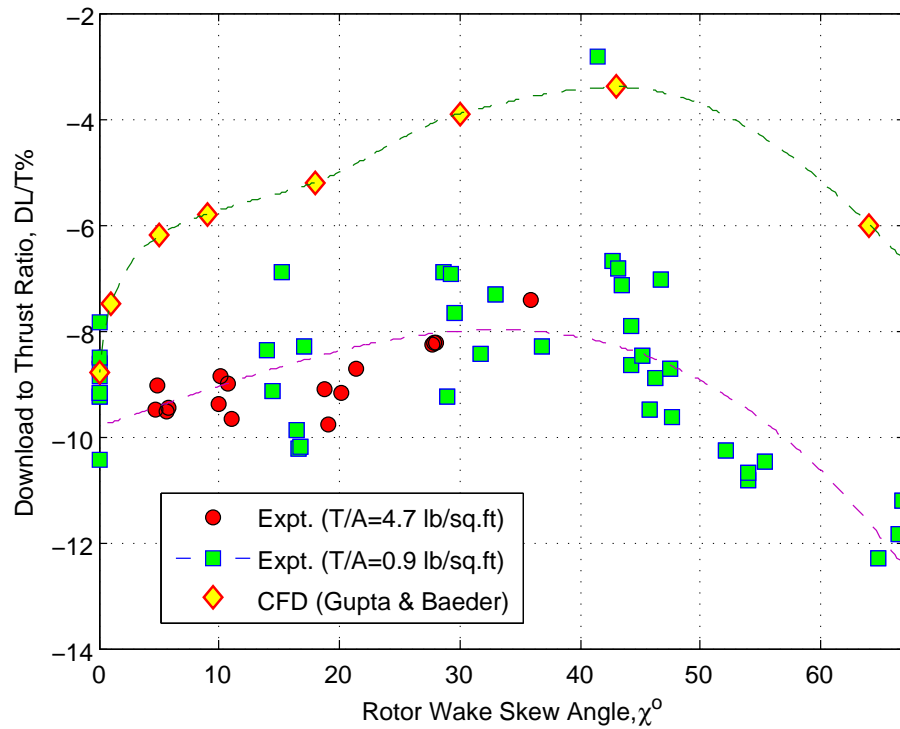


Figure 5.35: Comparison with CFD for $z=0.61$ (IGE, wheels on ground)

Chapter 6

Flow Visualization

The results from tuft flow visualization studies conducted on the QTR are presented in this chapter. It was mentioned in Chapter 2 that tufts are attached to the top and bottom surface of the fuselage and the wings and also on a rubber sheet placed on the ground. Tuft flow images of the top and bottom surface of the airframe and on the ground plane are presented for different heights above the ground, in hover. These are followed by results from low speed forward flight. These results are used to explain the features of the performance measurements that were presented in the previous chapters. Finally, these images are compared with flow images from previous experimental and CFD studies.

6.1 Camera Angles

Video images of the top surface of the fuselage and wings were obtained using a digital camcorder attached on the center of the mounting frame (Location A), as shown in Figure 6.1. A fish-eye lens was used on the camera to view the whole top surface without zooming out. To view the bottom surface, a mirror was placed on the ground underneath the vehicle. To view the reflection from the mirror, the

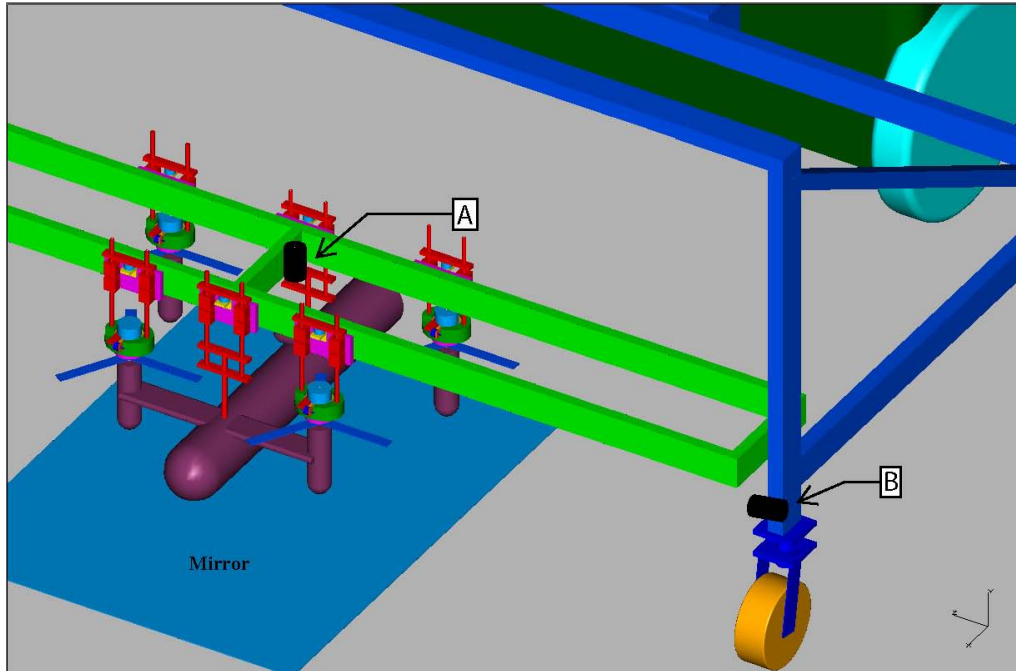


Figure 6.1: Camera Locations

camcorder was mounted on one of the legs of the support frame at Location B, shown in Figure 6.1. For recording the ground flow images, the camcorder is mounted on a tripod.

In forward flight, the camcorder moves with the vehicle, while recording the top and bottom surface images, as it is attached to the frame. For the ground flow images, the camera is mounted on a tripod located near the ground plane and the vehicle is moved over the ground plane at the required speeds.

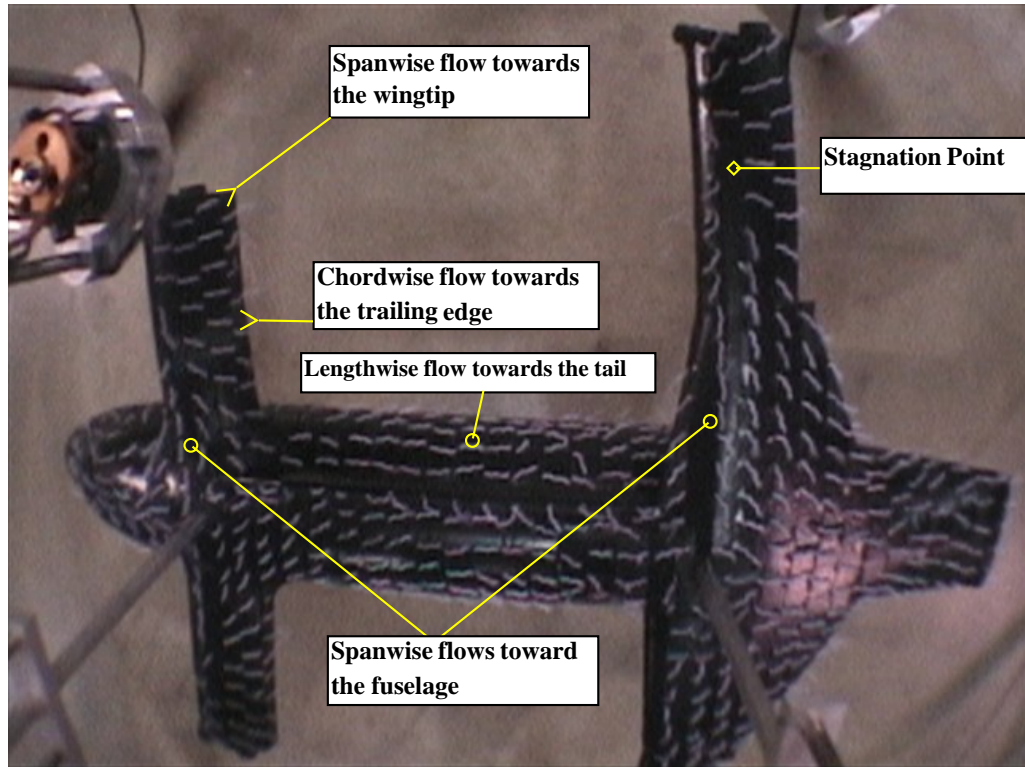
6.2 Hover

6.2.1 Top Surface

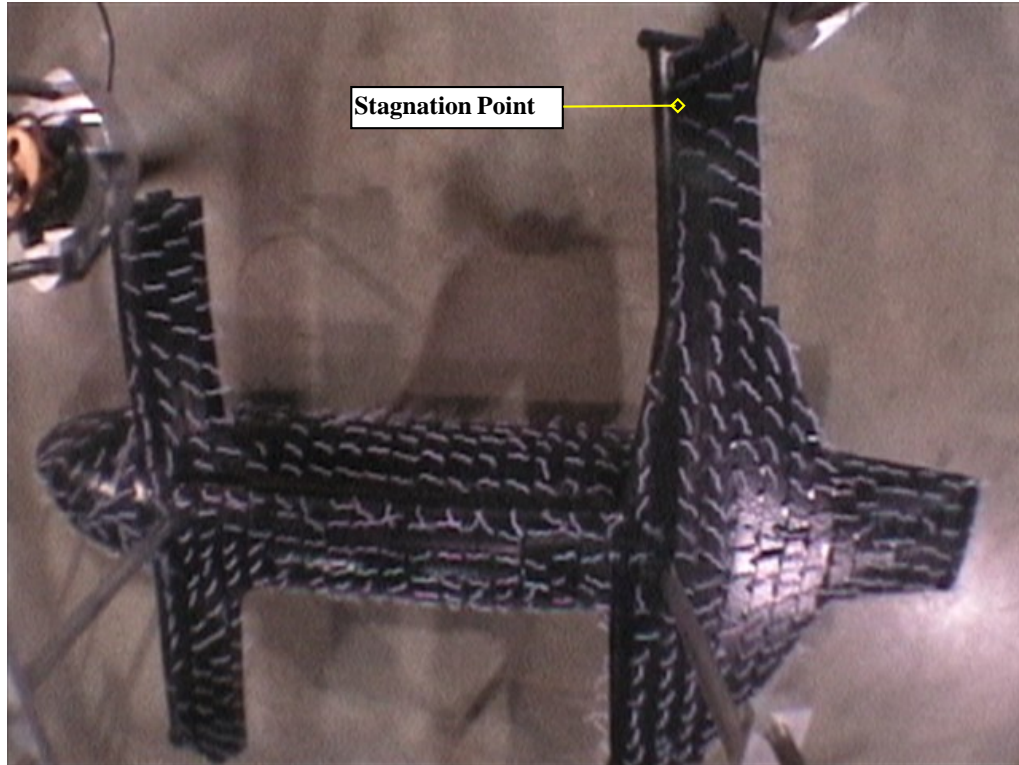
In hover, the flow images from the top surface of the fuselage and wings provide information about the fountain flows on the front and rear wings and the interaction of these flows over the fuselage. Also, the regions of chordwise and spanwise flow on the wings can be identified.

Figure 6.2 presents the tuft flow images of the top surface at two different heights above the ground, for a disk loading of 0.9 lb/sq.ft. For $z=1.5$, the flow is predominantly chordwise toward the outboard sections of the wings. At these sections, the chordwise flow near the leading edge of the wing is directed towards the leading edge, whereas the flow behind the quarter chord of the wing is directed towards the trailing edge. Closer to the wing root, there are spanwise flows towards the centerline of the fuselage on the top surfaces of the both the front and rear wings. This confirms the previous results that found fountain flows on the front and rear wings. These spanwise flows are concentrated mainly towards the leading edge of the wings. When the flows from the front rotors meet at the center-line of the front wing, they get turned upwards to form a fountain flow. This flow is also turned in a lengthwise direction along the fuselage. The presence of the cross-shafting on the fuselage skews the flow towards the starboard direction when it reaches the rear wing. Near the tips of both the front and the rear wings, the flow near the trailing edge gets deflected in a spanwise direction towards the wing tip.

Figure 6.2 (b) show that there is not much of a change in the flow on the

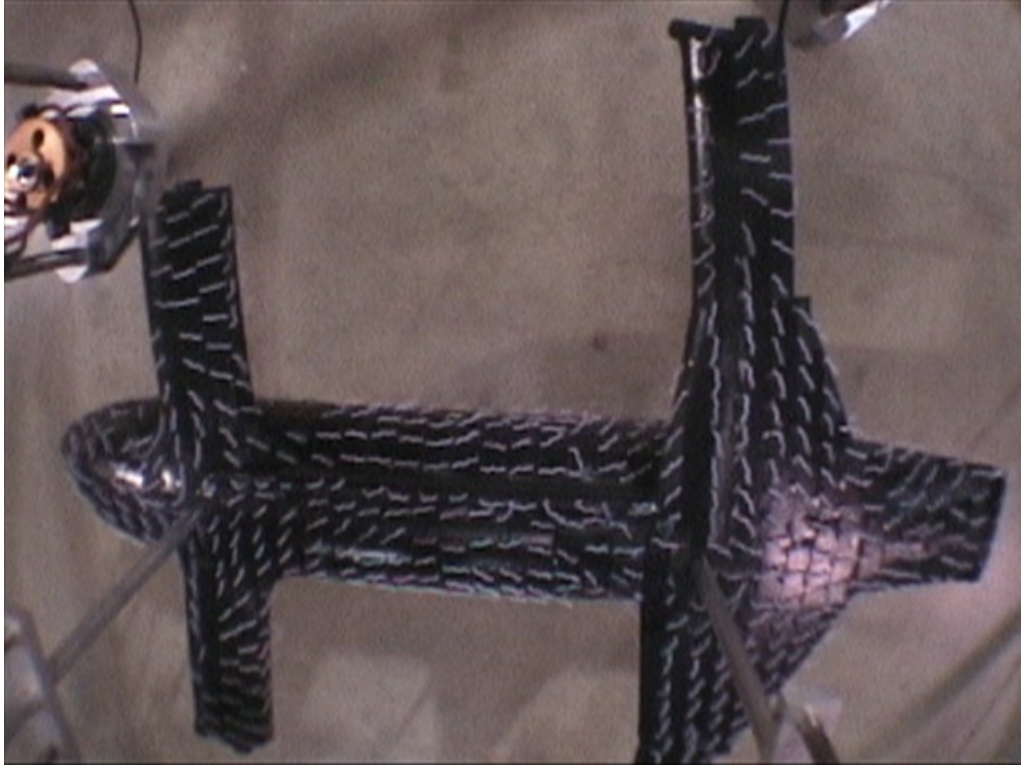


(a) $z=1.5$

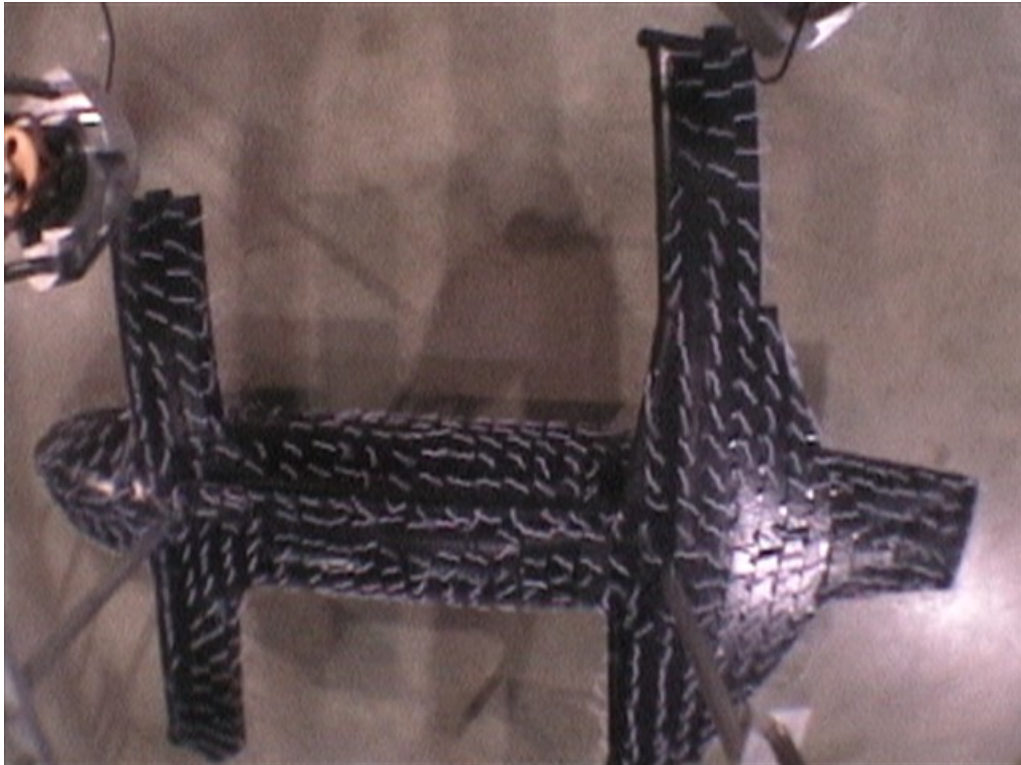


(b) $z=0.61$, wheels on ground

Figure 6.2: Tuft Flow Visualization of Top Surface for $T/A=0.9$ lb/sq.ft.



(a) $z=1.5$



(b) $z=0.61$, wheels on ground

Figure 6.3: Tuft Flow Visualization of Top Surface for $T/A=4.7$ lb/sq.ft.

top surface in hover, IGE, except that the stagnation point on the top surfaces of the wings moves slightly inboard. The video showed that the flow was a lot more unsteady because of recirculation from the ground.

Figure 6.3 presents the top surface images at the same heights, for a disk loading of 4.7 lb/sq.ft. The surface flow features at this higher disk loading are identical to the previously discussed images. However, the flow was found to be a lot more unsteady because of the higher velocities.

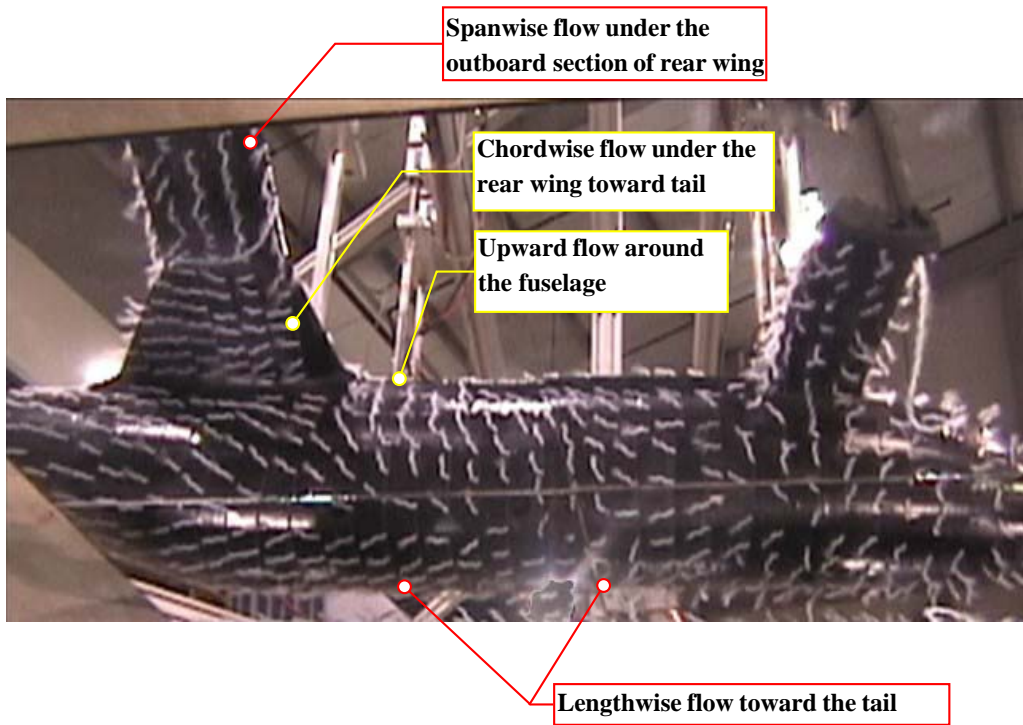
6.2.2 Bottom Surface

Tuft flow images from the bottom surface of the airframe and the wings are shown in Figure 6.4, for rotor disk loading of 0.9 lb/sq.ft. For the case where the wheels are on the ground, shown in Figure 6.4 (b), the flow on the bottom surface of the fuselage, under the front wing is relatively stagnant. Behind the front wing, the flow is predominantly directed to the rear of the vehicle. The reason for this could be because the front rotors are closer together and to the ground than the rear rotors. As a result, the pressure measured at the bottom of the fuselage under the front wing was found to be greater than at the rear of the fuselage. Therefore, the flow moves from the region of higher pressure formed under the front wing to the relatively lower pressure region under the rear wing.

It can also be noted that there is an upward flow around the fuselage just ahead of the rear wing. This could be a result of the the interaction between the wakes from the rear rotors with the wakes from the front rotors. These wakes meet



(a) $z=1.5$

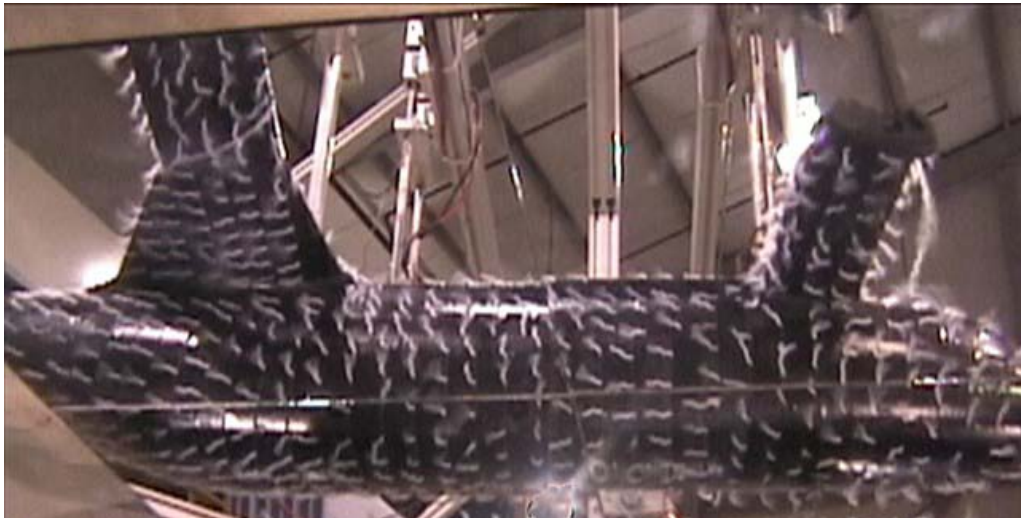


(b) $z=0.61$, wheels on ground

Figure 6.4: Tuft Flow Visualization of Bottom Surface for $T/A=0.9$ lb/sq.ft



(a) $z=1.5$



(b) $z=0.61$, wheels on ground

Figure 6.5: Tuft Flow Visualization of Bottom Surface for $T/A=4.7$ lb/sq.ft.

under the vehicle, just ahead of the rear wing and get turned in an upward direction as there is nowhere else for the flow to escape. A portion of upward flow around the fuselage can also be seen to be directed towards the tail. This flow impinges on the bottom surface of the inboard sections of the rear wing, which might cause an upload in those portions of the rear wing.

The surface flow features for $z = 1.5$, shown in Figure 6.4 (a), are similar to the case where wheels are on the ground. However, the intensity of the upward flow ahead of the rear wing was noted to be lower, as the height above the ground was greater.

Figure 6.5 shows the same images, but for a disk loading of 4.7 lb/sq.ft. The surface flow features for this disk loading were similar to those observed for the lower disk loading.

6.2.3 Ground Flow Images

Figure 6.6 shows the tuft flow image for the ground plane for the case where the wheels are on the ground at a disk loading of 0.9 lb/sq.ft. Under the front wing, there are spanwise flows along the ground, directed towards the centerline of the fuselage.

The ground plane tuft flow images at a disk loading of 4.7 lb/sq.ft are shown in Figure 6.7. These images show that the rotor wakes get deflected along the ground away from the hubs of the four rotors. Ahead of the front wing, the front rotor wakes get pushed forward ahead of the aircraft along the ground. Similarly, behind the

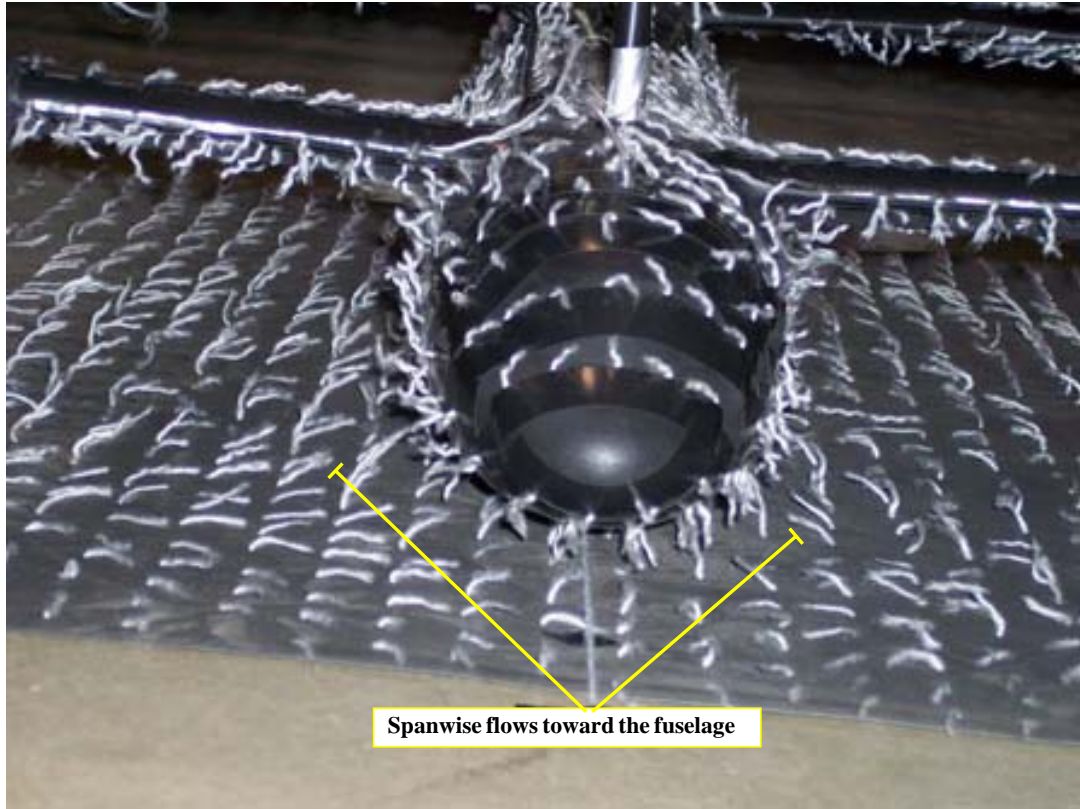
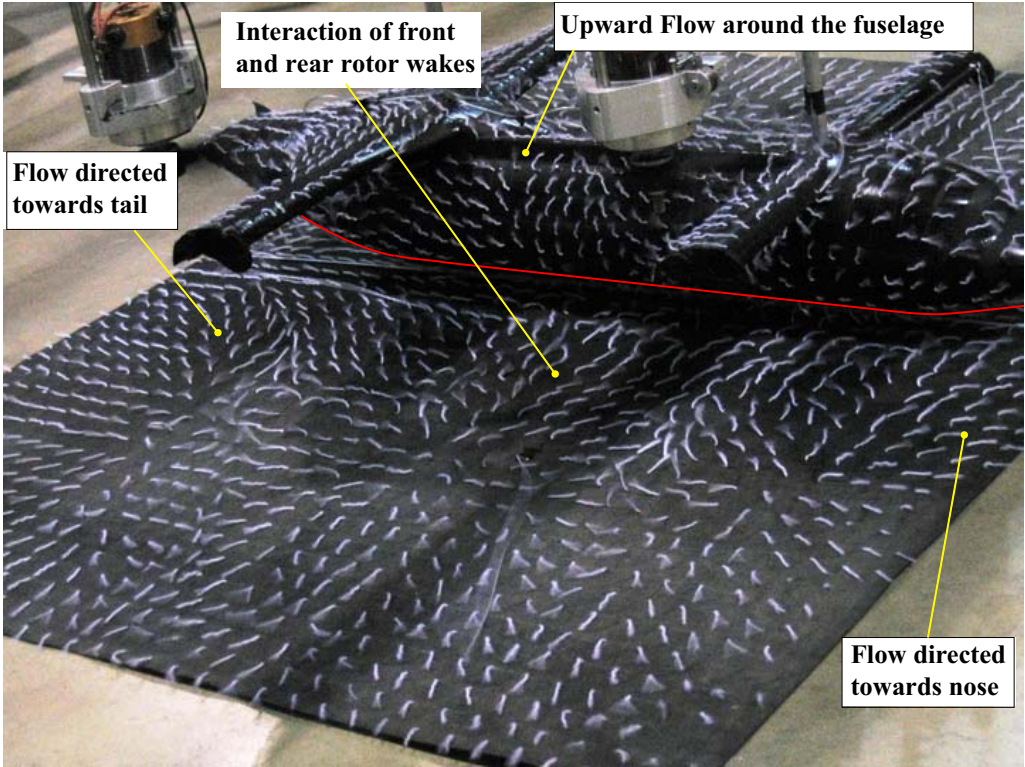


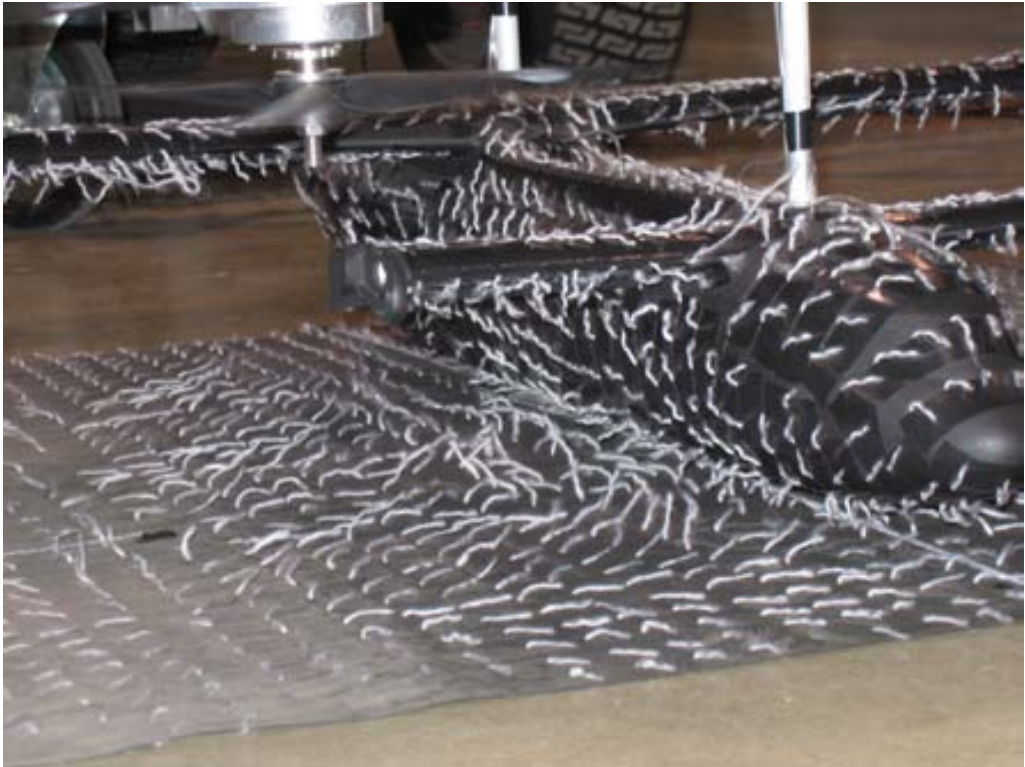
Figure 6.6: Tuft Flow Image of the Ground Plane at $z=0.61$, $T/A=0.9$ lb/sq.ft

rear wing, the wakes from the rear rotors meet and get turned behind the vehicle. Between the front and the rear wings, the flows from the front and rear rotor wakes meet and get fenced in, resulting in a high pressure region, which causes an upload on the vehicle. A portion of this flow gets turned upwards in a flow around the fuselage.

Figure 6.8 shows the ground tuft image for $z=1.14$, at a disk loading of 0.9 lb/sq.ft. The flow on the ground plane is similar to the height where the wheels are on the ground. The flows along the ground are clearly seen to be directed to the centerline of the fuselage. However, the vehicle is further from the ground and therefore, the intensity of the upward flow is lesser.



(a)



(b)

Figure 6.7: Tuft Flow Images of the Ground Plane at $z=0.61$, $T/A=4.7$ lb/sq.ft



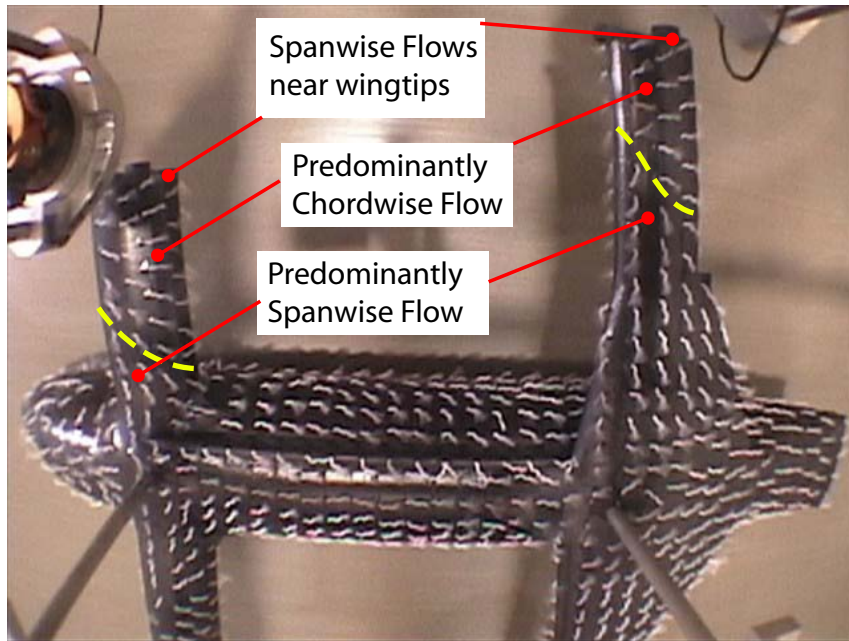
Figure 6.8: Tuft Flow Image of the Ground Plane at $z=1.14$, $T/A=0.9$ lb/sq.ft

6.3 Low Speed Forward Flight

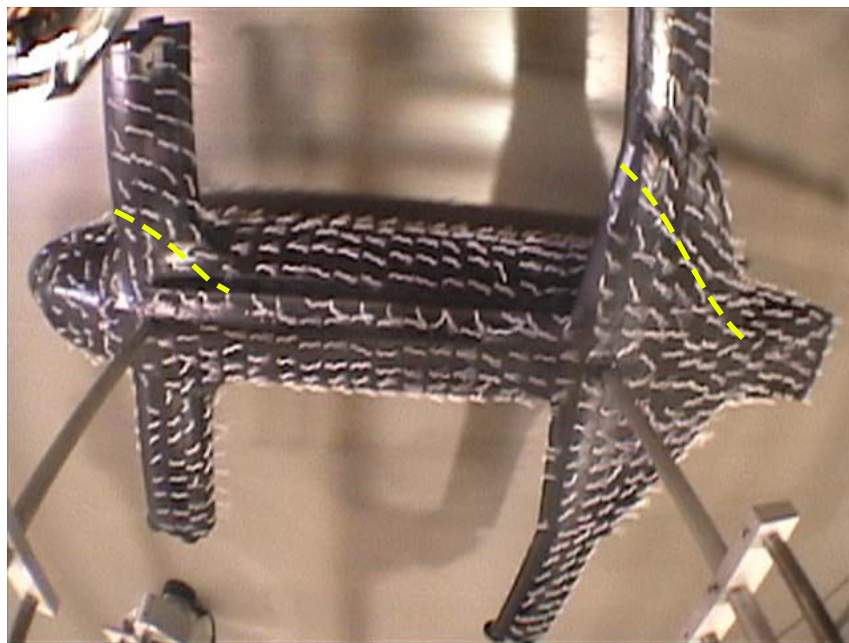
6.3.1 Top Surface Flow Patterns

Figure 6.9 shows the tuft flow patterns for the top surface of the airframe for the case where the wheels are on the ground, at two different skew angles. For a skew angle of 17° , the surface flow patterns are very similar to hover. As in hover, there are spanwise flows near the tips of both the front and rear wings, directed towards the wing tip. The flow is predominantly chordwise on the outboard sections of the wings and mostly spanwise closer to the inboard sections. The dotted yellow line shows the demarcation between the regions of spanwise and chordwise flow.

Figure 6.9 (b) shows the top surface flow for a skew angle of 67° . At this higher

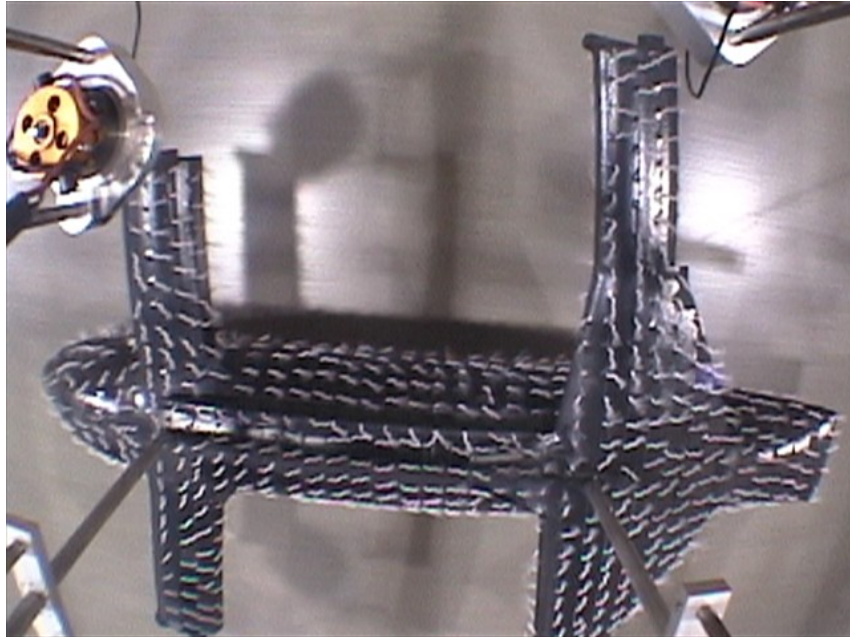


(a) $\chi=17^\circ$

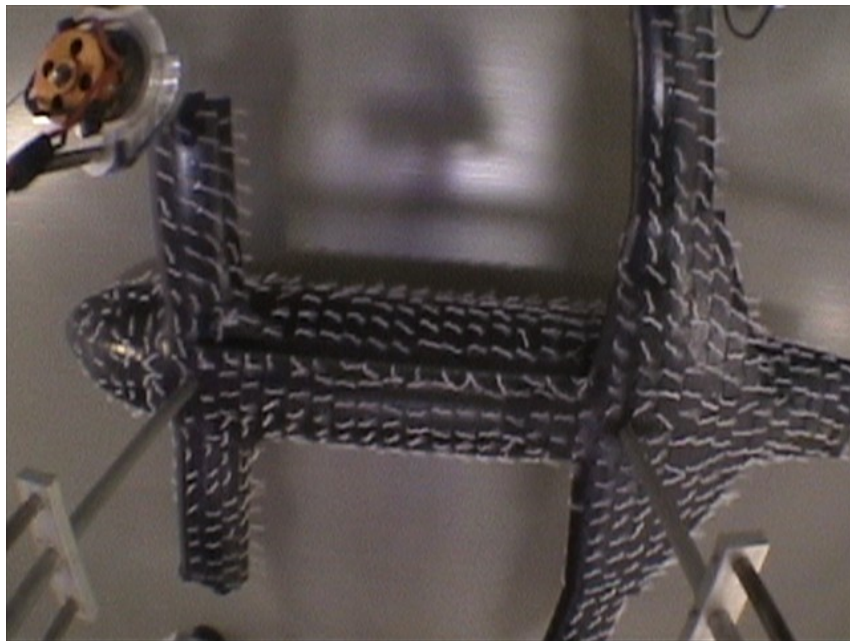


(b) $\chi=67^\circ$

Figure 6.9: Tuft Flow Visualization of Top Surface in Forward Flight ($z=0.61$)



(a) $\chi=17^\circ$



(b) $\chi=69^\circ$

Figure 6.10: Tuft Flow Visualization of Top Surface in Forward Flight ($z=0.75$)

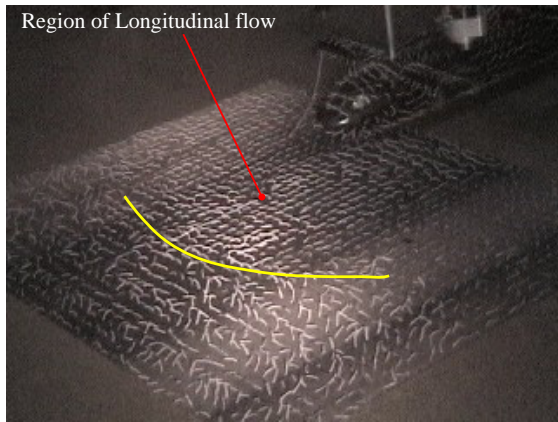
skew angle, the spanwise flow near the wingtips disappears and the flow becomes strictly chordwise. Except for a small region near the leading edges of the roots of the wings, the the flow over the entire wing span becomes predominantly chordwise. This implies that the the rotor wakes are mostly washed off the wings. This is possibly one of the causes for the reduction in download/increase in upload at the higher skew angles.

The top surface images were also obtained at different skew angles for $z=0.75$. These are shown in Figure 6.10. The behavior of the flow features is observed to be similar to the lower height.

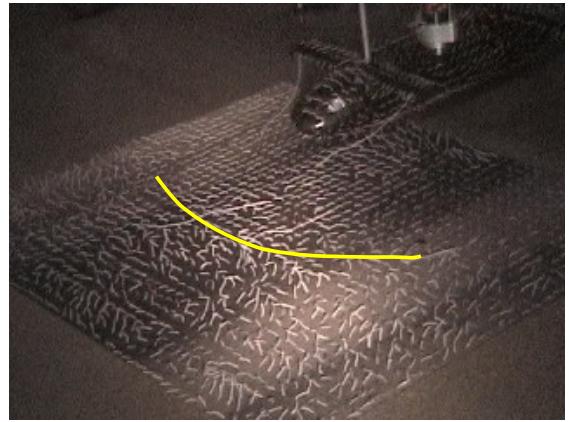
6.3.2 Ground Plane

The behavior of the helicopter rotor wakes at low forward speeds IGE, was discussed in Chapter 1 in Section 1.4.1.2. Based on the work of Curtiss, et al.[21], the formation of a ground vortex at certain speeds was illustrated in Figure 1.9. For a QTR, ground vortices are likely to be formed at the leading edge of the wakes of the front rotors and possibly a portion of the rear rotor wakes. The formation and interaction of these vortices could be responsible for some of the changes in download and pressure noticed at certain forward speeds.

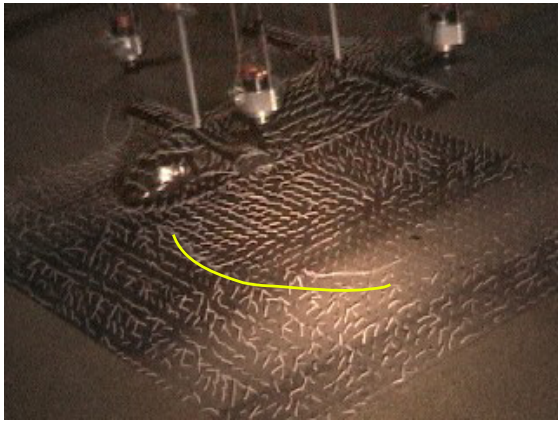
Flow features on the ground in forward flight were studied by recording the motion of the aircraft over the tufted ground plane at different speeds. The flow images at different speeds, for the case where the wheels are on the ground, are presented in Figure 6.11. In hover, it was found that the wakes from the front rotors



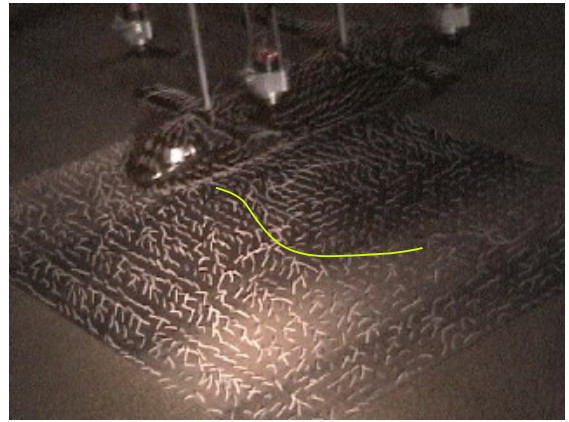
(a) $\chi=17^\circ$



(b) $\chi=29^\circ$

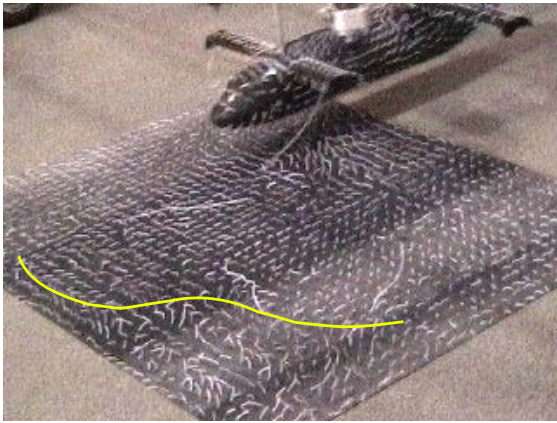


(c) $\chi=43^\circ$

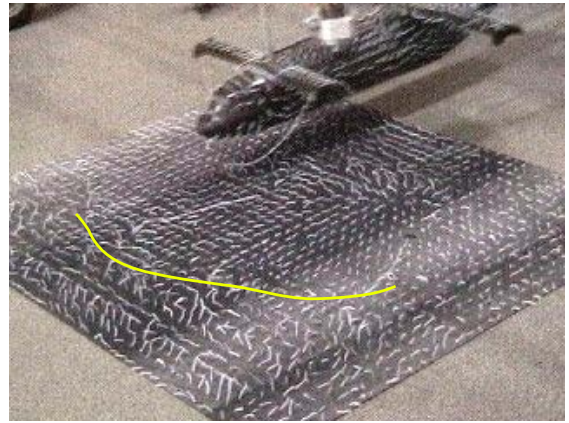


(d) $\chi=54^\circ$

Figure 6.11: Tuft Flow Visualization of the Ground Plane in Forward Flight
($z=0.61$)



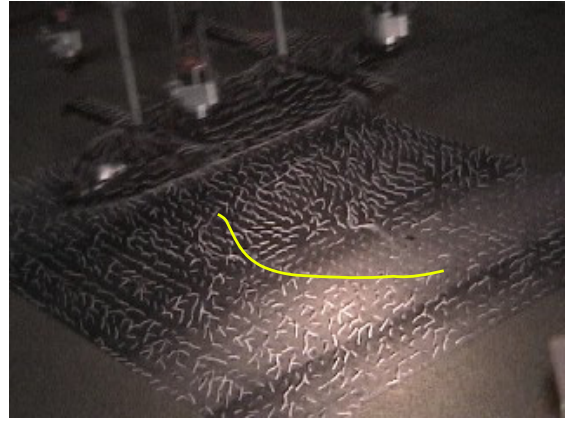
(a) $\chi=16^\circ$



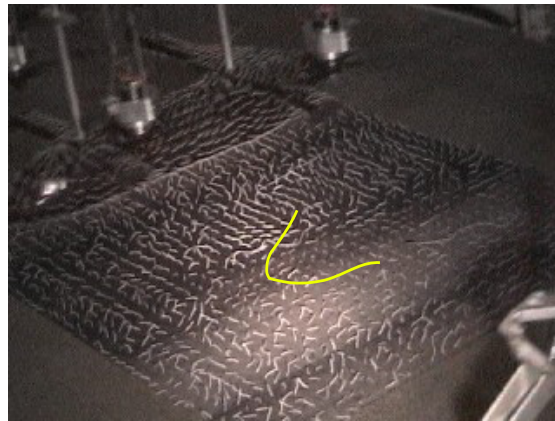
(b) $\chi=26^\circ$



(c) $\chi=44^\circ$

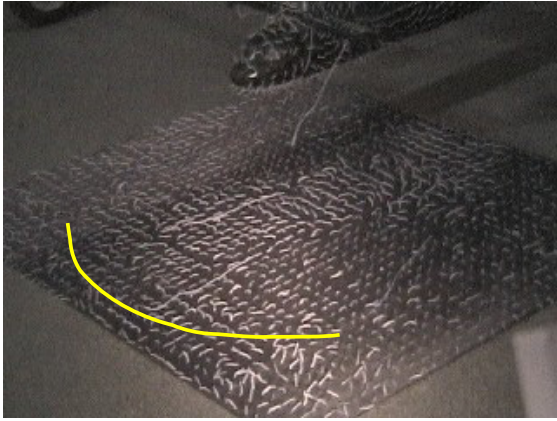


(d) $\chi=54^\circ$

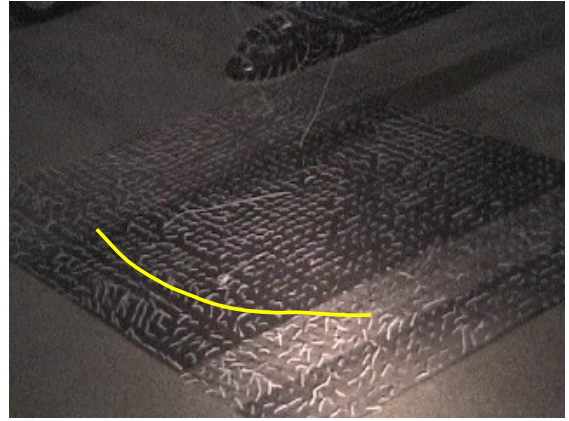


(e) $\chi=63^\circ$

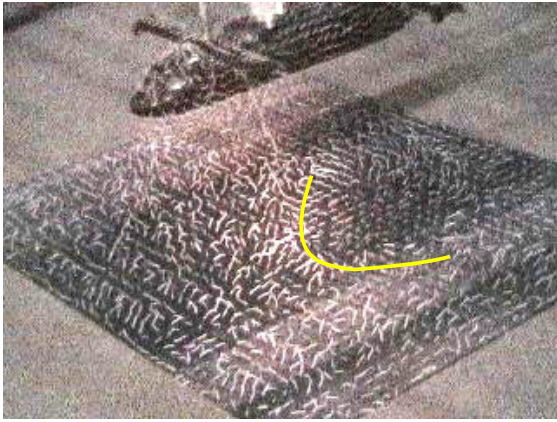
Figure 6.12: Tuft Flow Visualization of the Ground Plane in Forward Flight
($z=0.75$)



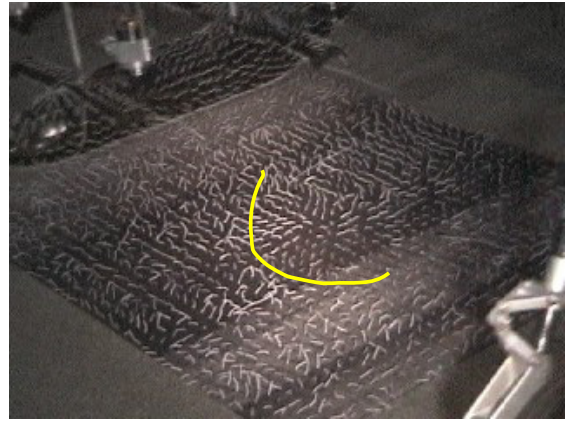
(a) $\chi=17^\circ$



(b) $\chi=24^\circ$



(c) $\chi=43^\circ$



(d) $\chi=54^\circ$

Figure 6.13: Tuft Flow Visualization of the Ground Plane in Forward Flight
($z=1.0$)

were redirected by the ground, in a longitudinal direction ahead of the vehicle. At a skew angle of 17° , this longitudinal flow ahead of the aircraft is found to start slightly ahead of the front wing and extends about 2 rotor diameters ahead of the fuselage nose. A yellow line has been drawn on the images to help identify this longitudinal flow region. The region behind the yellow line indicates the region of longitudinal flow. Ahead of the yellow line, the flow is quiescent. It can be seen that the longitudinal flow region gets convected backwards and shrinks, as the skew angle increases. At a skew angle of 29° , the longitudinal flow was found to start slightly behind the front wing. The extent of this longitudinal flow was found to be reduced to about 1 rotor diameter ahead of the nose. At a skew angle of 43° , this flow starts just slightly ahead of the rear wing and ends just under the front wing. At a skew angle of 54° , this flow begins under the rear wing and terminates about half way between the front and rear rotors.

The yellow line is likely to correspond to the location of a ground vortex formed along the ground. It is possible to relate this behavior to the flow regimes identified by Curtiss, et al., [21] in Figure 1.9. This would suggest that there is a region of recirculation that is formed ahead of the QTR at low speeds, for a skew angle of 17° . At a skew angle of 29° , this recirculation could develop into a weak region of vorticity ahead of the rotors. At a skew angle of 43° , this vorticity possibly tightens into a ground vortex that is convected back and located under the front wing. Pressure measurements for the same height, shown in Figure 5.33 in Chapter 5 indicate a sharp increase in pressure under the front wing at this skew angle. At a skew angle of 54° , this vortex is convected behind the front rotor and reduces in

scale. This also agrees with the measured pressure peak, which gets convected back for this skew angle.

Similar results are obtained for $z = 0.75$, shown in Figure 6.12. For this height, a skew angle of 63° was also studied. At this skew angle, the longitudinal flow along the ground seems to have shrunk to a small region under the rear wing. This would mean that the ground vortex would have almost completely vanished.

Figure 6.13 shows ground flow images for $z = 1.0$. This was the height which displayed the largest increase in download with an increase in forward speed. Figure 5.3 shows that the peak in download occurs at a skew angle of 30° . While results are not available at that skew angle, the flow image at 43° show that the longitudinal flow has been convected completely behind the front wing. This agrees with the download results, which show that the peak download occurs earlier than for the lower heights. Also, the pressure distribution under the front portion of the fuselage is essentially constant, for 43° , which agrees with the tuft flow images.

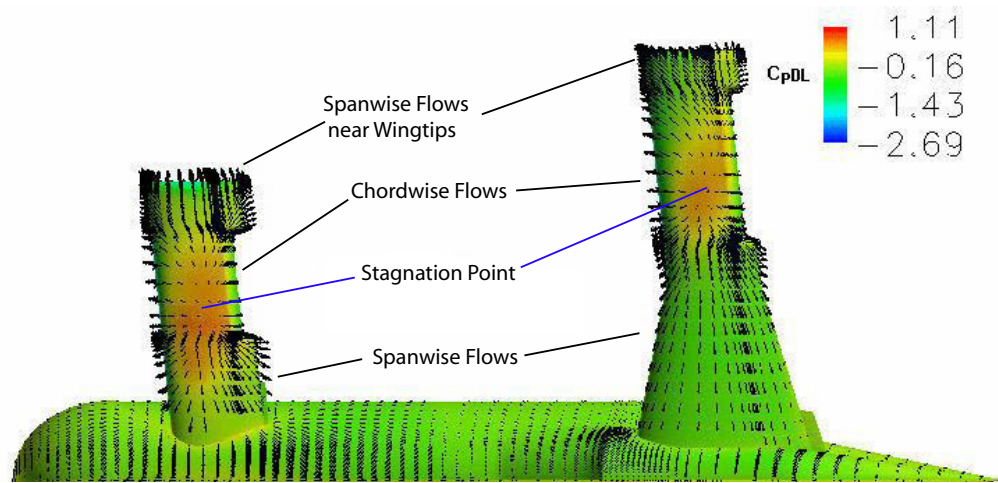
6.4 Comparison with CFD

6.4.1 Hover

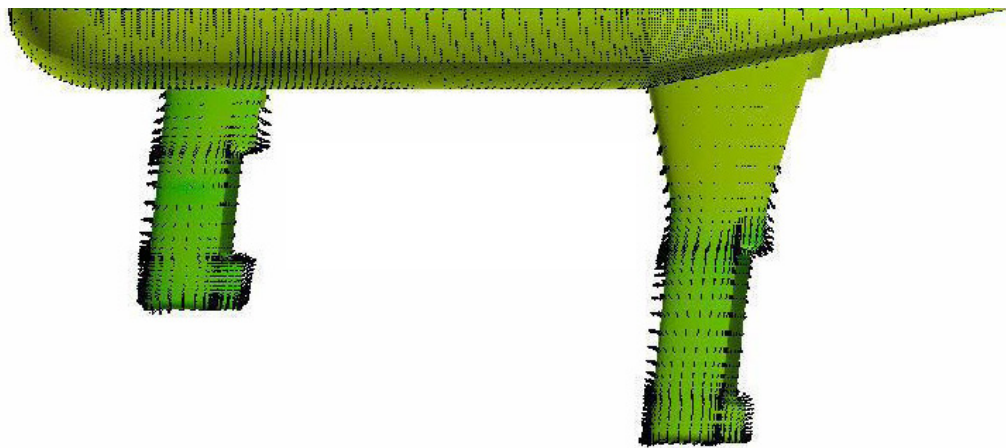
Gupta[12] presented surface flow vectors calculated from CFD, on the top and the bottom surfaces of the fuselage and wings, OGE and IGE. These are shown in Figures 6.14 and 6.15, respectively. In this section, these images are compared with the tuft flow visualization images obtained in hover. The top surface flow vectors,

shown in the top half of Figure 6.14, show regions of high pressure on the wings underneath the tips of the rotors. The surface flow features noted on the top of the wings are very similar to the tuft flow images that were presented in Figure 6.2. Predominantly chordwise flow is present on the outboard sections of the wings and predominantly spanwise flow is present on the inboard sections of the wing. A spanwise flow towards the wing tip can be noted near the trailing edge of the wing tip, as in the experiment. The flow over the bottom surface, shown in the the bottom half of the figure, shows that the flow is quite quiescent.

The CFD surface flow vectors from Gupta[12] IGE, when wheels are on the ground, are shown in Figure 6.15. The flow vectors on the top surface look quite similar to the OGE case, except that the intensity of the high pressures on the wings are greater. Also, an upward flow around the fuselage is noted, especially just ahead of the rear wing, as for the experiment. On the bottom surface of the fuselage, the flow is mostly directed longitudinally. Ahead of the front wing, the flow is directed towards the nose and behind the front wing, the flow is directed towards the tail. There is a high pressure region located on the bottom surface of the fuselage, underneath the front wing. There are also high pressure regions on the bottom surfaces of the front wing and the inboard sections of the rear wing. These flow features are all very similar to the experimentally recorded images.

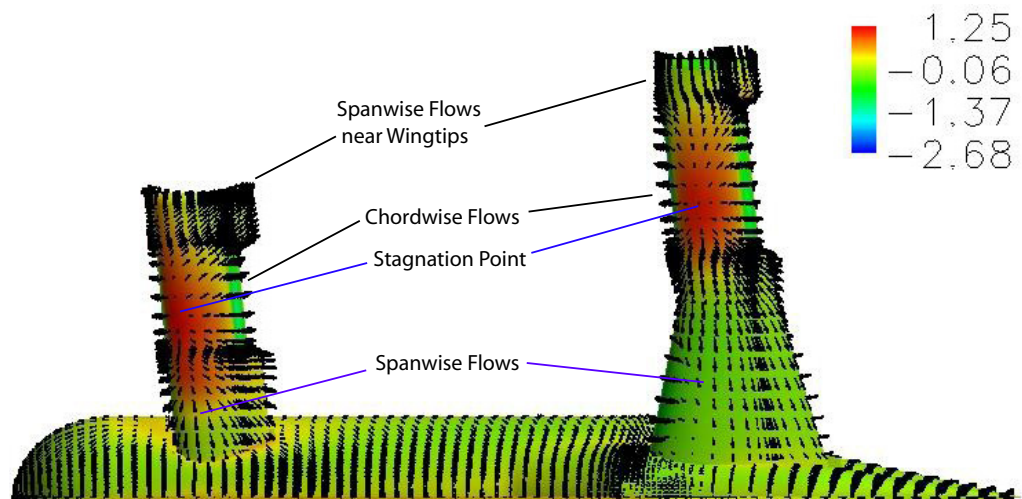


(a) Top Surface

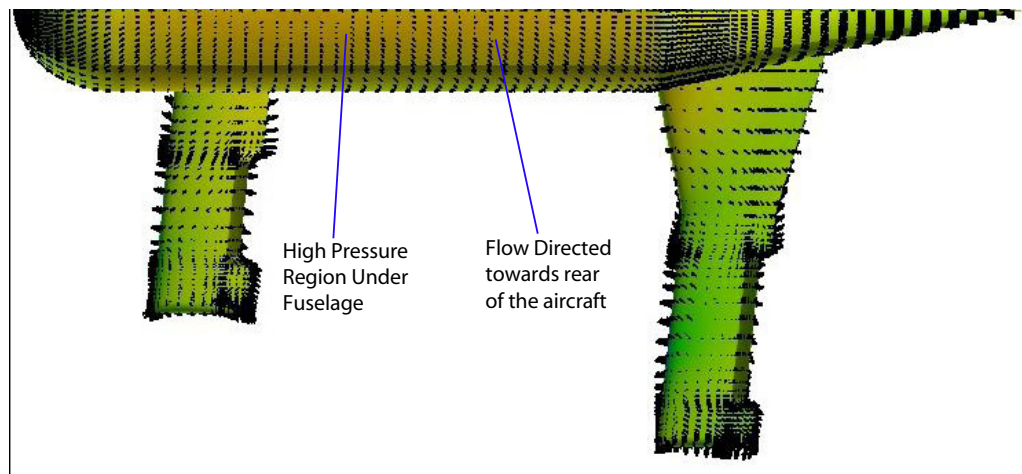


(b) Bottom Surface

Figure 6.14: CFD Surface velocity vectors in hover (OGE), from Gupta[12]

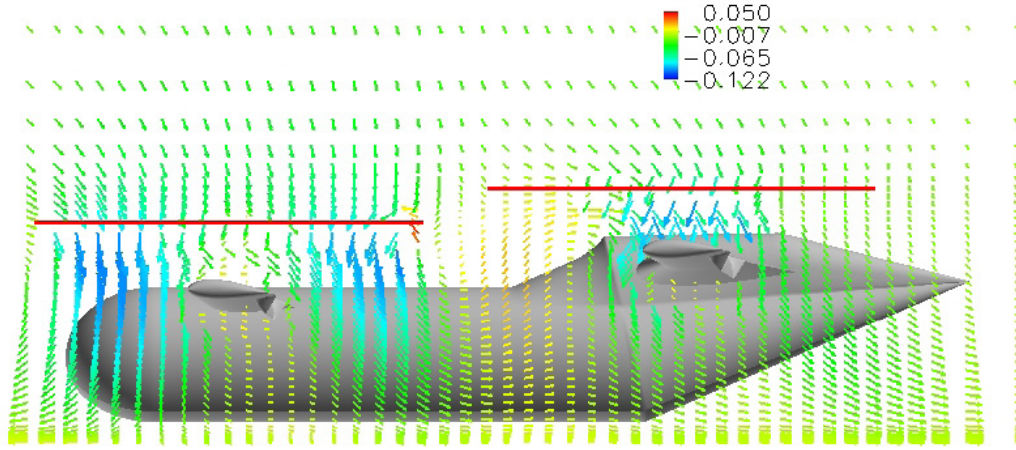


(a) Top Surface

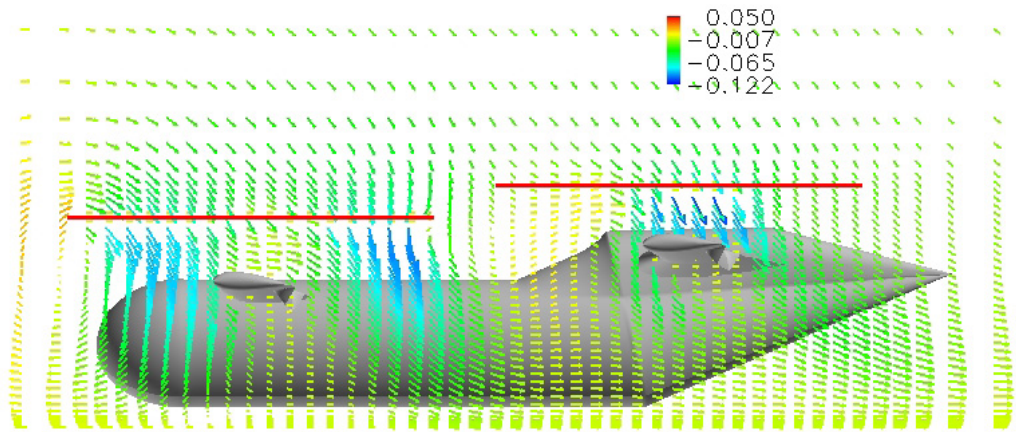


(b) Bottom Surface

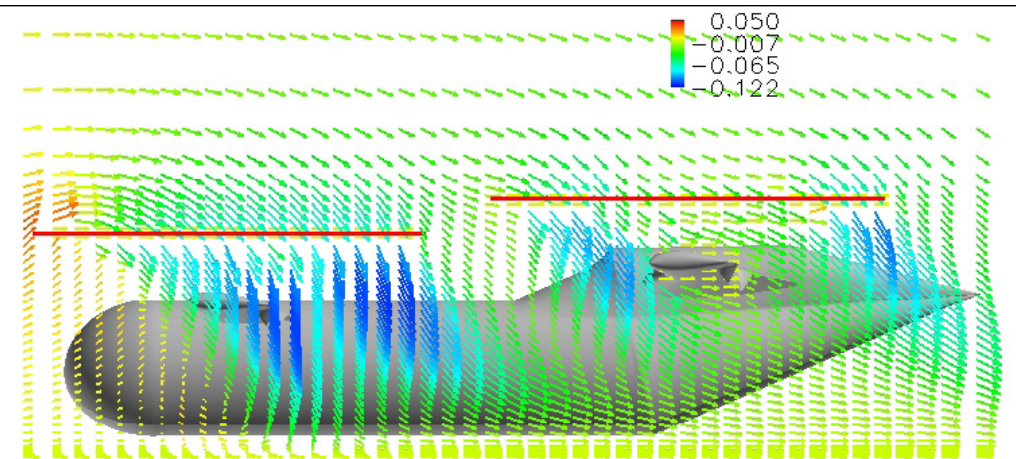
Figure 6.15: CFD Surface Velocity vectors in hover (wheels on ground, $z=0.61$), from Gupta[12]



(a) $\chi=1^\circ$

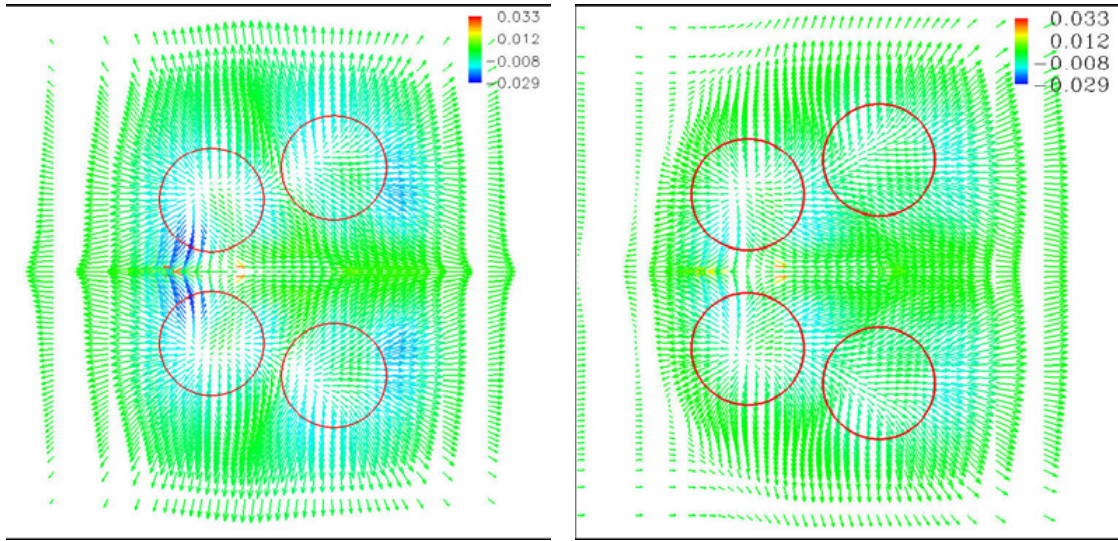


(b) $\chi=18^\circ$



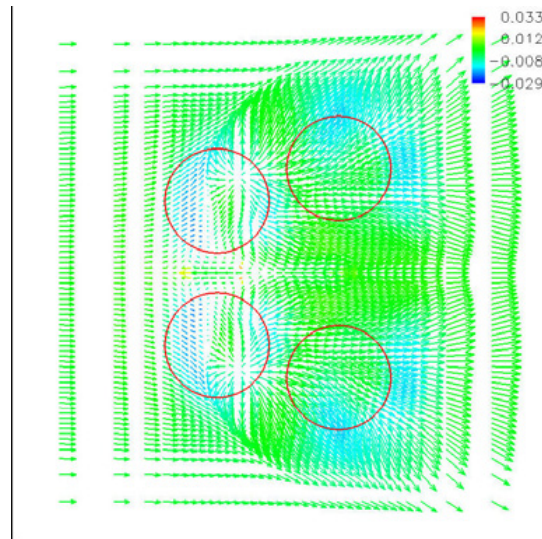
(c) $\chi=43^\circ$

Figure 6.16: CFD Velocity vectors at a vertical plane through the front rotor hub (wheels on ground, $z=0.61$), from Gupta[12]



(a) $\chi=1^\circ$

(b) $\chi=18^\circ$



(c) $\chi=43^\circ$

Figure 6.17: CFD Velocity vectors on a plane 2 feet above the ground in forward flight (wheels on ground, $z=0.61$), from Gupta[12]

6.4.2 Low Speed Forward Flight

In forward flight, for wheels on the ground, CFD velocity vectors on a vertical plane through the front rotor hub and parallel to the fuselage are shown in Figure 6.16. Also, velocity vectors along a plane parallel to the ground, at a height of 0.05 rotor diameters, are shown in Figure 6.17. These images will help in identifying the flow regimes discussed in Section 6.3.2. At near hover ($\chi = 1^\circ$), these figures show that ahead of the front wing, the flow from the front rotor wake is turned in a longitudinal direction toward the front of the aircraft. At a skew angle of 18° , this longitudinal flow forms recirculating vortical region just ahead of the front rotors in a horseshoe shape. At a skew angle of 43° , this vortical flow region is located directly under the front wing. Figure 6.17(c) shows that the two front rotors form separate horseshoe vortices which meet beneath the fuselage, under the front wing.

This behavior is very similar to the ground surface flow images presented in Section 6.3.2 and agrees with the explanation given for the changes in download and pressure measured on the vehicle.

6.5 Comparison with Previous Experiment

Wood, et al.[1] obtained smoke flow visualization images on the front and rear wings and also underneath the fuselage. A strong fountain flow was observed above the front wing. The fountain flow on the rear wing was observed to be much weaker. While smoke flow was not performed in the current research, these results agree with the surface flow images suggesting spanwise flows towards the center of the fuselage

on both the wings.



Figure 6.18: Smoke Flow Visualization, from Wood, et al.[1]

Figure 6.5 shows the smoke flow visualization image underneath the fuselage for $z = 0.86$. A fountain flow formed by interaction of the front rotor wakes can be noted. This was also suggested by the tuft flow visualization images obtained in the current study.

Chapter 7

Closure

The Quad Tilt Rotor (QTR) is a heavy lift V/STOL design concept, whose goal is to carry very large payloads over long distances. The payload carrying capacity of this vehicle is heavily dependent on its performance in the take-off flight regime, where it operates in helicopter mode. Therefore, the focus of this research was to study the performance characteristics of a QTR in hover and low speed forward flight, IGE.

To achieve this goal, an experimental approach was developed to study the lifting performance of a QTR in hovering/transition flight at various heights above the ground, IGE and OGE. For operation in low speed forward flight, a unique moving test apparatus was developed and utilized, in order to avoid the confined space and boundary layer problems associated with wind tunnel testing IGE, at these low forward airspeeds. A small geometrically scaled model of the QTR was used to obtain quantitative measurements of QTR performance, in terms of airframe download, rotor thrust and power measurements. Pressures along the centerline of the bottom of the fuselage were measured for different flight conditions, to explore the mechanisms causing changes in the download on the vehicle. Tuft flow visu-

alization was performed on the surfaces of the fuselage and wings and also on the ground plane, to relate the changes in the download and pressure measurements to the physical processes causing them.

The knowledge gained from these studies was used to estimate the improvements in lifting performance that might be possible when the vehicle is operated at low airspeeds near the ground in ground effect (IGE). This extra lifting capability is of prime importance to the military who is considering the development and use of new large vertical lift aircraft to move large payloads in unprepared areas. Additional lift and/or download reductions can theoretically be transformed into an additional payload.

7.1 Conclusions

The experimental approach developed in this dissertation expanded the understanding of QTR operation in the critical flight regime of very low speed forward flight near the ground. Overall, it was confirmed that there is a potential for significant gains in QTR performance QTR by operating in hover and low speed forward flight IGE. It was also shown that it might be possible to utilize these performance enhancements to increase the payload and/or reduce the power requirements of the vehicle IGE. The key conclusions from this study are summarized below:

7.1.1 Experimental Approach

- The moving test setup developed to facilitate low speed testing IGE was found to be effective at simulating the performance of a QTR in the take-off flight regime.
- Geometric parameters such as the shape and configuration of the model, normalized height above the ground and rotor wake skew angle were found to be the key scaling factors determining the performance of a QTR in hover and low speed forward flight, IGE.
- Varying the rotor disk loading (and therefore, the average downwash velocity) was found to cause a secondary effect on the performance and flowfield on this small-scale QTR model, at different flight conditions. This further confirms the previous statement identifying the geometry of the problem as the most important scaling parameter.

7.1.2 Hover Performance

- There is a strong download of about 9% of the total rotor thrust, OGE. This was caused by the presence of the wings in the rotor downwash, which also caused fountain flows on both the front and rear wings.
- With a decrease in height above the ground, the download was found to reduce from the OGE value. For close operation to the ground, the download disappeared and became an upload. The upload increased with a reduction in

height above the ground and attained a value of about 9% of the total rotor thrust, when the wheels of the QTR are on the ground.

- The reduction in download and the subsequent increase in upload IGE, was caused by a high pressure under the fuselage and the wings. Tuft flow visualization of the ground plane and the surfaces of the airframe indicated that the wakes from the four rotors meet underneath the fuselage and are turned upward around the fuselage. Pressure measurements along the bottom of the fuselage indicated high pressure regions between the front and rear wings, IGE.
- Because of the reduction in download, the rotor thrust required to hover at a given total vehicle thrust reduces. As a result, the total rotor power required to hover, for a given vehicle thrust, decreased with a reduction in height above the ground. When the wheels are on the ground, the power required to hover was about 70% of the OGE value, for a given vehicle thrust. As the rotors are only marginally IGE, a majority of this reduction in power occurs as a result of reduction in rotor thrust requirements.
- The total vehicle thrust for a given power, increased with a decrease in height above the ground. When the wheels are on the ground, the available vehicle thrust was about 125% of the OGE value in hover, for a given power.

7.1.3 Low Speed Forward Flight

- Out of ground effect (OGE), at low skew angles (less than 35°), the download reduced slightly with an increase in skew angle. At a skew angle of 35° ,

the download reduces to about 6.5% of the total rotor thrust. With further increase in skew angle, the download to thrust ratio decreased rapidly and became an upload of about 6% at a skew angle of 68°. The reduction in download from the hover value causes a reduction in rotor thrust and power requirements for a given vehicle thrust. At a skew angle of 68°, the power required for a constant vehicle thrust reduced by 40% from the hover value. The vehicle thrust available, at a given power, correspondingly increased by about 25% of the hover value, at this skew angle.

- In ground effect, at an intermediate range of skew angles, the upload reduced from the hover value (by about 2% to 3% of the total rotor thrust for front rotor heights less than 0.86 rotor diameters). With further increase in skew angle, the upload recovered and exceeded the hover value. The skew angle at which the maximum reduction in upload occurred, decreased with an increase in height above the ground from about 43° when the wheels were on the ground to about 27° at a front rotor height of 1.5 rotor diameters.
- A ground vortex that was formed ahead of the front rotors was found to be responsible for some of the changes in the upload. Using tuft flow visualization and by comparing with CFD flow images, the location of the ground vortex at different skew angles was identified IGE, for different heights above the ground. The skew angle at which the vortex was located just ahead of the nose, was associated with the reduction in upload on the front of the fuselage. Pressure

measurements confirmed the effect of this vortex on the pressure under the fuselage.

- The reduction in upload at the intermediate range of skew angles, IGE, caused an increase in rotor thrust and power requirements as compared to hover. When the wheels were on the ground, the required power (for a given vehicle thrust, normalized by OGE power in hover) at a skew angle of about 30° increased by about 5% from the hover value. The vehicle thrust available (for a given power, normalized by OGE vehicle thrust in hover) also correspondingly reduced from the hover value by about 5%, thereby reducing the net gain in lifting capacity to about 15%. However, in spite of this reduction, the lifting capacity of the vehicle is still greater than for OGE operation at the same skew angle, by about 10%.

7.1.4 Comparison with other studies

- The downwash velocity distribution of the propellers used for the experiment was found to compare well with full-scale V-22 rotor downwash measurements.
- The download results and the flow patterns that were obtained compare well with the results of the hover study of Wood, et al.[1].
- The measured download to thrust ratios and the recorded flow patterns agreed well with the CFD study of Gupta[12, 15], in hover and low speed forward flight, OGE.

- The measured upload, IGE, for the CFD study of Gupta[12] was lower than the experimental measurements, when the wheels were on the ground, by about 2% of the total rotor thrust. Some of this discrepancy is thought to be a result of the geometric configuration of the QTR used for the CFD study, which was slightly different from the model used for the experiment.
- However, the trends of the upload with an increase in skew angle were similar for both the experiment and the CFD study[12]. Also, the flowfields obtained by the CFD study IGE were similar to the surface flow images obtained by the experiment. This implies that the underlying physical mechanisms causing the performance changes IGE are likely to be similar.

7.2 Ramifications for a Full-Scale QTR

The results of this study have positive ramifications for the development of the QTR as a heavy lift design concept. By operating a QTR near the ground, in hover and at low forward speeds, there is a potential for significant performance gains. The change in the loads on the airframe from a download of about 9% of the total rotor thrust, OGE, to an upload of as much as 9% of the total rotor thrust, IGE, causes a total change of about 18% of the total rotor thrust. As the QTR has been designed to carry as much as 40% of its weight in payload, this would cause an increase of almost 50% in the payload carrying capacity in hover.

In order to show the increase in lifting capacity, the averaged trends of vehicle thrust for a given power is plotted versus skew angle for two cases in Figure 7.1.

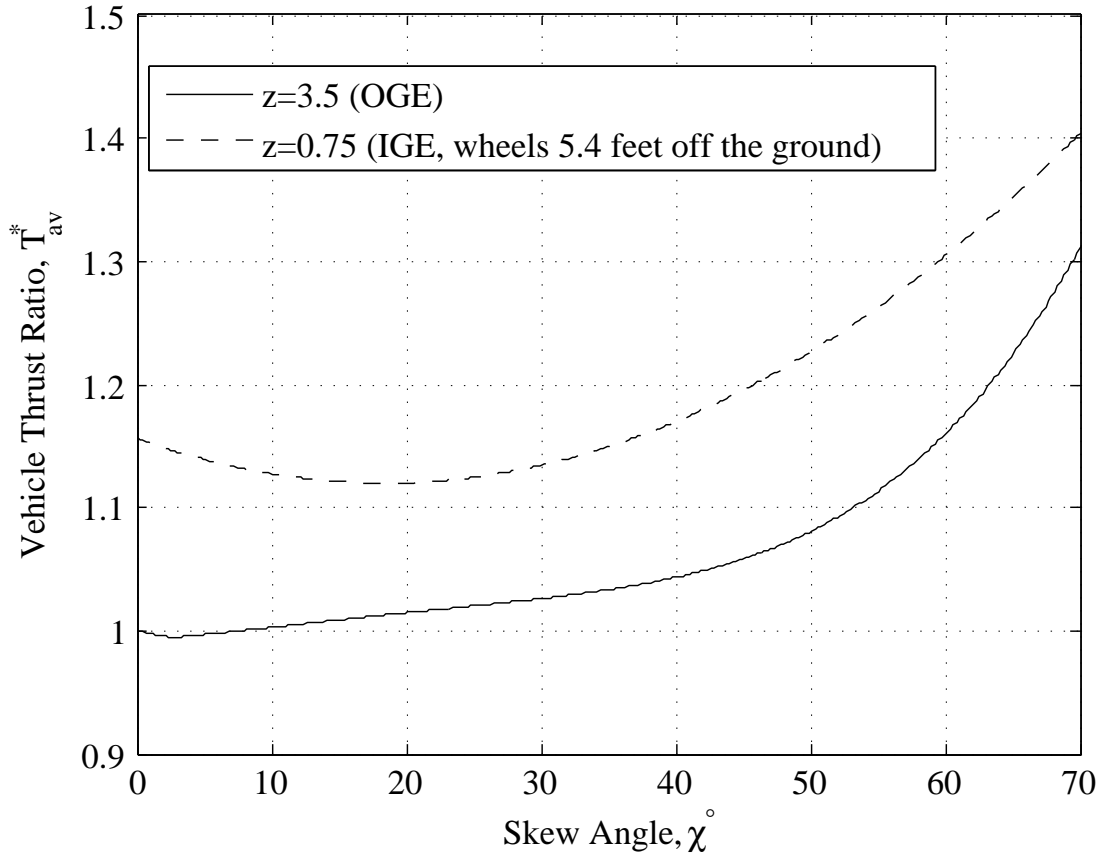


Figure 7.1: Trends of Vehicle Thrust for a Given Power in Forward Flight

The first case was for OGE operation (shown by the solid line) and the second case was for a front rotor height of 0.75 rotor diameters. The IGE case corresponds to a wheel height of 5.4 feet for a full-scale QTR, which is a feasible height for low speed operation near the ground.

The plot shows that there is about a 15% increase in vehicle thrust available at a given power, in hover, by operating at this height. The gain in vehicle thrust persists even as the vehicle starts moving at low skew angles. This implies that the takeoff trajectory of the aircraft could be adjusted to operate close to the ground in low speed forward flight in order to take advantage of the increase in payload

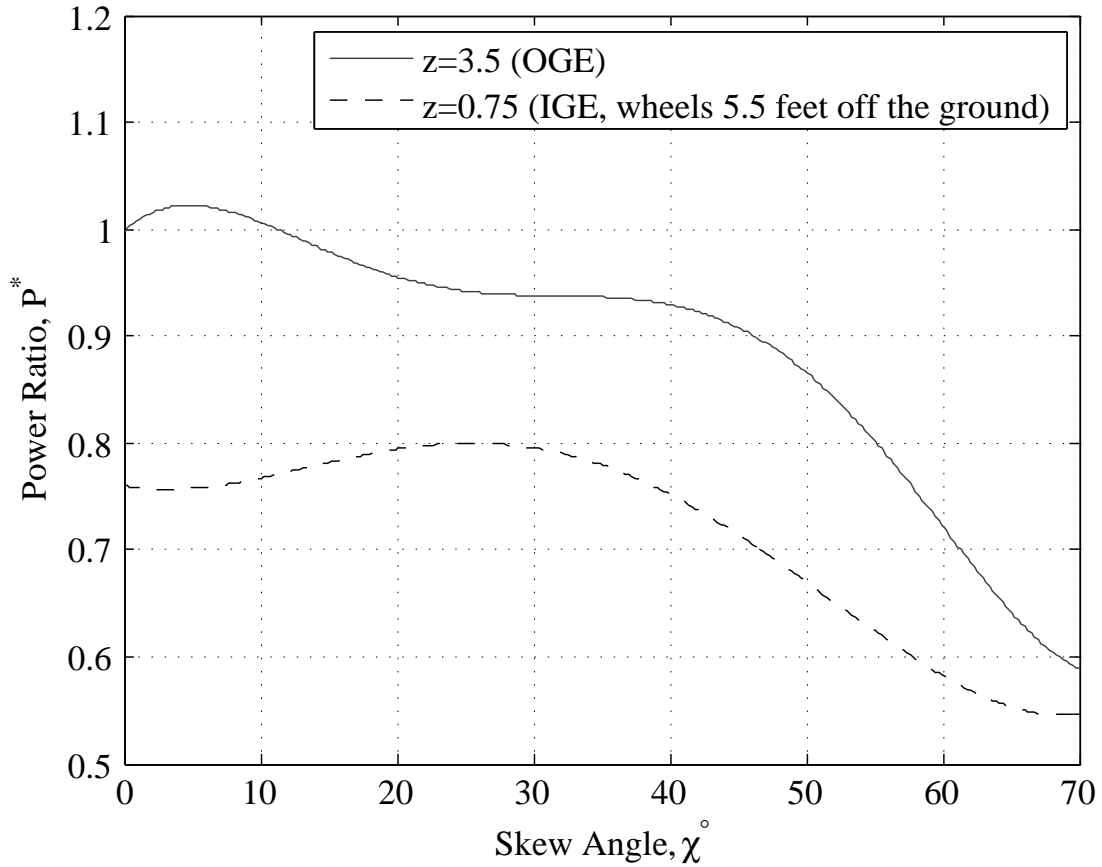


Figure 7.2: Trends of Power Required for a Given Vehicle Thrust in Forward Flight

carrying capacity.

These performance gains are also shown in Figure 7.2 as an increase in power for a given vehicle thrust for a range of skew angles, IGE and OGE. In hover, there is an excess power of about 25% of the OGE power by operating at a wheel height of 5.5 feet off the ground. As in the case of the gain in vehicle thrust, the excess power IGE persists even in forward flight and could potentially be used to accelerate the vehicle while carrying larger payloads.

7.3 Direction of Future Research

7.3.1 Studies on the QTR

Using the test setup developed for this study, further testing on the QTR design for other important parameters are suggested. The following topics are planned to be explored in subsequent testing:

7.3.1.1 Effect of Crossflow and Yaw

It was shown that the performance enhancements obtained by operating the QTR in close proximity to the ground do not fade away rapidly with an increase in forward speed, in an ideal forward flight environment. However, in practice, the QTR will be exposed to crosswinds and other disturbances as it operates in hover and low forward speeds. The crosswinds will have the effect of disturbing the longitudinal symmetry of the flow around the aircraft. The loss of symmetry might affect the ground cushion formed underneath the aircraft, which is responsible for the upload experienced by the aircraft IGE. The sensitivity of the upload to crosswinds is currently unknown. To simulate this effect, the QTR model needs to be tested at several yaw angles.

7.3.1.2 Effect of Nacelles and Sponsons

The experimental tests conducted to date, have been for the QTR model with the nacelles and sponsons removed. This simplification was made under the assumption that these modeling refinements would have a secondary effect on the

measured downloads. Adding the nacelles and sponsons as they are designed on the full-scale QTR configuration will result in a higher fidelity small-scale model. This model can be experimentally tested to confirm that the effect of adding the nacelles and sponsons (combined as well as independently) on the download and the power measurements is secondary.

7.3.1.3 Configuration Studies

The studies described in this dissertation were performed on a preliminary configuration of the QTR, which was provided by Bell Helicopter. It might be possible to improve the design of the QTR by studying the effects of varying different configuration parameters such as rotor/wing separation distance, direction of rotor rotation, relative position of the wings, etc. Using this experimental setup, it should be possible to extend the scope of this research to study such design changes.

7.3.2 Testing of Other Designs

The test rig developed for testing the performance of the small-scale QTR is unique in that it provides an inexpensive method to test various V/STOL aircraft models in low-speed forward flight, at different heights above the ground.

7.3.2.1 Tilt Rotors

The experiment has demonstrated the feasibility of obtaining reasonable measurements of QTR performance in the low speed IGE regime. The QTR shares a lot of technological features with the V-22, including the rotor system. With limited

modifications, the test rig can be adapted to obtain performance measurements for the V-22 tilt rotor in the low speed regime, at different heights above the ground.

7.3.2.2 Other V/STOL Designs

With appropriate modifications and scaling, it should be possible to test use this test setup to study other V/STOL designs. An example would be a jet engine aircraft using thrust vectoring to provide a ground cushion.

Appendix A

Power Corrections

Because fixed pitch propellers are used, the desired thrust is obtained by varying the rpm. The measured torque and power of the rotor are presented for different rpms in Chapter 3 in Figures 3.5 and 3.6.

The total measured power of the rotors, which contains contributions from induced power, P_i , and profile power, P_0 , can be expressed as follows:

$$P = P_i + P_0 \quad (\text{A.1})$$

where,

$$P_i = \kappa \frac{T^{3/2}}{\sqrt{2\rho A}} \quad (\text{A.2})$$

and

$$P_0 = C_{P0} \rho A (\Omega R)^3 \quad (\text{A.3})$$

Also,

$$C_P = C_{P_i} + C_{P_0} = \kappa \frac{C_T^{3/2}}{\sqrt{2}} + C_{P_0} \quad (\text{A.4})$$

where, κ , or the induced power correction factor, is the factor used to account for all non-ideal effects on rotor induced power. C_P , C_{P_i} and C_{P_0} are the total, induced and profile power coefficients.

On a real QTR, the rpm will be held constant and the desired thrust will be obtained by changing the collective pitch of the rotor. This will result in a change in thrust coefficient, C_T , and induced power on the rotor. It can be reasonably assumed that the profile power coefficient of the rotor will remain constant, as the rotor rpm is constant. Therefore, the profile power will also remain constant.

For the small-scale fixed-pitch propellers, the rotor rpm will be different for each case and because the rotor profile power varies as a function of rpm, the profile power will not remain constant. In addition, changes in rpm will cause changes in Reynolds number. At these low Reynolds numbers, this will mean that the C_{P0} , will no longer remain constant, and will vary as a function of rpm.

The measured power from the experiment can be corrected to represent the power consumed by a hypothetical constant rpm rotor, which varies the thrust by changing the collective pitch of the rotor. For this purpose, the behavior of κ and C_{P0} for different C_T and rpms need to be obtained.

In hover, the induced power can be computed from momentum theory using a correction for non-ideal effects, κ . The value of the induced power correction factor, κ , is quite dependent on the downwash distribution of the rotor. It is possible to calculate the value of κ for a rotor by varying the value of thrust coefficient and obtaining the slope of the curve between $C_T^{3/2}/\sqrt{(2)}$ and C_P . Because the C_T of the fixed-pitch propellers can't be varied at a given RPM, the value of κ cannot be obtained directly. However, the relationship between κ and C_T for an XV-15 rotor, which has also has a similar downwash distribution as a V-22 rotor, is available from previous literature[6, 79]. The variation of κ vs C_T , from McVeigh, et al.,[6]

and Bartie, et al.,[79] is shown in Figure A.1.

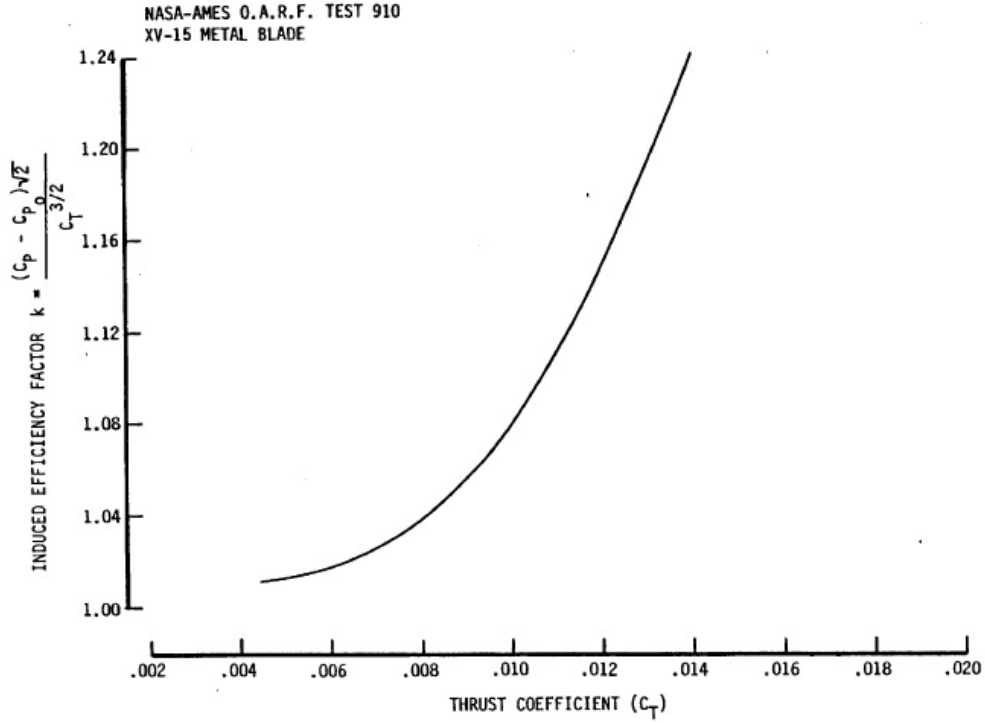


Figure A.1: Rotor Induced Power Correction Factor vs. Thrust Coefficient (from Bartie, et al.[79])

The downwash distribution of the rotors used in this experiment has been measured and compared with that of a V-22 rotor, as shown in Figures 3.10 and 3.9. For the isolated rotor in hover, by looking up the κ for a given C_T , the induced power can be calculated and subtracted from the total measured power in order to obtain the profile power coefficient, C_{P0} as a function of rpm.

$$C_{P0} = \frac{P - \kappa \frac{T^{3/2}}{\sqrt{2\rho A}}}{\rho A (\Omega R)^3} \quad (\text{A.5})$$

The relationship between C_{P0} and rpm can be used as a lookup table to determine the profile power for each test case.

Appendix B

Comparison with CFD QTR

Geometry

The QTR configuration used for the CFD studies of Gupta[12] and Gupta & Baeder[74, 15] featured some geometric differences from the Bell QTR design, which was used for this study. The geometry of the CFD and experimental studies are compared in this Appendix.

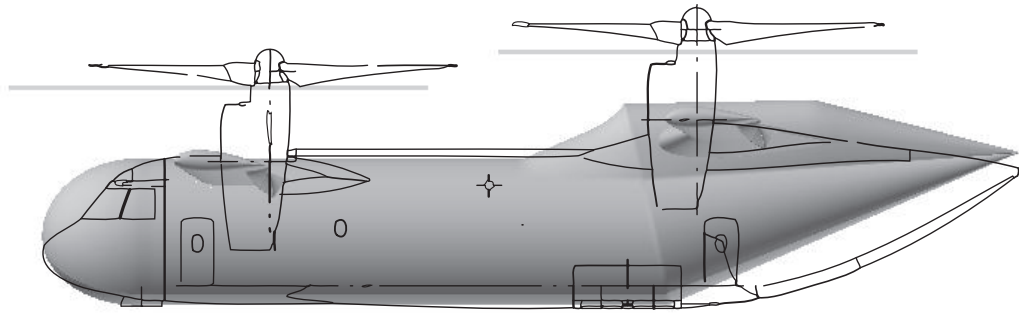
Figures B.1 (a) and (b) present the side and top views of Gupta's CFD configuration overlaid with a sketch of the Bell QTR design used by the experiment. The main differences are also quantified in Table B.1. The rotor/wing separation distance for Gupta's CFD grid was 0.16 rotor diameters, as compared to 0.21 rotor diameters for the experiment. The longitudinal separation of the front and rear rotors was 1.15 rotor diameters for the CFD design in comparison to 1.0 rotor diameters for the experiment. The CFD design did not incorporate the cross-shafting present in the experimental model. From the top view image in Figure B.1 (a), it can also be seen the the front wing span for the CFD design was also greater than the experiment, although the lateral separation of the rotors was identical. The

spanwise extent of the wing trailing edge flaps was also slightly less for the CFD design.

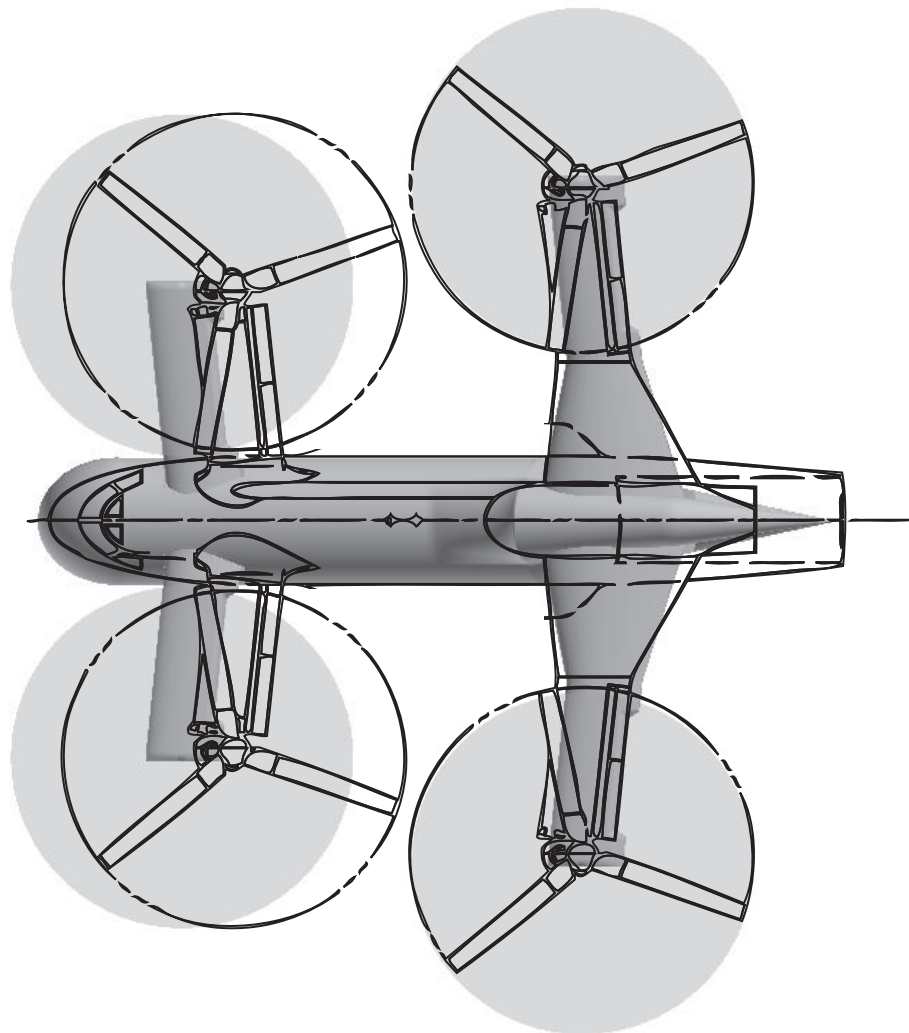
These differences in configuration could cause changes in the performance that is predicted by the CFD model, especially IGE. These differences are discussed in more detail in Chapters 4 and 5.

Table B.1: Differences between Gupta & Baeder’s CFD Geometry and the Experimental QTR Configuration

Feature	CFD	Experiment
Rotor/Wing Separation Distance	0.16D	0.21D
Longitudinal Distance between front and rear rotors	1.15D	1.0D
Cross-shafting	No	Yes
Nacelles & Sponsons	No	Removable



(a) Side View



(b) Top View

Figure B.1: Overlay of the QTR Geometries used for the experimental and CFD studies

Appendix C

Uncertainty analysis

Uncertainty analysis was performed on the measured quantities using the procedure detailed in the ASME manual on Test Uncertainty[80]. This was used to determine the 95% confidence levels of the data. As an example, the complete procedure followed in calculating the uncertainty in download to thrust ratio is presented below.

C.1 Example: Download to Thrust Ratio

C.1.1 Define the Measurement Process

The Download to Thrust ratio ($\frac{DL}{T}$) for a QTR is determined by dividing the sum of the downloads measured at the front and the back of the airframe by the sum of the thrust measured on the four rotors.

$$\frac{DL}{T}\% = \frac{DL_1 + DL_2}{T_1 + T_2 + T_3 + T_4} \quad (\text{C.1})$$

Several simplifying assumptions are made for these measurements:

- (a) Theists and airframe loads are measured by load cells constrained to measure

the load in a vertical direction by means of linear bearings.

(b) There is minimal friction in the bearings.

(c) Loads are primarily vertical.

(d) The output of the load cells is measured and recorded by a computerized data acquisition system (DAS).

(e) The DAS automatically makes the calibration corrections and unit conversions.

(f) The DAS takes 32160 samples at 8000 samples/second (approximately 4 seconds of data) for each reading.

(g) The average values of thrust and airframe loads are calculated for each reading and used to calculate $\frac{DL}{T}$.

(h) The experiment is repeated 31 times for the case where the QTR wheels are on the ground, in hover, in order to determine the random error in $\frac{DL}{T}$.

C.1.2 List Elemental Uncertainty Sources

The sources of uncertainty which are considered random in this measurement are those causing variation in 31 repeated readings of loads. The number of repeated readings is chosen to ensure that the number of degrees of freedom, ν , is at least 30, for using a value of student's t of 2. The sources of uncertainty that are considered systematic are the uncertainty of calibration of the instruments used to measure and record the loads.

C.1.3 Calculate Random Standard Deviation

The standard deviation, S_{X_i} , of the 31 readings, X_i , is calculated using the following formula:

$$S_{X_i} = \sqrt{\frac{1}{\nu} \sum_{j=1}^{30} (X_i - \bar{X})^2} \quad (\text{C.2})$$

The average of all the 31 readings is given by \bar{X} . Since there are 31 pairs, the degrees of freedom, ν is given by:

$$\nu_i = 31 - 1 = 30 \quad (\text{C.3})$$

C.1.4 Calculate Systematic Uncertainties

C.1.4.1 Calibration

The loads for each of the parameters is measured with a load cell, signal conditioning module, signal conditioning board and DAS. These are all calibrated together as a system to obtain the calibration slope, assuming that the load cell response is completely linear within the measurement range. Also, the manufacturer specified uncertainty values are factored into the systematic uncertainty. The calibration error can be obtained by performing repeated calibrations of the equipment and obtaining standard deviation of the calibration slope, B_S . Also, further calibration errors are introduced by the uncertainty in the standardized weights used for calibration, B_W . The maximum resolution of the DAS also contributes to the uncertainty of the readings, given by B_D .

C.1.4.2 Resolution of the DAS

The DAS that is used has a 12 bit resolution. This means that it can measure 2^{12} gradations in the range used for the sensor channel. The thrust load cells have a range of 25 lbs. Therefore, the resolution of the DAS for the thrust channels is given by $\frac{25}{2^{12}} = 0.0061$ lbs. The download load cells have a range of 10 lbs, which corresponds to a resolution of 0.0024 lbs.

C.1.4.3 Calibration weights

The weights used for the calibration have an uncertainty of 0.001 lbs. This uncertainty is also included in the analysis as B_W .

C.1.5 Combining Elemental Systematic Uncertainties

The systematic errors due to calibration slope, resolution and calibration weight are combined as follows:

$$B_R = \sqrt{B_S^2 + B_W^2 + B_D^2} \quad (C.4)$$

C.1.6 Total Uncertainty of the measurement

The total uncertainty of the measurement is determined as follows:

$$U_{95} = t \sqrt{\frac{B^2}{2} + S_{\bar{X}}^2} \quad (C.5)$$

where a value of 2 is used for Student's t.

Tables C.1, C.2 and C.3 display the results obtained from the methodology described for the uncertainty analysis at a nominal disk loading of 4.7 lb/sq.ft.

on each rotor. It can be seen that the random uncertainty dominates over the systematic uncertainty. There is an absolute uncertainty of 0.53% for an individual measurement, for the download to thrust ratio expressed as a percentage. However, depending on the number of times that each test case is repeated, the absolute uncertainty of the mean of download to thrust ratio will be reduced by $\frac{0.53}{\sqrt{n}}$, where n is the number of repetitions.

Table C.1: Absolute Values of Systematic Uncertainties of Independent Parameters for T/A=4.7 lb/sq.ft, at z=1.5

<i>Symbol</i>	Feature	units	Nominal Value	B_S Cal-ibration uncertainty	B_W Cal-ibration weight uncertainty	B_R Res-olution uncertainty	B_i Ab-solute Systematic Uncertainty
T_1	Thrust for Rotor 1	lb	5	0.00424	0.001	0.0061	0.0075
T_2	Thrust for Rotor 2	lb	5	0.00487	0.001	0.0061	0.00787
T_3	Thrust for Rotor 3	lb	5	0.00414	0.001	0.0061	0.00744
T_4	Thrust for Rotor 4	lb	5	0.00464	0.001	0.0061	0.00773
DL_f	Front Download	lb	0.73	0.00421	0.001	0.00244	0.00497
DL_r	Rear Download	lb	0.93	0.00517	0.001	0.00244	0.0058

For a nominal disk loading of 0.9 lbs on each rotor, the uncertainty analysis is displayed in table C.4. For this case, the systematic uncertainty provides a greater contribution to the total uncertainty than for the disk loading of 4.7 lb/sq.ft. The total uncertainty for the download to thrust ratio is much higher than the 4.7 lb/sq.ft. case and has a value of 1.13%.

From previous measurements, the download over thrust varies from a download of about 9% OGE to an upload of about 9% when the wheels are on the ground.

Therefore, the total range will be 18%.

Table C.2: Absolute Contributions of Systematic Uncertainties of Independent Parameters for T/A=4.7 lb/sq.ft, at z=1.5

<i>Symbol</i>	Feature	units	Nominal Value	Absolute Sensitivity (θ_i)	Absolute Systematic Uncertainty Contribution ($(\frac{B_i}{2}\theta_i)^2$)
T_1	Thrust for Rotor 1	lb	5.00	0.00417	2.449e-10
T_2	Thrust for Rotor 2	lb	5.00	0.00417	2.699e-10
T_3	Thrust for Rotor 3	lb	5.00	0.00417	2.415e-10
T_4	Thrust for Rotor 4	lb	5.00	0.00417	2.605e-10
DL_f	Front Download	lb	0.73	0.05	1.542e-8
DL_r	Rear Download	lb	0.93	0.05	2.103e-8

Table C.3: Summary: Nominal Value; Systematic, Random and Total Uncertainties in Absolute Terms for DL/T for T/A=4.7 lb/sq.ft, at z=1.5

<i>Symbol</i>	Feature	units	Nominal Value	Absolute Systematic Uncertainty, $t\sqrt{\sum(\frac{B_i}{2}\theta_i)^2}$	Sys- Un- B_R	Absolute Random Uncertainty, tS_R	Total Absolute Uncertainty, U_R $t\sqrt{\frac{B_i^2}{2} + S_R^2}$
$\frac{DL}{T}$	Download to Thrust ratio	%	8.355	0.0378914		0.5344	0.5358

Table C.4: Uncertainties in Absolute Terms for DL/T for T/A=0.9 lb/sq.ft., at z=1.5

<i>Symbol</i>	Feature	units	Nominal Value	Absolute Systematic Uncertainty, $t\sqrt{\sum(\frac{B_i}{2}\theta_i)^2}$	Sys- Un- B_R	Absolute Random Uncertainty, tS_R	Total Absolute Uncertainty, U_R $t\sqrt{\frac{B_i^2}{2} + S_R^2}$
$\frac{DL}{T}$	Download to Thrust ratio	%	8.67	0.194		1.115	1.132

C.2 Uncertainty Analysis of other measurements

Using a similar procedure to the uncertainty analysis described for download-to-thrust ratio, other quantities are also similarly evaluated. The absolute systematic, random and total uncertainty in these parameters are compiled for a nominal test case in Table C.5. This test case had a value of disk loading of 0.9 lbs/sq.ft., at a skew angle of 65° for the case where the wheels are on the ground. The uncertainty in power and available thrust are not presented, as they are semi-empirical quantities, with a lot of analytical assumptions.

Table C.5: Uncertainties in Absolute Terms for DL/T for T/A=0.9 lb/sq.ft.

<i>Symbol</i>	Feature	units	Nominal Value	Absolute Systematic Uncertainty, $t\sqrt{\sum (\frac{B_i}{2}\theta_i)^2}$	Sys- Un- certainty, B_R	Absolute Random Uncertainty, tS_R	Total Absolute Uncertainty, U_R $t\sqrt{\frac{B_i}{2}^2 + S_R^2}$
$\frac{DL_f}{T}$	Download to Thrust Ratio (front airframe mount)	%	4.3	0.13		0.98	1.0
$\frac{DL_r}{T}$	Download to Thrust Ratio (rear airframe mount)	%	8	0.16		0.4	0.43
χ	Rotor Wake Skew Angle	°	65	0.2		2.4	2.4
z	Normalized Front rotor height		0.607	0.006		0.018	0.019
C_{pDL}	Pressure Ratio (for Port 3)		0.54	0.02		0.04	0.042

Bibliography

- [1] Wood, T., Collins, B., and Isaac, M., “Quad Tiltrotor: A Solution for Intra-Theater Lift,” *Proceedings of the 58th Annual Forum*, American Helicopter Society, Montreal, Canada, June 2002.
- [2] Snyder, D., “The Quad Tiltrotor: Its Beginning and Evolution,” *Proceedings of the 56th Annual Forum*, American Helicopter Society, Virginia Beach, Virginia, May 2000.
- [3] Gervais, M., *Tiltrotor Noise Reduction Through Flight Trajectory Management and Aircraft Configuration Control*, Ph.D. thesis, Dept. of Aerospace Engineering, University of Maryland, 2004.
- [4] Felker, F. and Light, J., “Aerodynamic Interactions Between a Rotor and Wing in Hover,” *Journal of the American Helicopter Society*, Vol. 33, No. 2, April 1988, pp. 53–61.
- [5] Wood, T. and Peryea, M., “Reduction of Tiltrotor Download,” *Proceedings of the 49th Annual Forum*, American Helicopter Society, St. Louis, Missouri, May 1993, pp. 1177–1191.
- [6] McVeigh, M., “The V-22 Tilt-rotor Large-Scale Rotor Performance/Wing Download Test and Comparison with Theory,” *Proceedings of the 11th European Rotorcraft Forum*, London, England, September 1985.

- [7] Marr, R., Ford, D., and Ferguson, S., "Analysis of the Wind Tunnel Test of a Tilt Rotor Powered Force Model," Tech. Rep. CR 137529, NASA, June 1974.
- [8] Anon, "Wind Tunnel Test of a Powered Tilt Rotor Performance Model," Tech. Rep. TR-71-62, AFFDL, October 1972.
- [9] Fradenburgh, E., "Aerodynamic Factors Influencing Overall Hover Performance," Tech. Rep. C.P. 111, AGARD, September 1972.
- [10] Wilson, J. C., Mineck, R. E., and Freeman, C. E., "Aerodynamic characteristics of a powered tilt-proprotor wind tunnel model," Tech. Rep. NASA-TM-X-72818, National Aeronautics and Space Administration, 1976.
- [11] Desopper, A., Routhieau, V., Roth, G., von Grunhagen, W., and Haverdings, H., "Study of the Low Speed Characteristics of a Tiltrotor," *Proceedings of the 28th European Rotorcraft Forum*, Bristol, UK, September 2002.
- [12] Gupta, V., *Quad Tilt Rotor Simulations in Helicopter Mode using Computational Fluid Dynamics*, Ph.D. thesis, Dept. of Aerospace Engineering, University of Maryland, College Park, MD, 2005.
- [13] Felker, F., "A Review of Tilt Rotor Download Research," *Proceedings of the 14th European Rotorcraft Forum*, Milan, Italy, 1988.
- [14] Lestari, A., Niazi, S., and Rajagopalan, R., "Preliminary Numerical Analysis of a Quad Tilt rotor Flowfield and Performance," *Proceedings of the Tiltrotor/Runway Independent Aircraft Technology and Applications Specialists' Meeting*, American Helicopter Society, Arlington, Texas, March 2001.

- [15] Gupta, V. and Baeder, J., “Quad Tiltrotor Aerodynamics in Helicopter Mode,” *Proceedings of the 61st Annual Forum*, American Helicopter Society, Grapewine, TX, June 2005.
- [16] Curtiss, H., Erdman, W., and Sun, M., “Ground Effect Aerodynamics,” *Vertica*, Vol. 11, No. 1/2, 1987.
- [17] J.F. Boer, C. H. and Pengel, K., “Experimental and theoretical assessment of the helicopter ground vortex phenomenon,” Based on a presentation held at the CEAS - TRA3 Conference on 10-12 June 2002, Cambridge, UK.
- [18] Turner, T. R., “A Moving-Belt Ground Plane For Wind-Tunnel Ground Simulation and Results For Two Jet-Flap Configurations,” Tech. Rep. NASA TN D-4228, NASA, 1967.
- [19] Turner, T. R., “Endless-Belt Technique for Ground Simulation,” *Proceedings of the Conference on V/STOL and STOL Aircraft*, No. NASA SP-116, 1966.
- [20] Putman, W. and Curtiss, H., “Low Speed Testing Techniques for V/STOL Aircraft in the Princeton Dynamic Model Track,” *Proceedings of the 17th Aerospace Sciences Meeting*, AIAA, New Orleans, LA, Jan 1979.
- [21] Curtiss, H., Sun, M., Putman, W., and Hanker, E.J., J., “Rotor Aerodynamics in Ground Effect At Low Advance Ratios,” *Journal of the American Helicopter Society*, Vol. 29, No. 1, January 1984, pp. 48–55.

- [22] Tai, T. C. and Vorwald, J., "Simulation of V-22 Rotorcraft Hover Flowfield," *Proceedings of the AIAA International Powered Lift Conference*, American Institute of Aeronautics and Astronautics, Santa Clara, CA, December 1993.
- [23] Maisel, M., Giulianetti, D., and Dugan, D., *The History of the XV-15 Tilt Rotor Research Aircraft: From Concept to Flight*, No. SP-2000-4517, NASA, 2000.
- [24] Little, R., "V-22 Osprey Given Green Light," Dallas Morning News, 2005.
- [25] aerospace technology.com, WWW Page, 2006, Retrieved April 4, 2006 from <http://www.aerospace-technology.com/projects/ba609/>.
- [26] Wyatt, D., editor, *Eagle Eye Pocket Guide*, Bell Helicopter Textron, Inc., 2005.
- [27] Kussner, H., "Helicopter Problems," Tech. Rep. NACA-TM-827, NACA, 1937.
- [28] Betz, A., "The Ground Effect On Lifting Propellers," Tech. Rep. NACA-TM-836, NACA, 1937.
- [29] Knight, M. and Hefner, R., "Analysis of Ground Effect on the Lifting Airscrew," Tech. Rep. NACA TN 835, NACA, 1941.
- [30] Leishman, J., *Principles of Helicopter Aerodynamics*, Cambridge University Press, Cambridge, UK, 2000.
- [31] Zbrozek, J., "Ground Effect on the Lifting Rotor," Tech. Rep. R.&M. No. 2347, British A.R.C., 1950.

- [32] Cheeseman, I. C. and Bennett, W., "The Effect of the Ground on a Helicopter Rotor in Forward Flight," Tech. Rep. R.&M. No. 3021, British A.R.C., 1957.
- [33] Stepniewski, W. and Keys, C., *Rotary Wing Aerodynamics*, Dover Publications, New York, 1984.
- [34] Heyson, H., "Ground Effect for Lifting Rotors in Forward Flight," Tech. Rep. TN D-234, NASA, 1960.
- [35] Light, J., "Tip Vortex Geometry of a Hovering Helicopter Rotor in Ground Effect," *Proceedings of the 45th Annual Forum Proceedings*, American Helicopter Society, Boston, MA, May 1989.
- [36] Jenkins, J.L., J., "Trim Requirements and Static-Stability Derivatives from a Wind-Tunnel Investigation of a Lifting Rotor in Transition," Tech. Rep. NASA TN-D-2655, NASA, February 1965.
- [37] Huston, R. and Morris, C.E.K., J., "A Wind-Tunnel Investigation of Helicopter Directional Control in Rearward Flight in Ground Effect," Tech. Rep. TN D-6118, NASA, March 1971.
- [38] Empey, R. and Ormiston, R., "Tail Rotor Thrust on a 5.5 Foot Helicopter Model in Ground Effect," *Proceedings of the 30th Annual Forum*, Washington, DC.
- [39] Weisner, W. and Kohler, G., "Tail Rotor Performance in Presence of Main Rotor, Ground, and Winds," *Journal of the American Helicopter Society*, Vol. 19, No. 3, July 1974.

- [40] Heyson, H. H., "Theoretical Study of Conditions Limiting V/STOL Testing in Wind Tunnels with Solid Floor," Tech. Rep. NASA TN-D-5819, NASA, 1970.
- [41] Sheridan, P. and Weisner, W., "Aerodynamics of Helicopter Flight Near The Ground," *Proceedings of the 33rd Annual Forum*, American Helicopter Society, Washington, DC, May 1977.
- [42] Saijo, T., Ganesh, B., Huang, A., and Komerath, N., "Development of Unsteadiness in a Rotor Wake in Ground Effect," *Proceedings of the 21st Applied Aerodynamics Conference*, AIAA, Orlando, Florida, June 2003.
- [43] Ganesh, B. and Komerath, N., "Unsteady Aerodynamics of Rotorcraft in Ground Effect," *Proceedings of the 22nd Applied Aerodynamics Conference and Exhibit*, AIAA, Providence, RI, August 2004.
- [44] Ganesh, B., Komerath, N., Pulla, D., and Conlisk, A., "Unsteady Aerodynamics of Rotorcraft in Ground Effect," *Proceedings of the 43rd AIAA Aerospace Sciences Meeting and Exhibit*, AIAA, Reno, Nevada, Jan 2005.
- [45] Putman, W., "An Experimental Investigation of Ground Effect on a Four-Propeller Tilt-Wing V/STOL Model," Tech. Rep. 68-45, USAAVLABS, July 1968.
- [46] Branum, L. and Tung, C., "Performance and Pressure Data from a Small Model Tilt-Rotor in Hover," TM 110441, NASA, 1997.

- [47] Tung, C. and Brannum, L., “Model Tilt-Rotor Hover Performance and Surface Pressure Measurement,” *Proceedings of the 46th Annual Forum*, American Helicopter Society, Washington, DC, May 1990.
- [48] Felker, F., Signor, D., and Young, L., “Performance and loads data from a hover test of a full-scale advanced technology XV-15 rotor,” Tech. Rep. TM 86854, NASA, January 1986.
- [49] Felker, F., Signor, D., Young, L., and Betzina, M., “Performance and Loads Data From a Hover Test of a 0.658-Scale V-22 Rotor and Wing,” Tech. Rep. TM 89419, NASA, April 1987.
- [50] Felker, F. F., “Wing Download Results from a Test of a 0.658-Scale V-22 Rotor and Wing,” *Journal of the American Helicopter Society*, Vol. 37, No. 4, October 1992, pp. 58–63.
- [51] Swanson, A. A. and Light, J. S., “Shadowgraph Flow Visualization of Isolated Tiltrotor and Rotor/Wing Wakes,” *Proceedings of the 48th Annual Forum*, American Helicopter Society, Washington, D.C., June 1992, pp. 1323–1344.
- [52] Matos, C. and Komerath, N., “Download Modification using Surface Blowing,” *Proceedings of the Aeromechanics Specialists Meeting*, American Helicopter Society, Atlanta, GA, November 2000.
- [53] Mosher, M. and Light, J., “Study of Noise on a Small-Scale Hovering Tilt Rotor,” *Journal of the American Helicopter Society*, Vol. 41, No. 2, April 1996, pp. 27–36.

- [54] Conner, D. and Wellman, J., “Hover Acoustic Characteristics of the XV-15 with Advanced Technology Blades,” *Journal of Aircraft*, Vol. 31, No. 4, 1994.
- [55] Narramore, J., Grauer, W., and Farrell, M., “Aerodynamic Evaluation of the V-22 Osprey Wing Section,” *Proceedings of the 50th Annual Forum*, American Helicopter Society, Washington, DC, May 1994.
- [56] Polak, D., Rehm, W., and George, A., “Effects of an Image Plane on the Tiltrotor Fountain Flow,” *Journal of the American Helicopter Society*, Vol. 45, No. 2, April 2000, pp. 90–96.
- [57] Liu, S. R., Brieger, J., and Peryea, M., “Model Tiltrotor Flow Field/Turbulence Ingestion Noise Experiment and Prediction,” *Proceedings of the 54th Annual Forum*, Washington, DC, 1998.
- [58] Heuze, O., Diaz, S., and Desopper, A., “Simplified models for tiltrotor aerodynamic phenomena in hover and low speed flight,” *Proceedings of the Aerodynamics Research Conference*, CEAS Aerospace, Cambridge, UK, June 2002.
- [59] Clark, D. R., “Analysis of the Wing/Rotor and Rotor/Rotor Interactions Present in Tilt-Rotor Aircraft,” *Vertica*, Vol. 11, No. 4, 1987, pp. 731–749.
- [60] Fejtek, I. and Roberts, L., “Navier-Stokes Computation of Wing/Rotor Interaction for a Tilt Rotor in Hover,” *AIAA Journal*, Vol. 30, No. 11, November 1992, pp. 2595–2603.

- [61] Meakin, R. L., “Unsteady Simulation of the Viscous Flow About a V-22 Rotor and Wing in Hover,” *Proceedings of the Atmospheric Flight Mechanics Conference*, AIAA, Baltimore, MD, Aug 1995.
- [62] Tadghighi, H., Rajagopalan, G., and Burley, C., “Simulation of Fountain Flow Field Effects Using a Finite Volume Technique - An Aero/Acoustic Study,” *Proceedings of the 51st Annual Forum*, American Helicopter Society, Fort Worth, TX, 1995, pp. 77–92.
- [63] Poling, D. R., Rosenstein, H., and Rajagopalan, G., “Use of a Navier-Stokes Code in Understanding Tiltrotor Flowfields in Hover,” *Journal of the American Helicopter Society*, Vol. 43, No. 2, 1998, pp. 102–109.
- [64] Felker, F. and Light, J., “Rotor/Wing Aerodynamic Interactions in Hover,” *Proceedings of the 42nd Annual Forum Proceedings*, American Helicopter Society, Washington, DC, June 1996.
- [65] Young, L., Earl R. Booth, J., Yamauchi, G., and Botha, G., “Overview of the Testing of a Small-Scale Proprotor,” *Proceedings of the 55th Annual Forum*, American Helicopter Society, Montreal, Canada, May 1999.
- [66] Yamauchi, G. K., Burley, C., Merker, E., Pengal, K., and JanikiRam, R., “Flow measurements of an isolated model tilt rotor,” *Proceedings of the 55th Annual Forum*, American Helicopter Society, Montreal, Canada, May 1999.
- [67] Betzina, M. D., “Rotor Performance of an Isolated Full-Scale XV-15 Tiltrotor in Helicopter Mode,” *Proceedings of the Aerodynamics, Acoustics, and Test*

- and Evaluation Technical Specialists Meeting*, American Helicopter Society, San Francisco, CA, January 2002.
- [68] Weiberg, J. A. and Maisel, M. D., “Wind-tunnel tests of the XV-15 tilt rotor aircraft,” Tech. Rep. NASA-TM-81177, National Aeronautics and Space Administration, 1980.
- [69] McVeigh, M. A., Grauer, W., and Paisley, D., “Rotor/Airframe Interactions on Tiltrotor Aircraft,” *Journal of the American Helicopter Society*, Vol. 35, No. 2, April 1990, pp. 43–51.
- [70] Young, L., Lillie, D., McCluer, M., and Yamauchi, G., “Insights into Airframe Aerodynamics and Rotor-on-Wing Interactions from a 0.25-Scale Tiltrotor Wind Tunnel Model,” *Proceedings of the AHS International Aerodynamics, Acoustics, and Test and Evaluation Specialists Conference*, American Helicopter Society, San Francisco, CA, January 2002.
- [71] Yamauchi, G. K., Wadcock, A. J., and Derby, M. R., “Proceedings of the Measured Aerodynamic Interaction of Two Tiltrotors,” *59th Annual Forum*, American Helicopter Society, Phoenix, Arizona, May 2003.
- [72] Potsdam, M. A., Schaller, D. F., Rajagopalan, R. G., and Silva, M. J., “Proceedings of the Tilt Rotor Aeromechanics Phenomena in Low Speed Flight,” *4th Decennial Specialists’ Conference on Aeromechanics*, American Helicopter Society, San Francisco, CA, January 2004.

- [73] Gupta, V. and Baeder, J., “Quad Tiltrotor Aerodynamics in Ground Effect,” *Proceedings of the 58th Annual Forum*, American Helicopter Society, June 2002.
- [74] Gupta, V. and Baeder, J., “Low Mach Number Preconditioning for Tiltrotor Rotor-Wing Interaction,” *Proceedings of the 4th Decennial Specialist’s Conference on Aeromechanics*, American Helicopter Society, San Francisco, California, January, p. 2004.
- [75] Buckingham, E., “On Physically Similar Systems: Illustrations of the Use of Dimensional Equations,” Tech. Rep. 4, Physical Review, 1914.
- [76] Buckingham, E., “The principle of similitude,” Tech. Rep. 96, Nature.
- [77] Glauert, H., “On the Horizontal Flight of a Helicopter,” Tech. Rep. R.&M. No. 1730, British A.R.C., 1926.
- [78] Bennett, J., “Rotary Wing Aircraft: A series of articles,” *Aircraft Engineering*, 1940.
- [79] Bartie, K., Alexander, H., McVeigh, M., Lamon, S., and Bishop., H., “Hover Performance Tests of Baseline Metal and Advanced Technology Blade (ATB) Rotor Systems for the XV-15 Tilt Rotor Aircraft,” Tech. Rep. NASA CR 177436, NASA, 1982.
- [80] ASME, *Test Uncertainty*, ptc 19.1-1998 ed., 1998.

- [81] Radhakrishnan, A. and Schmitz, F., “An Experimental Investigation of a Quad Tilt Rotor in Ground Effect,” *Proceedings of the 21st Applied Aerodynamics Conference*, AIAA, Orlando, Florida, June 2003.
- [82] Radhakrishnan, A. and Schmitz, F., “An Experimental Investigation of a Quad Tilt Rotor in Low Speed Forward Flight,” *Proceedings of the 4th Decennial Specialists’ Conference on Aeromechanics*, American Helicopter Society, San Francisco, CA, January 2004.
- [83] Radhakrishnan, A. and Schmitz, F., “Quad Tilt Rotor Aerodynamics in Ground Effect,” *Proceedings of the 23rd Applied Aerodynamics Conference*, AIAA, Toronto, Canada, June 2005.
- [84] Radhakrishnan, A. and Schmitz, F., “Quad Tilt Rotor Download And Power Measurements In Ground Effect,” *Proceedings of the 24th Applied Aerodynamics Conference*, AIAA, San Francisco, CA, June 2006.